Stimulated Raman Adiabatic Passage between Metastable and Rydberg States of Helium

A Dissertation Presented

by

Yuan Sun

to

The Graduate School

in Partial Fulfillment of the Requirements

for the Degree of

Doctor of Philosophy

in

Physics

Stony Brook University

December 2013

Stony Brook University

The Graduate School

Yuan Sun

We, the dissertation committee for the above candidate for the Doctor of Philosophy degree, hereby recommend acceptance of this dissertation.

Harold Metcalf – Dissertation Advisor
Distinguished Teaching Professor, Department of Physics and Astronomy

Vladimir Goldman – Chairperson of Defense
Professor, Department of Physics and Astronomy

Tzu-Chieh Wei
Assistant Professor, Department of Physics and Astronomy & C. N. Yang Institute for Theoretical Physics

Nikita Nekrasov
Professor and Permanent Member
Simons Center for Geometry and Physics

This dissertation is accepted by the Graduate School.

Charles Taber
Dean of the Graduate School

Abstract of the Dissertation

Stimulated Raman Adiabatic Passage between Metastable and Rydberg States of Helium

by

Yuan Sun

Doctor of Philosophy

in

Physics

Stony Brook University

2013

Two directions are available in atomic physics research, namely, the internal degrees of freedom of the atom and the external degrees of freedom of the atom. Here I am going to present an experiment whose focus is on the internal degrees of freedom, namely, the coherent manipulations of atomic states. The motivation of this experiment is to investigate the coherent population transfer and associated effects of a three level atomic system, with the third level being a long–lived Rydberg state. The scheme adopted here is stimulated Raman adiabatic passage, often known as STIRAP.

The basic layout of this experiment is that an atomic beam of metastable helium ($n = 2$) with average velocity 1070 m/s orthogonally crosses two laser beams in

a tunable dc electric field. An infrared laser near $\lambda = 790$ - 830 nm connects the 3^3P state to the Rydberg states ($n = 12$ - 50) and an ultraviolet laser of $\lambda = 389$ nm connects the metastable 2^3S state to the 3^3P state. The positions of the two laser beams, the detunings of the lasers' frequencies with respect to the atomic transitions, and the polarizations of the lasers can all be varied. An ion detector is set up above the uv and ir lasers interaction region to detect ions produced by the Rydberg atoms.

A third laser beam is applied several mm downstream after the uv and ir lasers' interaction region, providing a strong bichromatic force acting on the $2^3S \rightarrow 2^3P$ transition with $\lambda = 1083$ nm. The atoms in the Rydberg states are not affected by this while the atoms remaining in the 2^3S state are deflected by a large angle. The absolute fraction of Rydberg atoms can be established by measuring the flux of the deflected atoms.

It has been known for a long time that the Rydberg atoms can be ionized by background thermal radiation at room temperature and this is observed in our experiment. This fact actually enables precise measurement, especially spectroscopy, of Rydberg atoms by simply looking at the ions, which are easy to detect. It is also confirmed that background thermal radiation could significantly redistribute the population among neighboring Rydberg states.

The 2^3S, 3^3P and the final Rydberg state all have magnetic sublevels, hence the linkage pattern of the excitation pathways has non-trivial crossings if the polarizations of the two lasers are not parallel to each other. Those crossings in the excitation paths can lead to interference which determines the excitation probability and the orientation of the excited atom. Calculations predict interesting

interference patterns as a function of laser polarizations and Rabi frequencies. However, detunings of lasers can wash these interesting details out and leave only the main features. Those interference features have been experimentally observed.

The transverse velocity distribution in the atomic beam turns out to be a limiting factor in the efficiency of production of Rydberg atoms. The transverse velocity of an atom can not only induce one-photon detuning but also two-photon detuning, which can effectively reduce the STIRAP process efficiency. By adding a laser to make Doppler molasses in the transverse direction, we can heat or cool the atomic beam transversely and verify this effect.

For my memories as a student, and for all of you who make my memories vivid.

Even when Ph.D students graduate, their spirits haunt the labs forever.

Contents

List of Figures

List of Tables

Chapter 1

Introduction

1.1 Survey and Motivation

Two relatively distinct directions exist in atomic physics research. One direction tends to focus on the internal degrees of freedom of an atom, such as Ramsey fringes, while the other direction tends to treat the atom as a whole and focus on atomic motion and atom-atom interactions, such as BEC. Often a lot of techniques would be shared in both directions, and sometimes a chemical interaction between both directions can lead to interesting consequences, such as the Rydberg-Rydberg blockade experiments [1].

Of particular interest is the vision about where the field of AMO physics is going. Let us first look at a few examples of currently emerging 'patterns'. In terms of super-fine resolution imaging technology, there is the single atom imaging of ultra cold atoms, which I find amusing if compared to the STORM of optical microscopy, and SEM from the condensed matter community. In terms of many body physics, ultracold atoms now have the name of 'quantum simulator'. In terms of high energy physics, AMO physicists are now experimentally searching for EDM. On the direction of the external degrees of freedom of the atom,

the trend seems to be that to build larger and larger quantum mechanical objects from the bricks of cold atoms/molecules, and then research many body physics with them. Yet, it is very hard to say what the vision for the entire field is just because AMO physics is now so broad and interdisciplinary.

The precision aspect of atomic physics has a profound influence on the common life. For instance, what would the world be without atomic physics? Well, my GPS would not work hence I could not drive home!

Rydberg atoms have the advantage of allowing the internal and external degrees of freedom to be exploited at the same time in a 'harmonic' way. The wavelengths of the transitions between Rydberg energy levels correspond to a very interesting frequency range in the electromagnetic wave spectrum. Therefore the Rydberg atom is a very hopeful candidate.

1.1.1 The Era of Quantum Mechanics

Quantum mechanics has deeply changed the way the science is, the way people's lives are, and more profoundly, the way we think. I could not imagine how atomic physics would be like without quantum mechanics. Within the realm of atomic physics, quantum mechanics is not merely some complicated math formulation. Rather, it provides a consistent picture which combines experimental results and interpretations together.

The way we approach a problem now, usually, is to begin with writing down the Schrödinger equation. This is fundamentally different than, say, 100 years ago, at which time we would first seek a classical description. We are so used to the quantum way of thinking that our ideas often advance our methods now, for example, the quantum communication and the quantum computer, which are rather hard to experimentally build because the world we live in is so classical.

Therefore, as our tools have been advancing all the time, more and more purely quantum devices will show up. What we will really enjoy doing is to perform the corresponding scientific research to embrace this era of quantum mechanics.

1.1.2 Recent Trends: Rydberg Atoms and Quantum Information

After the recent discovery of the Rydberg–Rydberg blockade phenomena, the Rydberg atom ensemble has become an ideal candidate for quantum information purposes [2] [3].

The underlying story is simple, and even belongs to the regime of classical physics only: the Rydberg atom has a large electric dipole moment, and then the electric field generated by the dipole moment of a Rydberg atom would induce Stark shift in neighboring Rydberg atoms. The story becomes interesting when quantum entanglement can be established by this Rydberg–Rydberg interaction. Namely, when two atoms are put next to each other and subject to a resonant excitation laser, only one of the two atoms can be excited into the Rydberg state because of this dipole induced Stark shift. This phenomenon is named Rydberg blockade. It has been observed extensively in many related experiments, especially in the form that only a certain portion of an atom cloud can be excited into the Rydberg states, provided the density is high enough for the dipole interaction to be strong enough.

Therefore, the entanglement can be viewed as that the system of these two atoms have a ground state $|g, g\rangle$ and an excited state $\frac{1}{\sqrt{2}}(|g, e\rangle + |e, g\rangle)$. The state $|e, e\rangle$ is out of the consideration for the fact that its energy in the dressed atom picture is quite different from $\frac{1}{\sqrt{2}}(|g, e\rangle + |e, g\rangle)$, as a consequence of the Rydberg blockade.

If we make N atoms entangled in this manner instead of two, then we have a system of the ground state $|g, \cdots, g\rangle$ and the excited state $\frac{1}{\sqrt{N}}(|e, g, \cdots, g\rangle + |g, e, \cdots, g\rangle + \cdots + |g, \cdots, g, e\rangle)$. This is essentially a two level system, and henceforth it gets the name 'super

atom' [4]. Again, the reason for this simplification is the entanglement established via the Rydberg blockade, which shifts the energy of all the other configurations of the excited states. The Rabi oscillations of a super atom will have a Rabi frequency different from that of a single atom, precisely by the factor of $\sqrt{N}$. This Rabi frequency has been experimentally observed in the Rabi oscillation of a super atom and hence the entanglement is verified.

One key issue in quantum information science is the entanglement, and the Rydberg atom is now a hopeful candidate for the entanglement established by the Rydberg blockade. Currently, various further exploitations are under way. The advantage of Rydberg atoms is the possibility of entangling many atoms all together.

Another recent development, led by Prof. Lukin and Prof. Vuletic's collaboration team at Harvard and MIT, is the new optically nonlinear medium realized by the Rydberg atoms. This is along the line of a series of innovations in quantum optics lead by Prof. Lukin, both theoretically and experimentally. The basic idea is to open a transparency window for photons via EIT in a cold atom ensemble, which relies upon a transition to the Rydberg state. Because of the Rydberg blockade, once one atom is excited by one photon, the other photon can not excite neighboring atoms and hence its group speed is no longer limited by the EIT. Therefore in the end, the two photons tend to 'combine' altogether.

1.1.3 Atom Optics and Motivation of Our Work

Atom optics is the field of manipulating atoms analogous to that of manipulating light with optics. The history dates back to Stern and Gerlach's experiments in the early 1920s [5] [6], followed by the atomic-diffraction experiments by Estermann [7] and others in the early 1930s . These experiments demonstrated unambiguously that wave mechanics also applies to composite particles. Recent progress in the area of matter waves greatly enhanced the

development of atom optics. The utilization of the wave property of the atoms makes the name 'atom optics' very appropriate.

We first do a little history digest. In the late 1970s, Hänsch and Schawlow proposed a method to cool atomic gases by laser radiation [8]. Further exploitations of this idea eventually led to the invention of laser-cooling, with a Nobel prize awarded in 1997. With the help of laser cooling, the atomic samples can be brought down to temperatures of the order of 10^{-6} K or less, and therefore the atomic de Broglie wavelengths are on the order of microns or longer [9]. The creation of Bose-Einstein condensates in a dilute gas of alkali atoms [10] follows as a natural consequence of the cooling technologies. It has been shown extensively that atomic beams can be reflected [11], diffracted [12][13] and focused [14][15][16][17], by applying laser beams around the atomic resonances. A static electric field (or magnetic field) gradient can also be used for the same purpose on a beam of slow neutral atoms [18] [19].

The atom optics has an application in neutral atom nanolithography [20]. The high internal energy of He* atoms can be utilized to print nanoscale structure through a resist assisted lithography mode [21]. Preliminary results showing the focusing effect of an electric hexapole lens on Rydberg atoms have been described in S-H. Lee's thesis [22], which relies upon the large electric dipole moment of the Rydberg atoms.

1.2 Atomic Absorption of Light

1.2.1 Energy Transfer between Atom and Light

During the interaction between the atom and the light field, energy transfer takes place. The atom undergoes absorption, spontaneous emission and stimulated emission. Once the properties of the light fields are given, it is straightforward to know the time evolution of

the atom by treating the light fields semi-classically and therefore the energy exchange from the atom's point of view can be figured out.

However, if the light field is composed of more than one light beam it would be interesting to figure out the energy exchange between the atom and each single one of the light beams. Many authors have treated this problem very well in the framework of quantum optics, such as in [23].

Here I am going to briefly present a method under the semi-classical picture, without arousing further quantum field theories.

When some external force is exerting work on a particle, the power is $\mathcal{P} = \vec{F} \cdot \vec{v}$. When some electromagnetic field is exciting an atom, it can also be viewed as the electromagnetic field is doing work on the electron. Then the power is $\mathcal{P} = (-e\vec{E} - e\vec{v} \times \vec{B}) \cdot \vec{v} = -e\vec{E} \cdot \vec{v}$, since the Lorentz force does not do work. Now we want to construct a corresponding (quantum) operator for the power. The operator $\frac{\vec{p}}{m}$ would be used for $\vec{v}$, therefore we have $\mathcal{P} = -e\vec{E} \cdot \frac{\vec{p}}{m}$, where e is positive as a charge unit.

The expectation value of the power operator describes the power delivered to the atom by the light field. $P(t) = \langle \alpha(t) | \mathcal{P} | \alpha(t) \rangle$ when the wavefunction of the atom (more precisely, the electron) is $|\alpha(t)\rangle$. Since the atom is treated semi-classically, the work (which is the integration of $P(t)$ over time) of the light field won't be automatically quantized by $\hbar\omega$.

Of particular interest is how this simple method could be applied to the case of a two level atom, with $|1\rangle$ being the ground state and $|2\rangle$ being the excited state. First let us look at the example without spontaneous emission. Then formally we have:

$$P(t) = -\frac{e}{m} \begin{pmatrix} \langle \alpha(t)|1\rangle & \langle \alpha(t)|2\rangle \end{pmatrix} \begin{pmatrix} 0 & \vec{E} \cdot \vec{p}_{12} \\ \vec{E} \cdot \vec{p}_{21} & 0 \end{pmatrix} \begin{pmatrix} \langle 1|\alpha(t)\rangle \\ \langle 2|\alpha(t)\rangle \end{pmatrix} \tag{1.1}$$

Here in (1.1), $\vec{p}_{ij} = \langle i|\vec{p}|j\rangle$ and the diagonal elements are zero because of the parity of the

momentum $\vec{p}$. This can be formally computed and linked to the dipole moment, by using commutators of $\vec{x}$ and $\mathcal{H}_0$: $[\vec{x}, \mathcal{H}_0] = i\hbar\frac{\vec{p}}{m}$.

$$\vec{p}_{12} = \langle 1|\vec{p}|2\rangle = m\langle 1|\frac{-i}{\hbar}[\vec{x}, \mathcal{H}_0]|2\rangle = -im\omega_0\langle 1|\vec{x}|2\rangle \tag{1.2}$$

Usually, when we are solving for $\langle 1|\alpha(t)\rangle$ and $\langle 2|\alpha(t)\rangle$, the solution is described in the rotating wave frame. Therefore, let us rewrite the above equation with respect to the rotating wave frame $|1'\rangle$ and $|2'\rangle$ assuming that $|2'\rangle$ is rotating at frequency ω', i.e. $|2'\rangle = e^{-i\omega' t}|2\rangle$.

$$\begin{aligned} P(t) &= -\frac{e}{m}\begin{pmatrix}\langle\alpha(t)|1'\rangle & \langle\alpha(t)|2'\rangle\end{pmatrix}\begin{pmatrix}0 & e^{-i\omega' t}\vec{E}\cdot\vec{p}_{12}\\ e^{i\omega' t}\vec{E}\cdot\vec{p}_{21} & 0\end{pmatrix}\begin{pmatrix}\langle 1'|\alpha(t)\rangle\\ \langle 2'|\alpha(t)\rangle\end{pmatrix} \\ &= -2\frac{e}{m}\,\mathrm{Re}(\langle\alpha(t)|1'\rangle\langle 2'|\alpha(t)\rangle e^{-i\omega' t}\vec{E}\cdot\vec{p}_{12}) \end{aligned} \tag{1.3}$$

Some caution is in order here. Usually some very high frequency term (most often, twice the optical frequency) will show up in the result of the above equation (1.3). However, this semi-classical method has no ability to predict or compute the details in such a short period of time as the reciprocal of the very high frequency. Our interest is not in what is going on during a very short time interval either. Therefore, the actual physical quantity of 'power', shall be viewed as the time-averaged value of (1.3) within a reasonable time interval. Then the very high frequency terms would cause no more worries. We will see examples in later discussions.

If the two level atom is only driven by a single frequency laser beam then according to (1.3) the laser does no net work on atom. Indeed this is the case, since if there is no spontaneous emission acting as dissipation, absorption and stimulated emission would balance out leaving the laser doing zero work on the atom.

1.2.2 Absorption of Light by a Two Level Atom with Spontaneous Emission

In the case of a two level atom with spontaneous emission, the method in 1.2.1 applies all the same. The change is that now the density matrix approach has to be taken and the expectation value of the power operator has to be taken under the density matrix approach too.

First, we solve the Optical Bloch Equation for the time evolution of $\rho(t) = \begin{pmatrix} \rho_{11} & \rho_{12} \\ \rho_{21} & \rho_{22} \end{pmatrix}$. We still want to write it in the rotating wave frame whose 'rotation frequency' ω' and the atomic resonance frequency ω_0 satisfy $\delta = \omega' - \omega_0$. And let $\tilde{\rho}_{12} = \rho_{12} e^{-i\delta t}$. Then we can write the Optical Bloch Equation as the follows:

$$\begin{aligned} \frac{d}{dt}\rho_{11} &= +\gamma\rho_{22} + \frac{i}{2}(\Omega^*\tilde{\rho}_{21} - \Omega\tilde{\rho}_{12}) \\ \frac{d}{dt}\rho_{22} &= -\gamma\rho_{22} + \frac{i}{2}(\Omega\tilde{\rho}_{12} - \Omega^*\tilde{\rho}_{21}) \\ \frac{d}{dt}\tilde{\rho}_{12} &= -(\frac{\gamma}{2} + i\delta)\tilde{\rho}_{12} + \frac{i}{2}\Omega^*(\rho_{22} - \rho_{11}) \\ \frac{d}{dt}\tilde{\rho}_{21} &= -(\frac{\gamma}{2} - i\delta)\tilde{\rho}_{21} + \frac{i}{2}\Omega(\rho_{11} - \rho_{22}) \end{aligned} \tag{1.4}$$

In (1.4) γ is the spontaneous decay rate, and Ω is the Rabi frequency of the laser field. Here Ω might be the consequence of many laser fields, not necessarily restricted to a single one. Formally, the definition of the Rabi frequency is $\hbar\Omega \equiv -eE_{\text{total}}\langle 2|r|1\rangle$.

In analogy to (1.3), we can compute $P(t)$ of one of the laser fields, once $\rho = \rho(t)$ is calculated from (1.4). Here the basis is with respect to the rotating wave frame too. Since we are in the world of only two levels for now, polarization effects aren't showing up, and I will drop the vector property of $\vec{E}$ and $\vec{p}$.

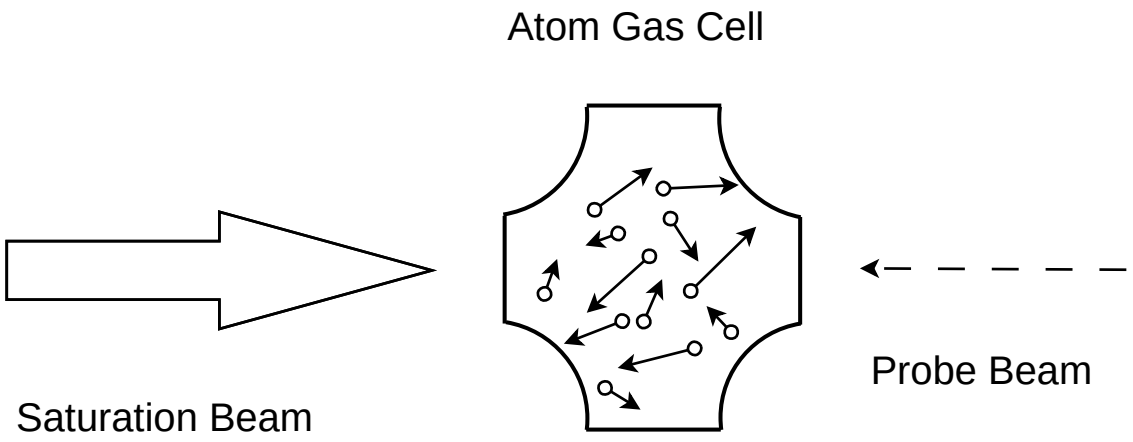

Figure 1.1: Schematic drawing of saturation absorption spectroscopy

$$P(t) = -\frac{e}{m} tr\left(\begin{pmatrix} \rho_{11} & \rho_{12} \\ \rho_{21} & \rho_{22} \end{pmatrix} \begin{pmatrix} 0 & e^{-i\omega' t} E p_{12} \\ e^{i\omega' t} E p_{21} & 0 \end{pmatrix} \right)$$
$$= -\frac{e}{m}(\rho_{12} e^{i\omega' t} E p_{21} + \rho_{21} e^{-i\omega' t} E p_{12}) = -2\frac{e}{m} \mathrm{Re}(\rho_{12} e^{i\omega' t} E p_{21}) \tag{1.5}$$

Let us now apply this method to saturation absorption spectroscopy. Namely, we have a strong saturation laser beam and a weak probe laser beam of the same frequency, counter-propagating and overlapping in the atom gas cell. The intensity of both laser beams are unchanged while the frequency of both lasers are scanned across the resonance of the two level atoms inside the cell. We are interested to know the absorption of the probe beam for a given velocity group of atoms.

Suppose the atom is an ideal two level atom with spontaneous emission rate γ and the resonance frequency is ω_0. Both the saturation beam and the probe beam are detuned at δ. Suppose the Rabi frequency of the saturation beam is Ω_s and the Rabi frequency of the probe beam is Ω_p. And suppose the velocity of the atom is v. Typically the probe beam is

much weaker than the saturation beam hence the internal time evolution of the atom can be regarded as being solely determined by the saturation beam, provided we assume the phases of the two lasers are the same. According to results of a steady state solution, the time evolution of the two level atom can be described by:

$$\rho_{21} = \frac{i\Omega_s}{2(\gamma/2 - i(\delta + kv))(1+s)} \tag{1.6}$$

Where the saturation parameter s is defined as:

$$s \equiv \frac{|\Omega_s|^2}{2|(\gamma/2 - i(\delta + kv))|^2} = \frac{|\Omega_s|^2/2}{(\delta + kv)^2 + \gamma^2/4} \tag{1.7}$$

According to (1.5), the work done on the atom by the probe beam can be computed in a similar way. Note that an atom traveling at speed v for the saturation beam is traveling at speed $-v$ for the probe beam. And note that the frequency belonging to the rotating frame is ω', in order to arrive at (1.6).

$$\begin{aligned} P_p(t) &= -2\frac{e}{m}\,\mathrm{Re}\{\frac{i\Omega_s}{2(\gamma/2 - i(\delta + kv))(1+s)} e^{-i\omega' t} E_p \cos((\omega' - kv)t) p_{12}\} \\ &= 2\hbar\omega_0 \frac{\Omega_p}{\Omega_s}\frac{s}{1+s}\{(\gamma/2\sin(kvt) + \cos(kvt)(\delta + kv))\sin\omega' t\cos\omega' t \\ &+ \sin(kvt)(\delta + kv)\cos^2\omega' t + \gamma/2\cos(kvt)\sin^2\omega' t\} \end{aligned} \tag{1.8}$$

Those terms as in (1.8) are fast oscillating at the laser frequency ω'. The real physical world responses at a speed much lower than that, henceforth the right way to interpret that high frequency ω' is to take the average over time. $\sin\omega' t\cos\omega' t$ would average to 0, while $\cos^2\omega' t$ and $\sin^2\omega' t$ would average to 1/2. So finally we arrive at the power of the probe

beam's work on the atom, or put in another way, the absorption of the probe beam by the atom.

$$P_p(t) = \hbar\omega_0 \frac{\Omega_p}{\Omega_s} \frac{s}{1+s} \{\sin(kvt)(\delta + kv) + \gamma/2 \cos(kvt)\} \tag{1.9}$$

Let us focus on the $v = 0$ atoms only, and then (1.9) becomes $P_p(t) = \hbar\omega_0 \frac{\Omega_p}{\Omega_s} \frac{s}{1+s} \cdot \gamma/2$. We can compare this to the scattering rate of the probe beam without saturation beam: $\hbar\omega_0 \frac{s_p}{1+s_p} \cdot \gamma/2$, where s_p is the saturation parameter for the probe beam. We see clearly that the absorption of the probe beam is suppressed, by the factor $\frac{\Omega_p}{\Omega_s}$.

(1.9) is valid for small kv and small δ. Since if the atom sees the two lasers different in frequency it is very likely that its internal motion is no longer dominated by the saturation beam and hence it voids my previous assumption for the calculation.

This simple method of calculating absorption of light, together with the momentum transfer associated, can of course be extended to a more general setting. The light field would be quantized and the Hamiltonian shall be given under the quantized light field setting, revoking the semi-classical picture. The expectation value of any operators shall be evaluated by wavefunctions obeying this Hamiltonian. And the operator which represents the power shall be written in an invariant way.

1.2.3 Quantum Nature of Light and Fluctuations

All we have done previously is around the expectation value of a 'power operator'. However, if we stop at any moment to make a measurement, or care about the classical and mechanical motion of the atom which is to be discussed in the following section, the atom is not going to necessarily follow this expectation value. Rather, the atom would drop into different eigenstates with certain probabilities, whose average value in the end would reduce

to the expectation value.

A complete and satisfactory answer to this issue could be complicated. Yet to get a better understanding of what is going on, we can take a look at the uncertainty, or variance, of this 'power operator' $\mathcal{P}$ whose expectation value $P(t)$ is computed in (1.5). In plain language, I am going to evaluate $\langle(\Delta\mathcal{P})^2\rangle = \langle\mathcal{P}^2\rangle - \langle\mathcal{P}\rangle^2$. So now it is time to check $\langle\mathcal{P}^2\rangle$, which requires to compute the operator p^2 in the 2 by 2 form first as a crucial step.

Actually it is a subtle task to compute p^2 under the two level atom setting. A seemingly very direct calculation would look like (1.10), but this is wrong. Since, the assumption of entering the two-level atom's world: 'The two levels form a complete set' is not applicable is this case. The operator p can couple $|1\rangle$ or $|2\rangle$ to essentially every eigenstate of the atom Hamiltonian with the correct parity.

$$\begin{pmatrix} 0 & e^{-i\omega' t}Ep_{12} \\ e^{i\omega' t}Ep_{21} & 0 \end{pmatrix} \cdot \begin{pmatrix} 0 & e^{-i\omega' t}Ep_{12} \\ e^{i\omega' t}Ep_{21} & 0 \end{pmatrix} = \begin{pmatrix} p_{12}p_{21} & 0 \\ 0 & p_{12}p_{21} \end{pmatrix} \tag{1.10}$$

The evaluation of p^2 can be viewed from another aspect too. We can start from $\mathcal{H}_0 = \frac{p^2}{2m} + V(x)$, and we know that: $-\langle 1|\mathcal{H}_0|1\rangle + \langle 2|\mathcal{H}_0|2\rangle = \hbar\omega_0$. The parity of $V(x)$ is the same as the parity of p^2: $V(x) = V(-x)$. However, the value of $-\langle 1|V(x)|1\rangle + \langle 2|V(x)|2\rangle$ depends on the details of the two level system we are talking about. If I am pursuing an 'approximate' answer, then the details can be forgotten and I will use $\mathcal{H}_0$ to approximate $\frac{p^2}{2m}$.

$$\langle \mathcal{P}^2 \rangle \approx \frac{e^2 E^2}{m^2} tr(\begin{pmatrix} \rho_{11} & \rho_{12} \\ \rho_{21} & \rho_{22} \end{pmatrix} \begin{pmatrix} 0 & 0 \\ 0 & 2m\hbar\omega_0 \end{pmatrix})$$
$$= 2\rho_{22}\hbar\omega_0 \frac{e^2 E^2}{m} \tag{1.11}$$

The term E^2 in (1.11) is fast oscillating, say, if $E = E_0 \cos \omega t$ and the time-averaged value is $\frac{1}{2}E_0^2$.

1.3 Momentum Transfer between Atom and Light

Once we can figure out the energy exchange between the atom and each single light field, we would be able to get the momentum exchange almost for free. Thanks to Einstein, we know that each $\hbar\omega$ of energy quanta corresponds to $\hbar k$ of momentum, provided $\omega = ck$. Put in another way, we are able to compute the optical force on an atom, though throughout the discussions here it would be packed under the name of 'momentum exchange'. All we have to do is to follow the procedure as in 1.2.1 and especially in 1.2.2, since generally we are talking about optical force on an atom with spontaneous emission.

Suppose the atom is 'pinned' at the origin, and three lasers are acting on it, see Fig 1.2. Each of those lasers would have their own characteristics, i.e. Rabi frequency $\Omega_i(t)$, detuning $\Delta_i(t)$, initial phase ϕ_i, and the direction of the k vector, $\hat{k}_i$, with $i = 1, 2, 3$. It is assumed that the atom does not move during the interaction, which is an idealization. At the site of the atom, the effect of the lasers is merely to provide an oscillating electric field, hence the spatial dependence of the lasers is irrelevant in order to solve for the time evolution of the density matrix of the two level atom.

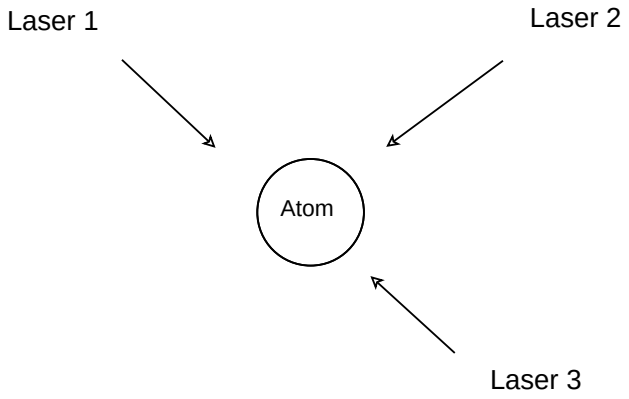

Figure 1.2: Schematic drawing of an atom in multiple laser fields

Then (1.4) could be numerically solved to acquire the time dependence of the density matrix. Then, according to (1.5), the work done on the atom by each of the individual lasers is known. As discussed at the beginning of this section, the energy transfer is exactly proportional to the momentum transfer. The spontaneous emission is usually regarded as symmetric hence it takes away energy while its net effect of carrying momentum is zero. Therefore the momentum Δp_i transfered to the atom by the ith laser is:

$$\Delta p_i = \frac{k}{\omega}\int_{t_0}^{t_1} P(t)dt = -\frac{2}{c}\frac{e}{m}\int_{t_0}^{t_1} \mathrm{Re}(\rho_{12}e^{i\omega' t}Ep_{21})dt \tag{1.12}$$

The momentum exchange for the ith laser takes place along the k vector of the ith laser. Hence the above equation shall be rewritten as:

$$\vec{\Delta p_i} = -\frac{2}{c}\frac{e}{m}\int_{t_0}^{t_1} \mathrm{Re}(\rho_{12}e^{i\omega' t}Ep_{21})\hat{k}_i \tag{1.13}$$

where $\hat{k}_i$ is the direction vector of the ith laser's k vector.

Then the total momentum transfered to the atom is just the vector sum of all the lasers. Here it reads:

$$\vec{\Delta p} = \sum_{i=1}^{3} \vec{\Delta p}_i \tag{1.14}$$

For example, first let us look at a sample calculation of the one dimensional Doppler Molasses by this method. A typical result is shown in Fig 1.3 for blue detuned optical molasses.

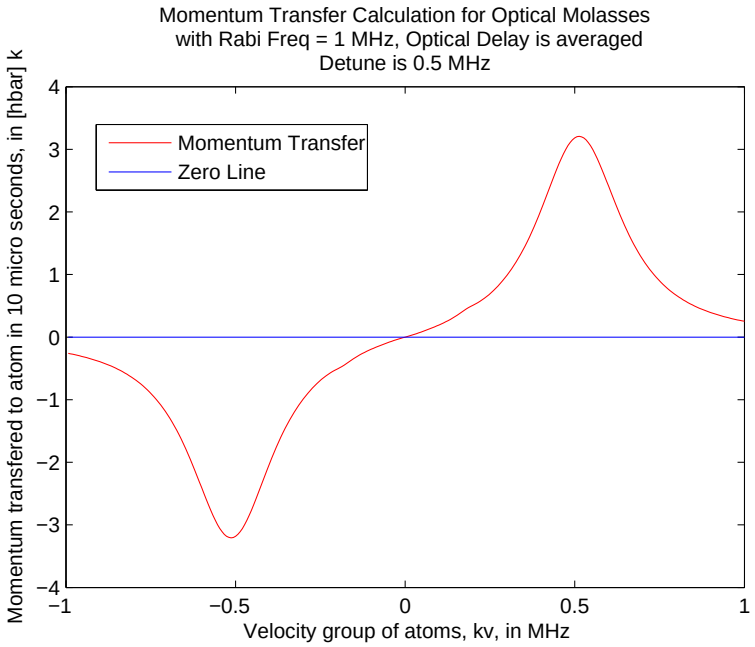

Figure 1.3: Sample calculation of momentum exchange to the 2 level atom from 1D blue detuned optical molasses, with interaction time 10 micro seconds. The decay rate γ is $2\pi \times 1$ MHz.

1.3.1 Coupling to the motion of the atom

The method of computing momentum exchange, described above, has a glaring point: the atom is assumed to be sitting still at one site throughout the interaction. This is obviously not the best approximation to the reality.

In the semi-classical description of the atom-light interaction, we are facing a strange combination when considering the light force on the atom. Namely, the center of mass motion of the atom is described classically, while the source of the force is from the quantum mechanical evolution of the 'inner degree of freedom' of the two level atom. It has consequences in both the interpretation and the idea of computation.

The purpose here is to establish a set of ODE's which couples the external and internal degree of freedoms of the atom at the same time. Namely, the expectation value of the quantum quantity, momentum exchange per unit time, is put in Newton's second law for the trajectory of the two level atom.

For the momentum exchange equivalent to that of a quanta of the electricmagnetic field $\hbar k$, the relative velocity change of the atom is one unit of a recoil frequency ω_r, namely, $2\omega_r/k$. So the exchange of momentum can be converted to the velocity change of the atom, assuming this relation always holds.

Let us consider the one dimensional case for the moment, in which only two directions have to be considered. Suppose the laser from one direction is described by $\Omega_L = \Omega_L(x,t)$ and the laser from the other direction is described by $\Omega_R = \Omega_R(x,t)$, with x is the coordinate in the lab frame. More explicitly, we have (1.15), (1.16) and (1.17).

$$\frac{d\rho_{21}}{dt} = -(\frac{\gamma}{2} - i\delta)\rho_{21} + \frac{iw(\Omega_L + \Omega_R)}{2} \tag{1.15a}$$

$$\frac{dw}{dt} = -\gamma w - i((\Omega_L + \Omega_R)\rho_{21}^* - (\Omega_L^* + \Omega_R^*)\rho_{21}) + \gamma \tag{1.15b}$$

(1.15) looks no different from any optical Bloch equation. However, now the atoms have both the internal motion (described by ρ_{21} and w) and the external motion (described by x and t). Explicitly, we have $\Omega_L = \Omega_L(x,t)$ and $\Omega_R = \Omega_R(x,t)$ where $x = x(t)$ is the position of the atom in the lab frame. In (1.15), the atom is no longer pinned at the origin and

the external motion of the atom would feed back to the internal motion via the position dependence of the optical field.

$$N_L = \mathrm{Re}(\rho_{21})\,\mathrm{Im}(\Omega_L) - \mathrm{Im}(\rho_{21})\,\mathrm{Re}(\Omega_L) \tag{1.16a}$$

$$N_R = \mathrm{Re}(\rho_{21})\,\mathrm{Im}(\Omega_R) - \mathrm{Im}(\rho_{21})\,\mathrm{Re}(\Omega_R) \tag{1.16b}$$

$N_L \Delta t$ is the number of photons absorbed by the atom from the laser represented by Ω_L within a given time interval Δt. The same interpretation holds for N_R too. Therefore, N_L and N_R can be viewed as the photon absorption rate. This concept is handy but in reality nothing is going to absorb a half photon in a completed process. Therefore, (1.16) is describing the rate of absorption of light in the sense of expectation value.

$$\frac{dx}{dt} = v \tag{1.17a}$$

$$k\frac{dv}{dt} = (N_R - N_L) \times 2\omega_r \tag{1.17b}$$

In (1.17), x and v's units shall be consistent with each other. Now we have a system of linear first order ordinary differential equations after combining (1.15), (1.16) and (1.17), whose solution will demonstrate the time evolution of the kinetic motion and wave function of the atom at the same time.

1.3.2 Bichromatic force

After its invention, the bichromatic force has been used more and more widely in cases where a large optical force not limited by γ is in need [24] [25] [26]. The bichromatic force is not only very powerful in the sense of practical applications, but also brings an interesting theoretical topic for us to understand its behavior. The intuitive π–pulse model and the

profound dressed atom model are well known by now. Here, we want to present a third method to explain the bichromatic force, from the point of view of the asymmetry of the atom's absorption of left-going and right-going laser beams.

Let us begin with the π–pulse model, which provides a basic and intuitive picture for the underlying physics. This is summarized in the following Fig.1.4.

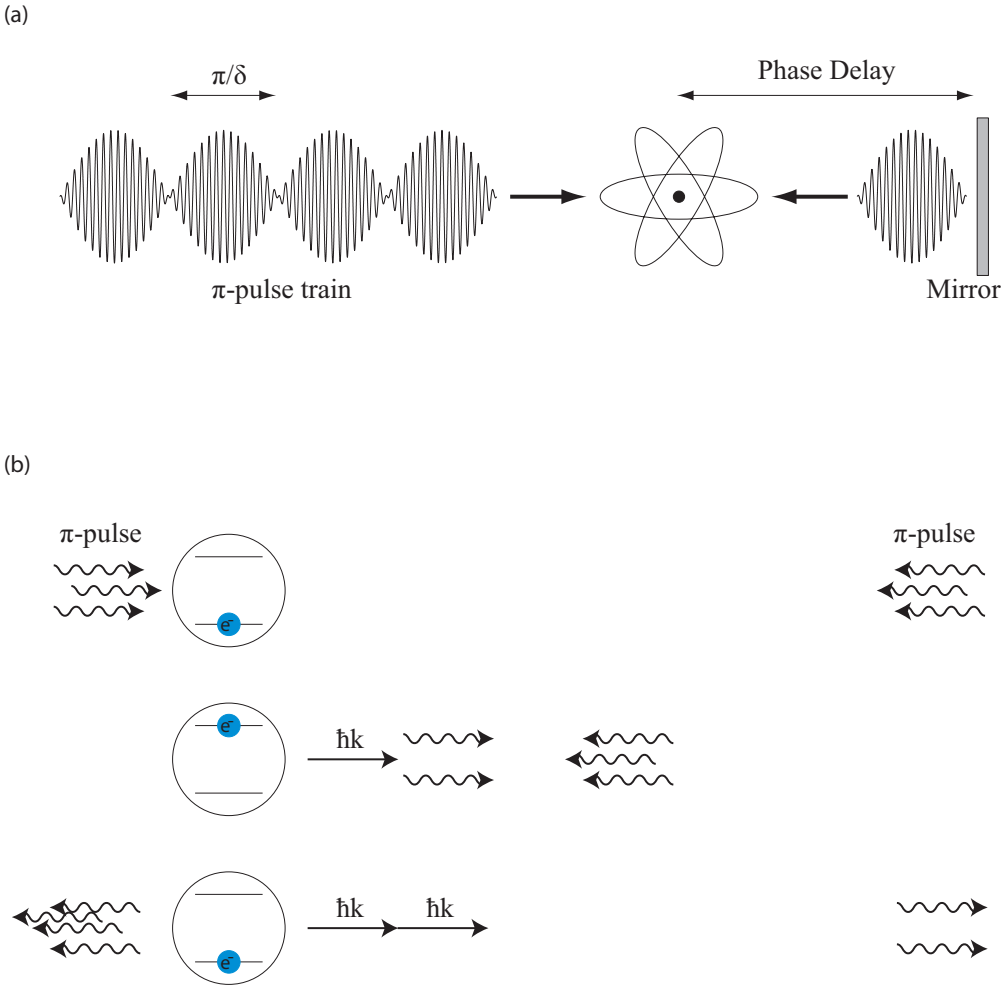

Figure 1.4: The bichromatic force explained by the π–pulse model. The lasers interacting with the atom can be viewed as π–pulse wave packets, coming from both the left and the right. The momentum exchange, and hence the force is from the stimulated emission caused by the second π–pulse. See also [27].

Based on the previous discussion about the atom's absorption of light, we can switch our

mind a little to see why the bichromatic force arises. This is a one dimensional problem and therefore we only have to consider the light from the left and the light from the right. The setup of the lasers, namely, two frequencies from each direction, drives the atom in such a way that the atom strongly absorbs the light from a particular direction, but not the other. In the situation where no spontaneous emission is present, the atom is essentially transferring energy/momentum from the light of one direction into the other. And this observation has close ties to the π–pulse model discussed in Fig.1.4. The quantitative details are shown in the following Fig.1.5.

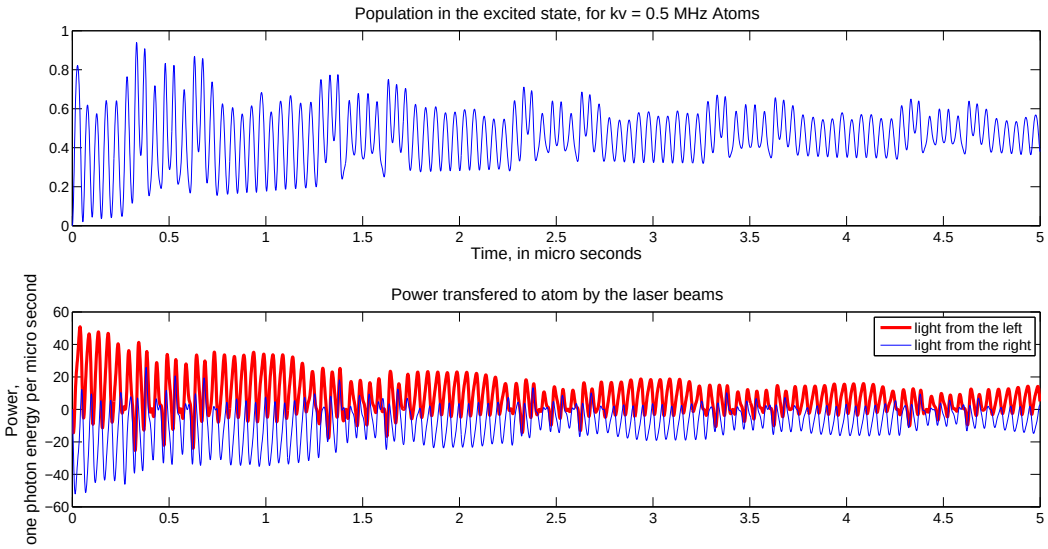

Figure 1.5: The internal motion of the atom and the atom's absorption of light, in the interaction between the atom and the bichromatic light. This shows the numerical results in the semi–classical picture following the methods of section 1.2 and 1.3. The atom is fixed at the origin and the bichromatic light from both the directions, left and right, are acting on it. The two frequency components are detuned at $+10$ MHz and -10 MHz separately, and are of Rabi frequency 8.5 MHz each. The light from the right has a phase delay of $\frac{2\pi}{5}$ rad. The initial phase difference between the two components are set to be $\frac{\pi}{2}$ rad. The atom is at the ground state initially. The line width of the transition is set at 1 MHz.

Fig.1.5 shows the quantitative details backing the π–pulse model. Let's try to make a

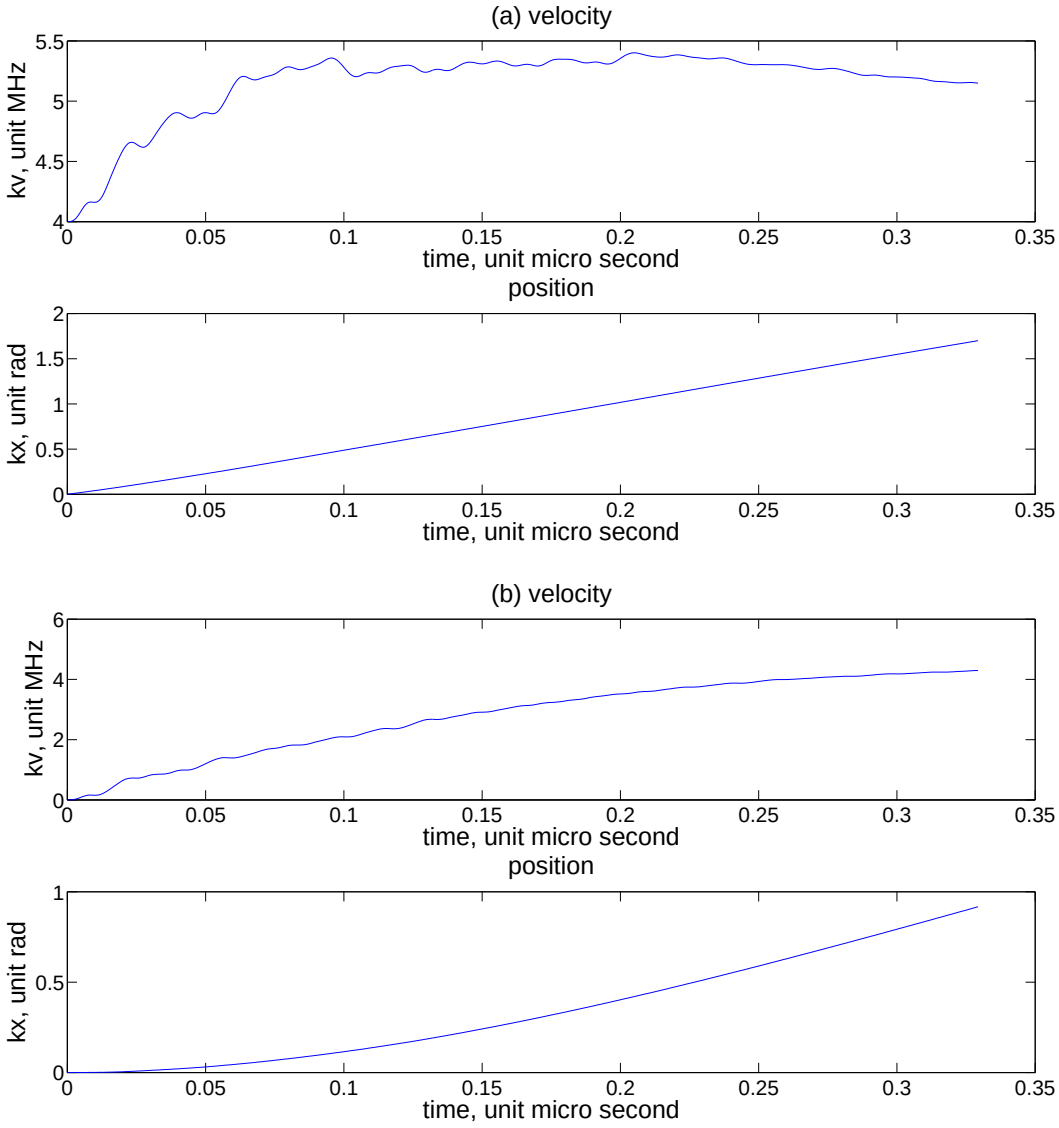

Figure 1.6: Numerical simulations of the trajectory of an atom moving in a bichromatic light field, for two different initial velocities (a) and (b). The change of velocity is due to the bichromatic force. The bichromatic force's feature of pushing the atom to a certain velocity is clear. This simulation is based on the transition of $2^3S_1 \rightarrow 3^3P_2$ of helium–4, driven by 389 nm laser. The velocity and position are evaluated in terms of kv and kx, where k is the wave vector of the 389 nm laser. The two frequency components of the bichromatic light field is set at $+/-30$ MHz separately, with the same Rabi frequency 25.5 MHz. The phases of the two frequency components are chosen to be the optimum values.

qualitative interpretation out of that. The sum of laser fields from both directions acting on the atom makes the atom wave function always in phase with the lasers from one direction while out of the phase with the lasers from other direction, therefore the atom always absorb light from one set and then stimulated emit into the other. Of particular interest is the fact that the bichromatic force does not rely upon the spontaneous emission. Even without spontaneous emission to scatter the power, this stimulated process can take place and the atom will always experience a force.

According to section 1.3.1, we can numerically trace the trajectory of an atom in a bichromatic light field. An example in given in Fig.1.6. From this example we clearly see the atom receives a force much larger than the radiative force $\hbar k\gamma$. The fact that the bichromatic force is not limited by $\hbar k\gamma$ is exactly its advantage.

The bichromatic force will be a powerful tool for purposes to be discussed later (see Chapter 5). However, before we close this brief introduction, we want to emphasize that the bichromatic force is not as simple as it appears to be. Because it requires a high intensity of light, many side effects like the Dopplerons can take place. Many parameters, like the optical delay, can affect its performance. All those will be kept in mind in the implementation of the bichromatic force.

1.4 Rydberg Atoms

The study of Rydberg atoms is a traditional old topic. Moreover, the study of Rydberg atoms is a vigorous currently on–going hot topic. The fascinating aspect of Rydberg atoms is that this topic repeatedly gives the community surprises in the form of amazing new physics. For instance, half a century ago it's hard for people to imagine one day the Rydberg atom is an ideal candidate for quantum computing. Here we want to offer a very brief review of

some general properties of Rydberg atoms, mostly according to the discussions of [28], which is one of the best, if not only, reference book on this topic.

Rydberg atoms are referring to those atoms in the states of high principle quantum number n. Rydberg atoms can be produced by charge exchange, electron impact, and photo–excitation. And all of the three production methods has a cross section that scales as $\sim n^{-3}$. The research in Rydberg atoms began long before the laser era, yet the invention of laser provides the means to coherently address a single Rydberg level.

Property	Formula	n-dependence
Binding energy E_n	$-\frac{R_y}{(n-\delta_l)^2}$	n^{-2}
Energy spacing	$E_n - E_{n-1}$	n^{-3}
Orbital radius $\langle r \rangle$	$\simeq \frac{1}{2}(3(n-\delta_l)^2 - l(l+1))$	n^2
Geo. cross section	$\pi \langle r \rangle^2$	n^4
Dipole moment	$\langle nl \vert er \vert nl+1 \rangle$	n^2
Polarizability	$2e^2 \sum_{n=n',l,m} \frac{\vert\langle nlm\vert z\vert n'l'm'\rangle\vert^2}{E_{nlm}-E_{n'l'm'}}$	n^7
Radiative lifetime	$(\frac{e^2}{3\hbar c^3 \pi \epsilon_0} \sum_{n<n'}^{l=l\pm1} \frac{l_{max}}{2l'+1} \omega^3 \vert\langle n'l' \vert r \vert nl\rangle\vert^2)^{-1}$	n^{-3}
Blackbody transition	$\frac{1}{\tau_{nl}^{bb}} = \frac{4\alpha^3 kT}{3n^2}$	n^{-2}
Fine Structure		n^{-3}

Table 1.1: The dependence of selected Rydberg atom properties on the principal quantum number [28]. The radiative life time here is considered at temperature 0 K. The blackbody transition rate does not take the photon thermal distribution into account.

Despite of the seemingly simple definition, the Rydberg atom has some very exaggerated properties compared to the low–lying excited states of the atoms. A summary of selected atomic properties of Rydberg atoms is shown in Table 1.1. The Rydberg atom is an ideal

example for the Bohr atom model. The Bohr radius scales as n^2 therefore the Rydberg atom can easily become very large. This has aroused a lot of research on the collisional cross sections. Rydberg H atoms are useful even for the radio astronomers because they are naturally formed among the interstellar space in the universe and output a signature 2.4 GHz radiation (from $n = 109 \rightarrow n = 108$ transition) [28].

Moreover, because the Rydberg levels' energies are close to each other, many of the transition frequencies are in the microwave range. This property allows the manipulation of the Rydberg states by microwave radiation. More profoundly, it allows the research into the interaction between the Rydberg atom and the engineered vacuum, to strengthen our understanding of QED. Rydberg atoms have very large electric dipole moments which naturally leads to pronounced Stark effect [29] and van der Waals interaction between pairs of Rydberg atoms [30][31]. Rydberg atoms can be easily ionized, and the ionization of Rydberg atoms is a standard research topic, with well–know techniques as state–selective field ionization. Rydberg atoms are very sensitive to black body radiation at room temperature, and this topic is to be discussed further in Chapter 4. By producing cold Rydberg atoms, people are pursuing the research interest in low temperature Rydberg systems for applications such as studies of collective effects [32] and formation and recombination of ultracold Rydberg plasmas [33] and quantum computing [34]. In the rest of this section we are going to discuss two more topics specifically, which are related to our experiments: the quantum defect and Stark effect of helium Rydberg states.

The helium Rydberg atom and the hydrogen Rydberg have one slight difference: the core of the hydrogen atom is merely a proton while the core of the helium atom is a nucleus carrying +2 electron unit of positive charge plus an inner electron, from the excited valence electron's point of view. This results in an energy shift in the Helium Rydberg atom energy levels, which is very well described by the quantum defect theory.

The energy levels of the hydrogen atoms are $E_n = -\frac{R_y}{n^2}$ where different l states are degenerate, without considering higher order corrections. In non-hydrogen atoms, such as the helium in our case, for highly elliptical low l states the radial wave function of the excited valence electron has a significant non-vanishing part penetrating into the core area which is made up of not only the nucleus but also the inner electron. This type of core penetration and polarization leads to an energy shift. At the kernel of the quantum defect theory is that the shifted energies can be written as in (1.19) (see also [35]):

$$E_n = -\frac{R_y}{(n-\delta_l)^2} \tag{1.18}$$

where the quantum defect term δ_l is a function of n, l and can be described effectively by the Rydberg-Ritz formula [36]

$$\delta_l = a + bE_n + cE_n^2 + dE_n^3 + ... \tag{1.19}$$

where a, b, c, d,... are the Rydberg-Ritz coefficients and they also depend on the angular momentum l. The corresponding values of triplet helium atoms are listed in Table 1.2.

l - value	a	b	c	d
0	0.296609	-0.038840	0.004960	0.000000
1	0.068320	0.017870	-0.017190	0.000000
2	0.002869	0.006220	0.000000	0.000000
3	0.000240	-0.002090	0.000000	0.000000

Table 1.2: Rydberg-Ritz coefficients for the calculation of quantum defect of triplet Helium without considering spin-orbit splitting [37]

The shielding is almost perfect for states of high orbital angular momentum, for example the circular Bohr orbits, since the electron in those states do not come to the core close enough to see anything different from a point charge. However, states of low l are depressed in energy. For helium, the S state has relatively larger quantum defect than the P state, and the P state has relatively larger quantum defect than the D state, etc.

The Stark effect, as the effect of an electric field on Rydberg atoms, provides an interesting example of how the Coulomb potential can be changed over the size of the radius of the atom. The potential difference $|e\vec{E}\cdot\vec{r}|$ is particularly significant for Rydberg atoms due to its large radius. For the hydrogen atom, an analytical solution is available because the Hamiltonian and wave function are still separable under parabolic coordinates. The helium atom is a bit more complicated and is not separable, yet we can numerically evaluate the radial matrix elements of the Stark operator as described by Zimmerman et al.[29].

As an example, Fig. 1.7 shows a sample Stark effect calculation of the energy levels for He triplet state $n = 26$. This figure demonstrates several important features: (1) the strong energy depression of the S, P, D states due to the quantum defect; (2) the degeneracy of the $|nl\rangle, l > 3$ states is lifted, which is a typical phenomena in the first order perturbation of degenerate states; (3) avoided crossings arise from the fact that a non-hydrogen core breaks the Coulomb symmetry and couples the Stark levels to each other. The size of an avoided crossing is given by the strength of the coupling.

Now we want to consider what happens to the transitions to those Stark shifted levels. Therefore we are to look into the oscillator strengths. The oscillator strength from level nlm to level $n'l'm'$ is defined by

$$f_{n'l'm',nlm} = 2\frac{m}{\hbar}\omega_{n'l',nl}|\langle n'l'm'|z|nlm\rangle|^2 \tag{1.20}$$

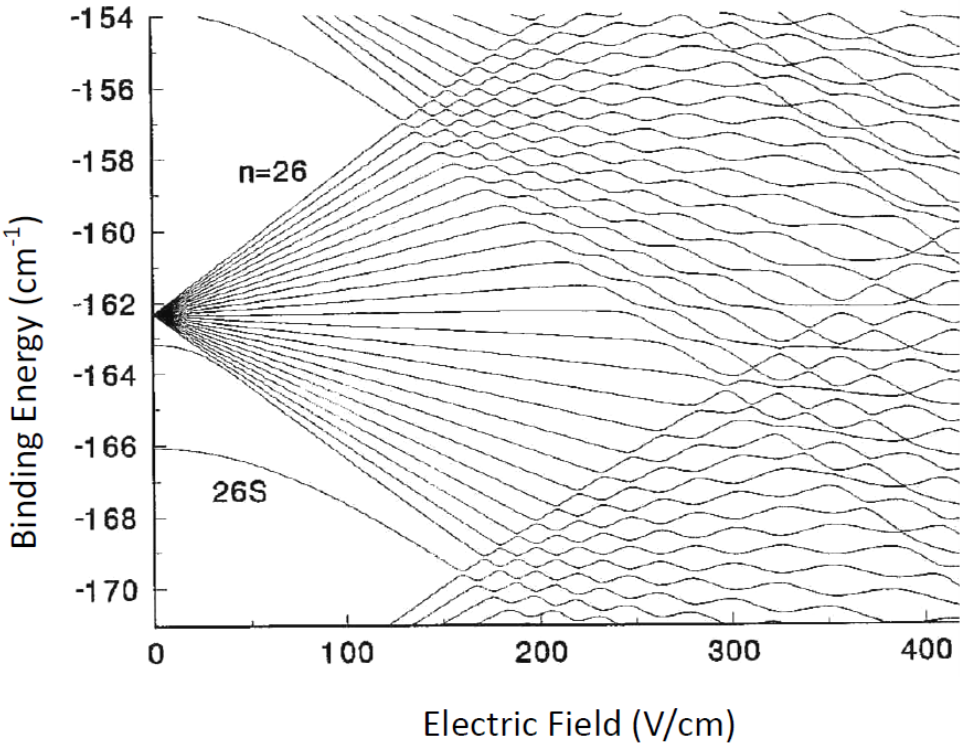

Figure 1.7: Stark map of Helium atom for $n = 26$ (without considering the fine structure) [37]

These oscillator strengths can be evaluated by numerical integration for He Rydberg Stark states. A sample calculation of transitions to $n = 25$ Stark states from the 3^3P_2 state is shown in Fig. 1.8 [37]. The qualitative feature of the results of $n = 25$ is shared by others states with different principle quantum states. There are dramatic changes in the distribution of the oscillator strengths across the Stark manifold as the electric field changes. These different transition strengths will lead to different Rabi frequencies for the same intensity of driving laser, which shall be kept in mind for the interest on the experimental aspect.

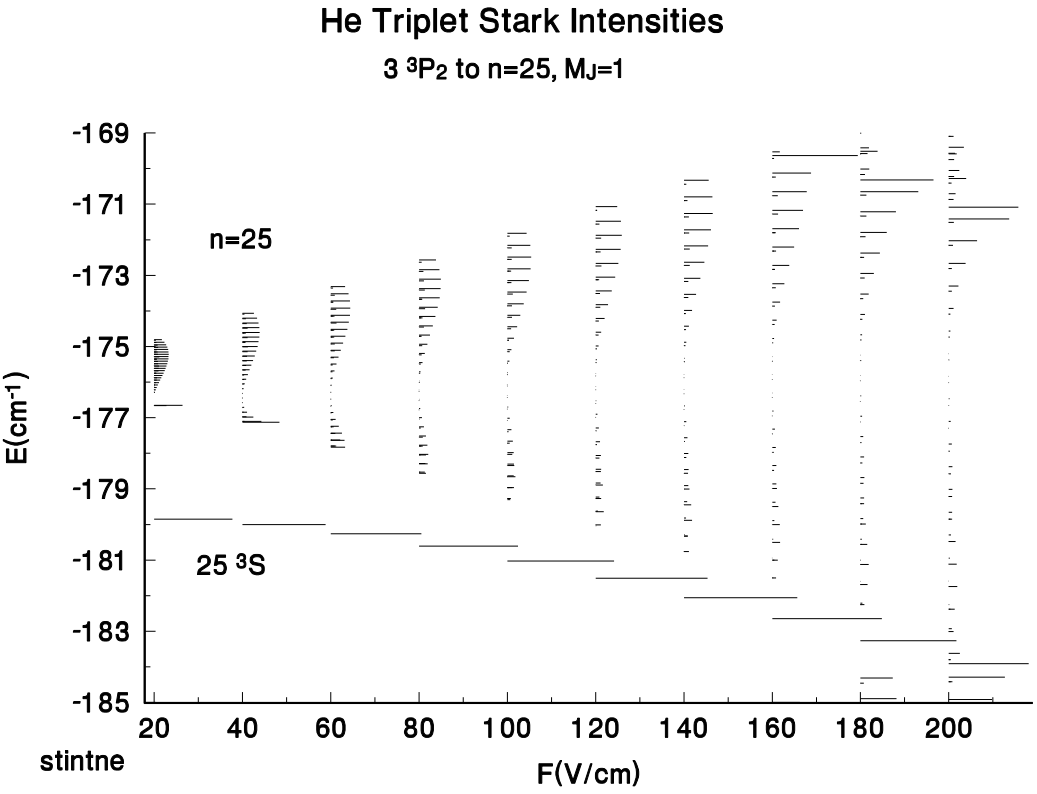

Figure 1.8: Relative Transition strength to $n = 25$ Stark map from 3^3P_2 for triplet Helium atom, which is given by the width of each line [37].

1.5 Overview of the Helium Rydberg Atom Excitation

The helium atom has one more electron than the hydrogen atom, and this extra electron–electron interaction makes it quite different. Even before the days of a thorough understanding of the electron spin, people know there are two kind of helium: the para–helium (states of symmetric eigenfunctions) and the ortho–helium (states of antisymmetric eigenfunctions). The interaction between the two electrons is basically their Coulomb interaction and spin–

spin interaction, if we neglect the spin–orbit interaction and the relativistic corrections. The total spin of the two electrons can be 1 (triplet states) or 0 (singlet state), which then specifies the spin degree of freedom. One advantage of helium–4 is that there is no hyperfine structure. A simple energy diagram of helium–4 triplet states is shown in Fig. 1.9, where some of the transitions associated with later experiments are also included.

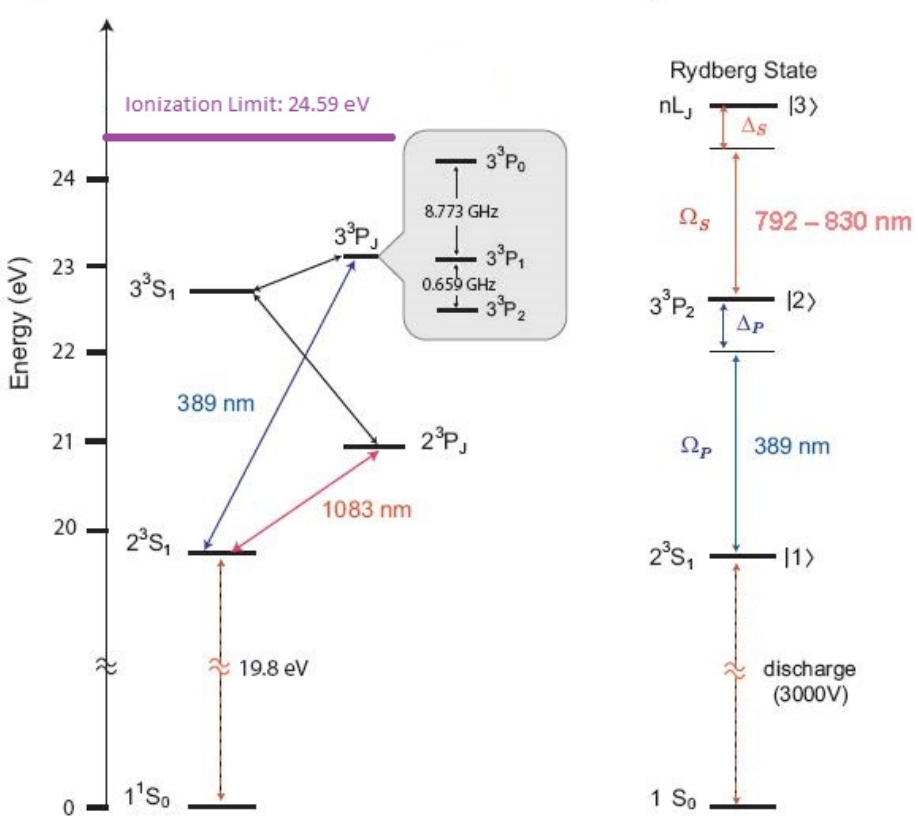

Figure 1.9: (a) Energy levels of the helium triplet states and (b) the transitions. Ω_S and Ω_P are referring to the Stokes and the Pump lasers, respectively. Δ_S and Δ_P are their detunings. Further discussion are presented in Chapter 3.

The decay from an excited triplet or singlet S state to the ground state 1^1S_0 is forbidden by the selection rule of the electric dipole transition. Consequently the singlet and triplet S states of low principle quantum number have the possibility to become metastable, and the 2^1S_0 state has a lifetime of ~ 19 ms. Moreover, decay from the 2^3S_1 state to the ground state

is doubly forbidden not only by the electric dipole transition rule but also a spin triplet to singlet transition. This gives rise to the extremely long metastable lifetime, predicted to be 8000 s [38] (a recent experimental measurement actually indicates an even longer lifetime), so that the metastable state can essentially be regarded as the effective ground state. The He* 2^3S_1 state is the longest lived of any atomic or molecular species and decays via a single-photon magnetic dipole transition at 62.5 nm rather than via a two-photon process [38] [39]. Meanwhile, the stored metastable energy (19.82 eV) is the highest among all the metastable species, enabling detection of single atoms using charged particle detectors, electron multipliers, or microchannel plates (MCPs) with near unity detection efficiency [40]. Moreover, the large stored energy in He* allows for efficient damage of photoresist-coated surfaces for possible applications in atom lithography.

The Rabi frequencies for the relevant transitions have been defined in (3.4). Suppose the laser polarization is linear and is driving the $\Delta m = 0$ transition, then the Rabi frequency is related to the laser intensity by the formula $\Omega = \frac{\mu}{\hbar}\sqrt{\frac{2I}{\epsilon_0 c}}$, where μ is the transition dipole moment $e\langle e|r|g\rangle$ with $|e\rangle$ and $|g\rangle$ the two states associated with the transition. A numerical conversion table is given in Table 1.3.

Transitions	$2^3S_1 \to 3^3P_2$	$3^3P_2 \to 24^3S_1$
$m = 0$	$\Omega_p(x,t) = 14.9 \times \sqrt{I_p(x,t)}$MHz	$\Omega_S(x,t) = 1.67 \times \sqrt{I_S(x,t)}$MHz
$m = \pm 1$	$\Omega_p(x,t) = 12.9 \times \sqrt{I_p(x,t)}$MHz	$\Omega_S(x,t) = 1.45 \times \sqrt{I_S(x,t)}$MHz

Table 1.3: Conversion relations between the intensities (unit: W/cm^2) and the Rabi frequencies for transitions of interest. (x,t) specifies the space–time coordinate of the atom interacting with the laser. I_p and I_S are referring to the intensities of the pump and Stokes beams, separately. From the table we see that to make the Rabi frequencies of the two transition relatively comparable the power of the Stokes laser beam needs to be $50\times$ that of the pump laser beam.

Table 1.3 does not cover the situations of transitions to different j's or other than $\Delta m = 0$. A detailed diagram of the relative strength of these transitions are given in Fig. 1.10.

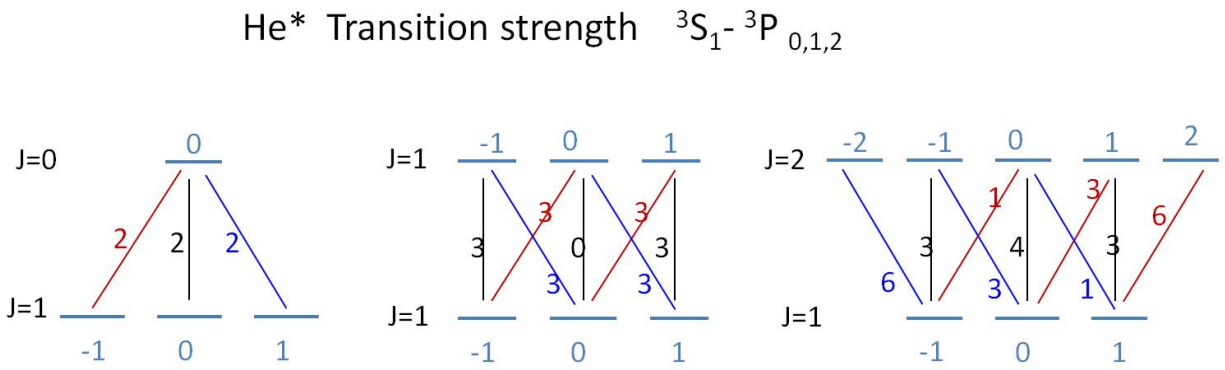

Figure 1.10: Relative transition strength for $j = 1 \rightarrow j = 0, 1, 2$, with all the possible m's considered.

We need to start from the metastable ground state for any practical laser–atom interaction of helium. Therefore we rely upon a constant metastable helium flow to perform the experiment that follows. A reverse flow dc discharge source is employed for this purpose. We also need various detection schemes for the metastable helium for the flux or spatial distribution. To drive the three different transitions $2^3S \rightarrow 2^3P$, $2^3S \rightarrow 3^3P$ and $3^3P \rightarrow$ Rydberg as illustrated in Fig. 1.9, we need three lasers working at different wavelengths. The discussion of all those experimental setup is included in Chapter 2.

We research the stimulated Raman adiabatic passage (STIRAP) of a three level ladder system and apply this technology to excite metastable helium into the Rydberg states. A theoretical discussion of STIRAP's principle is provided in Chapter 3.

The Rydberg atom has a strong and non–trivial interaction with the black body radiation at room temperature. The black body radiation will induce the transitions to neighboring Rydberg states and ionization. This topic is discussed in Chapter 4.

To establish the count of the Rydberg atom's flux, we set up a scheme to physically

separate the Rydberg atoms and the metastable atoms. Based on this scheme we are able to establish the absolute efficiency measurement of STIRAP. Some inherent properties of our atomic beam has some interesting effects on this efficiency measurement. Those contents are provided in Chapter 5.

The helium energy levels have magnetic sub–levels and those sub–levels have well–defined m_j's. Then the simple three level transition diagram will have interesting sub–structures, which depend on the driving lasers' polarizations. Chapter 6 studies some of this effect and the associated interferences.

There are quite a few interesting spectroscopic topics related to STIRAP, for example, the Autler–Townes effect of a three level system. Also, we want to know the effect of the laser noise on STIRAP. These discussions are included in Chapter 7.

Chapter 2

Experimental Design and Setup

2.1 Vacuum System

The vacuum system for the experiment is sketched in Fig. 2.1. It is made up of mostly stainless steel parts and conflat flanges sealed with copper gaskets. It contains three major parts: the source chamber where the metastable helium is generated, the interaction chamber where the laser–atom interaction takes place and the detection chamber.

The source chamber is pumped by a Pfeiffer TPH 330 turbo pump backed by a Welch mechanical pump model 1397, and the interaction chamber is pumped by a Pfeiffer TPH 270 turbo pump backed by a Welch mechanical pump model 1376. The backflow outlet of the source chamber is connected to a Welch mechanical pump model 1402. Since the detection chamber and the interaction chamber are separated by a long beamline, we have installed an ion pump on the detection chamber to keep the low pressure there. With no atomic beam running, typical pressure in this vacuum system is $\sim 3.2 \times 10^{-7}$ Torr in the source chamber, $\sim 3.6 \times 10^{-7}$ Torr in the interaction chamber and $\sim 2.5 \times 10^{-7}$ in the detection chamber. When the atomic beam is running down the system, the pressure in the interaction chamber

is on the scale of 10^{-6} Torr.

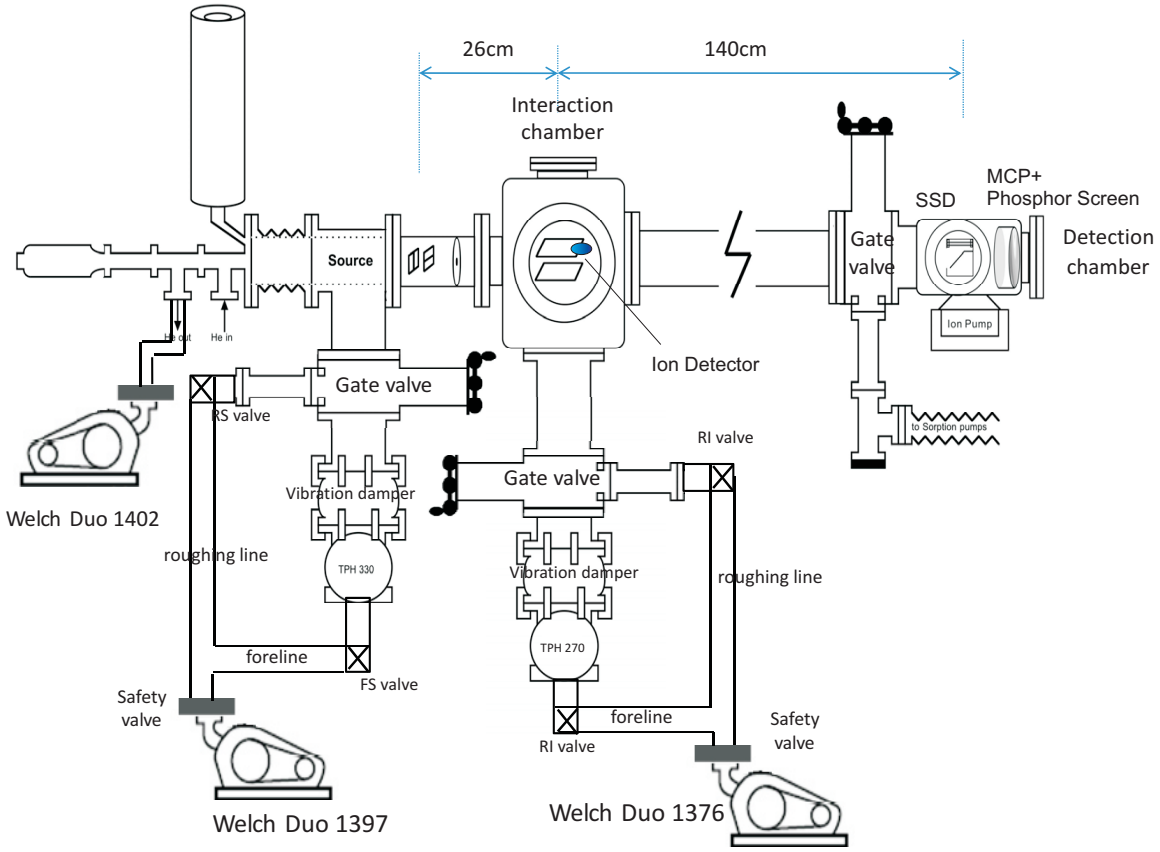

Figure 2.1: Schematics of the vacuum system. The atomic beam from the source chamber is traveling through the interaction chamber, between the metal field plates, and arrives at the detection chamber.

It takes very special design to produce the metastable ground state 2^3S_1 helium atoms. The reason is that, 2^3S_1 is ~ 19.8 eV above the true ground state 1^1S_0, and the transition is doubly forbidden (triplet $\rightarrow$ singlet, $S \rightarrow S$). Our source was built at Utrecht University in the Netherlands, according to the reverse flow design developed by Kawanaka et al. [41] with minor modifications by Mastwijk et al. [42]. The schematics is shown in the following

Fig. 2.2.

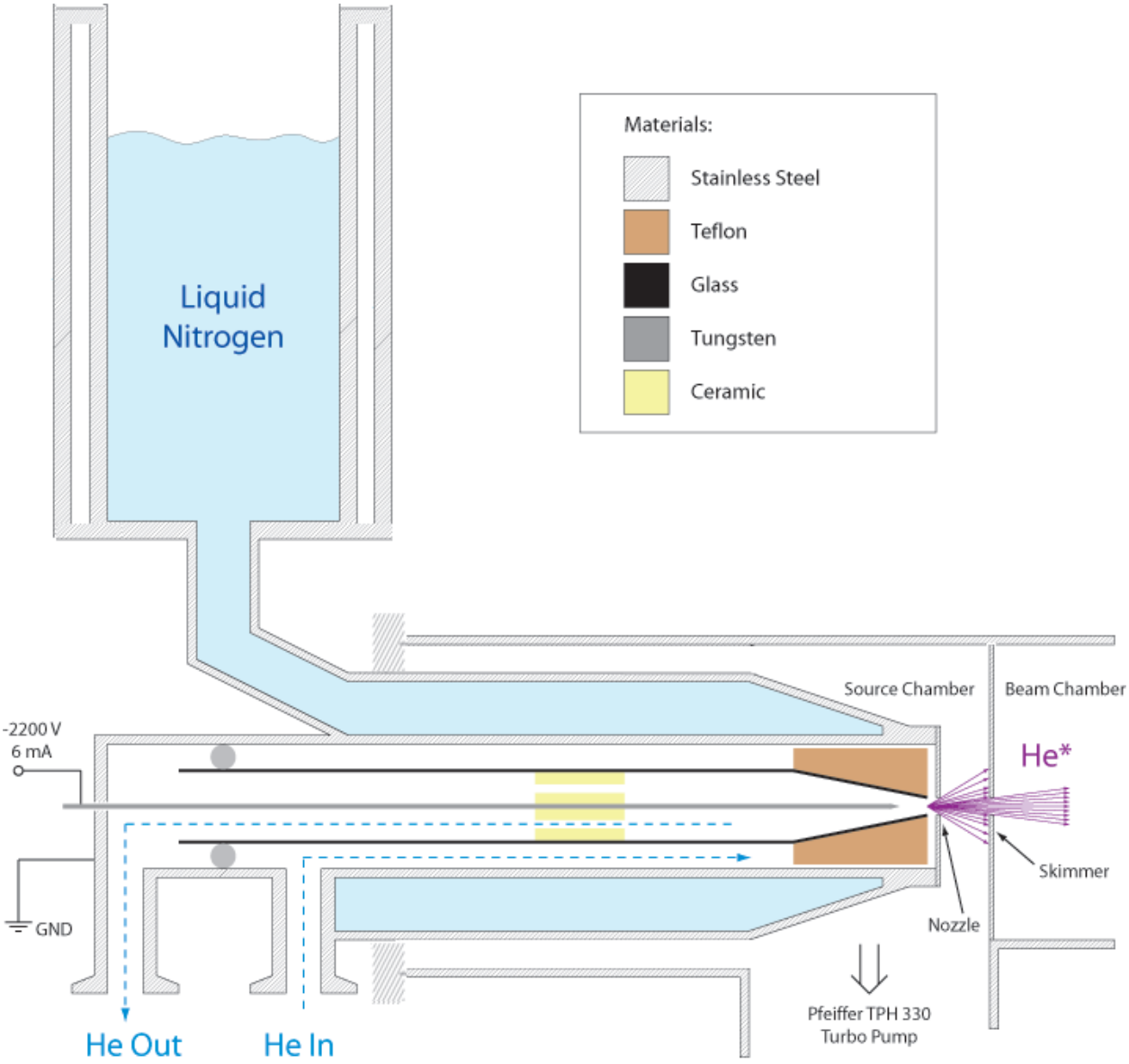

Figure 2.2: Schematic of the metastable helium source chamber. This helium gas is designed to go through a backflow. The helium is guided to be in good thermal contact with the wall of the jacket which is cryogenically cooled by the liquid nitrogen. The metastable helium is generated from an electric discharge process, with -2200 V supplied to the tungsten needle while the nozzle plate is grounded.

The voltage difference between the tungsten needle and the nozzle plate induces a high

electric field. This electric field ionizes the helium gas and forms a plasma. Metastable helium atoms are thereafter generated as a result of the re–combination process. The production efficiency is usually on the order of $10^{-5} \rightarrow 10^{-4}$ compared to the total numbers of the helium atoms involved. A skimmer plate with 3 mm aperture is immediately after the nozzle plate. The output of the source contains the metastable helium atoms, stray uv light from the plasma, and other charged particles. Many parameters affect this process and they have to be optimized. Under steady operational conditions, our source outputs $\sim 0.5 \times 10^{14}$ He* atoms/(sr·s) with an average longitudinal velocity about 1070 m/s and full width at half maximum of about 480 m/s, as verified by the time of flight measurement [43].

2.2 Detectors

Various detection schemes for the atoms have been installed in our system. In this section, we are going to briefly discuss three types of the detectors: the ion detector, the phosphor screen detector and the stainless steel detector.

A crucial element in all of the three detectors is the microchannel plate (MCP). A microchannel plate is a slab made from highly resistive material of typically 2 mm thickness with a regular array of tiny tubes or slots (microchannels) leading from one face to the opposite, densely distributed over the whole surface. The microchannels are typically approximately 10 micrometers in diameter (6 micrometer in high resolution MCPs) and spaced apart by approximately 15 micrometers; they are parallel to each other and often enter the plate at a small angle to the surface ($\sim 8^\circ$ from normal) [44] [45].

The ion detector we use is sketched in Fig. 2.3. It consists of two MCPs with angled channels rotated from each other producing a v–like shape. Ions incident on the channel walls will bring secondary electron emissions which are then collected by the anode. The

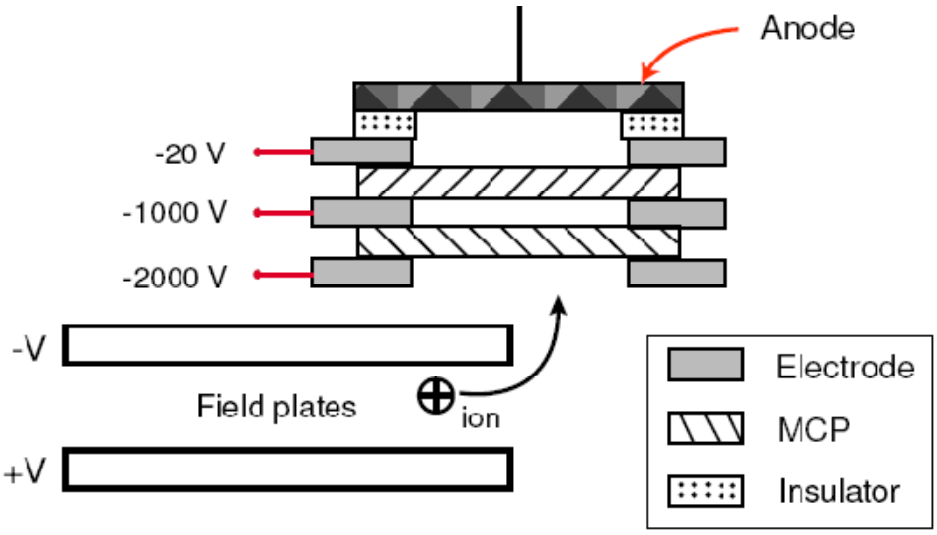

Figure 2.3: Schematics of the ion detector. It is mounted above the field plates. A portion of the heliums ions in the interaction region will be directed upwards and collected by the detector. Its detailed mission is mostly associated with the discussions in Chapter 4.

MCPs in use have a channel diameter of 10 microns with a center–to–center spacing of 12 microns, a bias angle of $\sim 12^\circ$ and a length–to–diameter ratio $40:1$, and the gain is $\sim 10^3$ at 750 V bias voltage and $\sim 2 \times 10^3$ at 800 V.

The MCP+phosphor screen detector is shown in Fig. 2.4, whose target is to image the spatial profile of the metastable helium atoms. A metastable helium atom carries 19.8 eV of internal energy, and when it is incident on the MCP it can easily generate a cascade of electrons. Because of the 'channel' nature of the MCP, it will have a spatial resolution determined by the channel spacing. The electrons will subsequently hit the phosphor screen and the phosphor excited by the electrons will emit light. A CCD camera is used to image the phosphor screen.

Our phosphor screen is from the Lexel Imaging System, which is basically a glass substrate coated with Indium Tin Oxide (ITO), covered by P43 phosphor. The light emitted from

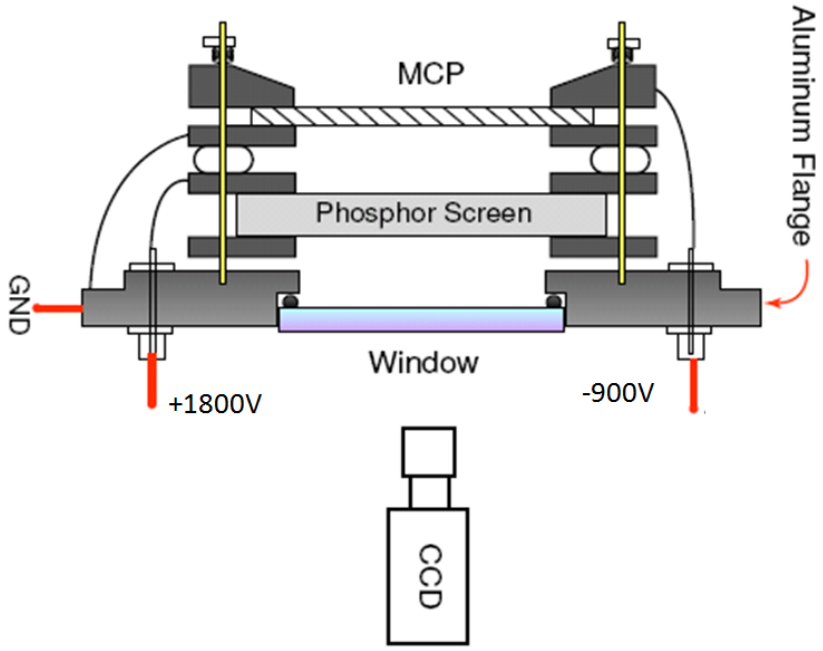

Figure 2.4: Schematics of the MCP+phosphor screen detector.

P43 is in the region from yellow to green which peaks around 545 nm. Though the phosphor screen is a convenient device to image the metastable helium, it is generally not true that the emitted light intensity is proportional to the atom numbers.

If we need a good quantitative measurement of the metastable helium flux instead of the spatial resolution, the stainless steel detector (SSD) is an appropriate choice which is shown in Fig. 2.5. The advantage of SSD is that it outputs a current proportional to the incident numbers of the metastable helium atoms.

The work function of the stainless steel is about $4.7 \rightarrow 5.6$ eV. One metastable helium atom is supposed to liberate one electron during its impact with a probability $\sim 70\%$ [46]. The electrons ejected from the surface of the stainless steel is accelerated to the MCPs by the applied high voltage electric potential. This conversion from He^* into electrons (of the

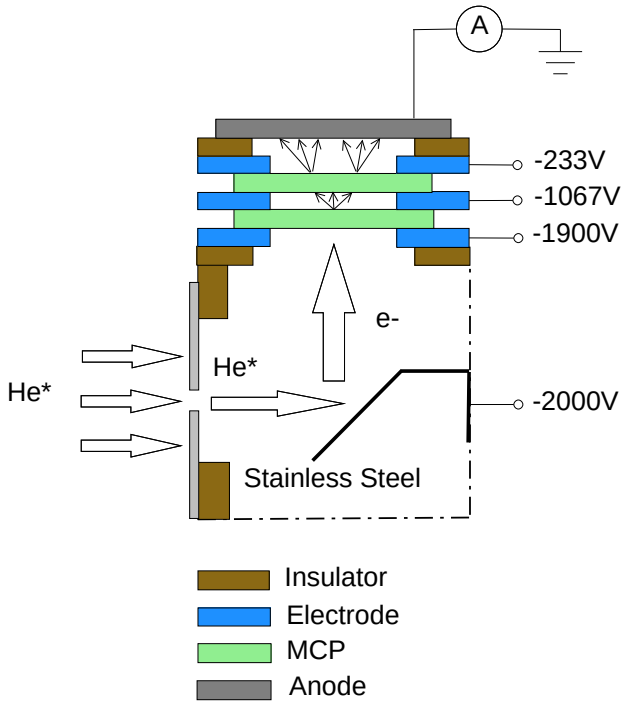

Figure 2.5: Schematic of the stainless steel detector. This detector is mounted on a 2 inch linear feedthrough (Huntington Mechanical Laboratories, Inc.) and therefore its transverse position with respect to the atomic beam can be adjusted. During daily operations we have the choice to either use the phosphor screen the monitor the spatial profile or use the SSD to monitor the absolute flux.

same kinetic energy) makes the electric current signal from the anode proportional to the total He^* flux through the aperture.

2.3 Laser Systems

Three laser systems are used in this experiment. They are the 389 nm laser system driving the $2^3S_1 \rightarrow 3^3P_2$ transition, the 760–800 nm laser system driving the $3^3P_2 \rightarrow$ Rydberg transition, and the 1083 nm laser system driving the $2^3S_1 \rightarrow 2^3P_2$ transition. They are all frequency stabilized by various mechanisms.

2.3.1 389 nm Laser System

The 389 nm laser light is generated by frequency doubling the output of a Ti:Sapphire laser. The sketch of the system is shown in Fig. 2.6. We use an SEO Ti:Sapphire laser pumped by a Sprout–G laser of Lighthouse Photonics (it replaces the older version of Coherent Verdi V–10 which is aging). During daily operations, the Sprout–G laser outputs 10 W multi–wavelength light at 532 nm (green light) in single TEM_{00} mode, to pump the Ti:Sapphire laser. With this 10 W pumping light, the Ti:Sapphire laser is producing $\sim 1.7 - 2$ W of single longitudinal mode TEM_{00} at $\sim$ 777.951 nm. This ir laser is subsequently frequency doubled by the Coherent MBD–200 commercial frequency doubling system to generate $\sim$ 389 nm light for the $2^3S_1 \rightarrow 3^3P_2$ transition.

The SEO Ti:Sapphire laser has a ring configuration with an optical diode installed to ensure uni–directional propagation of the light in the cavity. A birefringent filter provides a coarse wavelength adjustment while an etalon provides a fine frequency adjustment. A PZT is attached to one of the cavity mirrors to allow very fine frequency control.

The 'active' element of MBD–200 is a Lithium Triborate (LBO) crystal, whose nonlinear effect allows the generation of the second harmonic light. However, a single pass through the nonlinear crystal is not enough to generate enough power in the second harmonic; therefore, an external resonant enhancement cavity is used in MBD–200. The Hänsch-Couillaud (HC) technique is used to lock the external cavity on resonance.

The schematics of the MBD–200 frequency doubling cavity is shown in Fig. 2.7. The HC locking technique was first developed by Hänsch and Couillaud based on polarization spectroscopy [47]. Briefly speaking, this mechanism is based on the birefringence property of the LBO crystal, to use the one polarization component irrelevant of the frequency doubling process to serve as the reference in order to detect the phase of the polarization component

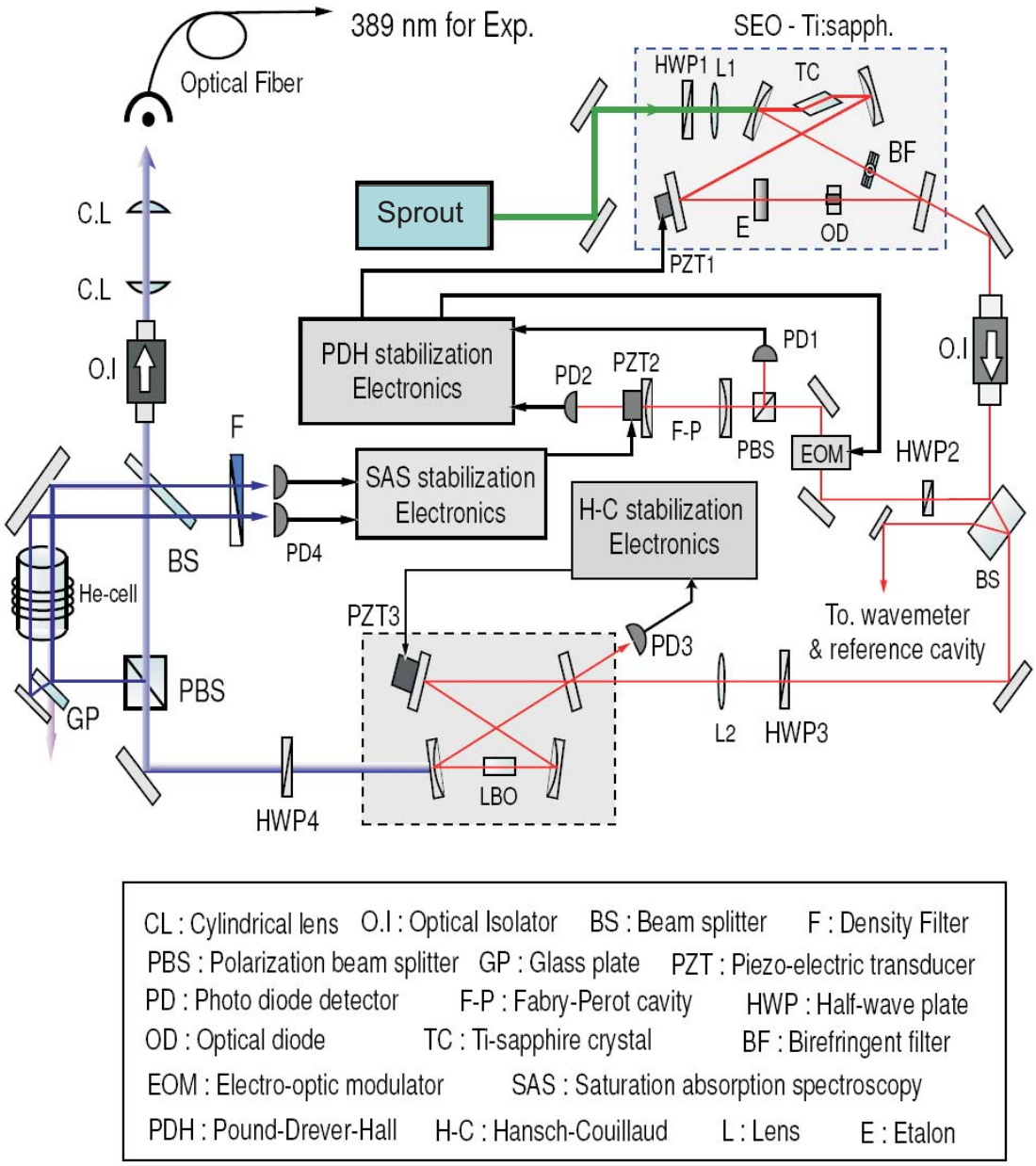

Figure 2.6: A sketch of the 389 nm laser system.

of interest. Detailed discussions can also be found at [43] and [22].

The SEO Ti:Sapphire laser is frequency stabilized by the Pound–Drever–Hall (PDH) locking technique [48] [49], and further locked to the atomic transition by saturation absorp-

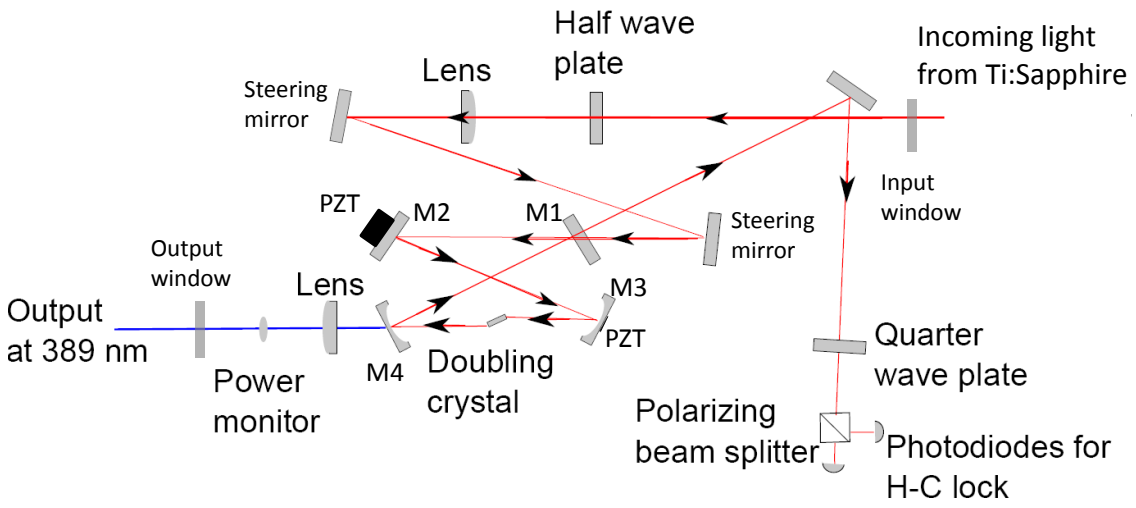

Figure 2.7: Optical setup of the MBD–200 frequency doubling cavity .

tion spectroscopy (SAS). The PDH mechanism has numerous applications nowadays, and its idea is deep and fundamental. If some system has a frequency–dependent response (in this particular case, a Fabry–Perot cavity), then the detuning of the carrier frequency off the resonance can be detected by interfering with sidebands (of course, a lock–in with the modulation frequency that generates the sidebands is necessary). The purpose of the PDH locking system here is to stabilize the Ti:Sapphire laser against environmental noise. SAS is the standard technique that is widely used to lock the laser frequency precisely to the atomic transitions [50][51] (for the performance details of our SAS system, see also the discussions in [43]).

2.3.2 796 nm Laser System

The 760–800 nm ir laser system for the $3^3P_2 \rightarrow$ Rydberg transition is relatively simpler. The diagram of the system is shown in Fig. 2.8. It is also a Ti:Sapphire laser system.

A Coherent Verdi V–10 laser is pumping the Tekhnoscan Model TIS-SF-07e Ti:Sapphire

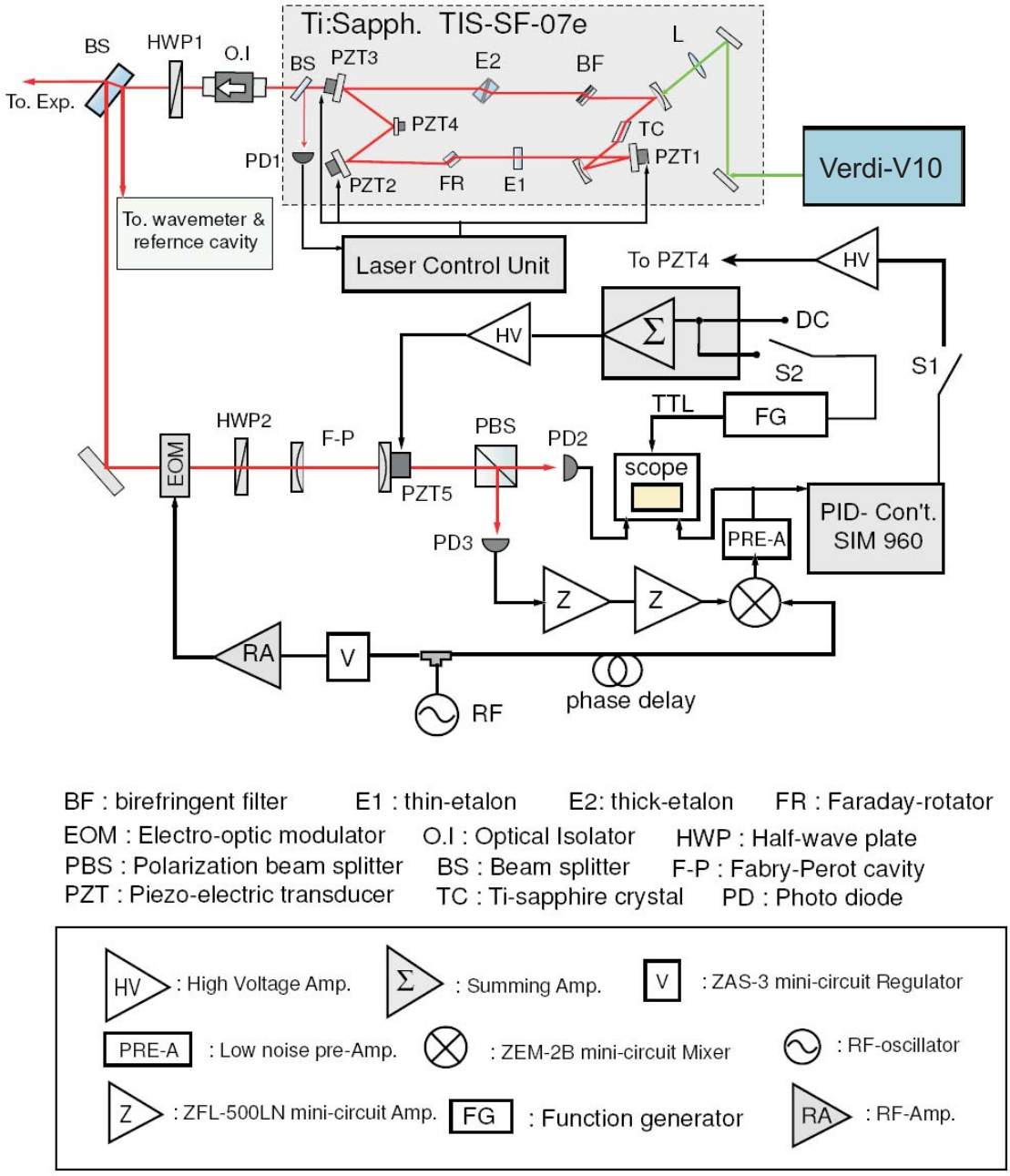

Figure 2.8: The optical scheme of ir laser system for STIRAP experiment.

laser. During daily operations, the Coherent Verdi V–10 typically outputs 10 W while the Tekhnoscan outputs ~ 1 W.

Since there is no stable convenient atomic transition to lock to, no SAS locking system is set up for the ir laser system, although it has a same PDH locking system as the 389 nm laser system. The Tekhnoscan laser has a internal frequency stabilization scheme to lock the laser to the transmission of an internal etalon. Since the performance of the internal locking is adequate and since we usually scan the ir laser frequency, its PDH system is used less frequently. The internal frequency stabilization scheme is very similar to that of PDH locking. A small AC dithering voltage of 1 kHz is first applied to PZT on the thick etalon. This leads to a minor modulation in the output power which is monitored by a photo-detector. Later on, the signal from the photo-detector goes through a 1 kHz filter to get synchronously detected and integrated as the error signal. Then the error signal is fed into a high-voltage amplifier, which drives the PZT on the thick etalon [52].

2.3.3 1083 nm Laser System

The $\lambda = 1083.33$ nm laser for the $2^3S_1 \rightarrow 2^3P_2$ transition is from a Spectra Diode Labs (SDL) model SDL-6702-H1 distributed Bragg reflector (DBR) diode laser. The diode is packaged in an 8 pin TO–3 window mount equipped with a thermistor and a thermoelectric cooler. The temperature of the diode is kept stable to ± 0.1°C by an ILX Lightwave LDT-590 temperature controller. A Thorlabs LDC 500 laser diode controller is used for the current regulation. The laser diode wavelength and output power depends on the current of the diode, and this relation has been extensively examined in previous theses [53][54][27].

The direct laser output of the SDL-6702-H1 diode laser has a linewidth about 3 MHz, which is larger than the 1.6 MHz natural linewidth of the transition $2^3S_1 \rightarrow 2^3P_2$. To narrow down the linewidth and stabilize the frequency, an extended cavity is used, as shown in Fig. 2.9. To shield the laser against external temperature fluctuations and mechanical vibrations,

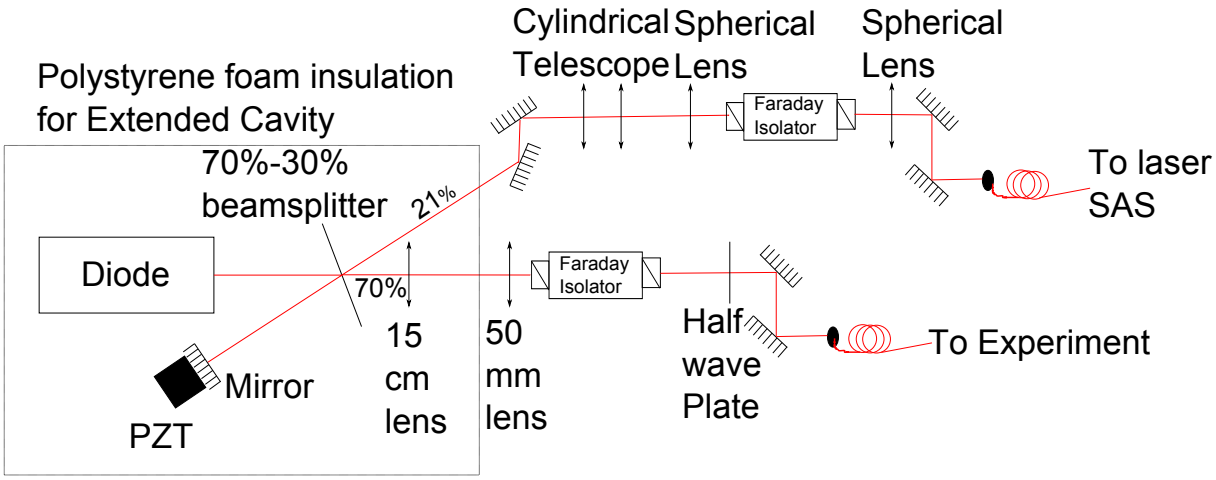

Figure 2.9: The optical scheme of the 1083 nm diode laser system [27]. A beam splitter picks 30% of the diode output towards the retro–reflecting mirror which has a PZT attached to it to allow for frequency control. With the extended cavity, the laser linewidth is reduced to $\sim$ 125 kHz [55]. In the design there is an optical isolator in the 21% leakage beam, yet in the actual setup no optical isolator is installed in that line. Therefore, a great care is in need to avoid any optical feed–back in that line or the laser would be disturbed.

the diode and the extended cavity are placed on a 305 mm x 710 mm x 76 mm Aluminum slab, and covered by a box made of polystyrene foam insulation. Although there are long-term temperature drifts during the course of a day, the temperature inside the box is stable to better than 0.5 °C/hr in a short term [27].

There are two output beams from the design in Fig. 2.9: The main beam ($\sim$ 70% of the total power) used for the experiment, and the leakage beam ($\sim$ 21% of the total power) used for the SAS to lock the laser to the atomic transition. The SAS locking setup is shown in Fig. 2.10.

To check the performance of the SAS locking system, we monitor and record the real time error signal and feedback signal by a digital data acquisition card, which are shown in

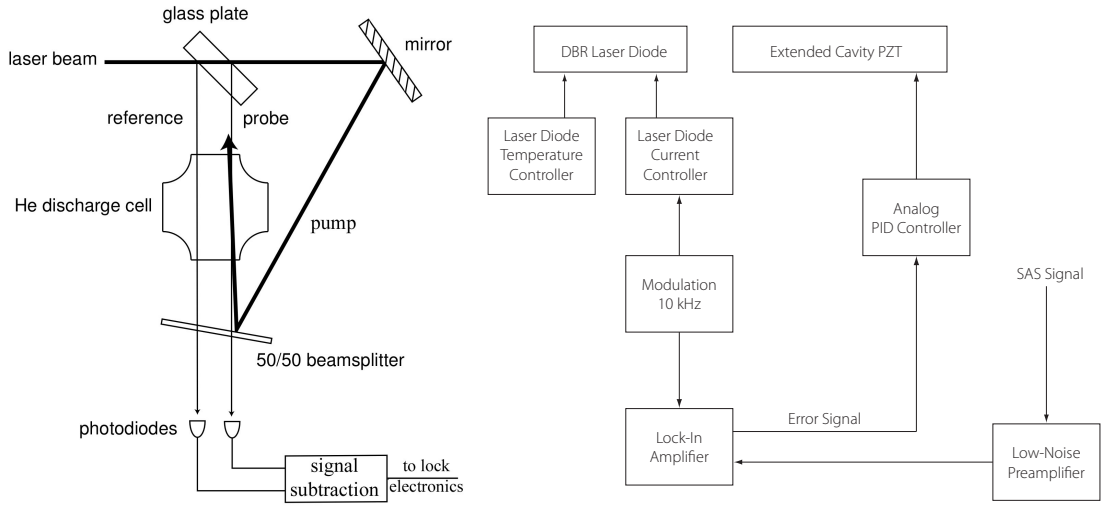

(a) Optical setup. (b) Electronic setup.

Figure 2.10: SAS locking scheme for the 1083 nm diode laser [27].

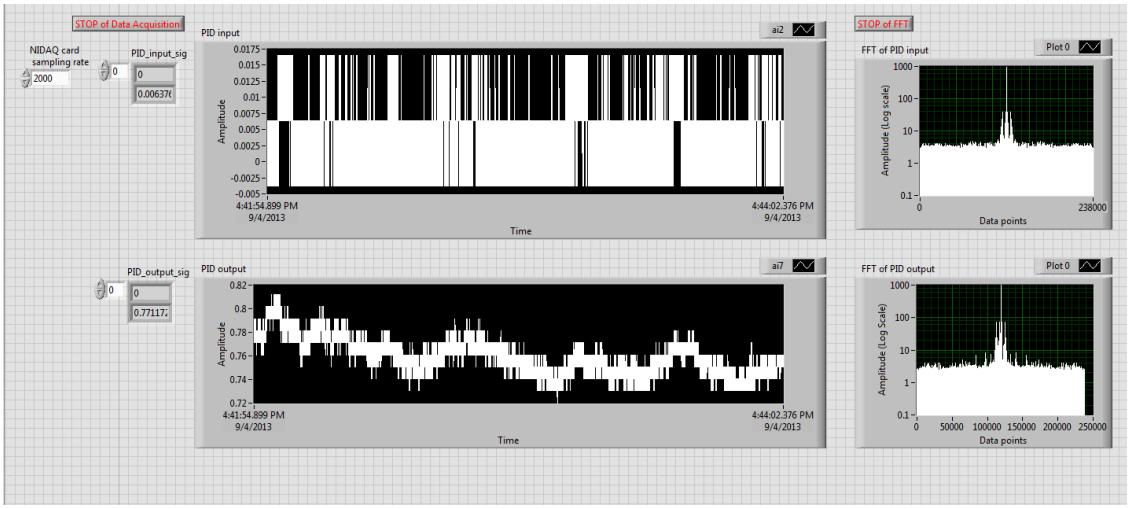

Figure 2.11: 1083 nm diode laser SAS locking signal.

Fig. 2.11. The Fourier transform of the time signal is shown on the right. When the laser is locked, we see that the error signal (PID input) stays constant at zero (the fluctuations are due to the smallest step in the digitization of the voltage), while the feedback changes slowly to offset whatever is causing the laser frequency to shift. The Fourier transform does not show any suspicious components in higher frequencies.

We need two–frequency component light for the bichromatic force, and the mechanism to generate the two–frequency component light is shown in Fig. 2.12 [27].

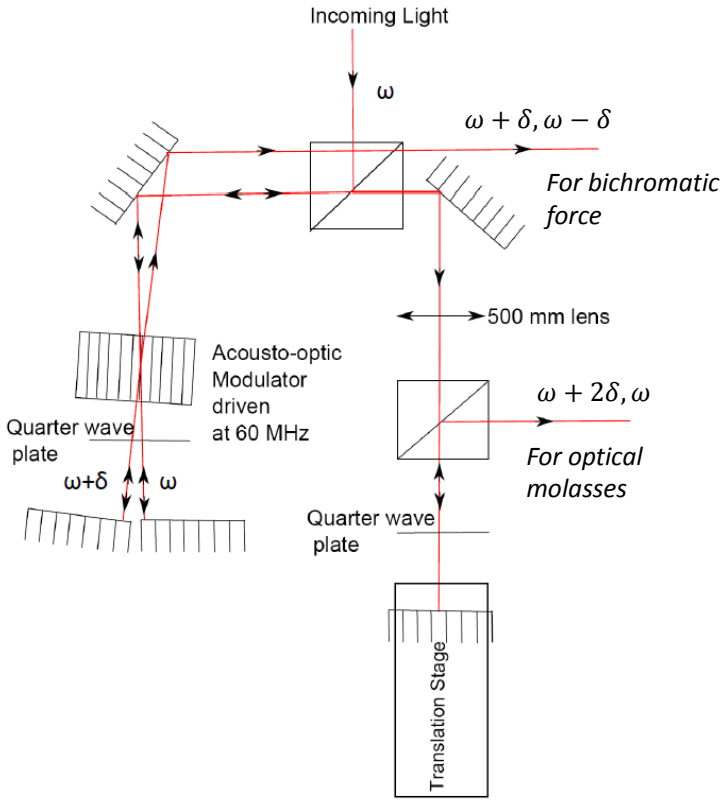

Figure 2.12: Two–frequency light generation by double passing an AOM [27]. The translation stage controls the π–pulse phase delay between the $\omega + \delta, \omega - \delta$ and $\omega + 2\delta, \omega$ components.

We see from Fig. 2.12 that by double passing the AOM, we acquire one beam containing $\omega \pm \delta$ frequencies and the other beam containing ω and $\omega + 2\delta$ frequencies. We drive the AOM at $\delta = 2\pi \times 60$MHz b rf signal from HP 3200B (amplified by a MiniCircuits ZHL-1-2W RF amplifier). The light containing $\omega \pm \delta$ frequencies are then amplified by fiber amplifiers, to be used for the bichromatic force and optical molasses.

Chapter 3

Three Level STIRAP and Complications beyond the Simple Picture

3.1 A Brief Introduction to STIRAP

STIRAP stands for Stimulated Raman Adiabatic Passage, which is a particular process to transfer population between different quantum levels. The concept of this process was first brought about by Hioe and Eberly [56] [57]. The first experimental realization was achieved by Klaas Bergmann et al. in 1988 [58], and in a subsequent paper in 1990 [59] they assigned the name STIRAP which is now widely accepted.

Here I want to give a quick tour of the three level STIRAP process based on our experiment. Two typical three level systems are shown in Fig. 3.1. A more detailed discussion of STIRAP can be found at a series of papers published by Bruce Shore and Klaas Bergmann et al. [60] [61] [62] [63]. The original goal of the current experiment was to excite metastable

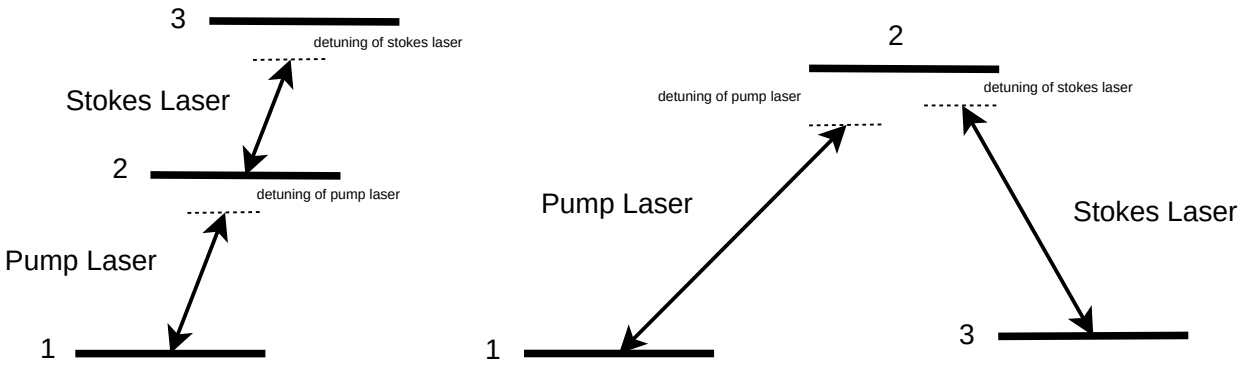

Figure 3.1: Two typical three-level systems: the ladder system and the lambda system. There is a tiny subtle difference between those two systems with regard to STIRAP, which is not usually brought up. The STIRAP of lambda system whose excited level can decay down to both the ground levels is in some sense easier to implement. The reason is that, even when the pump laser and Stokes laser are cw in time, as long as the ratio of their Rabi frequency is proper, the optical pumping process like that in EIT will put the wavefunction of the atom in the correct dark state which makes atom transparent to the lasers. This dark state is exactly the STIRAP workhorse state that will be discussed a lot in the following.

Helium atoms from their metastable ground state into the n=24 Rydberg state by a 2-photon process via an intermediate state. The states involved are: $2^3S_1 \longrightarrow 3^3P_2 \longrightarrow$ n=24 Rydberg state. This is a typical 3 level system with excitations by two lasers whose frequencies correspond to the energy intervals separately. The first laser (uv laser) is at 389 nm, corresponding to $2^3S_1 \longrightarrow 3^3P_2$ transition, while the second laser (ir laser) is at around 796 nm, corresponding to $3^3P_2 \longrightarrow$n=24 Rydberg state transition. This is a ladder system. But the Hamiltonian is essentially the same for a lambda system as well.

Take the 2^3S_1 state to be $|1\rangle$, take the 3^3P_2 state to be $|2\rangle$, and take one of the n=24 Rydberg states (it is highly degenerate) to be $|3\rangle$.

Let's start the discussion by writing down the 3 by 3 Hamiltonian (3.1) for this 3 level system. We neglect the effect of spontaneous emission for the moment. Then the equation of motion for a wavefunction φ (which is a time-dependent 3 by 1 column vector) is (3.2).

$$\hat{H} = \hbar \begin{pmatrix} 0 & \frac{1}{2}\Omega_p(t) & 0 \\ \frac{1}{2}\Omega_p(t) & \Delta_p & \frac{1}{2}\Omega_S(t) \\ 0 & \frac{1}{2}\Omega_S(t) & \Delta_p + \Delta_S \end{pmatrix} \tag{3.1}$$

$$i\hbar \frac{d}{dt}\varphi = \hat{H}\varphi \tag{3.2}$$

Here the subscript 'p' stands for the pump laser, while the subscript 'S' stands for the Stokes laser. Despite the simple appearance, it takes a little caution to derive this Hamiltonian.

Let us first describe the electric field of the laser as a 'plane wave at a fixed space point'.

$$\vec{E} = \mathcal{E}(t)\hat{\epsilon}\cos(\omega t) \tag{3.3}$$

$\mathcal{E}(t)$ is the slow-varying envelope of the pulse, $\hat{\epsilon}$ is the unit complex polarization vector. Now we can give the definition of the Rabi frequency.

$$\begin{aligned} \hbar\Omega_p(t) &= |\mathcal{E}_p(t)e\langle 1|\vec{r}|2\rangle \cdot \hat{\epsilon_p}^*| \\ \hbar\Omega_S(t) &= |\mathcal{E}_S(t)e\langle 2|\vec{r}|3\rangle \cdot \hat{\epsilon_S}^*| \end{aligned} \tag{3.4}$$

In this simple three level system, $\Omega(t)$ can be always chosen to be a real number, through a process which absorbs the phase into the base kets in the rotating wave frame. Since, the Hamiltonian in (3.1) is written in the rotating wave frame, which means, its base kets are not $|n\rangle,\ n = 1, 2, 3$; rather, the actual base kets have a phase difference between them. These phases are time-dependent. Say, the base kets in the rotating wave frame are $|n'\rangle,\ n = 1, 2, 3$, and E_n stands for the energy eigenvalue of $|n\rangle$.

$$|n'\rangle = e^{-i\zeta_n(t)}|n\rangle,\ n = 1, 2, 3; \tag{3.5}$$

$$\begin{aligned} \zeta_1(t) &= \tfrac{t}{\hbar}\mathrm{E}_1 \\ \zeta_2(t) &= \tfrac{t}{\hbar}(\mathrm{E}_1 + \hbar\omega_p) \\ \zeta_2(t) &= \tfrac{t}{\hbar}(\mathrm{E}_1 + \hbar\omega_p + \hbar\omega_S) \end{aligned} \tag{3.6}$$

And accordingly we have the detunings between the laser and the exact atomic transition energy.

$$\begin{aligned} \hbar\Delta_p &= \mathrm{E}_2 - \mathrm{E}_1 - \hbar\omega_p \\ \hbar\Delta_S &= \mathrm{E}_3 - \mathrm{E}_2 - \hbar\omega_S \end{aligned} \tag{3.7}$$

Then after the rotating wave approximation which neglects the fast oscillating terms, we end up with the Hamiltonian in (3.1). To simplify the discussion, we consider the STIRAP when the two photon resonance condition is satisfied, i.e. $\Delta_p + \Delta_S = 0$. We soon notice that this matrix of (3.1) is now singular, i.e. its rank is only 2 though it is a 3 by 3 matrix. Let us try to find the null vector of this matrix at any time.

$$\begin{pmatrix} 0 & \Omega_p(t)/2 & 0 \\ \Omega_p(t)/2 & \Delta_p & \Omega_S(t)/2 \\ 0 & \Omega_S(t)/2 & 0 \end{pmatrix} \begin{pmatrix} \alpha(t) \\ 0 \\ \beta(t) \end{pmatrix} = 0 \tag{3.8}$$

To satisfy (3.8), we have $\alpha(t)\Omega_p(t) + \beta(t)\Omega_S(t) = 0$. Further if we want this null vector to be normalized, we may define $\theta(t)$ as:

$$\tan\theta(t) = \frac{\Omega_p(t)}{\Omega_S(t)} \tag{3.9}$$

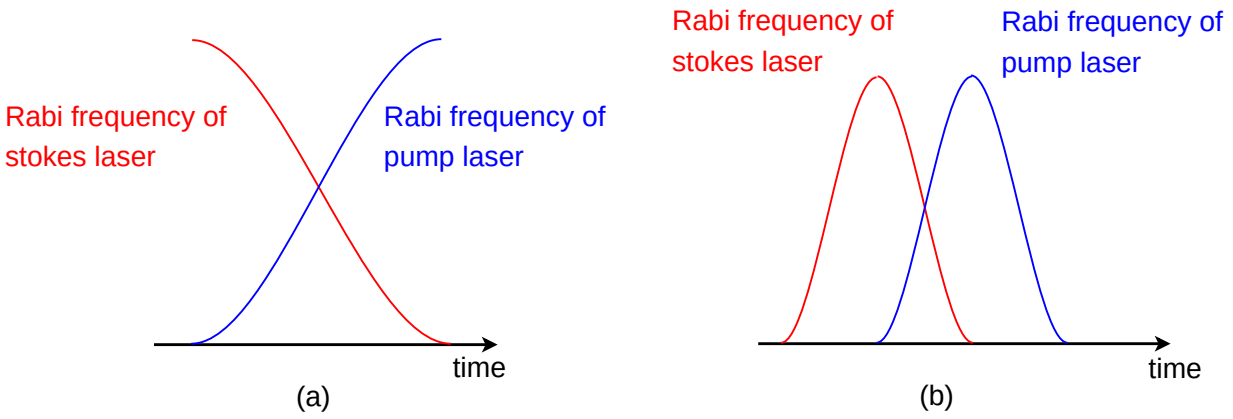

Figure 3.2: Smooth pulse shapes to achieve population transfer

And then this null vector can be written as $|0\rangle = (\cos\theta, 0, -\sin\theta)^T$. From an eigenvector point of view, this null vector is an instantaneous energy eigenstate of the Hamiltonian in (3.8), which is the so called adiabatic state. More interesting is that the instantaneous energy eigenvalue of this adiabatic state does not change – it always stay at 0.

The idea of adiabatic following asserts that, then the quantum state of the system would always follow an adiabatic state as long as some adiabatic condition is satisfied.

Assume for now that the adiabatic condition is fulfilled and the system is following the adiabatic state $(\cos\theta, 0, -\sin\theta)^T$. Let us see how we can make use of this to achieve a complete population transfer from $|1\rangle$ to $|3\rangle$. Basically we want $|0\rangle$ to be $|1\rangle$ at the beginning and $|3\rangle$ in the end. For this, we need θ to go from 0 to $\pi/2$. Of course θ had better change smoothly to avoid abrupt interruption of the adiabatic following. Then $\Omega_S(t)$ and $\Omega_p(t)$, as functions of time, ought to look like Fig. 3.2(a).

This is the so called "counter-intuitive pulse pairs" and is the essence of three level STIRAP. The system starts to evolve, i.e. start on the adiabatic state $|0\rangle$ which is just the ground state $|1\rangle$ at the beginning, as soon as Ω_p goes up from zero; and the system ends, i.e. finish the adiabatic state $|0\rangle$ as $|3\rangle$, as soon as Ω_S decreases to zero. A numerical simulation

of such a process using the abrupt pulses shown in Fig. 3.2(a) has been provided in Fig. 3.3. The Rabi frequency and time evolution of lasers have been chosen close to experimental values.

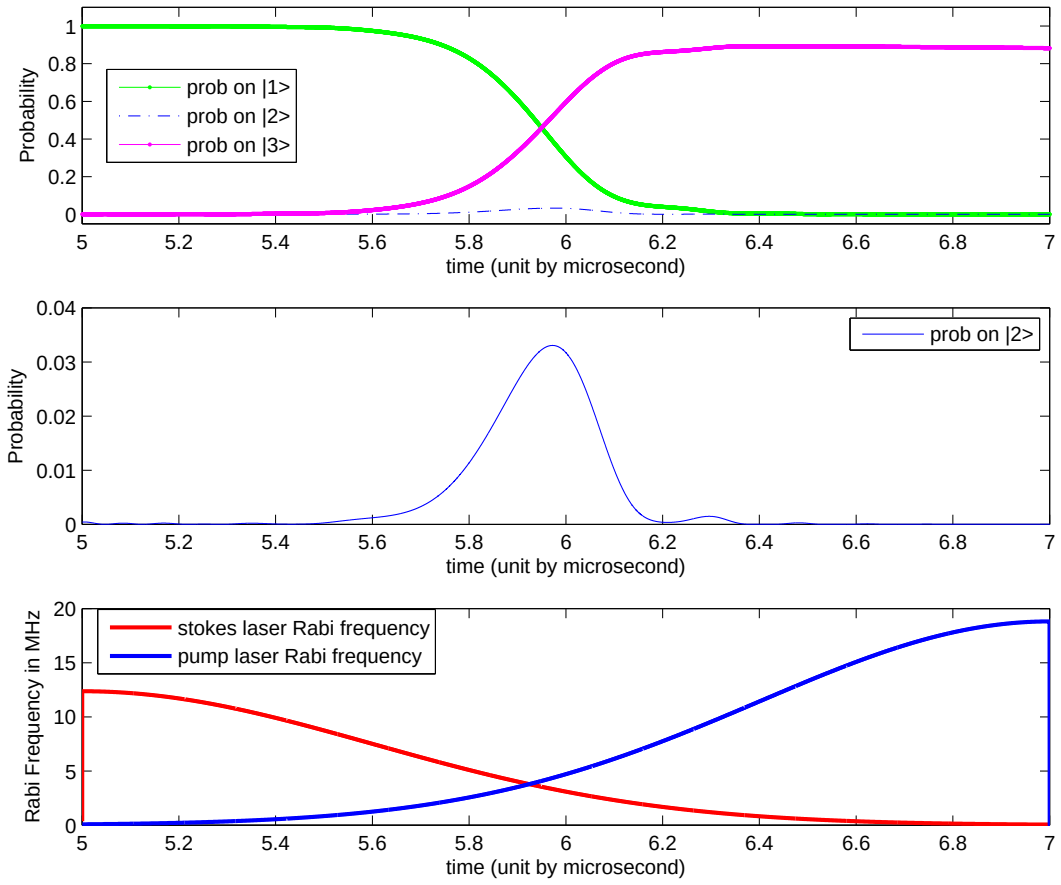

Figure 3.3: Numerical simulation of STIRAP by abrupt pulses. The top subplot shows how the population in each individual level evolves with time. The center subplot shows how the population in the intermediate level evolves with time. The scale is different for the center subplot. The bottom subplot shows the Rabi frequency of the laser pulses. The decay of state $|2\rangle$ and $|3\rangle$ have been taken into consideration.

Yet practically it is hard and unnecessary to use abrupt pulses such as in Fig. 3.2(a) and Fig. 3.3. Instead, we may use a complete nice pulse, such as a Gaussian pulse. A typical

practically used counter-intuitive STIRAP pulse pairs are shown in Fig. 3.2(b). This does not change the nature of the system since at the beginning $\tan\theta$ is always zero before the pump pulse is turned on, and in the end $\tan\theta$ is always infinity when the Stokes pulse is turned off. Further discussions along this line can be found in [64].

All these are very nice except for one glaring question: how come the atom does not even see the intermediate level? Put in another way, what is 'adiabatic following'? Moreover, we may wonder that why the value of Δ_p in (3.8) seems irrelevant, though we already knew that one photon detuning is a crucial factor in STIRAP?

Let us go back to the Schrödinger equation and take a closer look at the time evolution of a state vector strictly conciding with $|0\rangle$. According to (3.8) and (3.10), the time derivative of $|0\rangle$ is 0 at all times, which leads to this apparent contradiction: how could this state change with time if its time derivative is 0?

$$i\frac{d}{dt}|0\rangle = \begin{pmatrix} 0 & \Omega_p(t)/2 & 0 \\ \Omega_p(t)/2 & \Delta_p & \Omega_S(t)/2 \\ 0 & \Omega_S(t)/2 & 0 \end{pmatrix} \begin{pmatrix} \cos\theta \\ 0 \\ -\sin\theta \end{pmatrix} = 0 \tag{3.10}$$

The answer to the above glaring question is that, during the process of STIRAP, there is a small population in level $|2\rangle$. Actually we can see a hint of this point in Fig. 3.3, where the time evolution of the population of the intermediate level is shown. The advertisement of STIRAP claims the intermediate level never gets populated, but we know what it comes to when advertisement vs. reality. The physics determines it is a two step process and the intermediate level is required to have footprints. Let us see why and how.

To see the reason that intermediate states get population after the interaction starts, we are going to use the important method in ordinary differential equations, namely, iteration, also know as the Dyson expansion in quantum perturbation theory. First we rewrite the

target differential equation (3.2) into the integral form (3.11). Here, as in (3.8), we assume $\Delta_p + \Delta_S = 0$ for $\hat{H}$. The integral for the vector is regarded as taking integral of each individual component.

$$\varphi(t) = \int_0^t \frac{1}{i\hbar}\hat{H}\varphi dt + \varphi(0) \tag{3.11}$$

The iteration process is described as in (3.12), where we get $\varphi'(t)$ as the next order solution based on the solution $\varphi(t)$ from the previous order. The range of the integral is a small period of time immediately after the interaction is turned on, i.e. $t < \delta t$ for a fixed small value of time δt. The choice of a short time interval is to address our interest to see how probability amplitude gets into $|2\rangle$ in the first place, and to ensure convergence for the iteration process.

$$\varphi'(t) = \int_0^t \frac{1}{i\hbar}\hat{H}(t')\varphi(t')dt' + \varphi(0) \tag{3.12}$$

We already know that $|0\rangle$ is at most an approximate solution. Let us rename $|0\rangle$ as ϕ_0 and iterate once to get a 'better' solution ϕ_0' (as the 1st order solution). Then we get $\phi_0' = (1, 0, 0)^T$ and this basically tells us that nothing is going on at the lowest order. We carry on the iteration to get ϕ_0'' (as the 2nd order solution) and ϕ_0''' (as the 3rd order solution) according to (3.12).

$$\phi_0''(t') = \int_0^{t'} \frac{1}{i\hbar}\hat{H}(t)\phi_0'(t)dt + \phi_0'(0) \tag{3.13}$$

and therefore:

$$= -i \int_0^{t'} \begin{pmatrix} 0 & \Omega_p(t)/2 & 0 \\ \Omega_p(t)/2 & \Delta_p & \Omega_S(t)/2 \\ 0 & \Omega_S(t)/2 & 0 \end{pmatrix} \begin{pmatrix} 1 \\ 0 \\ 0 \end{pmatrix} dt + \begin{pmatrix} 1 \\ 0 \\ 0 \end{pmatrix} = \begin{pmatrix} 1 \\ -i \int_0^{t'} \frac{\Omega_p(t)}{2} dt \\ 0 \end{pmatrix}$$

$$\phi_0'''(t'') = \int_0^{t''} \frac{1}{i\hbar} \hat{H}(t') \phi_0''(t') dt' + \phi_0''(0)$$

$$= -i \int_0^{t''} \begin{pmatrix} 0 & \Omega_p(t')/2 & 0 \\ \Omega_p(t')/2 & \Delta_p & \Omega_S(t')/2 \\ 0 & \Omega_S(t')/2 & 0 \end{pmatrix} \begin{pmatrix} 1 \\ -i \int_0^{t'} \frac{\Omega_p(t)}{2} dt \\ 0 \end{pmatrix} dt' + \begin{pmatrix} 1 \\ 0 \\ 0 \end{pmatrix}$$

$$= \begin{pmatrix} 1 - \int_0^{t''} \frac{\Omega_p(t')}{2} dt' \\ -i \int_0^{t''} \frac{\Omega_p(t')}{2} dt' - \Delta_p \int_0^{t''} \int_0^{t'} \frac{\Omega_p(t)}{2} dt dt' \\ - \int_0^{t''} \frac{\Omega_S(t')}{2} \int_0^{t'} \frac{\Omega_p(t)}{2} dt dt' \end{pmatrix} \tag{3.14}$$

During this iteration process, it is understood that all the time variables are within the δt interval, i.e. $t', t'' < \delta t$. This iteration process can be continued, yet the result of ϕ_0''' is enough for some preliminary observations. As seen in (3.13) and (3.14), when the interaction begins, a little tiny population is moved into the state $|2\rangle$ with a correct phase. Then this small probability amplitude in $|2\rangle$ helps to transfer a lot of the population from $|1\rangle$ into $|3\rangle$. The population in $|3\rangle$ would grow significantly and continuously if the pulse shape of the Stokes and pump lasers are chosen right, while the population in $|2\rangle$ shall always stay tiny. This is an alternative way of explaining STIRAP to the mysterious adiabatic following of a three level system. We will come back to this point later.

The effect of one photon detuning is also revealed by the term $-\Delta_p \int_0^{t''} \int_0^{t'} \frac{\Omega_p(t)}{2} dt dt'$ in (3.14). But we also observe that it only affects the intermediate level through a higher order, which means its overall effect on STIRAP can not be too significant for small Δ_p values.

However, the method of iteration in (3.12) is cumbersome and can only address the problem locally in the time domain, i.e. it only tells us the evolution of the system within a short period of time. Now that we qualitatively know that there is indeed a small population is in $|2\rangle$ during STIRAP, we can cheat a bit to get a global solution. Namely, a 'better' wavefunction can be constructed as $|0'\rangle = (\cos\theta, \eta, -\sin\theta)^T$ where $\eta = \eta(t)$ is small, and then its time evolution can be examined.

$$i\frac{d}{dt}\begin{pmatrix} \cos\theta \\ \eta \\ -\sin\theta \end{pmatrix} = i\begin{pmatrix} -\dot{\theta}\sin\theta \\ \dot{\eta} \\ -\dot{\theta}\cos\theta \end{pmatrix} \tag{3.15}$$

$$\frac{1}{\hbar}\hat{H}\begin{pmatrix} \cos\theta \\ \eta \\ -\sin\theta \end{pmatrix} = \begin{pmatrix} 0 & \Omega_p(t)/2 & 0 \\ \Omega_p(t)/2 & \Delta_p & \Omega_S(t)/2 \\ 0 & \Omega_S(t)/2 & 0 \end{pmatrix}\begin{pmatrix} \cos\theta \\ \eta \\ -\sin\theta \end{pmatrix} = \begin{pmatrix} \eta\frac{\Omega_p}{2} \\ \eta\Delta_p \\ \eta\frac{\Omega_S}{2} \end{pmatrix} \tag{3.16}$$

The equality of (3.2) shall be maintained by (3.15) and (3.16), which leads to (3.17).

$$\begin{aligned} -i\dot{\theta}\sin\theta &= \eta\tfrac{\Omega_p}{2} \\ i\dot{\eta} &= \eta\Delta_p \\ -i\dot{\theta}\cos\theta &= \eta\tfrac{\Omega_S}{2} \end{aligned} \tag{3.17}$$

The first and third equation of (3.17) is compatible and essentially redundant, since if we divide one by the other then we have $\frac{\sin\theta}{\cos\theta} = \frac{\Omega_p}{\Omega_s}$, which is essentially (3.9). Since $|00\rangle$ is again

a approximate solution and η is small, though the second equation of (3.17) is not exactly compatible with the others we can safely neglect it for now. Therefore, (3.17) indicates the requirement on the population of the intermediate level which is simply summarized in (3.18).

$$\eta = \frac{-2i\dot{\theta}}{\sqrt{\Omega_p^2 + \Omega_S^2}} \tag{3.18}$$

3.2 Adiabatic Conditions of STIRAP

K. Bergmann et al [60] discussed the robustness of the STIRAP process from the point of view of how good the adiabatic following to $|0\rangle$ is. Basically the idea is, during the evolution in time, to maintain a small overlapping between $|0\rangle$ and the other two adiabatic states of $\hat{H}$ in (3.1), hence the conditions are given the name 'adiabatic conditions'. Yet the ideas of 'adiabatic' is a bit of *ad hoc* such that I won't quite follow that line of argument, though I still borrow the name adiabatic conditions.

Let us gather what we have so far. In order to make STIRAP via $|0\rangle$ happen, we want $|0'\rangle$ to behave very similar to $|0\rangle$, i.e. $|\eta(t)|$ has to be small all the time. Then according to (3.18) the criteria for STIRAP can be written as:

$$|\eta| = 2|\frac{\dot{\theta}}{\sqrt{\Omega_p^2 + \Omega_S^2}}| \ll 1 \tag{3.19}$$

(3.19) has to be satisfied at all times during the interaction. We can simplify it bit. Set $\Omega_{eff} = \sqrt{\Omega_p^2 + \Omega_S^2}$, then (3.19) is saying that $2|\dot{\theta}| \ll \Omega_{eff}$. We can integrate both sides over the interaction time τ, which can be viewed as the time interval θ changes from 0 to $\pi/2$ or the pulses' overlapping time. The value of Ω_{eff} does not change much during the

overlapping time. In summary, we have (3.20):

$$\Omega_{eff} \cdot \tau \gg \pi \tag{3.20}$$

A further analysis of $|0'\rangle$ is due here. Any time dependent vector $(A(t), B(t), C(t))^T$ is a linear superposition [1] of $|0\rangle = (\cos\theta, 0, -\sin\theta)^T$, $|2\rangle = (0, 1, 0)^T$ and $|2'\rangle = (\sin\theta, 0, \cos\theta)^T$. Here $|2\rangle$ and $|2'\rangle$ are just names and shall not be confused with other adiabatic states. $|0\rangle$, $|2\rangle$ and $|2'\rangle$ are unimodular and orthogonal to one another hence at any time t they form an orthonormal basis. Say the exact wave function for the STIRAP process is $|\varsigma\rangle$. From previous discussions we know that $|\varsigma\rangle$ is composed of mostly $|0\rangle$ together with a small contribution of $|2\rangle$ which we named as η in (3.15). Yet there is no reason why $|\varsigma\rangle$ does not contain anything from $|2'\rangle$. Formally, we have (3.21) in first order perturbation, where η and ξ are small compared to 1.

$$|\varsigma\rangle = |0\rangle + \eta|2\rangle + \xi|2'\rangle \tag{3.21}$$

By this definition, $|\varsigma\rangle$ is not normalized. I am going to carry out an analogous discussion of $|0'\rangle$ for $|\varsigma\rangle$. First, the time derivative part.

$$i\frac{d}{dt}|\varsigma\rangle = i\begin{pmatrix} -\dot{\theta}\sin\theta + \xi\dot{\theta}\cos\theta \\ \dot{\eta} \\ -\dot{\theta}\cos\theta - \xi\dot{\theta}\sin\theta \end{pmatrix} \tag{3.22}$$

Then, the Hamiltonian part.

[1] Essentially this is a projection onto the orthonormal basis. Of course this projection is time-dependent via $\theta(t)$

$$\frac{1}{\hbar}\hat{H}|\varsigma\rangle = \begin{pmatrix} \eta\frac{\Omega_p}{2} \\ \eta\Delta_p + \xi\frac{\Omega_p}{2}\sin\theta + \xi\frac{\Omega_S}{2}\cos\Theta \\ \eta\frac{\Omega_S}{2} \end{pmatrix} \tag{3.23}$$

As before, we require that (3.22) and (3.23) are equal according the Schrödinger equation. Up to the 1st order, the equations about the wavefunction components in level 1 and level 3 of $|\varsigma\rangle$ are the same as (3.17). We are interested in what happens in the equation for level 2 component of $|\varsigma\rangle$ since now it is compatible with the other two equations.

$$i\dot{\eta} = \eta\Delta_p + \xi\frac{\Omega_p}{2}\sin\theta + \xi\frac{\Omega_S}{2}\cos\theta \tag{3.24}$$

An assumption can be added here that the magnitude of $\frac{\dot{\eta}}{\eta}$ and $\frac{\dot{\eta}}{\xi}$ is small compared to Ω_{eff} and Δ_p. Then we can drop the term $i\dot{\eta}$ in (3.24).

$$0 = \eta\Delta_p + \xi\frac{\Omega_p}{2}\sin\theta + \xi\frac{\Omega_S}{2}\cos\theta \tag{3.25}$$

Immediately we can solve for ξ. Because of the assumption we made, this is a 'stable' solution such that the value of ξ does not change a lot during the entire time of interaction.

$$\xi = -\frac{\eta\Delta_p}{\frac{\Omega_p}{2}\sin\theta + \frac{\Omega_S}{2}\cos\theta} \tag{3.26}$$

From (3.21) and the definition of $|2'\rangle$ we see that ξ basically describes how much population is left in the level 1 in the end. (3.26) tells us that ξ is proportional to Δ_p. Based on (3.18) and (3.20), we can use $\frac{\pi}{\tau}\frac{1}{\Omega_{eff}}$ as η approximately in (3.26). Also $\frac{\Omega_p}{2}\sin\theta + \frac{\Omega_S}{2}\cos\theta = \Omega_{eff}/2$. Combine all these observations:

$$\xi \approx 2\pi\frac{\Delta_p}{\Omega_{eff}^2\tau} \tag{3.27}$$

Arguments following (3.14) show that Δ_p does affect the STIRAP process. Here we have quantified its effect. As long as Δ_p deviates from zero, some population is going to stay in level 1 after STIRAP, up to 1st order. The larger $|\Delta_p|$ is, the more population gets put back in level 1. If we want to keep ξ at the same order as $\frac{1}{\Omega_{eff}\tau}$, the criteria is $\Omega_{eff} > \Delta_p$. We also see that STIRAP is tolerant to Δ_p provided the two-photon resonance condition is satisfied. Say experimentally $\Omega_{eff}\tau$ is about 20 and $\Delta_p \approx \Omega_{eff}/2$, then $\xi \approx 0.15$. ξ is probability amplitude and the population shall be ξ^2, which is 0.02 – only 2% population is lost.

3.3 Feynman's Path Integral for Discrete States and STIRAP

To begin, we need a little setup for notations and conventions. We will keep using what is in the previous sections, namely, $\Omega_{eff} = \Omega_{eff}(t) = \sqrt{\Omega_p^2 + \Omega_S^2}$. The Hamiltonian we are dealing with is still:

$$H = \hbar \begin{pmatrix} 0 & \Omega_p(t)/2 & 0 \\ \Omega_p(t)/2 & \Delta & \Omega_S(t)/2 \\ 0 & \Omega_S(t)/2 & 0 \end{pmatrix} \tag{3.28}$$

The adiabatic states (i.e. the instantaneous energy eigen-states) are:

$$|\widehat{+1}, t\rangle = \sin\theta \sin\phi|1\rangle + \cos\phi|2\rangle + \cos\theta \sin\phi|3\rangle \tag{3.29a}$$

$$|\widehat{0}, t\rangle = \cos\theta|1\rangle - \sin\theta|3\rangle \tag{3.29b}$$

$$|\widehat{-1}, t\rangle = \sin\theta \cos\phi|1\rangle - \sin\phi|2\rangle + \cos\theta \cos\phi|3\rangle \tag{3.29c}$$

Here $\theta = \theta(t)$ and $\phi = \phi(t)$ are time-dependent and are defined as following:

$$\tan\theta = \frac{\Omega_p(t)}{\Omega_S(t)} \tag{3.30a}$$

$$\tan(2\phi) = \frac{\Omega_{eff}}{\Delta} \tag{3.30b}$$

The instantaneous energy eigen-values of those adiabatic states are:

$$E(\widehat{+1}, t) = \frac{1}{2}(\Delta + \sqrt{\Omega_{eff}^2 + \Delta^2}) \tag{3.31a}$$

$$E(\widehat{0}, t) = 0 \tag{3.31b}$$

$$E(\widehat{-1}, t) = \frac{1}{2}(\Delta - \sqrt{\Omega_{eff}^2 + \Delta^2}) \tag{3.31c}$$

We need some more relations about the adiabatic states.

$$\textit{Identity and Projection: } \mathbf{1} = |\widehat{+1}\rangle\langle\widehat{+1}| + |\widehat{0}\rangle\langle\widehat{0}| + |\widehat{-1}\rangle\langle\widehat{-1}| \tag{3.32}$$

$$\textit{Energy Eigenstates: } H(t)|\widehat{j}, t\rangle = E(\widehat{j}, t)|\widehat{j}, t\rangle,\ j = -1, 0, +1. \tag{3.33}$$

$$\textit{Orthogonality and normality: } \langle\widehat{j}, t|\widehat{k}, t\rangle = \delta_{jk},\ j = -1, 0, +1. \tag{3.34}$$

With all these preparations now let us look at the problem. We are trying to solve the time evolution of such a system: $i\hbar\frac{d}{dt}|\varphi\rangle = H(t)|\varphi\rangle$. Suppose the interaction starts at time $t = 0$ and we are looking at $t = T$. Now we are trying to evaluate the propagator $\Theta(T) = \langle 3|\exp -\frac{i\int_0^T H dt}{\hbar}|1\rangle$. We are going to evaluate that by Feynman's Path Integral. By the methods we are going to explain next, all propagators of this type can be acquired hence it would become a satisfying solution of the time evolution problem.

First, we need to 'split' the time, which is the typical first step of the Feynman's Path

Integral.

$$\Theta(T) = \langle 3| \exp -\frac{i\int_0^T H(t)dt}{\hbar}|1\rangle = \lim_{\Delta t\to 0}\langle 3|(1-i\frac{H(t_{n-1})\Delta t}{\hbar})\cdots(1-i\frac{H(t_0)\Delta t}{\hbar})|1\rangle \quad (3.35)$$

Here, $\Delta t = T/n$ hence $\Delta t \to 0$ is the same as $n \to \infty$. t_0 is when the interaction starts and $t_n = T$ is when the interaction ends. In the next step, we insert the identity operator as in (3.32) for each t_n in (3.35).

$$\lim_{\Delta t\to 0}\langle 3| \sum_{j_n=-1,0,1} |\widehat{j_n}, t_n\rangle\langle\widehat{j_n}, t_n|(1-i\frac{H(t_{n-1})\Delta t}{\hbar}) \sum_{j_{n-1}=-1,0,1} |\widehat{j_{n-1}}, t_{n-1}\rangle\langle\widehat{j_{n-1}}, t_{n-1}|\cdots$$
$$\sum_{j_1=-1,0,1} |\widehat{j_1}, t_1\rangle\langle\widehat{j_1}, t_1|(1-i\frac{H(t_0)\Delta t}{\hbar}) \sum_{j_0=-1,0,1} |\widehat{j_0}, t_0\rangle\langle\widehat{j_0}, t_0|1\rangle \quad (3.36)$$

To proceed further from (3.36), we are going to evaluate one type of inner product as in the following definition (3.37), and then multiply them all together in the time–ordered manner as specified in (3.36).

$$g^m_{lk} = \langle\widehat{l}, t_m + \Delta t|(1-i\frac{H(t_m)\Delta t}{\hbar})|\widehat{k}, t_m\rangle \quad (3.37)$$
$$m = 0, \cdots, n-1;\ l, k = -1, 0, +1.$$

In order to evaluate (3.37), we would need to work out the infinitesimal time translation of the adiabatic states. To make the life easier at the beginning, we shall assume that the one-photon detuning Δ is 0. Henceforth ϕ is a constant $\frac{\pi}{4}$. With all these in mind, we are able to get the following relations, under the condition that Δt is small and $\to 0$.

$$|\widehat{+1}, t+\Delta t\rangle - |\widehat{+1}, t\rangle = \Delta t \frac{d}{dt}|\widehat{+1}, t\rangle = \frac{\dot{\theta}}{\sqrt{2}}\Delta t|\widehat{0}, t\rangle \tag{3.38}$$

$$|\widehat{0}, t+\Delta t\rangle - |\widehat{0}, t\rangle = \Delta t \frac{d}{dt}|\widehat{0}, t\rangle = -\frac{\dot{\theta}}{\sqrt{2}}\Delta t(|\widehat{+1}, t\rangle + |\widehat{-1}, t\rangle) \tag{3.39}$$

$$|\widehat{-1}, t+\Delta t\rangle - |\widehat{-1}, t\rangle = \Delta t \frac{d}{dt}|\widehat{-1}, t\rangle = \frac{\dot{\theta}}{\sqrt{2}}\Delta t|\widehat{0}, t\rangle \tag{3.40}$$

Since now $|\widehat{j}, t+\Delta t\rangle$ is expressed in terms of $|\widehat{j}, t\rangle$ we are able to compute g^m_{lk} in (3.37). The following equation (3.41) is the result written in the matrix format. Note that the time in (3.41) is $t = t_m = m \cdot \Delta t$ and that $\dot{\theta} = \dot{\theta}(t)$.

$$g^m = \begin{pmatrix} 1 - i\frac{E(\widehat{+1},t)\Delta t}{\hbar} & \frac{\dot{\theta}}{\sqrt{2}}\Delta t & 0 \\ -\frac{\dot{\theta}}{\sqrt{2}}\Delta t & 1 & -\frac{\dot{\theta}}{\sqrt{2}}\Delta t \\ 0 & \frac{\dot{\theta}}{\sqrt{2}}\Delta t & 1 - i\frac{E(\widehat{-1},t)\Delta t}{\hbar} \end{pmatrix} \tag{3.41}$$

If we want to continue to work the propagator out we will have to inevitably evaluate a product of the type $g^n \cdots g^2 g^1$. Before the discussion of the general case, let us look at what happens in the adiabatic limit, i.e. $\dot{\theta} \to 0$. Then g^m in (3.41) becomes:

$$g^m = \begin{pmatrix} 1 - i\frac{E(\widehat{+1},t)\Delta t}{\hbar} & 0 & 0 \\ 0 & 1 & 0 \\ 0 & 0 & 1 - i\frac{E(\widehat{-1},t)\Delta t}{\hbar} \end{pmatrix} \tag{3.42}$$

As defined in (3.42), g^l and g^m commute with each other since they are all diagonal. Then it is legitimate to take the ln and convert the product into a sum. Yet we have to know how to take this ln. The formula I am going to use is $\ln(I-T) = -\sum_{k=1}^{\infty}\frac{T^k}{k}$ (provided $\|T\| < 1$) and here essentially I only need the 1st order: $\ln(I-T) = -T$.

$$\ln g^m = \begin{pmatrix} -i\frac{E(\widehat{+1},t)\Delta t}{\hbar} & 0 & 0 \\ 0 & 0 & 0 \\ 0 & 0 & -i\frac{E(\widehat{-1},t)\Delta t}{\hbar} \end{pmatrix} \tag{3.43}$$

In the limit of $\Delta t \to 0$ or equivalently $n \to \infty$, the sum is just like doing an integral. With all those information at hand, we may compute the propagator g.

$$\ln g = \lim_{n\to\infty} \ln(g^n \cdots g^2 g^1) = \lim_{n\to\infty} \sum_1^n \ln g_m = \begin{pmatrix} -i\int \frac{E(\widehat{+1},t)}{\hbar} dt & 0 & 0 \\ 0 & 0 & 0 \\ 0 & 0 & -i\int \frac{E(\widehat{-1},t)}{\hbar} \end{pmatrix} \tag{3.44}$$

$$g = \begin{pmatrix} \exp(-i\int \frac{E(\widehat{+1},t)}{\hbar} dt) & 0 & 0 \\ 0 & 1 & 0 \\ 0 & 0 & \exp(-i\int \frac{E(\widehat{-1},t)}{\hbar} dt) \end{pmatrix} \tag{3.45}$$

(3.44) and (3.45) are precisely telling us the idea of the adiabatic following (of course, in the adiabatic limit/approximation). The system would honestly follow those adiabatic states, and the time evolution is merely a phase accumulation on these adiabatic states. No cross talk is possible between different adiabatic states. From the path integral's point of view, the paths are just straight lines in time, as can be seen from Fig. 3.4.

Now let us come back to the general problem as in (3.41). The method to evaluate this is again to take the ln and convert that product into a sum. However a subtle problem is in the sense that different g^m's do not commute with each other. The crucial step of (3.44) is essentially a special case of the Baker–Campbell–Hausdorff formula, which requires commutativity to be valid in (3.44). Nevertheless, we can still first formally compute $\ln g^m$

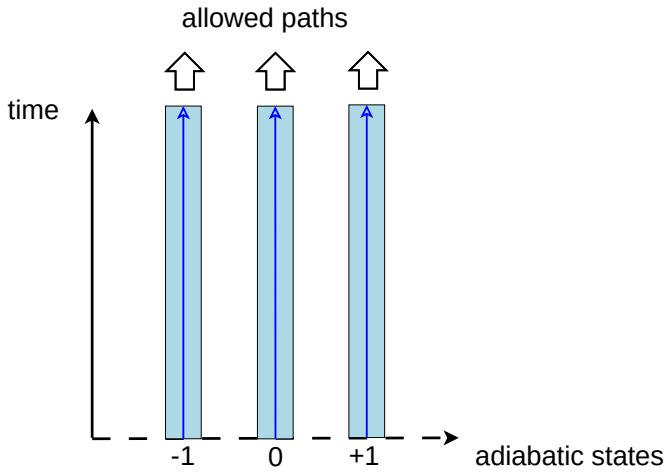

Figure 3.4: A schematic for paths in the pure adiabatic situation

for the infinitesimal time:

$$\textit{Up to 1st order: } \ln g^m = \begin{pmatrix} -i\frac{E(\widehat{+1},t)\Delta t}{\hbar} & \frac{\dot\theta}{\sqrt{2}}\Delta t & 0 \\ -\frac{\dot\theta}{\sqrt{2}}\Delta t & 0 & -\frac{\dot\theta}{\sqrt{2}}\Delta t \\ 0 & \frac{\dot\theta}{\sqrt{2}}\Delta t & -i\frac{E(\widehat{-1},t)\Delta t}{\hbar} \end{pmatrix} \tag{3.46}$$

By the virtue of (3.18), we observe that $\dot\theta$ in (3.46) is smaller by one order of magnitude than the diagonal terms $-i\frac{E(\widehat{+1},t)\Delta t}{\hbar}$ and $-i\frac{E(\widehat{-1},t)\Delta t}{\hbar}$. Therefore we can treat $\dot\theta$ as a 'small parameter' and look for solutions up to certain orders of this parameter, like a perturbative approach. According to the Baker–Campbell–Hausdorff formula, all the terms that result from the non–commuting nature of $\ln g^m$'s are those with higher orders in $\dot\theta$. Therefore for a first order result in $\dot\theta$ we can copy exactly what we did in (3.44). Another argument can be made according to a condition we experimentalists love: to assume that during the interaction $E(\widehat{+1},t)$, $E(\widehat{-1},t)$ and $\dot\theta$ stay as constants, and then the commuting criteria is satisfied. If the deviation from the constants are small along the time, then the non–commuting part is also small and can be neglected for a first order result. We can always

check in the end if the final result satisfies the Schrödinger equation or not. Then, in the limit of $\Delta t \to 0$ or equivalently $n \to \infty$, the sum is just like doing an integral:

$$g = \lim_{n\to\infty} \ln(g^n \cdots g^2 g^1) = \lim_{n\to\infty} \sum_1^n \ln g^m = \begin{pmatrix} -i\int \frac{E(\widehat{+1},t)}{\hbar} dt & \frac{\theta}{\sqrt{2}} & 0 \\ -\frac{\theta}{\sqrt{2}} & 0 & -\frac{\theta}{\sqrt{2}} \\ 0 & \frac{\theta}{\sqrt{2}} & -i\int \frac{E(\widehat{-1},t)}{\hbar} \end{pmatrix} \tag{3.47}$$

With (3.47) at our hand, we are finally able to treat the propagator $\Theta(T)$ we want, combining all the information we have so far.

$$\begin{aligned}
\Theta(T) &= \sum_{j_n=-1,0,1} \sum_{j_0=-1,0,1} \langle 3|\widehat{j_n}, T\rangle \lim_{n\to\infty} (g^n \cdots g^2 g^1) \langle \widehat{j_0}, t_0|1\rangle \\
&= \sum_{j_n=-1,0,1} \sum_{j_0=-1,0,1} \langle 3|\widehat{j_n}, T\rangle \exp\{\lim_{n\to\infty} \ln(g^n \cdots g^2 g^1)\} \langle \widehat{j_0}, t_0|1\rangle \\
&= \left(\langle 3|\widehat{+1}, T\rangle \quad \langle 3|\widehat{0}, T\rangle \quad \langle 3|\widehat{-1}, T\rangle \right) \exp \begin{pmatrix} -i\int \frac{E(\widehat{+1},t)}{\hbar} dt & \frac{\theta}{\sqrt{2}} & 0 \\ -\frac{\theta}{\sqrt{2}} & 0 & -\frac{\theta}{\sqrt{2}} \\ 0 & \frac{\theta}{\sqrt{2}} & -i\int \frac{E(\widehat{-1},t)}{\hbar} \end{pmatrix} \begin{pmatrix} \langle \widehat{+1}, t_0|1\rangle \\ \langle \widehat{0}, t_0|1\rangle \\ \langle \widehat{-1}, t_0|1\rangle \end{pmatrix}
\end{aligned} \tag{3.48}$$

As mentioned earlier, we need to do a sanity check on this $\Theta(T)$, since in the crucial step of (3.47), which leads to (3.48), we are actually performing an (seemingly) unjustifiable approximation. We would verify whether a wavefunction corresponding to this $\Theta(T)$ satisfies the Schrödinger equation or not. Let us proceed as follows.

First, it is helpful to explicitly write down the wavefunction $|\phi\rangle = |\phi(T)\rangle$ corresponding to $\Theta(T)$.

$$\begin{pmatrix} \langle 1|\phi\rangle \\ \langle 2|\phi\rangle \\ \langle 3|\phi\rangle \end{pmatrix} = \begin{pmatrix} \langle 1|\widehat{+1},T\rangle & \langle 1|\widehat{0},T\rangle & \langle 1|\widehat{-1},T\rangle \\ \langle 2|\widehat{+1},T\rangle & \langle 2|\widehat{0},T\rangle & \langle 2|\widehat{-1},T\rangle \\ \langle 3|\widehat{+1},T\rangle & \langle 3|\widehat{0},T\rangle & \langle 3|\widehat{-1},T\rangle \end{pmatrix} \exp \begin{pmatrix} -i\int \frac{E(\widehat{+1},t)}{\hbar}dt & \frac{\theta}{\sqrt{2}} & 0 \\ -\frac{\theta}{\sqrt{2}} & 0 & -\frac{\theta}{\sqrt{2}} \\ 0 & \frac{\theta}{\sqrt{2}} & -i\int \frac{E(\widehat{-1},t)}{\hbar} \end{pmatrix} \begin{pmatrix} \langle \widehat{+1},t_0|1\rangle \\ \langle \widehat{0},t_0|1\rangle \\ \langle \widehat{-1},t_0|1\rangle \end{pmatrix} \tag{3.49}$$

The next step is to put $|\phi\rangle$ into the Schrödinger equation $i\hbar\frac{d}{dT}|\phi\rangle = H|\phi\rangle$ for H as defined in (3.28), to check if the LHS and RHS are equal. For this purpose we need to take the time derivative of (3.49).

From the three equations following (3.38), we know that:

$$\frac{d}{dT}\begin{pmatrix} \langle 1|\widehat{+1},T\rangle & \langle 1|\widehat{0},T\rangle & \langle 1|\widehat{-1},T\rangle \\ \langle 2|\widehat{+1},T\rangle & \langle 2|\widehat{0},T\rangle & \langle 2|\widehat{-1},T\rangle \\ \langle 3|\widehat{+1},T\rangle & \langle 3|\widehat{0},T\rangle & \langle 3|\widehat{-1},T\rangle \end{pmatrix} = \begin{pmatrix} \langle 1|\widehat{+1},T\rangle & \langle 1|\widehat{0},T\rangle & \langle 1|\widehat{-1},T\rangle \\ \langle 2|\widehat{+1},T\rangle & \langle 2|\widehat{0},T\rangle & \langle 2|\widehat{-1},T\rangle \\ \langle 3|\widehat{+1},T\rangle & \langle 3|\widehat{0},T\rangle & \langle 3|\widehat{-1},T\rangle \end{pmatrix} \cdot \begin{pmatrix} 0 & -\frac{\dot{\theta}}{\sqrt{2}} & 0 \\ \frac{\dot{\theta}}{\sqrt{2}} & 0 & \frac{\dot{\theta}}{\sqrt{2}} \\ 0 & -\frac{\dot{\theta}}{\sqrt{2}} & 0 \end{pmatrix} \tag{3.50}$$

The next step is to differentiate $e^{X(t)}$, the method of which is described in the following formula, a natural proposition of the *Hadamard lemma*.

$$(\frac{d}{dt}e^{X(t)})e^{-X(t)} = \frac{d}{dt}X(t) + \frac{1}{2!}[X(t),\frac{d}{dt}X(t)] + \frac{1}{3!}[X(t),[X(t),\frac{d}{dt}X(t)]] + \cdots \tag{3.51}$$

If we only keep the $1st$ order in (3.51), then $\frac{d}{dt}e^{X(t)} = \frac{d}{dt}X(t)e^{X(t)}$. That approximation leads to:

$$\frac{d}{dT}\exp\begin{pmatrix} -i\int^T \frac{E(\widehat{+1},t)}{\hbar}dt & \frac{\theta}{\sqrt{2}} & 0 \\ -\frac{\theta}{\sqrt{2}} & 0 & -\frac{\theta}{\sqrt{2}} \\ 0 & \frac{\theta}{\sqrt{2}} & -i\int^T \frac{E(\widehat{-1},t)}{\hbar} \end{pmatrix}$$

$$= \begin{pmatrix} -i\frac{E(\widehat{+1},T)}{\hbar} & \frac{\dot{\theta}}{\sqrt{2}} & 0 \\ -\frac{\dot{\theta}}{\sqrt{2}} & 0 & -\frac{\dot{\theta}}{\sqrt{2}} \\ 0 & \frac{\dot{\theta}}{\sqrt{2}} & -i\frac{E(\widehat{-1},T)}{\hbar} \end{pmatrix} \exp\begin{pmatrix} -i\int^T \frac{E(\widehat{+1},t)}{\hbar}dt & \frac{\theta}{\sqrt{2}} & 0 \\ -\frac{\theta}{\sqrt{2}} & 0 & -\frac{\theta}{\sqrt{2}} \\ 0 & \frac{\theta}{\sqrt{2}} & -i\int^T \frac{E(\widehat{-1},t)}{\hbar} \end{pmatrix} \tag{3.52}$$

By combining all the information contained in (3.49), (3.50) and (3.52), we can finally evaluate $\frac{d}{dT}|\phi\rangle$, to the $1st$ order in the sense of (3.51).

$$\frac{d}{dT}\begin{pmatrix} \langle 1|\phi\rangle \\ \langle 2|\phi\rangle \\ \langle 3|\phi\rangle \end{pmatrix} = \begin{pmatrix} \langle 1|\widehat{+1},T\rangle & \langle 1|\widehat{0},T\rangle & \langle 1|\widehat{-1},T\rangle \\ \langle 2|\widehat{+1},T\rangle & \langle 2|\widehat{0},T\rangle & \langle 2|\widehat{-1},T\rangle \\ \langle 3|\widehat{+1},T\rangle & \langle 3|\widehat{0},T\rangle & \langle 3|\widehat{-1},T\rangle \end{pmatrix} \cdot \Big(\begin{pmatrix} 0 & -\frac{\dot{\theta}}{\sqrt{2}} & 0 \\ \frac{\dot{\theta}}{\sqrt{2}} & 0 & \frac{\dot{\theta}}{\sqrt{2}} \\ 0 & -\frac{\dot{\theta}}{\sqrt{2}} & 0 \end{pmatrix} +$$

$$\begin{pmatrix} -i\frac{E(\widehat{+1},t)}{\hbar} & \frac{\dot{\theta}}{\sqrt{2}} & 0 \\ -\frac{\dot{\theta}}{\sqrt{2}} & 0 & -\frac{\dot{\theta}}{\sqrt{2}} \\ 0 & \frac{\dot{\theta}}{\sqrt{2}} & -i\frac{E(\widehat{-1},t)}{\hbar} \end{pmatrix} \Big) \cdot \exp\begin{pmatrix} -i\int \frac{E(\widehat{+1},t)}{\hbar}dt & \frac{\theta}{\sqrt{2}} & 0 \\ -\frac{\theta}{\sqrt{2}} & 0 & -\frac{\theta}{\sqrt{2}} \\ 0 & \frac{\theta}{\sqrt{2}} & -i\int \frac{E(\widehat{-1},t)}{\hbar} \end{pmatrix} \cdot \begin{pmatrix} \langle\widehat{+1},t_0|1\rangle \\ \langle\widehat{0},t_0|1\rangle \\ \langle\widehat{-1},t_0|1\rangle \end{pmatrix}$$

$$= \begin{pmatrix} \langle 1|\widehat{+1},T\rangle & \langle 1|\widehat{0},T\rangle & \langle 1|\widehat{-1},T\rangle \\ \langle 2|\widehat{+1},T\rangle & \langle 2|\widehat{0},T\rangle & \langle 2|\widehat{-1},T\rangle \\ \langle 3|\widehat{+1},T\rangle & \langle 3|\widehat{0},T\rangle & \langle 3|\widehat{-1},T\rangle \end{pmatrix} \cdot \begin{pmatrix} -i\frac{E(\widehat{+1},t)}{\hbar} & 0 & 0 \\ 0 & 0 & 0 \\ 0 & 0 & -i\frac{E(\widehat{-1},t)}{\hbar} \end{pmatrix} \cdot$$

$$\exp\begin{pmatrix} -i\int \frac{E(\widehat{+1},t)}{\hbar}dt & \frac{\theta}{\sqrt{2}} & 0 \\ -\frac{\theta}{\sqrt{2}} & 0 & -\frac{\theta}{\sqrt{2}} \\ 0 & \frac{\theta}{\sqrt{2}} & -i\int \frac{E(\widehat{-1},t)}{\hbar} \end{pmatrix} \cdot \begin{pmatrix} \langle\widehat{+1},t_0|1\rangle \\ \langle\widehat{0},t_0|1\rangle \\ \langle\widehat{-1},t_0|1\rangle \end{pmatrix}$$

$$= \frac{H(T)}{i\hbar} \begin{pmatrix} \langle 1|\widehat{+1},T\rangle & \langle 1|\widehat{0},T\rangle & \langle 1|\widehat{-1},T\rangle \\ \langle 2|\widehat{+1},T\rangle & \langle 2|\widehat{0},T\rangle & \langle 2|\widehat{-1},T\rangle \\ \langle 3|\widehat{+1},T\rangle & \langle 3|\widehat{0},T\rangle & \langle 3|\widehat{-1},T\rangle \end{pmatrix} \exp \begin{pmatrix} -i\int \frac{E(\widehat{+1},t)}{\hbar}dt & \frac{\theta}{\sqrt{2}} & 0 \\ -\frac{\theta}{\sqrt{2}} & 0 & -\frac{\theta}{\sqrt{2}} \\ 0 & \frac{\theta}{\sqrt{2}} & -i\int \frac{E(\widehat{-1},t)}{\hbar} \end{pmatrix} \begin{pmatrix} \langle \widehat{+1},t_0|1\rangle \\ \langle \widehat{0},t_0|1\rangle \\ \langle \widehat{-1},t_0|1\rangle \end{pmatrix} \tag{3.53}$$

In the last step of (3.53), we have used the following fact, which is a natural consequence of the definition of the adiabatic states for H as defined in (3.28).

$$\begin{aligned} &\begin{pmatrix} \langle 1|\widehat{+1},T\rangle & \langle 1|\widehat{0},T\rangle & \langle 1|\widehat{-1},T\rangle \\ \langle 2|\widehat{+1},T\rangle & \langle 2|\widehat{0},T\rangle & \langle 2|\widehat{-1},T\rangle \\ \langle 3|\widehat{+1},T\rangle & \langle 3|\widehat{0},T\rangle & \langle 3|\widehat{-1},T\rangle \end{pmatrix} \cdot \begin{pmatrix} -i\frac{E(\widehat{+1},t)}{\hbar} & 0 & 0 \\ 0 & 0 & 0 \\ 0 & 0 & -i\frac{E(\widehat{-1},t)}{\hbar} \end{pmatrix} \\ &= \frac{H(T)}{i\hbar} \begin{pmatrix} \langle 1|\widehat{+1},T\rangle & \langle 1|\widehat{0},T\rangle & \langle 1|\widehat{-1},T\rangle \\ \langle 2|\widehat{+1},T\rangle & \langle 2|\widehat{0},T\rangle & \langle 2|\widehat{-1},T\rangle \\ \langle 3|\widehat{+1},T\rangle & \langle 3|\widehat{0},T\rangle & \langle 3|\widehat{-1},T\rangle \end{pmatrix} \end{aligned} \tag{3.54}$$

Up to this point, we have verified that the propagator derived in (3.48) does lead to a wavefunction that satisfies the time-dependent Schrödinger equation. However, an approximation is involved, namely, we have only taken into consideration the $1st$ order term in (3.51). We have yet to explain what we mean by this approximation.

In (3.51), if $X(t)$ commutes with $\frac{d}{dt}X(t)$, then it would reduce to $\frac{d}{dt}e^{X(t)} = \frac{d}{dt}[X(t)]e^{X(t)}$, and all our verification of the time-dependent Schrödinger equation would then become precise. To be explicit, if we want the approximation made to (3.51) to be lifted, we would like to require:

$$\begin{pmatrix} -i\frac{E(\widehat{+1},t)}{\hbar} & \frac{\dot{\theta}}{\sqrt{2}} & 0 \\ -\frac{\dot{\theta}}{\sqrt{2}} & 0 & -\frac{\dot{\theta}}{\sqrt{2}} \\ 0 & \frac{\dot{\theta}}{\sqrt{2}} & -i\frac{E(\widehat{-1},t)}{\hbar} \end{pmatrix} \textit{commutes with} \begin{pmatrix} -i\int\frac{E(\widehat{+1},t)}{\hbar}dt & \frac{\theta}{\sqrt{2}} & 0 \\ -\frac{\theta}{\sqrt{2}} & 0 & -\frac{\theta}{\sqrt{2}} \\ 0 & \frac{\theta}{\sqrt{2}} & -i\int\frac{E(\widehat{-1},t)}{\hbar} \end{pmatrix} \tag{3.55}$$

(3.55) would be true if the following simple condition is satisfied.

$$\frac{\dot{\theta}}{\theta} = \frac{E(\widehat{+1},t)}{\int_0^T E(\widehat{+1},t)dt} = \frac{E(\widehat{-1},t)}{\int_0^T E(\widehat{-1},t)dt} \tag{3.56}$$

In a real experiment of STIRAP, we are always trying to keep Ω_{eff} and $\dot{\theta}$ constant over the course of the laser-atom interaction. Therefore the condition of (3.56) is well approximated in a situation of real interest. An offense against (3.56) would lead to higher order corrections to this problem, but the $1st$ order situation would satisfy us for the moment.

Of course for a real problem the quantities of $\langle 3|\widehat{j_n},T\rangle$ and $\langle\widehat{j_0},t_0|1\rangle$ are known or given, and they contain parts of the information of the time evolution of the system. Therefore the secrets (including the myth of adiabatic following) are actually contained in this matrix:

$$\exp\begin{pmatrix} -i\int\frac{E(\widehat{+1},t)}{\hbar}dt & \frac{\theta}{\sqrt{2}} & 0 \\ -\frac{\theta}{\sqrt{2}} & 0 & -\frac{\theta}{\sqrt{2}} \\ 0 & \frac{\theta}{\sqrt{2}} & -i\int\frac{E(\widehat{-1},t)}{\hbar} \end{pmatrix} \tag{3.57}$$

The STIRAP condition expressed in terms of $E(\widehat{+1},t)$, $E(\widehat{-1},t)$ and θ is that:

$$|-i\int_0^T \frac{E(\widehat{+1},t)}{\hbar}dt| \gg |\theta|, \quad |-i\int_0^T \frac{E(\widehat{-1},t)}{\hbar}dt| \gg |\theta| \tag{3.58}$$

This condition would yield:

Up to 0th order: $\exp\begin{pmatrix} -i\int\frac{E(\widehat{+1},t)}{\hbar}dt & \frac{\theta}{\sqrt{2}} & 0 \\ -\frac{\theta}{\sqrt{2}} & 0 & -\frac{\theta}{\sqrt{2}} \\ 0 & \frac{\theta}{\sqrt{2}} & -i\int\frac{E(\widehat{-1},t)}{\hbar} \end{pmatrix} \rightarrow$

$$\exp\begin{pmatrix} -i\int\frac{E(\widehat{+1},t)}{\hbar}dt & \frac{\theta}{\sqrt{2}} & 0 \\ -\frac{\theta}{\sqrt{2}} & 0 & -\frac{\theta}{\sqrt{2}} \\ 0 & \frac{\theta}{\sqrt{2}} & -i\int\frac{E(\widehat{-1},t)}{\hbar} \end{pmatrix} = \begin{pmatrix} \exp(-i\int\frac{E(\widehat{+1},t)}{\hbar}dt) & 0 & 0 \\ 0 & 1 & 0 \\ 0 & 0 & \exp(-i\int\frac{E(\widehat{-1},t)}{\hbar}dt) \end{pmatrix} \tag{3.59}$$

(3.59) would again give us the propagator of the usual STIRAP picture, i.e. no population in the intermediate level, the state vector follows the adiabatic state all the time.

Yet, it does not take too much effort to fully work out (3.57) and realize that the state vector is following a path 'jiggling' around the adiabatic state. I will give a rough picture here just for entertainment.

Suppose $\beta \ll 1$. Then up to 1st order in β, we have:

$$\exp\alpha\begin{pmatrix} 1 & \beta & 0 \\ -\beta & 0 & -\beta \\ 0 & \beta & -1 \end{pmatrix} = \begin{pmatrix} 1 & \beta & 0 \\ -\beta & 0 & -\beta \\ 0 & \beta & -1 \end{pmatrix}\begin{pmatrix} \exp(i\alpha) & 0 & 0 \\ 0 & 1 & 0 \\ 0 & 0 & \exp(-i\alpha) \end{pmatrix}\begin{pmatrix} 1 & \beta & 0 \\ -\beta & 0 & -\beta \\ 0 & \beta & -1 \end{pmatrix} \tag{3.60}$$

From the above equation it can be seen that during the interaction time the intermediate level has to be populated a little in order for things to work.

In summary, the time evolution of STIRAP can be described by the propagator as in (3.48), with reasonable approximation to the $1st$ order in the sense of (3.51). And the discussion here provides support and fundamental reasons to what we were doing in section 3.1.

3.4 An Extra Nearby Intermediate Level

For Helium-4, the atomic state 3^3P_1 is not that far away from our intermediate state 3^3P_2 of the STIRAP interaction. Actually, 3^3P_2 is only 650 MHz below 3^3P_1. If we forget about the complexity of polarizations and magnetic sublevels for a moment, a laser coupling 2^3S_1 and 3^3P_2 right on resonance is also coupling 2^3S_1 and 3^3P_2 with -650 MHz detuning.

A possible concern is that this extra intermediate level would cause an ac Stark shift of some kind to the ground level. And this indeed has been pointed out, such as in the recent work of Marsman et al., [65]. Here we are going to show a relatively complete argument to clarify and lift this concern.

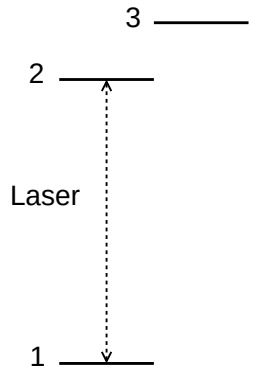

Figure 3.5: A nearby energy level

The first model we will look at is composed of the ground level, the excited level and the extra nearby excited level. A single laser is coupling the ground level and the excited level right on resonance. The system is briefly shown in Fig. 3.5.

$$\begin{pmatrix} 0 & \Omega \\ \Omega & 0 \end{pmatrix} \xrightarrow[\text{as the 3rd level}]{\text{Adding the extra excited level}} \begin{pmatrix} 0 & \Omega & \Omega \\ \Omega & 0 & 0 \\ \Omega & 0 & \Delta \end{pmatrix} \tag{3.61}$$

The above Hamiltonian is acquired after the rotating wave approximation. We assume here the laser induces the same Rabi frequency for both the on and off resonance excited levels. Also, the Rabi frequency Ω is regarded as small compared to the detuning Δ.

We will apply a first order perturbation treatment to compute the energy eigenstates for this three level Hamiltonian. We start from the unperturbed state $(1, 1, 0)^T$, and keep track of the order by Ω/Δ. Then we would get, up to order of $O(\Omega/\Delta)$:

$$\begin{pmatrix} 0 & \Omega & \Omega \\ \Omega & 0 & 0 \\ \Omega & 0 & \Delta \end{pmatrix} \begin{pmatrix} 1 - \frac{\Omega}{\Delta} \\ 1 - \frac{1}{2}\frac{\Omega}{\Delta} \\ -\frac{\Omega}{\Delta} \end{pmatrix} = (\Omega - \frac{1}{2}\frac{\Omega^2}{\Delta}) \begin{pmatrix} 1 - \frac{\Omega}{\Delta} \\ 1 - \frac{1}{2}\frac{\Omega}{\Delta} \\ -\frac{\Omega}{\Delta} \end{pmatrix} \tag{3.62}$$

Similarly, for $(1, -1, 0)^T$, we have:

$$\begin{pmatrix} 0 & \Omega & \Omega \\ \Omega & 0 & 0 \\ \Omega & 0 & \Delta \end{pmatrix} \begin{pmatrix} 1 + \frac{\Omega}{\Delta} \\ -1 - \frac{1}{2}\frac{\Omega}{\Delta} \\ -\frac{\Omega}{\Delta} \end{pmatrix} = -(\Omega + \frac{1}{2}\frac{\Omega^2}{\Delta}) \begin{pmatrix} 1 + \frac{\Omega}{\Delta} \\ -1 - \frac{1}{2}\frac{\Omega}{\Delta} \\ -\frac{\Omega}{\Delta} \end{pmatrix} \tag{3.63}$$

The existence of the off-resonance nearby extra level would lead to a small population into itself, and hence change the adiabatic states by a little. As a consequence, the magnitude of the ac Stark shift changes, which is the energy difference between those adiabatic states. This change of the adiabatic energy is certainly observable, and will be revealed in related experiments such as the frequency of Rabi oscillation and Autler-Townes effect (Section 7.1).

Yet, some care is in need to describe it. The ac Stark shift is always in place, and the existence of the extra level changes this ac Stark shift from Ω to $\Omega - \frac{1}{2}\frac{\Omega^2}{\Delta}$, for one of the adiabatic states. It is not correct to view this change as a shift in the energy of the level when talking about energy conservation of the laser excitation.

Then, would this extra intermediate level affect the STIRAP process? The answer is no.

For this, we need to look into the whether the essence of the STIRAP process changes, with this extra level's presence.

Assume again that the lasers are on the two photon STIRAP resonance of the atom. Moreover for the moment assume that the coupling of the extra intermediate level to the other states are the same as the original intermediate state. First we examine whether the adiabatic state $|0\rangle$ of (3.8) still persists. Set $|0\rangle_4 = (\cos\theta, 0, 0, -\sin\theta)^T$ and name the Hamiltonian for this 4 level system to be $\hat{H}_4$.

$$\frac{1}{\hbar}\hat{H}_4|0\rangle_4 = \begin{pmatrix} 0 & \Omega_p(t)/2 & \Omega_p(t)/2 & 0 \\ \Omega_p(t)/2 & \Delta_p & 0 & \Omega_S(t)/2 \\ \Omega_p(t)/2 & 0 & \Delta_p + \Delta & \Omega_S(t)/2 \\ 0 & \Omega_S(t)/2 & \Omega_S(t)/2 & 0 \end{pmatrix} \begin{pmatrix} \cos\theta \\ 0 \\ 0 \\ -\sin\theta \end{pmatrix} = 0 \tag{3.64}$$

(3.64) shows $|0\rangle_4$ is an (null) adiabatic state of $\hat{H}_4$, which is completely analogous to the situation of $|0\rangle$ and $\hat{H}$ as in section 3.1. Hence we have reasons to trust STIRAP could work well for $\hat{H}_4$ too. Yet (3.64) does not provide an insight to the role of the intermediate levels. We believe the population transfer is achieved via the 'on resonance' intermediate level instead of the extra nearby level. Now I am going to show the analogue to (3.15), (3.16) and (3.17), in order to prove the claim. Set $|0'\rangle_4 = (\cos\theta, \eta, 0, -\sin\theta)^T$, and then let's examine $i\frac{d}{dt}|0'\rangle_4$ and $\frac{1}{\hbar}\hat{H}|0'\rangle_4$.

$$i\frac{d}{dt}\begin{pmatrix} \cos\theta \\ \eta \\ 0 \\ -\sin\theta \end{pmatrix} = i\begin{pmatrix} -\dot{\theta}\sin\theta \\ \dot{\eta} \\ 0 \\ -\dot{\theta}\cos\theta \end{pmatrix} \tag{3.65}$$

$$\frac{1}{\hbar}\hat{H}\begin{pmatrix}\cos\theta\\ \eta\\ 0\\ -\sin\theta\end{pmatrix}=\begin{pmatrix}0 & \Omega_p(t)/2 & \Omega_p(t)/2 & 0\\ \Omega_p(t)/2 & \Delta_p & 0 & \Omega_S(t)/2\\ \Omega_p(t)/2 & 0 & \Delta_p+\Delta & \Omega_S(t)/2\\ 0 & \Omega_S(t)/2 & \Omega_S(t)/2 & 0\end{pmatrix}\begin{pmatrix}\cos\theta\\ \eta\\ 0\\ -\sin\theta\end{pmatrix}=\begin{pmatrix}\eta\frac{\Omega_p}{2}\\ \eta\Delta_p\\ 0\\ \eta\frac{\Omega_S}{2}\end{pmatrix} \tag{3.66}$$

(3.65) shall be equal to (3.66), then we arrive at exactly the same expression of (3.17). The population transfer between the initial and final states are through one single intermediate state only, and the situation is the same as the simple three level STIRAP. In other words, during STIRAP process, the atom is steered in such a way that it does not see the extra intermediate level.

Yet, the above nice results are relying upon the assumption that the coupling to the extra intermediate level is the same. In reality, no reason requires this assumption to be true. And this difference in the couplings will finally lead to the disruption of the three level STIRAP from this fourth level. The extent of this disrupt, according to the brief discussion at the beginning of this section, is on the order of Ω/Δ, where Δ is the energy difference between the target level and the extra nearby level.

Chapter 4

Black Body Radiation Interaction with Rydberg Atoms

4.1 Why do we bring it up again now?

More than thirty years ago, Gallagher and Cooke [66] [67] discovered that blackbody radiation at room temperature has a significant impact on Rydberg atoms and that discovery solved many puzzles associated with strange behavior of ion signals from Rydberg atoms. I would like to quote this remark from Ref. [67]: *"While the effect of blackbody radiation of the radiative lifetimes can be very dramatic, it is the rapid diffusion of population from an initially excited Rydberg state to other nearby states which is of general importance for experiments with Rydberg atoms. We can get a feeling for the magnitude of the effect by considering a specific example, the Na 18s state. The thermal bath of photons transfers population from the 18s state to the two neighboring p states at a rate of* $4 \times 10^4 sec^{-1}$*, while the radiative decay rate is only* $1.6 \times 10^5 sec^{-1}$*. Thus roughly a quarter of the initial population can become redistributed over nearby Rydberg states!"*

Around that time many detailed investigations were carried out, both experimental and theoretical. Strong proofs come from experimental work of P. R. Koch et al. [68] and William P. Spencer et al. [69] where the ambient temperature is varied. John Farley and William Wing published a long theory paper [70] in 1981 discussing the interaction of blackbody radiation with Rydberg atoms in great detail. In that paper, the authors were concerned mostly with the ac Stark shift and the diffusion to other states, which they called the depopulation of the original Rydberg state. Exact numbers were calculated for the depopulation rates for several atoms, including Helium.

A more recent calculation on the same subject has been done by Glukhov et al. [71] [72]. Their work focused on the ionization rate and transition rate induced by the blackbody radiation. Through private communications Glukhov provided very specific blackbody radiation induced transition rates related to our experiment to our research group.

Since all these results seem so nice and complete, the the question is, why do we bring it up again now? It would be boring and dull to repeat what had been done over 30 years ago.

The truth is, of course, we are NOT repeating old recipes. As described in [73], all the related experimental work around that time is utilizing the field ionization technique to detect the Rydberg atoms. Here we do not use field ionization because we have ample number of atoms and we are exciting them to the Rydberg state via highly efficient STIRAP which is described in Chapter 3. The ions in our experiment are coming from blackbody radiation induced ionization of Rydberg atoms, and usually on the order of a few percent of the total population, which is enough to be detected with a high signal to noise ratio, thanks to our ion detector based on MCP's. This actually provides us with an easy method to detect Rydberg atoms.

We can do even more. Blackbody radiation induced ionization of Rydberg atoms is fast and can be regarded as 'instantaneous' for a microsecond time scale experiment. Therefore it

provides a convenient tool for spectroscopic study of Rydberg atoms. We can experimentally measure the relation between the ionization rate and the temperature of the blackbody radiation, to further prepare for the possible application of detecting ir radiation by Rydberg atoms, etc.

4.2 Background blackbody radiation induced ionization

A macroscopic object emits electromagnetic radiation when it is hot, which is famously known as black body radiation or thermal light. The characteristics of the spectrum of such radiation is solely related to the temperature of the blackbody, as can be seen from the famous Planck's law Eq. (4.1).

$$\rho(\omega, T)d\omega = \frac{\hbar\omega^3}{\pi^2 c^3}\frac{1}{\exp(\hbar\omega/k_B T) - 1}d\omega \tag{4.1}$$

The apparatus of our experiment is filled with the black body radiation at room temperature, including the part where the STIRAP interaction happens. Intuitively we would imagine such thermal radiation has little effects on Rydberg atoms for many reasons, for example, the population of the Rydberg state by STIRAP is highly non-thermal in nature, and the blackbody radiation is very broad band light which should not have any coherent effects. However, it turns out the interaction between Rydberg atoms and the black body radiation at room temperature is highly non–trivial with significant experimental signatures. We must see why and how.

It is convenient to re–express (4.1) in terms of the photon occupation number $\bar{n}$ per mode Eq. (4.2). When the photon energy $\hbar\omega$ of the associated transition is very much larger than

k_BT, the photon occupation number is low and can hardly cause any results. However, at room temperature $T = 300\text{K}$, $k_BT \gg \hbar\omega$ for typical energy separations between adjacent Rydberg states. For example, $\bar{n} \approx \frac{k_BT}{\hbar\omega}$, which is about 10, for a Rydberg transition of 0.6 THz at room temperature. Compared to the photon occupation number that causes the spontaneous emission which is 1 (or $\frac{1}{2}$ depending on your taste of quantum optics), black body radiation would induce a much more significant transition rate.

$$\bar{n} = \frac{1}{\exp(\hbar\omega/k_BT) - 1} \tag{4.2}$$

Since black body radiation is broadband and the Rydberg states are close to each other, it can cause excitation, decay, and ionization into the continuum. The transition rate (absorption or stimulated emission) between two definite Rydberg states can be given in terms of oscillator strength as in Eq. (4.3), which is essentially stating $K_{n'l',nl} = \bar{n}A_{n'l',nl}$: the black body radiation induced transition rate is $\bar{n}$ times that of the spontaneous decay rate since the black body radiation contains $\bar{n}$ photons per mode while the vacuum fluctuations populate only one photon per mode.

$$K_{n'l',nl} = 2\bar{n}\alpha^3\omega^2_{n'l',nl}|\bar{f}_{n'l',nl}| \tag{4.3}$$

Here $\bar{f}_{n'l',nl}$ is the oscillator strength of the transition given by:

$$\bar{f}_{n'l',nl} = \frac{2}{3}\omega_{n'l',nl}\frac{\max(l',l)}{2l+1}|\langle n'l'|r|nl\rangle|^2 \tag{4.4}$$

Besides driving transitions into other discrete states, the black body radiation can also excite the Rydberg atoms into the ionization continuum. The ionization rate $1/\tau^P_{nl}$ is given by Eq. (4.5), see reference [28]. The matrix elements in (4.5) are the radial matrix elements

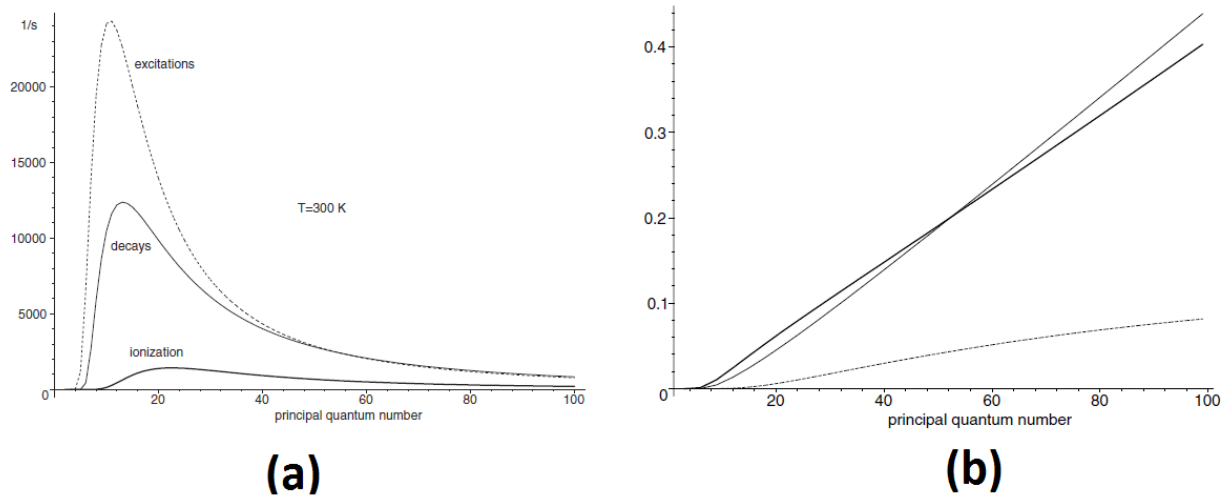

Figure 4.1: The calculated black body radiation induced transition rates for hydrogen at room temperature $T = 300$K. (a) shows the decay (thin solid curve), excitation (dashed curve) and ionization (thick solid) rates for the nP–series of hydrogen at $T = 300$k. (b) shows the relative rates of decay (thin solid line), excitation (thick solid line) and ionization (dashed line) for nD–series of hydrogen atoms. Figures are from reference [72].

of r between the initial nl state and continuum $l-1$ and $l+1$ waves which are normalized per unit energy.

$$\frac{1}{\tau_{nl}^{P}} = \frac{2\pi}{3}\int_{1/2n^2}^{\infty}\{\frac{l}{2l+1}|\langle nl|r|\varepsilon l-1\rangle|^2 + \frac{l+1}{2l+1}|\langle nl|r|\varepsilon l+1\rangle|^2\}\rho(\omega)d\omega \tag{4.5}$$

Fig. 4.1 gives a sense of those rates for the hydrogen atoms at room temperature. The basic idea is that the black body radiation induced transition rate is large compared to spontaneous emission. Moreover, the ionization rate is small. We will come back to this later in this chapter.

4.2.1 Ion Detection

We set up an ion detector close to the interaction region. Basically it is composed of two MCP's supplied with negative high voltage. Experimentally any ions produced will be attacted to the ion detector and hence be detected. The electric field of the ion detector is well shielded in the interaction region such that it can not field ionize the Rydberg atoms. Metastable atoms have no way of arriving at the ion detector, since an atom does not have a permanent electric dipole moment, though if an electric dipole is put in an non-uniform electric field, it would move to the regions of higher fields.

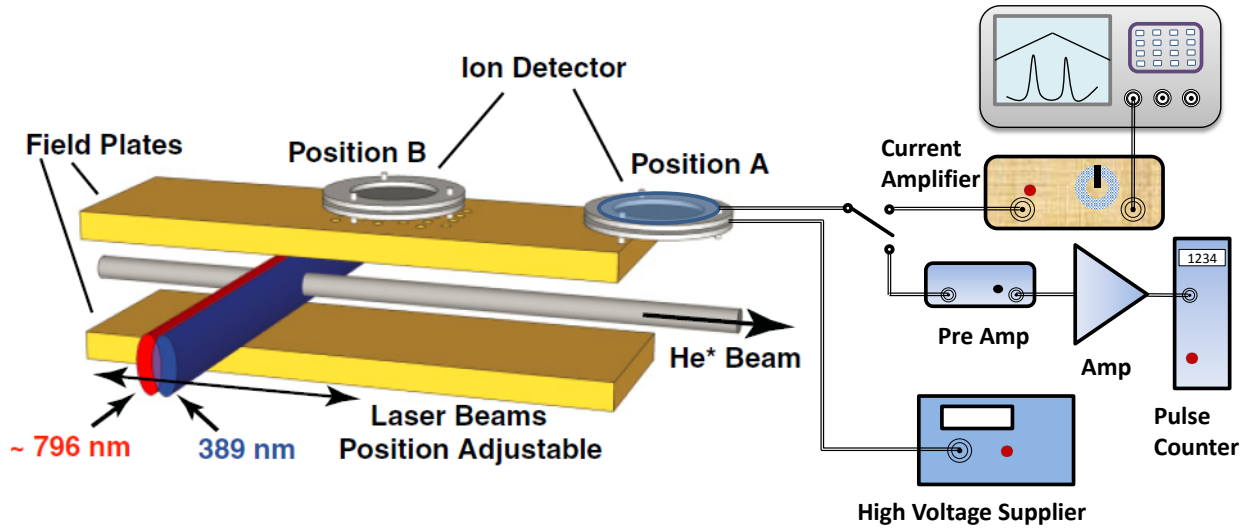

Figure 4.2: The schematic of the experimental setup to detect ions from Rydberg atoms. In earlier experiments the upper plate was solid and the ion detector was at position A just downstream, at the end of the plates. Later the upper plate had an array of 30 holes 0.5 mm diam spaced by $\sim$ 4mm arranged in a triangular array near its center, and the ion detector was mounted at position B just above these holes.

The basic setup to detect the ion signal is shown in Fig. 4.2. The metastable helium atoms are excited into the Rydberg states by a uv laser and an ir laser in STIRAP configuration. The excitation region is between two well–polished parallel aluminum field plates which are

about 7×17 cm and separated by ~ 6 mm and a electric voltage difference can be applied to the plates.

The output signal from the anode of the ion detector can be fed to either a display circuit (the current amplifier and the oscilloscope) or a counting circuit (basically the pulse counter). We first utilize them to establish the ion counts.

In the display circuit, we can skip the current amplifier and directly feed the output of the ion detector to the oscilloscope with 50 Ω coupling. Then we can see individual pulses of ~ 5 ns width and ~ 3.5 mV height, and this also allows the gain of the MCP to be estimated. Therefore, we can set up the counting circuit to count those pulses.

In the counting circuit, we have connected in series a pre–amp (ORTEC 113), a multi–mode amplifier (ORTEC 410) and a 50 MHz pulse counter (HP 5302A). The total MCP gain of the ion detector is $\sim 2.2 \times 10^6$ (see also reference [43]), hence we can convert the counted pulses' numbers into the actual ion counts from the Rydberg atoms. For the state $24S$ of helium, when the lasers are on resonance, the ion count rate is $\sim 10^5$/s.

From the above data of the counted ions, we can estimate the ionization rate. This count is performed with the ion detector at position A which is downstream, hence this count rate is only 15% of the total ions at the interaction point since the Rydberg atoms decay during their travel. Then the ion production rate at the interaction point is $\sim 6.7 \times 10^5$. Compare this to the total metastable helium flux $\sim 3 \times 10^8$ atoms/s [1] which has a STIRAP efficiency of $\sim 30\%$, we know the ionization rate is $\sim 0.5\%$. This agrees with the reference [72] and the authors' private communications with us.

In the following experiments we only connect the ion detector's output to the display circuit. The current amplifier (KEITHLEY 427) is essentially a current to voltage converter

[1] The helium flux is deduced from the specifications of our source which has an output of $\sim 0.5 \times 10^{14}$ He* atoms/(sr $\cdot$ s), and this is verified by the counts recorded by the SSD in the detection chamber

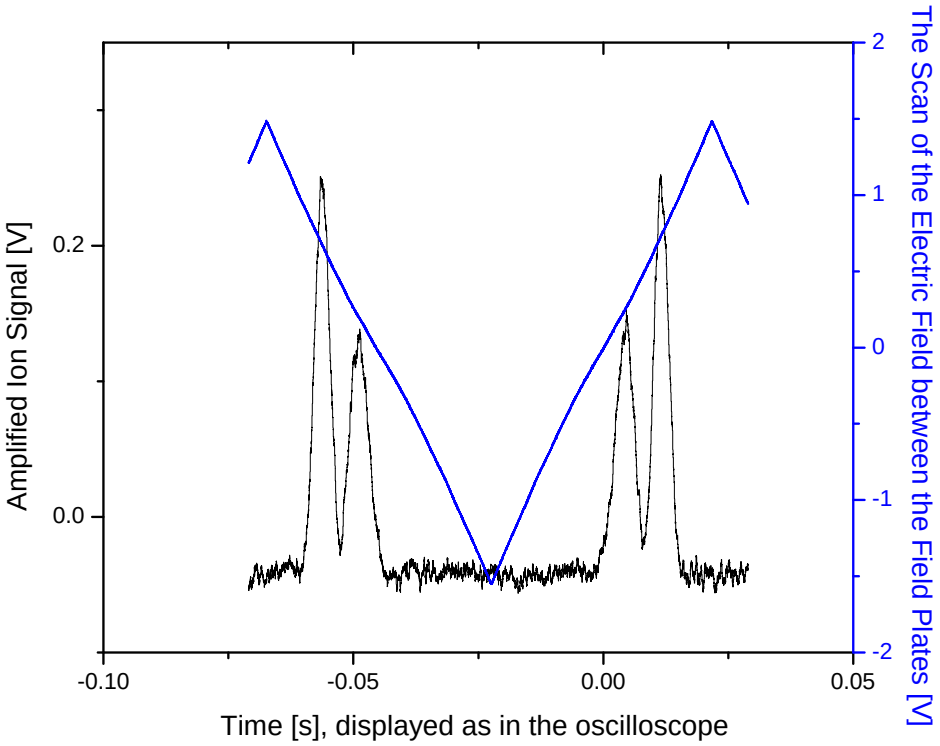

Figure 4.3: Typical ion signals from Helium Rydberg atoms, in the case of scanning the electric field. The dc voltage offset between the field plates is ~ 6 V while the scan voltage is on the order of 2V. The ir laser frequency is tuned around the resonance of a Stark state of $n = 24$ Stark manifold. The double peak structure here is a result of the Stark splitting for non–zero angular momentum $l \neq 0$. If it is an S state then only a single peak will show up at the low electric fields. The ion detector for these measurements is located at position A at the end of the field plates.

with amplification and integration time constant, which is larger than the individual pulse widths from MCP but much smaller than the time scale of the scanning. A typical current to voltage conversion rate for the current amplifier is 10^7 V/A. Therefore when we scan either the electric field or the ir laser frequency across the resonance of the Rydberg state, we typically see Fig. 4.3. An ion signal peak in Fig. 4.3 shows the strength of the ion signal and the exact spectroscopic position at the same time, which is superior than the counting circuit, and this is the exact reason why we stick to it. This ion peak can be intuitively

regarded as if we are summing up all the individual ~ 5 ns pulses for each time interval of ~ 1 μs (the time constant of the current amplifier).

We can move the laser beams' positions upstream or downstream. It means that, the time delay between the Rydberg production and detection is flexible and this serves as a basic tool for many investigations. One of such measurements is shown in Fig. 4.4. The interpretations will be discussed later. Most of this section's content is also summarized in reference [74].

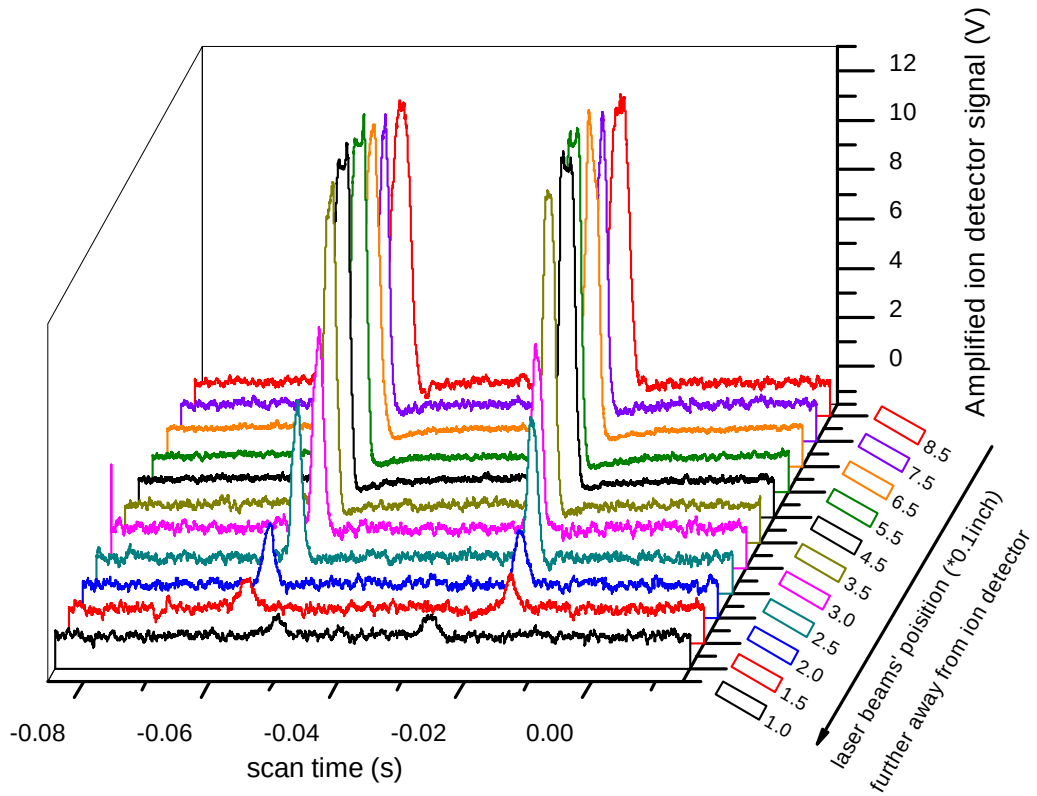

Figure 4.4: A typical time delay measurement of ion signals from Rydberg atoms. The lasers are moved further away from the ion detector. Since the Rydberg atoms spontaneously decay to the metastable ground state, the ion signal is smaller when the time delay is larger. The ion detector for these measurements is located at position A (see Fig. 4.2) at the end of the field plates.

4.3 Time Delay measurement and Population Redistribution

In this section we are going to take a closer look at the time delay measurement and see what information we can extract. For the purpose of controlling more precisely the delay, in terms of the distance between the lasers and the position of the ion detector, we move the ion detector to the position B shown in Fig. 4.2.

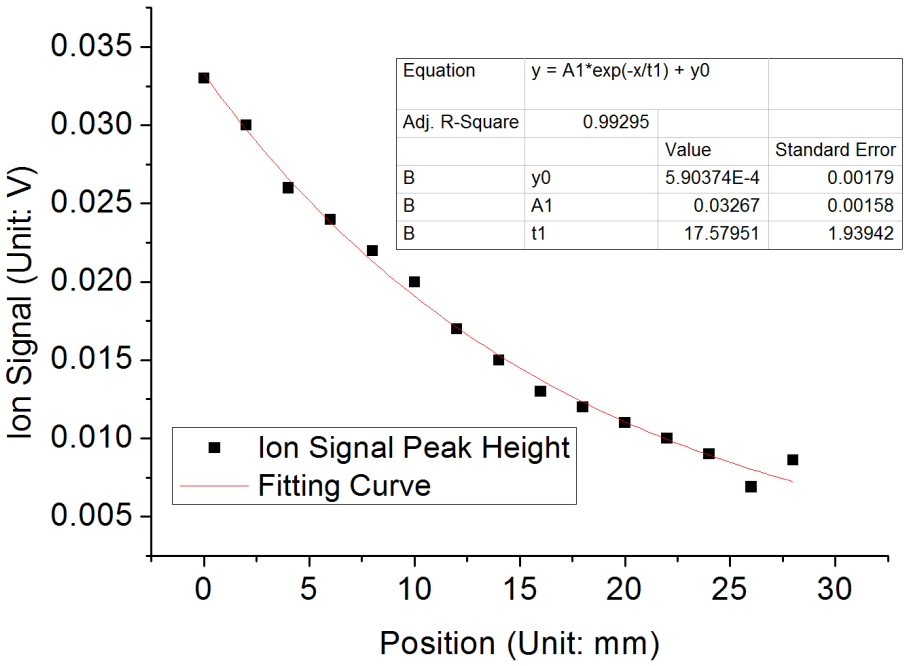

Figure 4.5: The measurement for the ion signal strength of 24^3S as a function of the distance between the interaction point (STIRAP laser beams' position) and the ion detector region (position B). This type of time delay experiment measures the ions generated by the Rydberg atoms left over in the beam, a certain time interval after they were initially excited at 24^3S. The absolute number of the Rydberg atoms of all states decreases over time because of spontaneous emission to the metastable ground state. This set of data is taken at room temperature of 300K. The data points have been fitted to an exponential curve and the result of fitting is shown.

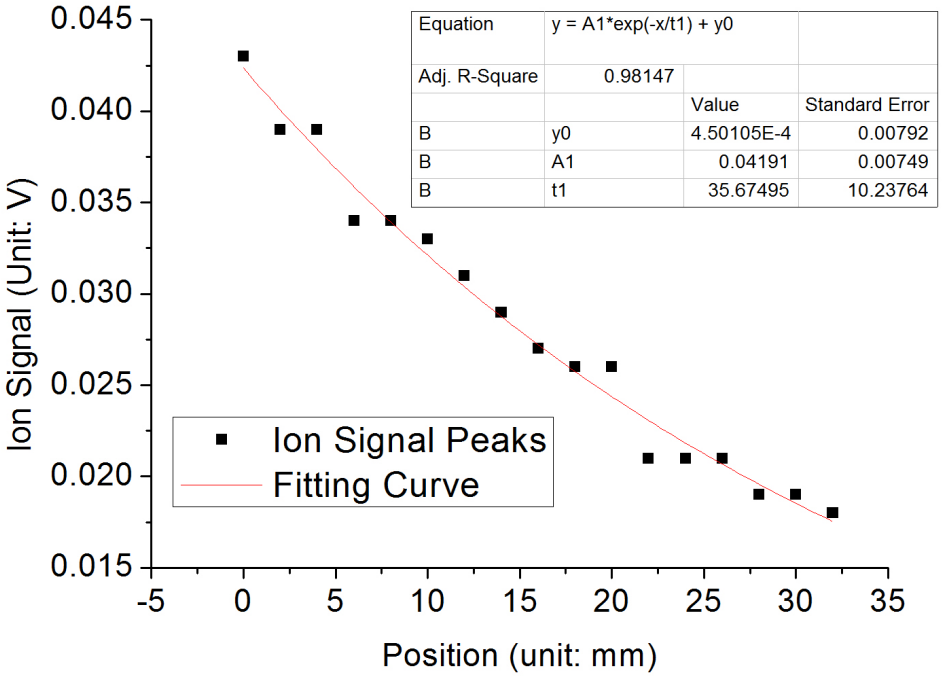

Figure 4.6: The measurement for the ion signal strength of 30^3S as a function of the distance between the interaction point (STIRAP lasers' position) and the ion detector region (position B). This is the same type of measurement as in Fig. 4.5. An exponential fitting is also performed.

For this series of experiments, the ir laser frequency is scanned over the resonance of the corresponding S states and all the field plates have been grounded to ensure no Stark effect. The result for 24^3S is shown in Fig. 4.5 and the result for 30^3S is shown in Fig. 4.6. Those points fit well to an exponential decay. Since the peak of the atomic beam velocity distribution is $\sim$ 1070 m/s, we can convert distance into average time and acquire the 'lifetime' of the phenomenological 'ion signal decay'. They are 16.4 μs for 24^3S and 33.4 μs for 30^3S.

Compared to the radiative lifetime of 24^3S (10.4 μs) and 30^3S (20.1 μs) separately, those numbers differ a lot. We also have other methods to establish the absolute counts of metastable ground state helium (which will be discussed in details later), and those abso-

n	$24S - nP$ transition rates (1/s)	nP ionization rates (1/s)
20	1127.8	1386.5
21	1726.2	1410.7
22	3135.2	1420.6
23	9337.3	1419.0
24	3762.4	1408.3
25	142.6	1390.3
26	133.4	1366.8
27	101.7	1339.2
28	78.1	1308.5
29	61.4	1275.7

Table 4.1: Transition rates for $24S \rightarrow n$P and ionization rate for np states at T = 300 K (from Glukhov et al. through private communications).

lute counts show that the total number of Rydberg atoms left in the atomic beam decay at a lifetime agreeing well with that of 24^3S and 30^3S correspondingly. If we are to insist that the Rydberg atoms are at the state of 24^3S or 30^3S all the way throughout this time delay experiment, we would find it impossible to explain this time-varying ionization rate.

The answer to this conflict is that the Rydberg atoms do not stay in their initially excited states when black body radiation is present. As explained previously, the black body radiation at room temperature is a broad–band radiation, which covers a wide spectrum including those corresponding to the transitions between adjacent Rydberg states of different principle quantum numbers. It turns out [72], the transition to the neighboring Rydberg states with $+/-1$ principle quantum number is usually stronger. It is the time for a closer look at those rates for helium.

The direct ionization rate at $T = 300$K for 24^3S is 299.41/s, which corresponds to an ionization of 0.45% of the atoms over a time interval of 15 μs. From the above table we see that the direct ionization rate is much smaller than the transition rates to a nearby P state, as also shown in Fig. 4.1. In this sense, the population of the Rydberg atoms is diffused into

many nearby states.

The population diffusion caused by the black body radiation takes place immediately after the Rydberg atoms are produced in the 24^3S state. Once some population is diffused into other states, say, 23^3P, it will be subject to a higher ionization rate. This process can be described as $24^3S \rightarrow n^3P \rightarrow$ ion, and is the reason why the 'lifetime of the ion signal decay' is so different from the corresponding radiative lifetime of the Rydberg state.

Since the transition rates are strong, it does not take too much time for the black body radiation to diffuse the population in the single initial state to many other states (see also Fig. 4.1 for an idea of this). At the same time, the ions are from all those states which get the diffused population.We want to go one more step further from a conceptual understanding of the result of the ion signal time delay measurement, to an effective model.

The basic time evolution of this effective model is summarized in Eq's. (4.6). At $t = 0$, the atom is excited to a definite Rydberg state e. All the states with longer radiative lifetime are summarized as a single state s (stands for slow), while those states with shorter lifetime are summarized as a single state f (stands for fast). Their population are N_e, N_s and N_f separately. γ represents the population loss due to spontaneous emission back to the metastable ground state, σ_s stands for the transition rate from e to s caused by the black body radiation, and σ_f stands for the transition rate from e to f. Since the ionization rate is so small its presence in the depopulation process is neglected here; or its effect can be incorporated into the term γ. See also [74].

$$\frac{d}{dt}N_e = -\gamma_e N_e - \sigma_f N_e - \sigma_s N_e \tag{4.6a}$$
$$\frac{d}{dt}N_f = -\gamma_f N_f + \sigma_f N_e \tag{4.6b}$$
$$\frac{d}{dt}N_s = -\gamma_s N_s + \sigma_s N_e \tag{4.6c}$$

Let us see how Eq's. (4.6) explain the experiment of ion signal delay of atoms initially excited to the 24^3S state. According to Table 4.1, both N_f and N_s can be regarded as having a higher ionization rate than N_e. Therefore, as more and more population is transfered to N_f and N_s, the population going to the metastable ground state won't be too much different from the case of e state only, but the ionization rate will become higher.

The characteristics of the black body radiation are determined by the temperature. Generally when the temperature is higher the population diffusion among Rydberg states caused by the black body radiation is stronger. We have set up an experiment to heat up the field plates to 380 K and perform the same experiment of ion signal time delay measurement for 30^3S, the result of which is shown in Fig. 4.7. More details of the experiment to heat up the field plates can be find in Section 4.4 and reference [43].

The 'lifetime' of the 'ion signal exponential decay curve' at 380K (Fig. 4.7) is even longer than that of 300K (Fig. 4.6), which implies that the overall ionization rate changes more dramatically over time. In other words, at 380K, the population is diffused more quickly among the Rydberg states. In terms of Eq's. (4.6), σ_s and σ_f are larger at higher temperature for blackbody radiation at 380K, hence N_s and N_f will occupy more proportion of the total Rydberg population, and then lead to more deviation between the ion signal time delay measurement and the expected radiative decay of only state e (in this case it is 30^3S).

Moreover, the temperature dependence of the ion signal time delay measurement provides

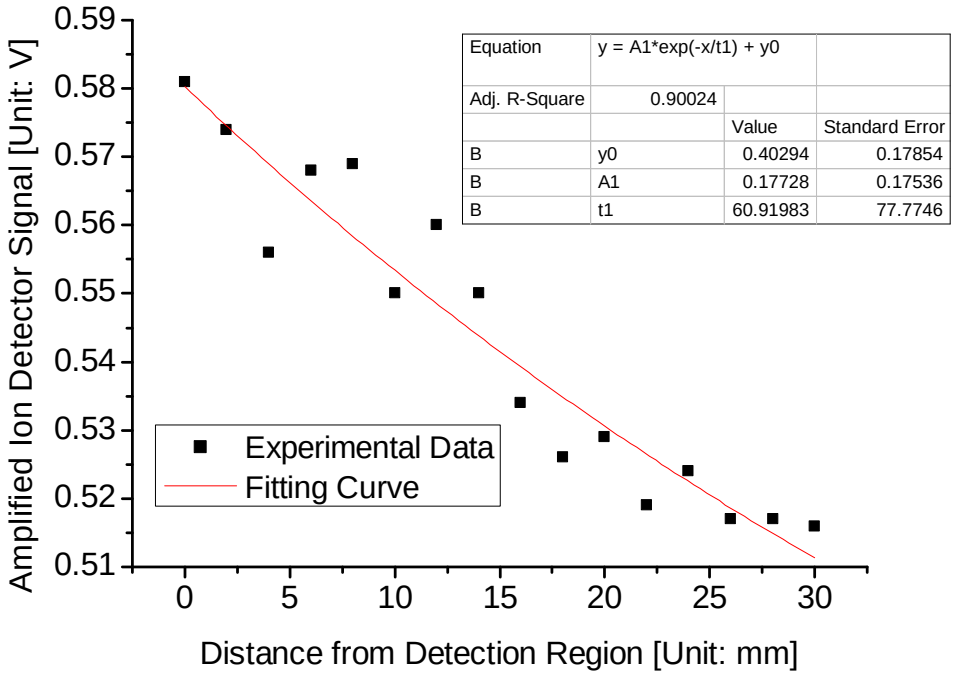

Figure 4.7: The measurement for the ion signal strength of 30^3S as a function of the distance between the interaction point (STIRAP lasers' position) and the ion detector region (position B). This is the same type of measurement as in Fig. 4.6. However, here the temperature is very different: 380K.

an extra hard evidence that it is the black body radiation that is causing the ionization.

4.4 Verification of the Ionization Mechanism, Lineshape and Fano Interference

In order to verify the assertion that the ions we detect are from the black body radiation induced ionization, we heat up the metal field plates surrounding the STIRAP interaction region. The dimension of the interaction region, namely laser width $\times$ atomic beam height $\times$ atomic beam width, which is typically on the order of 0.5 mm $\times$ 0.5 mm $\times$ 0.5 mm, is

very much smaller than the dimension of the region contained within the two field plates. Therefore the full solid angle of the interaction region can be safely regarded as all covered by the plates, hence the characteristics of the black body radiation at the point where interaction really happens is solely determined by the temperature of the plates.

The aluminum field plates are heated by four attached 1 Ω power resistors (up to 25 W) in good thermal contact. The temperature of the resistors is controlled by the electric current flowing through them and a thermocouple is physically touching the surface of one of the resistors to measure the actual temperature.

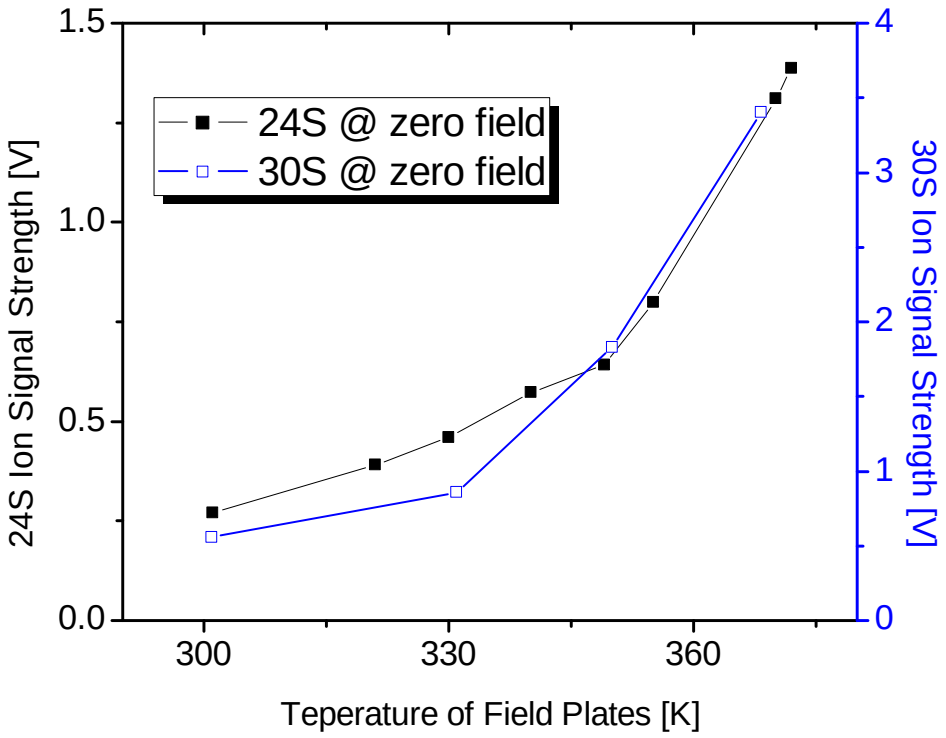

Figure 4.8: The relation of the ion signal strength and the temperature for 24^3S and 30^3S. Both measurements are at zero electric field, hence there is no concern about the electric field messing up the states or participating in the ionization process. The error bar of the ion signal is smaller than the size of the scatter and therefore is not shown.

According to the the previous sections' discussions, when the temperature is moderately

increased from room temperature, the direct ionization rates and population diffusion rates increase. Therefore the observed ion signal, which can be regarded as representing the total ionization rate, will simply be enhanced for higher temperature. This is exactly the information presented in Fig. 4.8. Moreover, it serves as evidence supporting the argument that the ionization is caused by the black body radiation, because hardly anything else depends on the temperature of the environment.

Also, when the field plates were heated, we have observed a line shape of the ion signal that could possibly be a signature of Fano interference as illustrated in Fig. 4.9.

In his famous 1961 paper [75], U. Fano introduced a phenomena now known as 'Fano interference', which he described as configuration interaction in the generality. Basically speaking, when the Hamiltonian allows both a continuum and a set of discrete states, with possibly degenerate energy and there is a coupling between them, Fano interference takes place. As a result of the coupling between the discrete states and the continuum, the new 'diagonalized' energy eigenstates would become a superposition of both discrete and continuum bare states. The experimental signature is usually the asymmetric lineshape.

An atom's Hamiltonian allows both discrete states (when it is technically an atom) and continuum states (when an atom becomes an ion). The black body radiation at room temperature provides the coupling between the discrete states of the Helium Rydberg series and the ionization continuum. Therefore it is not surprising to observe similar experimental signatures as Fano interference. Similar results on the Fano profile of ionization peaks have been observed long ago, see [76], which provides an in-depth discussion.

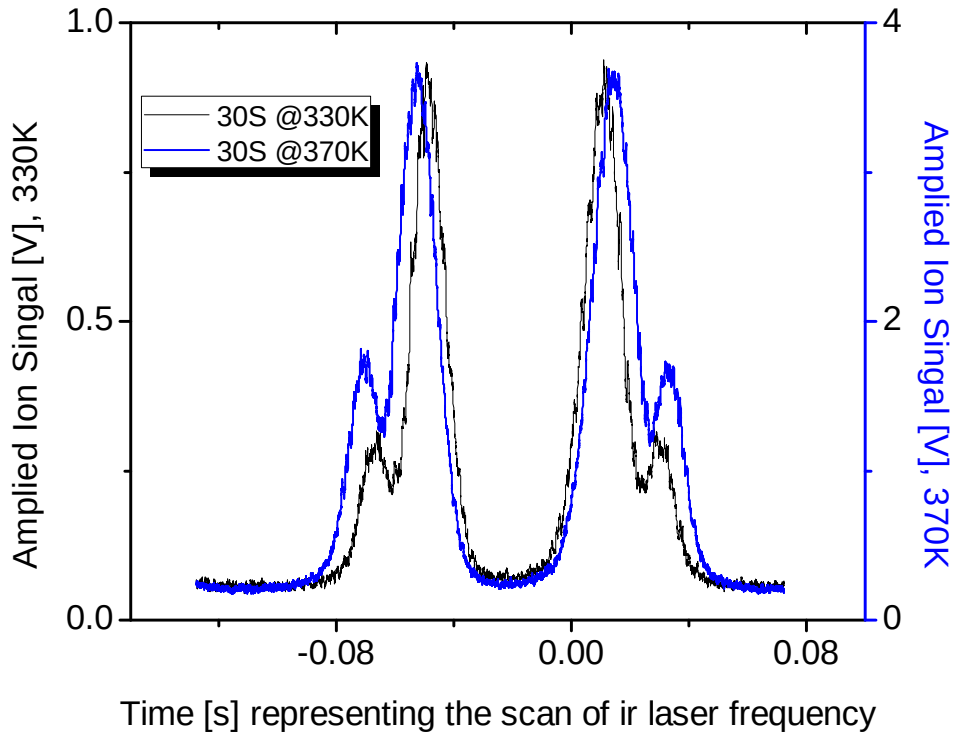

Figure 4.9: The ion signal of 30^3S at temperature 330K and 370K separately. For both traces the ir laser frequency is scanned, the electric field is set at zero, and the detector is at position B while the interaction point is directly under one set of holes of the upper plate. The amplitude of the ion signal is bigger when the temperature is higher, as is shown in Fig. 4.8, which is the evidence that the ionization is induced by the blackbody radiation. The ion signal has a clear asymmetric line shape, and is more asymmetric when the temperature is higher. Also, the signal is broadened at the higher temperature. The smaller peak is always occurring on a higher ir laser frequency, namely the smaller peak corresponds to a higher energy resonance. We think this is a clear experimental signature of a Fano line shape. Other possibilities are possible, such as the splitting of magnetic sub–levels or Autler–Townes splitting, but they could not explain the temperature dependence. In summary, this lineshape is the result of the configuration interaction between the Rydberg state $30S$ and the blackbody radiation induced ionization continuum.

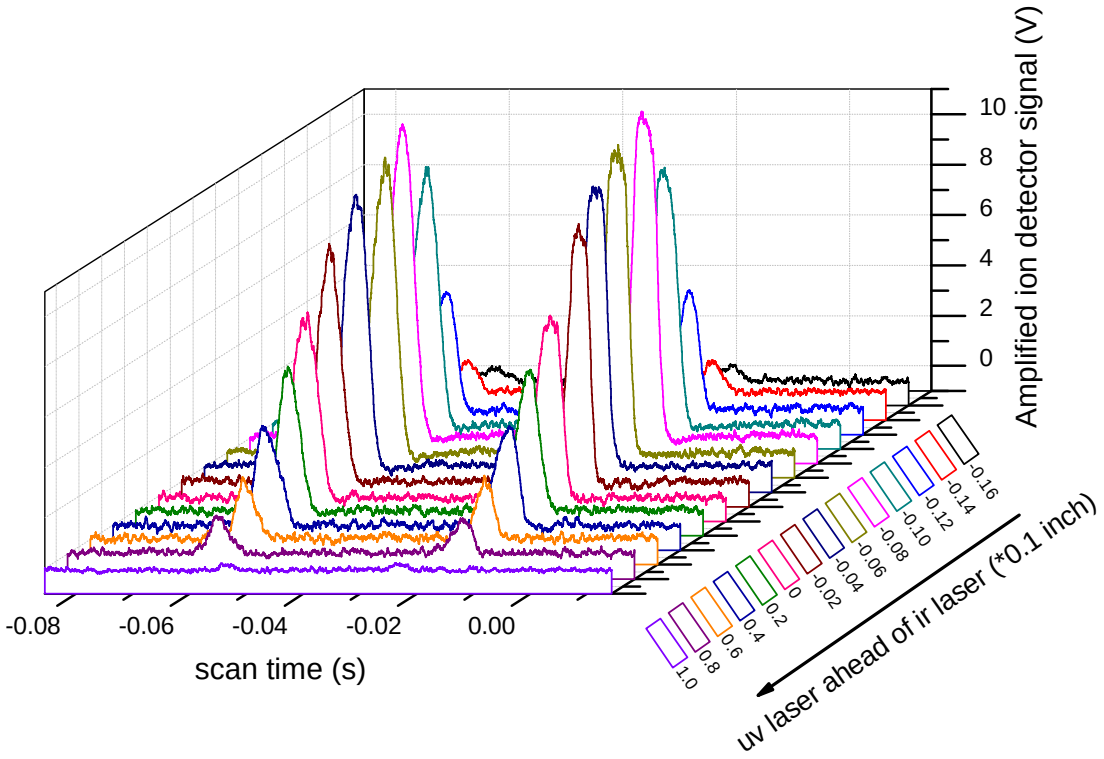

Figure 4.10: The experimental signature of STIRAP.The relation between the ion signal strength and the relative position of the ir and uv lasers is shown, which makes it clear that the ion signal is higher when the lasers are in STIRAP configuration, namely ir ahead of uv. The ion detector is at position A for these measurements.

4.5 Rydberg Atom Spectroscopy Enabled by Black-body Radiation Ionization

Isn't it a free lunch when the black body radiation ionizes the helium atom when it is in some Rydberg state? No extra effort is in need and all left to do is to detect ions.

The first obvious observation is that the strength of the ion signal is proportional to the amount of Rydberg atoms produced. Therefore we can use the ion signal as a counting tool.

A direct application is to verify that counter–intuitive order of the Stokes and pump laser pulses make more Rydberg atoms, which is the evidence that we do have STIRAP realized in our experiment. The result is shown in Fig. 4.10.

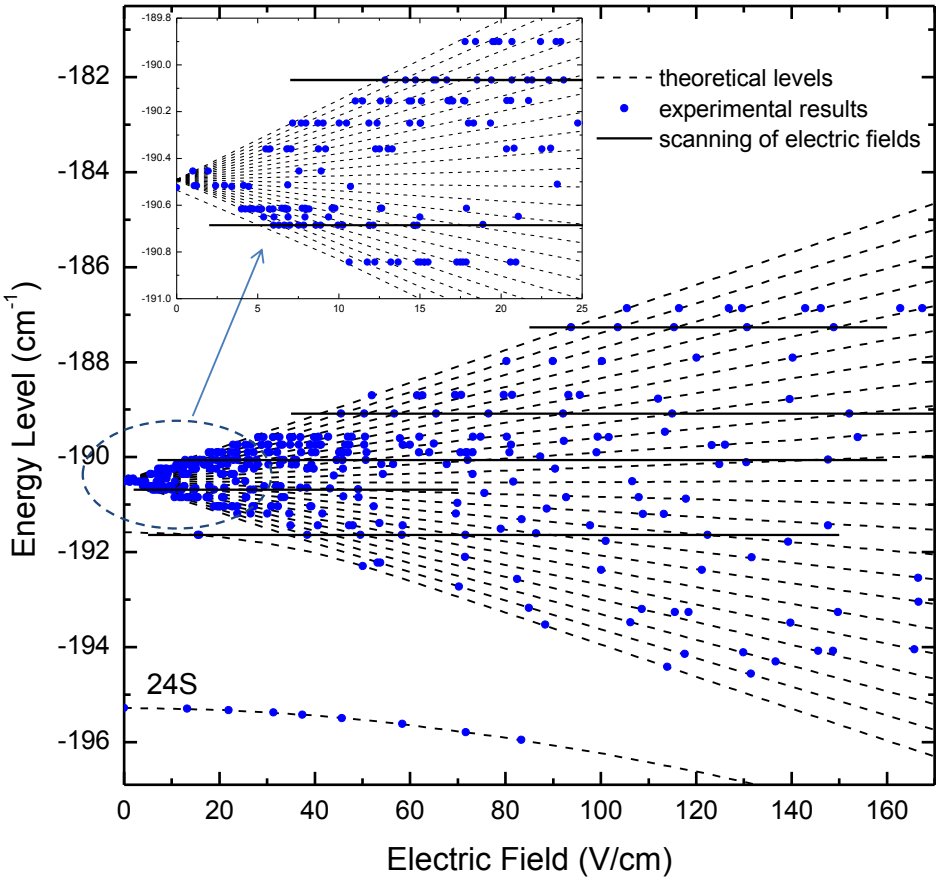

Figure 4.11: The experimental measurement of the $n = 24$ Stark map. See also discussions in reference [43].

Another application is to spectroscopically resolve the Stark map. Since STIRAP is sensitive to the two–photon detuning, the width of the ion signal peak is on the order of several MHz, which serves as a tool to determine where the resonance occurs. When the interaction region is subject to a uniform electric field, the Stark effect would cause the

resonant energy to shift, which can be theoretically calculated as in a Stark map. The experimental spectroscopic data can be fitted to the calculation, as shown in Fig. 4.11.

4.5.1 Direct Ionization by High Electric Fields

To make the story complete, we set up an experiment to directly excite the metastable Helium atom into the ionization continuum, and thereafter compare its ionization behavior with that of blackbody radiation induced ionization, which we have been discussing so far.

A typical way is to pass the Rydberg atoms through high electric fields which will ionize them. Yet, for convenience, what we actually do is to scan either the ir laser frequency or the ac electric field across a Stark resonance when there is already a high dc electric field applied. That Stark state, usually above the classical ionization limit, then auto ionizes. This phenomena is named as the ionizing Stark resonance, which is also discussed extensively in [76]. The experimental setup is shown in Fig. 4.12.

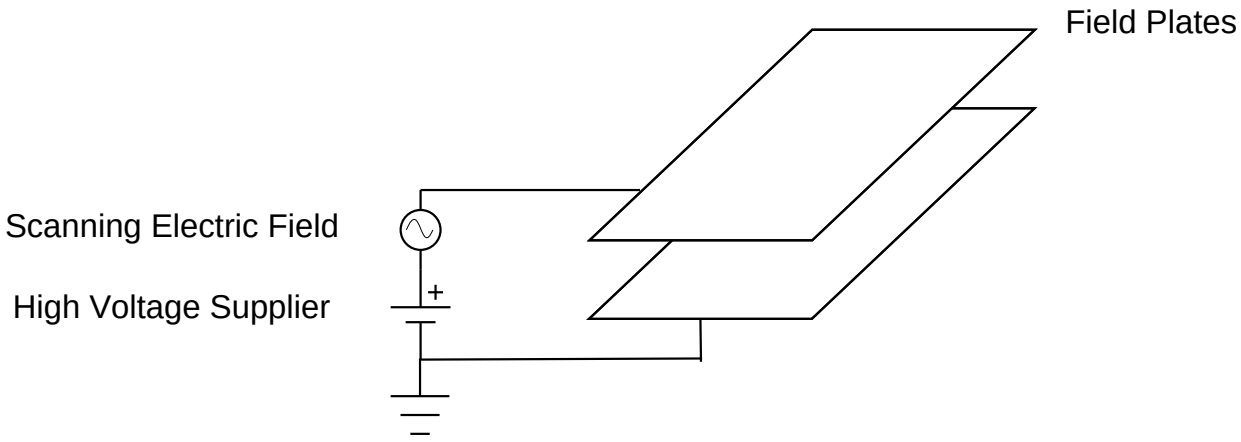

Figure 4.12: The schematics of the experimental setup of direct ionization with high fields. The electric

The ion detector for the field ionization experiment is at position B as shown in Fig. 4.2. When the helium atom goes through the ionizing Stark resonance, all the atom excited

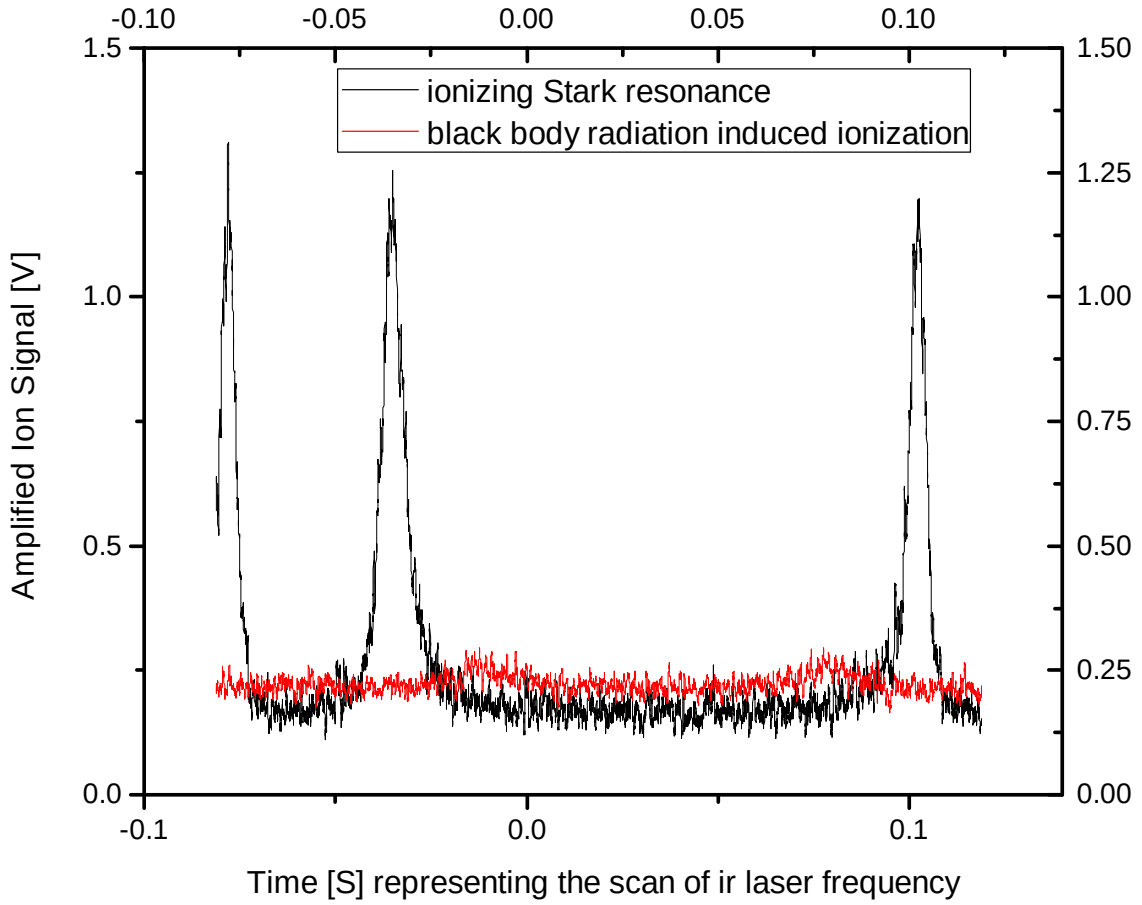

Figure 4.13: With a setup shown in Fig. 4.12, the ion signal when scanning the small ac electric field across a ionizing Stark resonance. The principle quantum number is 24, and this is at the highly crossed region of Stark map of $l \neq 0$, with the ir laser wavelength at ≈ 796.4611nm. The black body radiation (at 300K) induced ionization signal (from a Stark state of 24 $l \neq 0$ at a very low electric field at several volts per centimeter) is also included as a comparison.

will turn into ions and be gone in the electric field, in contrast to the case of ionization by black body radiation in which most of the helium atoms are still 'alive' in certain Rydberg states. For the case of the field ionization via ionizing Stark resonance, if the interaction point is not directly under some holes of the upper field plate, then at the instant when the resonance is scanned across, all the ions generated would be swept to the plate by the electric

field and can no longer be detected. Therefore, by moving the STIRAP lasers to change the interaction position we can readily map out the position of the holes on the upper field plate.

The result of such field ionization via ionizing Stark resonance is shown in Fig. 4.13.

Chapter 5

STIRAP Efficiency Measurement

We have analyzed the ion signal generated by the Rydberg atoms induced by the thermal radiation in Chapter 4, which is the unique signature of Rydberg atoms. We can also argue that the strength of the ion signal is proportional to the population of the Rydberg atoms. Yet, we still need to establish the absolute count of the Rydberg population, if we want to investigate further into the dynamics of the STIRAP process.

5.1 Absolute STIRAP Efficiency Measurement

We set up an experiment to measure the exact population excited in to the Rydberg state, whose mechanism is shown in Fig. 5.1. The basic idea to physically separate the Rydberg atoms and the metastable atoms immediately after the STIRAP interaction, by applying a force only acting on the metastable atoms. We choose the bichromatic force (see discussions in Section 1.3.2), for the reason that it is strong, robust and can push the metastable atoms to a large final transverse velocity which would result in a better separation.

As Fig. 5.1 illustrates, the STIRAP interaction region is between the metal field plates.

The 1083 nm bichromatic force laser beam is applied immediately downstream of the STIRAP laser beams, driving the $2^3S_1 \rightarrow 2^3P_2$ transition of the metastable ground state atoms while doing nothing to the Rydberg atoms. The metastable atoms acquire a large transverse velocity when they leave the bichromatic force interaction region. When the Rydberg atoms and the metastable atoms both arrive at the detection region, they are physically apart transversely, and the population count is performed by using the SSD.

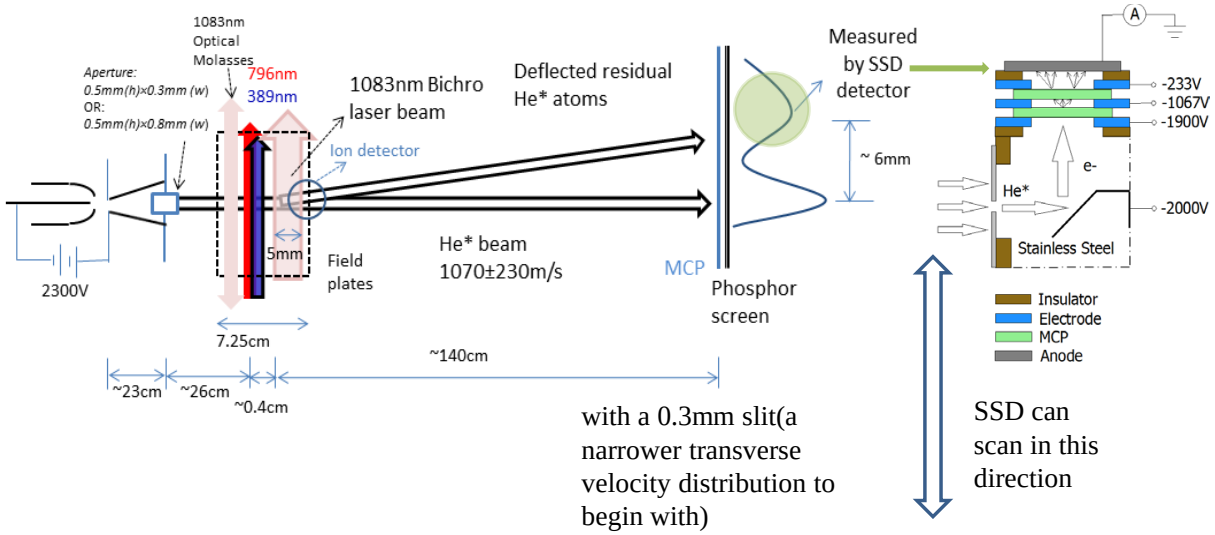

Figure 5.1: Experimental setup of the absolute efficiency measurement of STIRAP by physically separating the Rydberg atoms from the metastable ground state atoms. The the optical molasses laser beam applied before the STIRAP interaction will be discussed in Section 5.3, and it can also serve as the optical pumping laser as discussed in Section 6.3.1.

We set the detuning $\Delta = 2\pi \times 60$ MHz for our bichromatic laser beam, with the π–pulse length to be 250 cm. According the numerical simulations of the same type discussed in Section 1.3.2, to reach to optimum π–pulse condition for the force, we need the laser to have an intensity $\sim 4000 I_{\rm sat}$, where $I_{\rm sat}$ is the saturation intensity for this transition. The two frequency light $\omega \pm \delta$ (~ 0.1 mW) out from the four frequency generation mechanism shown in Fig. 2.12 does not have high enough intensity. Therefore, it is fed to a 1 W fiber amplifier

for preamp and subsequently fed to a 5 W fiber amplifier.

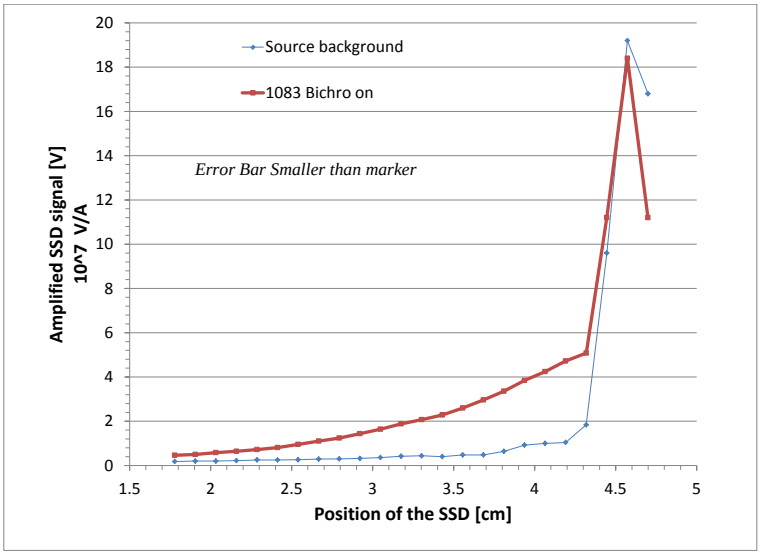

Figure 5.2: The atom profile measured by the SSD, which is scanned transversely in the detection chamber. With the 1083 nm bichromatic laser on, the atoms receive the bichromatic force and get deflected, resulting in a physical separation between the pushed metastable atoms and the center. What's left in the center is mostly the stray uv light from the source discharge. The wide spread of the final velocities of the atoms is an inherent signature of the bichromatic force, however, by optimizing the parameters of the bichromatic laser, even better separation between the deflected atoms and the center can be achieved.

The amplified two frequency light passes through a telescope and a beam defining slit of ~ 0.5 mm to form a rectangular beam shape of uniform intensity. A quarter–wave plate is put in the optical path to make circular polarization to induce optical pumping effects into the stronger transition of $\Delta m = \pm 1$. A retro–reflection is set up to provide the counter–propagating light and allows for the control of the optical delay. The metastable atoms pass through the bichromatic light interaction region are deflected and we measure them in the detection chamber after a long beam path, with a typical result shown in Fig. 5.2.

By the mechanism demonstrated by Fig. 5.1 and Fig. 5.2, we are able to perform the

measurement for the absolute efficiency of the STIRAP interaction. A typical experimental data recorded by the oscilloscope is shown in Fig. 5.3.

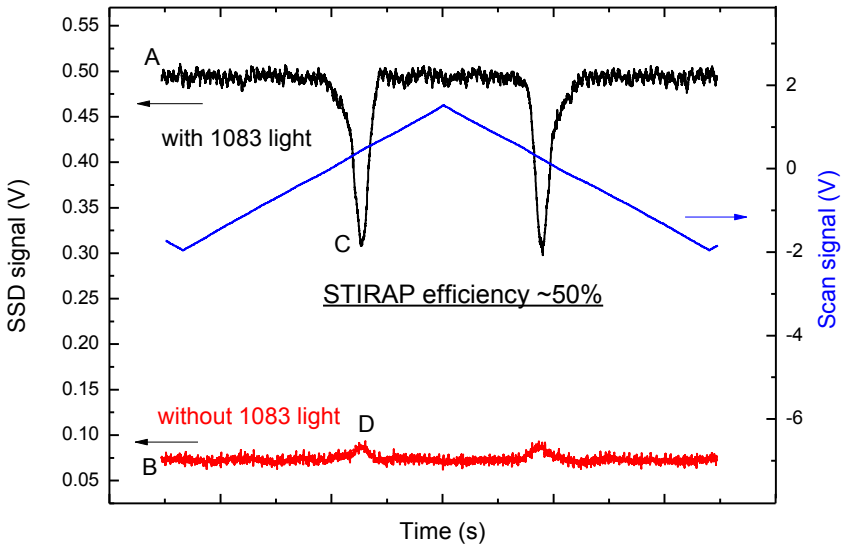

Figure 5.3: Sample data of absolute efficiency measurement of STIRAP. The resonance shown in this graph is a Stark shifted state with non–zero orbital angular momentum of $n = 24$. The ir laser wavelength is ~ 796.4414 nm while the frequency of the ir and uv lasers are all kept constant. The voltage on the top field plate is 115.2 V while the voltage of the lower plate is scanned across the resonance.

This type of data as in Fig. 5.3 reveals the quantity of the 'missing metastable heliums', which are the atoms excited into the Rydberg state. We can scan across the resonance either by scanning the ir laser frequency or scanning the electric field. More discussions on the data acquisition and processing can be found at [43].

According to the theoretical understandings of the principles of STIRAP (see Chapter 3), an efficiency of close to $\sim 100\%$ is intuitively expected. However, surprisingly enough, the best out of all the efficiency measurement data we gathered shows only a raw efficiency of $\sim 50\%$ [43]. We were puzzled by this fact and conducted a series of tests trying to identify the possible causes.

We have chosen different source parameters to change the metastable helium density significantly in the atomic beam, and we have observed no change in efficiency hence ruling out the possibility of the collisional effects. We have also measured the efficiency of STIRAP excitation to different Rydberg states (different principle quantum number n, or different Stark states); after compensating for the corresponding decays, those measurements yield the same efficiency value. We are also concerned about the possibility that the Rabi frequency of the ir laser driving the transition from the 3^3P state to the Rydberg state is not big enough, therefore we have measured the efficiency as a function of the ir laser intensity. We have seen a pattern indicating the saturation of the efficiency as the the ir laser Rabi frequency goes up, especially for the smaller n's. More details of the exclusion of all these factors are provided in [43].

5.2 Detunings Caused by Transverse Velocity Spread

As we have already discussed, STIRAP is tolerant to one-photon detuning if the two-photon detuning is zero, namely, energy conservation is satisfied. In the experiment, since the laser beams cross the atomic beam at nearly a right angle, in the ideal case there would be no relative movement between the atom and the laser, henceforth causing no detuning at all.

However, as first suggested by Dr. Peter Anisimov, realistically, the atomic beam would have a transverse velocity spread, and the angle at which the laser crosses the atomic beam might be slightly different from 90 degrees. Both of those could lead to a Doppler shift of the pump and Stokes laser frequencies, in the frame of the atom. The annoying fact is that, since the ir and uv lasers are co-propagating, the Doppler shift for both of the lasers are of the same sign, namely, both of the frequencies will be shifted up or down depending on the

atom's motion. This shift could not only cause one-photon detuning but also two-photon detuning. Fig. 5.4 provides an illustrative explanation.

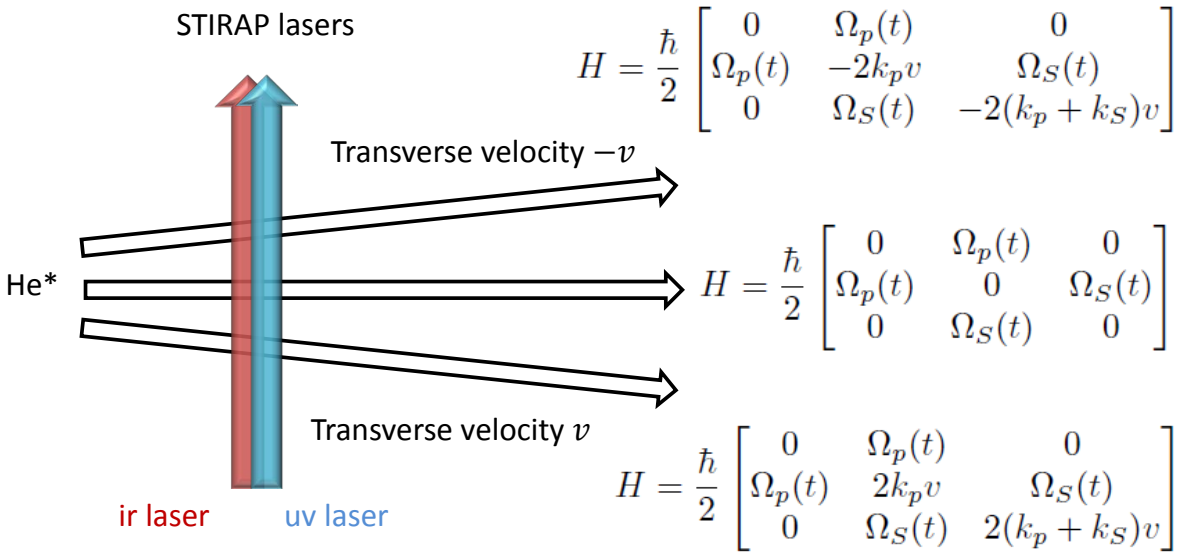

Figure 5.4: The effect of the transverse velocity spread. Suppose the STIRAP lasers are on-resonance for the zero transverse velocity atoms, then for atoms with different transverse velocities, the lasers are not on resonance any more. Here the Hamiltonians in the atoms' own reference frames are shown pictorially.

Let us first estimate the associated effects for different transverse velocity groups through numerical calculations by the method of time-dependent Schödinger equation. In the numerical simulation, we set the ir and uv lasers to be on–resonance with the zero transverse velocity group, and then in the eyes of the other velocity groups they see both the one–photon and two–photon detunings as illustrated in Fig. 5.4. The result is shown in the following Fig. 5.5.

From Fig. 5.5, we see that STIRAP efficiency is very sensitive to the two–photon detuning caused by the transverse velocity spread's Doppler shift, the discussions of which can also

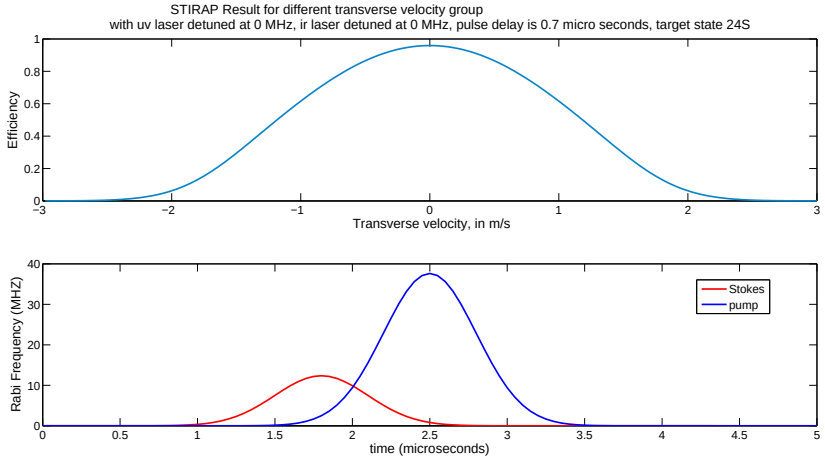

Figure 5.5: The numerical simulation of the STIRAP efficiency (as how much population ends up in the final state) for different transverse velocity groups. The ir and uv laser pulses are in STIRAP configuration, whose Rabi frequencies are shown in red and blue respectively (ir is ahead of uv). We use the Hamiltonian as in Fig. 5.4 and no polarization effect is considered. The effect of spontaneous emission is not included either.

be found in Figure 4.6 of [43]. As mentioned in Chapter 2, we scan the ir laser frequency to measure the efficiency as a function of the ir laser frequency detuning. The recorded efficiency is the collective response of the atoms of all the transverse velocity groups. A direct numerical simulation of this scenario is shown in Fig. 5.6.

Ideally, STIRAP will result in 100% efficiency in population transfer. However, as revealed by Fig. 5.5 and Fig. 5.6, the experimentally measured efficiency in a atom beam type experiment would be compromised at a significant level due to the transverse velocity spread. Therefore we have to be careful when comparing the data with the theory and shall not simply take the peak value of the efficiency curve as the ultimate measured STIRAP efficiency.

There is yet another purely mechanical side effect that will reduce the measured STIRAP efficiency, which is the longitudinal velocity spread. We first determine the longitudinal velocity by a time of flight measurement whose result is shown in Fig. 5.7 (see also Chapter

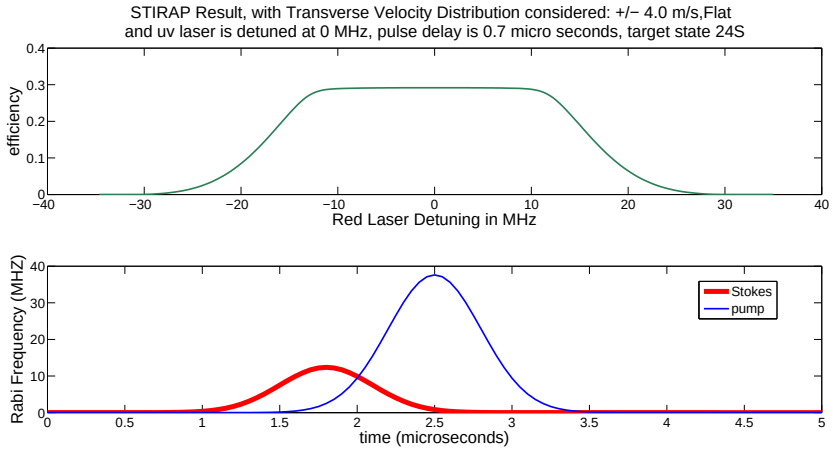

(a) A relatively wide transverse velocity spread.

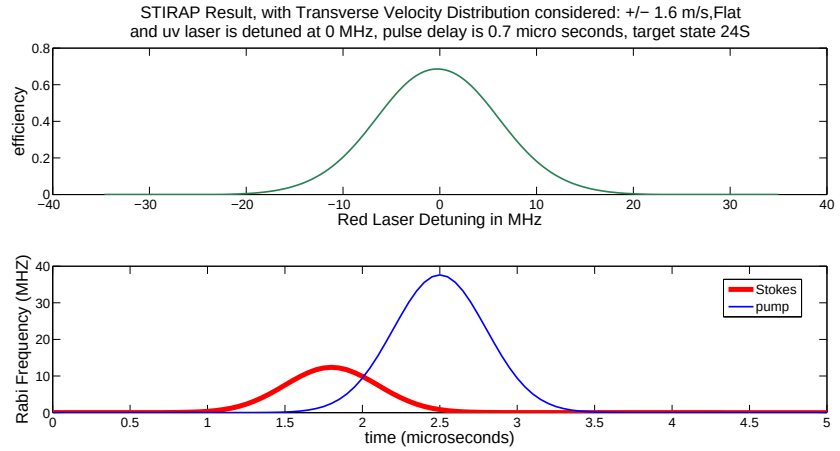

(b) A relatively narrow transverse velocity spread.

Figure 5.6: Numerical simulation of STIRAP efficiency for different transverse velocities. The ir and uv pulses are in STIRAP configuration, whose Rabi frequencies are shown in red and blue respectively (ir is ahead of uv). The transverse velocity profile is assumed to be a uniform distribution within the specified spread. This is a direct simulation of the experimental scenario where the frequency of the ir laser is scanned and the efficiency is recorded as a function of the ir laser frequency. Note the difference of scales between (a) and (b).

2 of [43]).

In the sense of what's been done to the atomic beam, our STIRAP efficiency measurement

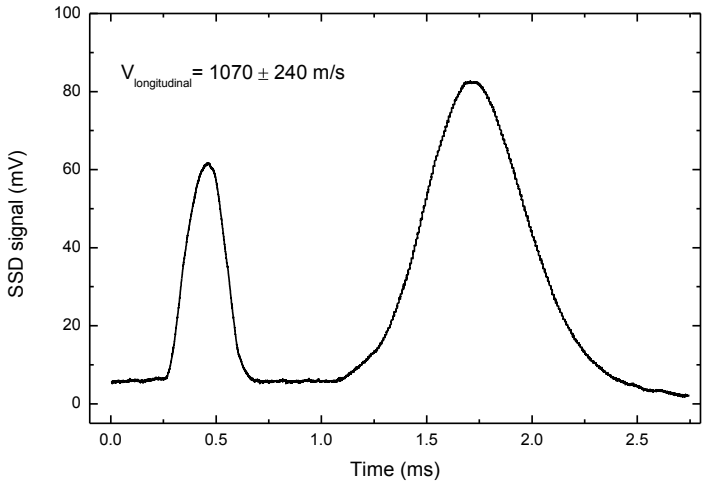

Figure 5.7: Time of flight measurement for the longitudinal velocity distribution. The source outputs both uv stray light and He^*. A chopper selects a portion in the beam line and lets it travel downstream. The SSD in the detection chamber collects the signal as a function of time. The first narrow peak is the SSD's response to the uv light and shows the time resolution of the system. The second wide peak demonstrates the longitudinal velocity distribution.

by scanning the ir laser frequency is very similar to the time of flight measurement by a chopper. During the ir laser on–resonance time, a little pulse of Rydberg atoms is produced. When this pulse of Rydberg atoms travels down the beam line, it spreads because it contains many longitudinal velocity groups, as sketched in Fig. 5.8.

The practical experimental scenario is a bit more complicated than described in Fig. 5.8. We are detecting the 'missing' Rydberg atoms after separating them from the metastable heliums by the bichromatic force. Therefore the profile in Fig. 5.8 should be viewed as the 'missing' profile. More directly, we are constantly monitoring the pushed metastable heliums, and the 'gap' corresponding to the Rydberg atoms is going to be partially impinged by different longitudinal velocity groups of the metastable heliums surrounding the 'gap'.

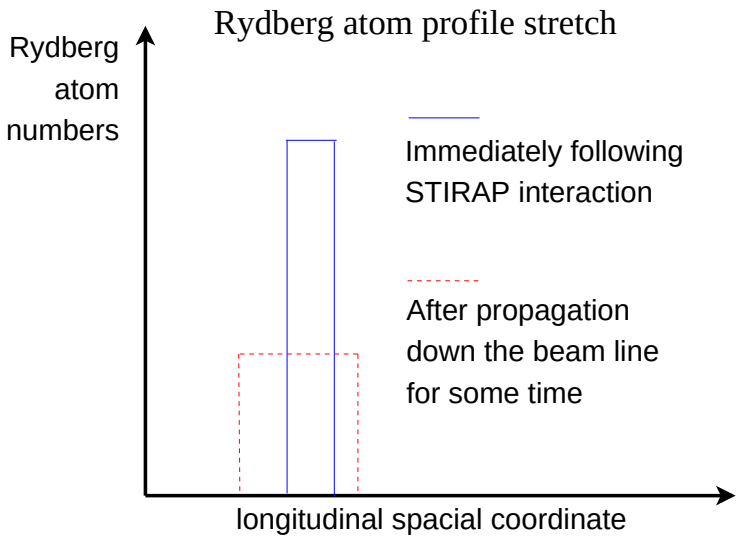

Figure 5.8: An illustration of the effects on the STIRAP efficiency measurement due to the longitudinal velocity distribution.

5.3 Observing Effects Associated with Transverse Velocity Spread of the Atomic Beam

The transverse velocity spread can first be roughly estimated from the size of the spot on the MCP + phosphor screen. An illustration is shown in Fig. 5.9.

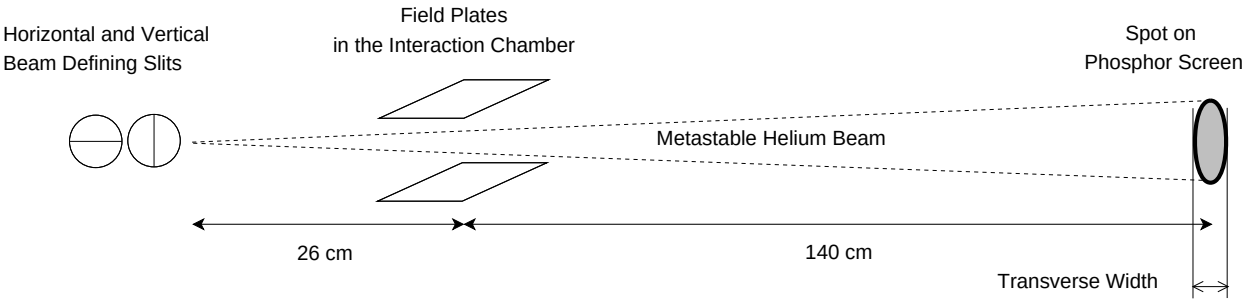

Figure 5.9: Estimating the transverse velocity spread from the transverse atomic beam size of the spot in the phosphor screen.

According to the geometry of Fig. 5.9, plus our knowledge of the longitudinal velocity of the atomic beam, the transverse velocity spread $\pm v_{\text{trans}}$ can be estimated by $\frac{w/2}{v_{\text{trans}}} =$

$\frac{140\text{cm}+26\text{cm}}{1070\text{m/s}}$, where w is is width of the atom spot shown on the phosphor screen and 1070 m/s is the longitudinal velocity of the. As already demonstrated in Fig. 5.1, the width of the beam defining slit can be changed. We have used two different sizes, the narrower one with ~ 0.3 mm and the wider one with ~ 0.8 mm. When the slit size is set at ~ 0.8 mm, the spot shown on the phosphor screen has a width of ~ 8 mm. This corresponds to a transverse velocity spread of ± 2.6 m/s. According to the discussions and numerical simulations in Section 5.2, the wider beam defining slit will immediately introduce a significant drop in the measured efficiency of Rydberg production.

To further identify the transverse velocity spread of the atom beam and study the effects, we set up a one dimensional optical molasses laser in the transverse direction before the STIRAP interaction lasers as shown in Fig. 5.1. The optical molasses laser [9] allows us to transversely cool or heat the atom beam, and henceforth to change the transverse velocity spread. The optical molasses laser is at 1083 nm driving the $2^3S_1 \rightarrow 2^3P_2$ transition, whose frequency can be detuned by the AOM.

The interesting thing to do, however, is to use the optical molasses to heat up the atomic beam in the transverse direction. If there is a drop in the Rydberg atom production due to the heating, then this fact will serve as the experimental signature for our propositions that the efficiency measurement is compromised by the transverse velocity spread.

We want to establish this verification without using the efficiency measurement method we have discussed so far, to provide an independent check. Therefore we choose the ion signal from the Rydberg atoms (ionization by blackbody radiation at room temperature, see discussions in Chapter 4) as the measure of the Rydberg atom population. The result is presented in Fig. 5.10. According to the analysis of Section 5.2, we ought to look for two types of features in the data: the peak Rydberg production rate is to be lower, and the width of the signal during ir laser frequency scan is to be larger. A close look at Fig. 5.10 assures

both of the two observations.

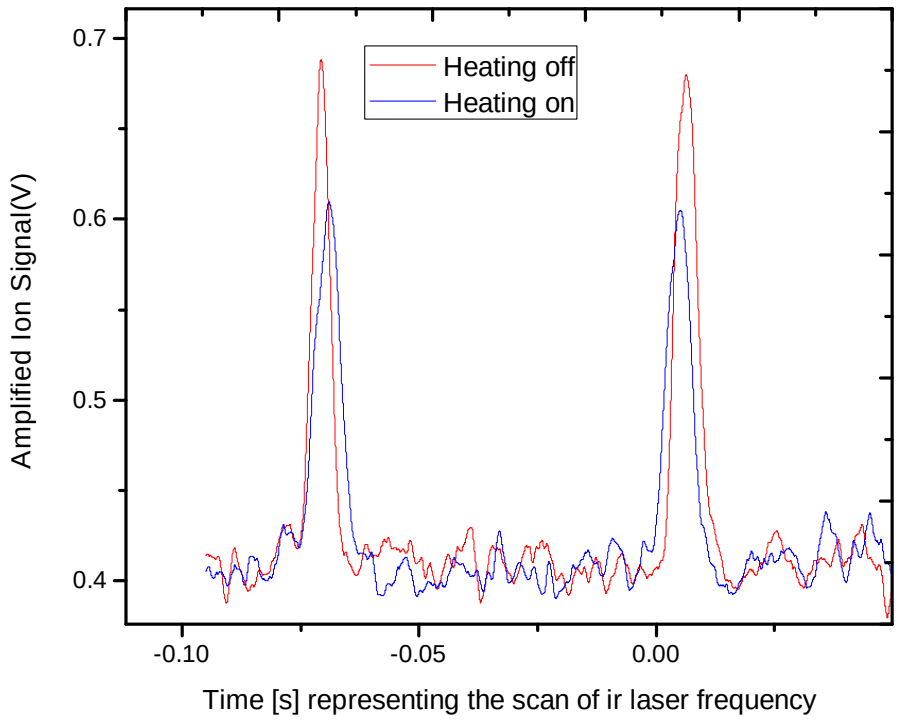

Figure 5.10: Ion signals from the Rydberg atoms produced by STIRAP, via the blackbody radiation induced ionization. The ir laser frequency is scanned across the resonance, as represented by the horizontal axis. The ion detector is put right above the interaction region for this data. This is the data with the atomic beam defined by the narrower slit. The optical molasses laser beam is blue detuned at 2 MHz to heat the atomic beam in the transverse dimension. This diagrams shows the ion signals when the heating optical molasses laser is on and off, respectively. It clearly indicates that when the transverse velocity spread is larger, the peak Rydberg atom production rate is lower, as we are expecting. Since the ion signal is proportional to the Rydberg atom population and is physically separated from the efficiency measurement mechanism, this is an independent verification of the argument of the atomic beam transverse velocity spread's role in STIRAP interaction.

The next step is to adjust the optical molasses to cool the atomic beam transversely and see if the cooling could enhance the measured STIRAP efficiency. First we establish the one dimensional cooling in the transverse direction again as shown in Fig. 5.1, with the red detuned 1083 nm laser driving the $2^3S_1 \rightarrow 2^3P_2$ transition. We measure the atomic beam

profile to verify the cooling power with the result given in Fig. 5.11.

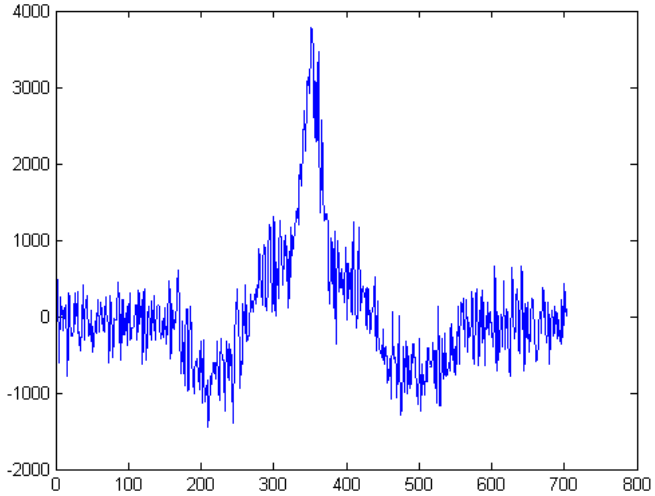

Figure 5.11: Atomic profile of transverse cooling by one dimensional optical molasses. The one dimensional optical molasses laser is red detuned by 3 MHz for large capture range. This diagram is the one dimensional layout from the subtracting the background out of the cooled atoms, based on the pixel values recorded by the CCD from the phosphor screen. The horizontal axis is the pixel position, while the vertical axis represents the subtracted pixel value. Basically, the negative value means that the atoms are pushed out from that region, while the positive value means that the atoms accumulate there. The atomic beam has a significant transverse spread to begin with because it comes from the wider beam defining slit. As for the scale, it corresponds to ~ 1.5 cm from 0 to 700 pixel values.

We then apply the optical molasses laser to transversely cool the atomic beam immediately before the STIRAP interaction in the configuration shown in Fig. 5.1. The efficiency measurement data, without compensating for the decay from the Rydberg level, is presented in Fig. 5.12. The first observation is that the efficiency is overall lower than what's in Fig. 5.3, which is a direct consequence of beginning with a larger transverse velocity. According to our estimates, the condition of the transverse velocity spread is very close to that described in Fig. 5.6a, and therefore we are expecting the peak efficiency to be around $\sim 30\%$. The second observation is that the transverse cooling increases the peak efficiency,

which is the consequence of all our discussions so far in this chapter: the one–photon and two–photon detunings caused by the transverse velocity spread manifest themselves in the STIRAP interaction.

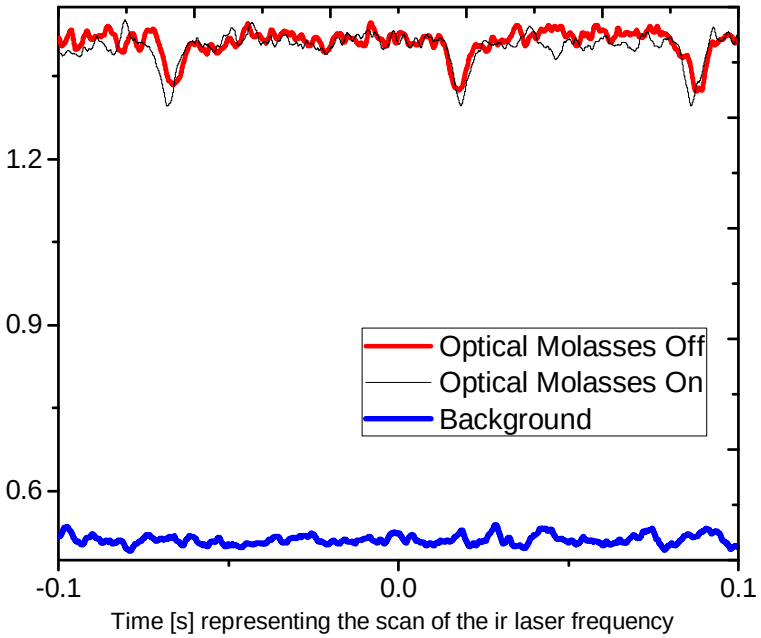

Figure 5.12: The absolute efficiency measurement data with the transverse cooling on/off. The transverse velocity spread of the atomic beam is significant to begin with, where the wider beam defining slit is used.

However, Fig. 5.12 does not solve all the puzzles. Namely, why the cooling only enhances the peak efficiency by a limited amount instead of close to $\sim 100\%$. There can be several possible causes to this. The first one is that the the optical molasses laser and the STIRAP lasers may not be aligned perfectly parallel to each other. The second one is that the optimal condition for STIRAP may not be easily satisfied with a large transverse velocity spread. The third one is that there might be other factors impeding the peak efficiency, for example, the longitudinal velocity spread whose properties are discussed in the end of Section 5.2.

To further explore the direct evidence for the transverse velocity's role in the STIRAP efficiency (or possibly other spectroscopically detectable effects influencing the STIRAP efficiency) and to corroborate the measurement of Autler–Townes effect (Section 7.1), we carry out a STIRAP experiment with the uv laser containing two frequency components. We fix the frequency difference of the two components of the uv laser, and the Rydberg resonance corresponding to these two components will be separated by the same amount. Therefore, we acquire a frequency scale in the STIRAP signal automatically.

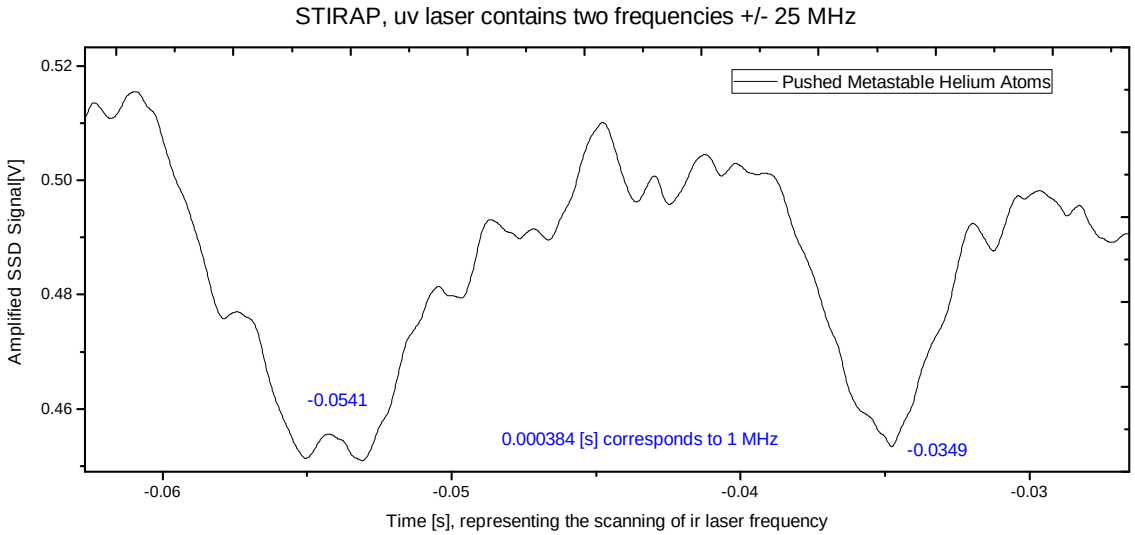

Figure 5.13: The SSD signal recording the pushed metastable heliums for the efficiency measurement experiment where the uv laser contains two frequency components ±25 MHz. The intensities of the two frequency components of the uv laser are a little different due to fluctuations and that is the reason why the widths of the two dips are different. This data is taken with the narrower beam defining slit.

The two dips of Fig. 5.13 represent the Rydberg atoms, or the 'missing' metastable atoms. The peak Rabi frequencies for the ir laser is $\sim 2\pi \times 7$ MHz, and the peak Rabi frequencies for the two components of the uv laser are $\sim 2\pi \times 5$ MHz when they are equal in intensity. According to numerical calculations, the lineshape of the dips in Fig. 5.13 roughly

correspond to a transverse velocity spread $\sim 2.5 - 3$ m/s, even thought the atomic beam is through the narrower defining slit.

Chapter 6

Polarization Induced Path Interference

People have already extensively researched the magnetic sub–levels' effects on STIRAP [77] [78] [79] [80] [81], with different focuses and motivations, mostly concerned with the robustness of STIRAP. The general consensus is that the magnetic sub–levels add to the complexities by a lot since they create complicated linkage patterns [82], and that STIRAP does not populate the intermediate levels so that in favorable situations STIRAP is still robust against this complication. Here we are going to present another point of view under a special setting in this category of problems.

In atomic physics, the study of various kinds of dark states is always an interesting topic. In the STIRAP experiment we are conducting, because of all the magnetic sub–levels in the seemingly simple three level system, particular combinations of the polarizations of the pump and Stokes laser beams would induce non–trivial dark states and even interferences of different excitation paths, in the classical sense. In this chapter, we hope to provide a brief and preliminary discussion on this topic.

6.1 An Analysis of the Diamond Structure

Throughout this chapter, we establish a Cartesian coordinate system whose z–direction is along the k vector of the co–linear laser beams, as shown in Fig. 6.1. And we choose this z–direction to be the quantization axis. The polarizations of both the laser beams are in the $x-y$ plane, and therefore can be regarded as a linear combination of σ_+ and σ_- light. The atomic level scheme of associated transitions is sketched in Fig. 6.2.

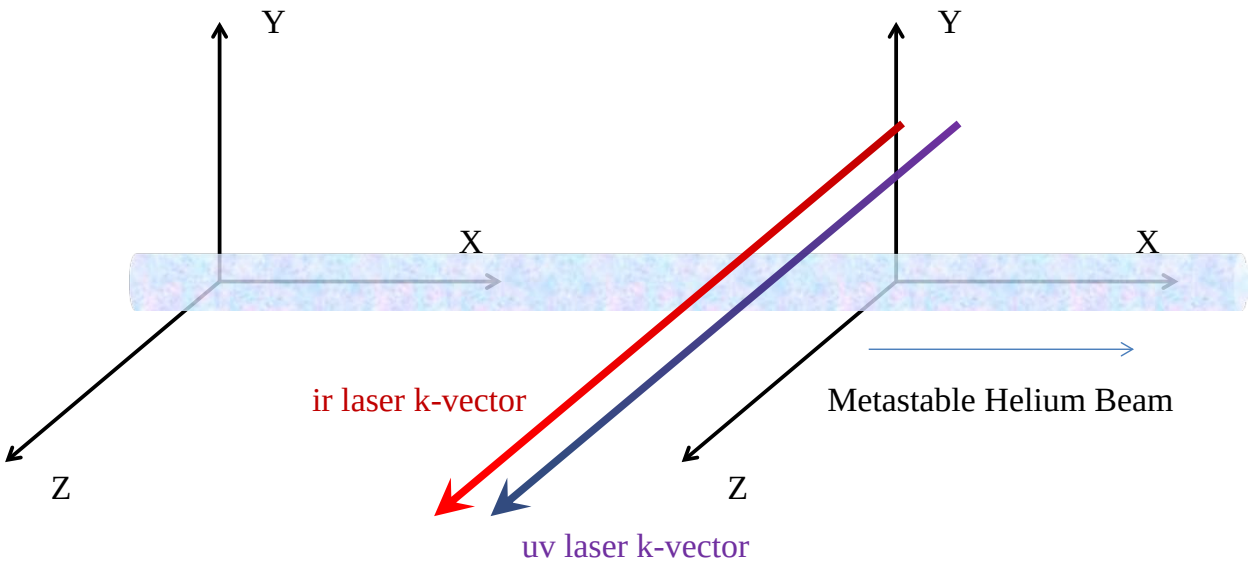

Figure 6.1: The coordinate system with the z direction along the k-vectors of the STIRAP laser beam.

We choose to first analyze the linkage pattern of a diamond shape whose level scheme is shown in Fig. 6.2 as the starting point of the discussion of the path interference phenomena. Before delving into the details, it shall be noted that this effect is purely semi-classical, and the quantum nature of the light does not have a role here. Moreover, we are going to stick to two major simplifications to begin with: 1) the atomic system is driven by steady light, i.e.

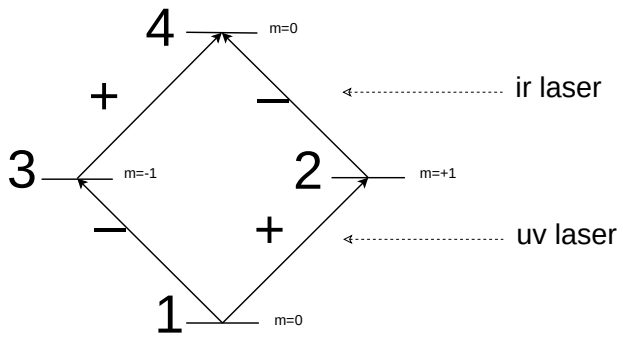

Figure 6.2: The level scheme of a diamond shape connection.

no pulse is involved; 2) we leave out the spontaneous emission. Then an analytical discussion with a clear picture is allowed.

To be more specific in the case of the helium atom, in Fig. 6.2, the ground level is the $m = 0$ sub–level of the metastable ground state 2^3S_1, the intermediate level now contains two sub–levels: the $m = -1$ and $m = +1$ sub–levels of the state 3^3P_2, and the final level is the $m = 0$ sub–level of a Rydberg S state, for example 30^3S. The lower transitions out of $|1\rangle$ are driven by the uv laser and the upper transitions going to $|4\rangle$ are driven by the ir laser.

We discuss the situation where the ir and uv lasers driving those transitions have linear polarizations, and re–express the polarizations in the circular basis P_+ and P_- as in the following equation, where $|\alpha| = |\beta| = 1$. There should be a factor of $\frac{1}{\sqrt{2}}$ in (6.1), but for simplicity we do not write it out. The constants can always be viewed as absorbed into the definition of the Rabi frequencies Ω_{uv} and Ω_{ir}, which are chosen to be real.

$$P_{uv} = P_+ + \alpha P_- \tag{6.1a}$$

$$P_{ir} = P_+ + \beta P_- \tag{6.1b}$$

And now we can write down the Hamiltonian and solve for the time evolution of the four sub–level total system's wavefunction, which is $(c_1, c_2, c_3, c_4)^T$ if expressed in the bare states basis.

$$i\frac{d}{dt}\begin{bmatrix} c_1 \\ c_2 \\ c_3 \\ c_4 \end{bmatrix} = \begin{bmatrix} 0 & \Omega_{uv} & \alpha\Omega_{uv} & 0 \\ \Omega_{uv} & 0 & 0 & \beta\Omega_{ir} \\ \alpha^*\Omega_{uv} & 0 & 0 & \Omega_{ir} \\ 0 & \beta^*\Omega_{ir} & \Omega_{ir} & 0 \end{bmatrix} \begin{bmatrix} c_1 \\ c_2 \\ c_3 \\ c_4 \end{bmatrix} \tag{6.2}$$

In the situation when the uv and ir lasers' polarizations are parallel, namely, $\alpha = \beta$, the linkage pattern would reduce to the trivial case as shown in Fig. 6.3. This reduction is acquired by linearly transforming the states in a process (known as the Morris–Shore transformation) described by [83] whose method is intended for a two–level system (see also an extension at [82]). Explicitly, instead of the two original intermediate sub–levels $|2\rangle$ and $|3\rangle$, we describe the system by two newly transformed states $|+\rangle = \frac{1}{\sqrt{2}}(|2\rangle + |3\rangle)$ and $|-\rangle = \frac{1}{\sqrt{2}}(|2\rangle - |3\rangle)$. In this situation, the time evolution described by (6.2) has no difference whether there are two or one sub–levels in the intermediate state. This is equivalent to a rotation of the coordinate system in Hilbert space.

However, if the uv and ir lasers' polarizations are orthogonal to each other, namely, $\alpha = 1$ but $\beta = -1$, the situation becomes quite different. A numerical simulation of this situation is shown in Fig. 6.4, based on (6.2). The population is oscillating back and forth between the ground level and the two intermediate sub–levels during the time evolution, but never gets transfered to the final level. In other words, the population is trapped and the level $|4\rangle$ becomes dark.

If we apply the same Morris–Shore transformation which leads to Fig. 6.3, we will have

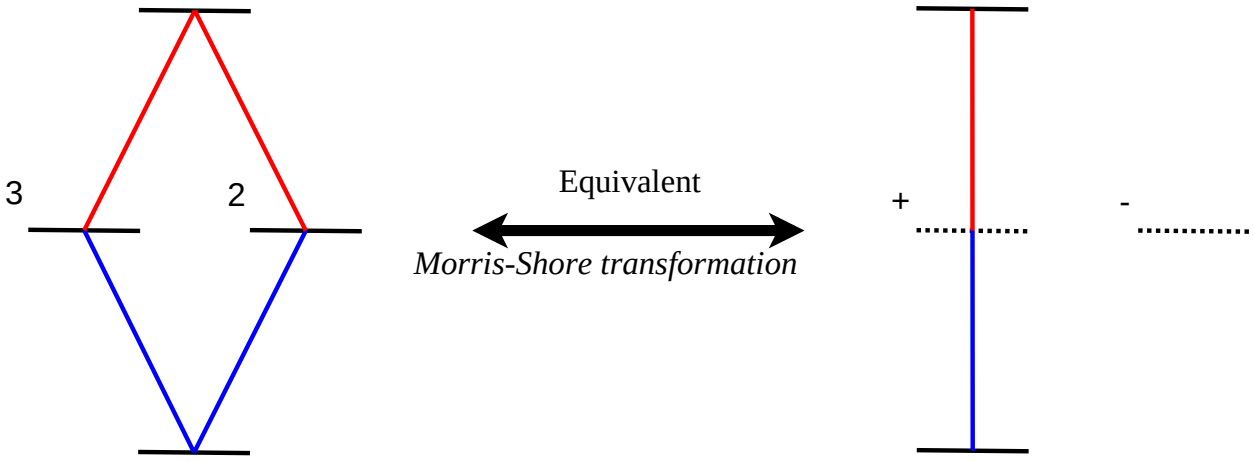

Figure 6.3: The reduction of the linkage pattern in the case when the lasers' polarizations are parallel to each other.

a linkage pattern shown in Fig. 6.5. We see that the final level $|4\rangle$ together with one of the intermediate states $|-\rangle$ becomes dark, if all the population were to start from $|1\rangle$. They stay dark no matter whether the lasers are pulsed or cw. This is solely a consequence of the polarizations' differences between the uv and ir lasers.

From the linkage reduction mechanisms shown in Fig. 6.3 and Fig. 6.5, it is clear that the one–photon detuning won't change the nature of the linkage pattern in these two extreme situations. Namely, when the polarizations are parallel to each other, the one–photon detuning is acting like it normally does on a three level system; when the polarizations are orthogonal to each other, the one–photon detuning does nothing because no population can be excited to level $|4\rangle$.

When the two intermediate levels receive probability amplitude pumped by the uv laser from the ground state, they have a phase difference printed onto them by the polarization of the uv laser. If the polarization of the ir laser is perpendicular to that of the uv laser, then this particular phases of the two intermediate levels make them dark to the transition corresponding to the ir laser. The linkage pattern described in Fig. 6.2 says nothing dictating

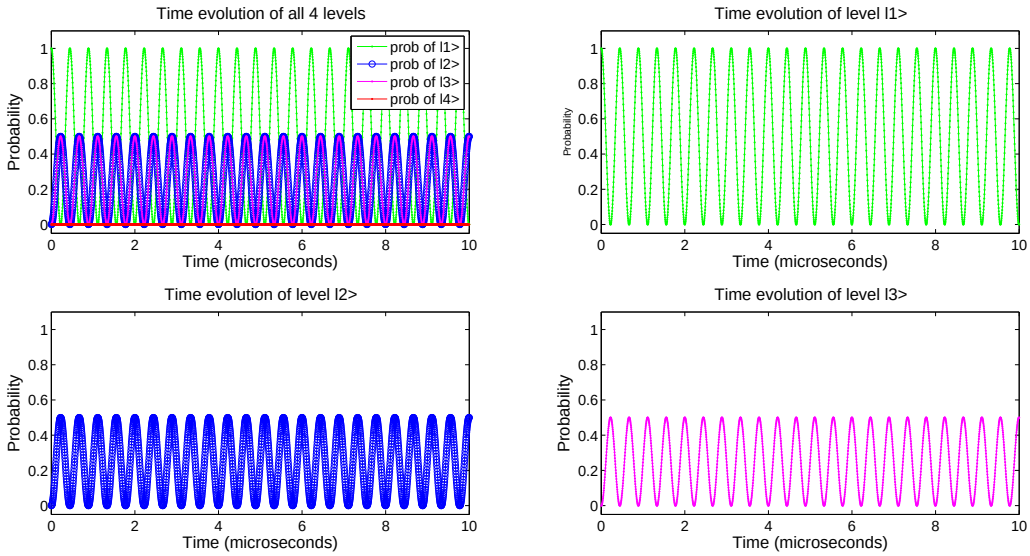

Figure 6.4: The numerical simulation of the time evolution of the total four level system with diamond linkage pattern, when the lasers' polarizations are orthogonal to each other. It is simulating (6.2) with cw lasers, where both Ω_{uv} and Ω_{ir} are set as constants to be $2\pi \times 1.6$ MHz in time.

that $|4\rangle$ shall be trivially dark; the excitation to the final level $|4\rangle$ is made dark by the phase differences induced by the polarizations of the ir and uv lasers.

What's the consequence of this one more sub–level to STIRAP? The adiabatic state that STIRAP relies on exists only when $\det \begin{bmatrix} \Omega_{uv} & \beta\Omega_{ir} \\ \alpha^*\Omega_{uv} & \Omega_{ir} \end{bmatrix} = 0$ (i.e. the Hamiltonian allows a null adiabatic state, see also discussions in Chapter 3) or explicitly $\alpha = \beta$, namely, the polarizations of the two linearly polarized lasers are parallel to each other. When the two lasers' polarizations deviate from the parallel situation, the usual STIRAP fails to occur.

6.1.1 An Interferometer Built inside an Atom

For the general case of different polarizations, let us first consider the situation where Ω_{ir} and Ω_{uv} are real constants, namely, the lasers are cw. Rewrite (6.2) in a slightly different

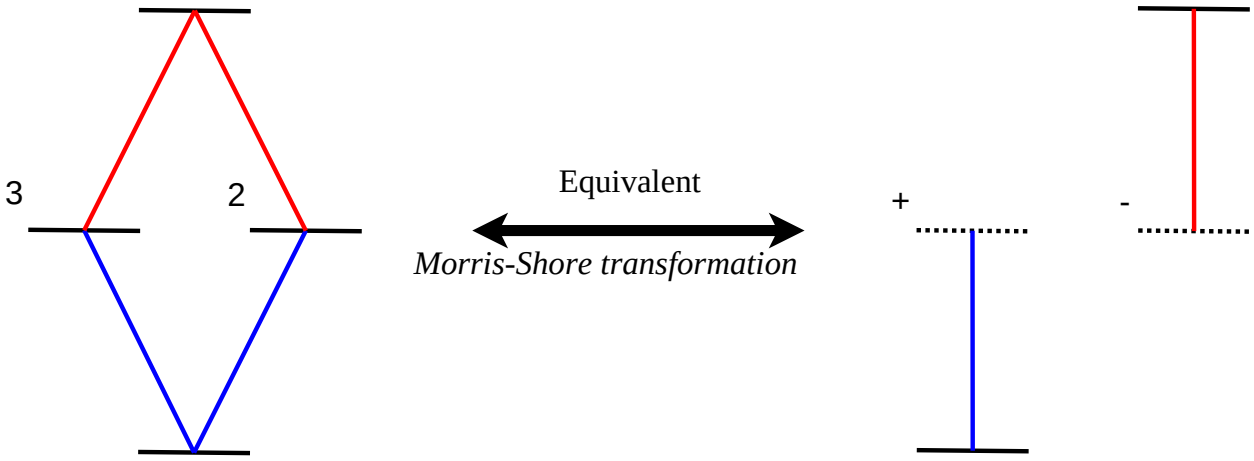

Figure 6.5: The reduction of the linkage pattern in the case when the lasers' polarizations are orthogonal to each other.

form to begin:

$$i\frac{d}{dt}\begin{bmatrix} c_1 \\ c_4 \\ c_2 \\ c_3 \end{bmatrix} = \underbrace{\begin{bmatrix} 0 & 0 & \Omega_{uv} & \alpha\Omega_{uv} \\ 0 & 0 & \beta^*\Omega_{ir} & \Omega_{ir} \\ \Omega_{uv} & \beta\Omega_{ir} & 0 & 0 \\ \alpha^*\Omega_{uv} & \Omega_{ir} & 0 & 0 \end{bmatrix}}_{H_4} \begin{bmatrix} c_1 \\ c_4 \\ c_2 \\ c_3 \end{bmatrix} \tag{6.3}$$

$$\lambda \begin{bmatrix} c_1 \\ c_4 \end{bmatrix} = \underbrace{\begin{bmatrix} \Omega_{uv} & \alpha\Omega_{uv} \\ \beta^*\Omega_{ir} & \Omega_{ir} \end{bmatrix}}_{M} \begin{bmatrix} c_2 \\ c_3 \end{bmatrix} \tag{6.4a}$$

$$\lambda \begin{bmatrix} c_2 \\ c_3 \end{bmatrix} = \underbrace{\begin{bmatrix} \Omega_{uv} & \beta\Omega_{ir} \\ \alpha^*\Omega_{uv} & \Omega_{ir} \end{bmatrix}}_{M^\dagger} \begin{bmatrix} c_1 \\ c_4 \end{bmatrix} \tag{6.4b}$$

To examine the time evolution described by (6.3), we look for the eigenstates and eigenvalues of H_4. Then the eigenvalue problem of (6.3) reduces to find a λ to make sure the eigen–equation described in (6.4) holds.

A little observation of the symmetry between (c_1, c_4) and (c_2, c_3) of (6.4) would lead to a simplified eigenvalue problem for 2 by 2 matrices:

$$\lambda^2 \begin{bmatrix} c_1 \\ c_4 \end{bmatrix} = MM^\dagger \begin{bmatrix} c_1 \\ c_4 \end{bmatrix} \tag{6.5a}$$

$$\lambda^2 \begin{bmatrix} c_2 \\ c_3 \end{bmatrix} = M^\dagger M \begin{bmatrix} c_2 \\ c_3 \end{bmatrix} \tag{6.5b}$$

where $MM^\dagger$ and $M^\dagger M$ are explicitly given in the following:

$$MM^\dagger = \begin{bmatrix} 2\Omega_{uv}^2 & (\alpha+\beta)\Omega_{uv}\Omega_{ir} \\ (\alpha^*+\beta^*)\Omega_{uv}\Omega_{ir} & 2\Omega_{ir}^2 \end{bmatrix} \tag{6.6a}$$

$$M^\dagger M = \begin{bmatrix} \Omega_{uv}^2+\Omega_{ir}^2 & \alpha\Omega_{uv}^2+\beta\Omega_{ir}^2 \\ \alpha^*\Omega_{uv}^2+\beta^*\Omega_{ir}^2 & \Omega_{uv}^2+\Omega_{ir}^2 \end{bmatrix} \tag{6.6b}$$

Clearly $MM^\dagger$ and $M^\dagger M$ have the same eigenvalues and they are all positive. From the form of $MM^\dagger$ we see that the value of $\alpha+\beta$ determines how much c_1 and c_4 are mixed in the adiabatic states. Let us revisit the two extreme conditions. When α and β are π out of phase: $\alpha+\beta=0$, there is no mixing at all between c_1 and c_4 components, and this case can be viewed as total destructive interference. When α and β are in phase $\alpha=\beta$, the mixing is maximum, and the population transfer rate to the final level $|4\rangle$ is the highest during the time evolution. This can be viewed as constructive interference.

Generally, we can set the criteria for judging how good the excitation is to be the time averaged value of the population in the final level $|4\rangle$, if we assume at the beginning all population is in the ground state $|1\rangle$. Then we ought to look into the time evolution described by (6.3). Like in the case of a simple two level atom, the time evolution can be found from the adiabatic states of the Hamiltonian in (6.3). Different adiabatic states' time evolutions are different in the sense that they oscillate at different frequencies corresponding to their separate adiabatic energies. As a consequence of taking the time average, those detailed frequencies of the adiabatic states average out. The time averaged value of the population in the final level $|4\rangle$ is determined by how much population is in the c_4 component of the adiabatic states when the light is turned on when the initial wave function (all population in the ground state $|1\rangle$, bare state) is projected onto the adiabatic states. Roughly speaking, we are to evaluate how much mixing the lasers induce between $|1\rangle$ and $|4\rangle$ in the adiabatic states.

Let us denote the two eigenvalues of $MM^\dagger$ as $\lambda_{MM^\dagger,1}$ and $\lambda_{MM^\dagger,2}$. The mixing depends on the difference $|\lambda_{MM^\dagger,1} - \lambda_{MM^\dagger,2}|$ as in the following equation. The closer $\lambda_{MM^\dagger,1}$ and $\lambda_{MM^\dagger,2}$ comes together, the larger the mixing is.

$$(\lambda_{MM^\dagger,1} - \lambda_{MM^\dagger,2})^2 = 4(\Omega_{uv}^2 + \Omega_{ir}^2)^2 - 8(1 - \mathrm{Re}(\alpha^*\beta))\Omega_{uv}^2\Omega_{ir}^2 \tag{6.7}$$

Pictorially, the phase differences in the transition amplitudes (in terms of the Rabi frequencies) induced by the different linear polarizations manifest themselves in the excitation process which very much looks like an interference pattern. From this point of view Fig.6.2 is just a two slit interferometer experiment, whose paths' phases are determined by the 'total sum' of the two lasers' polarizations. Therefore, this effect, non-rigorously speaking, is one example of an interferometer built inside an atom.

The discussion above does not include the effect of spontaneous emission. If the intermediate levels $|2\rangle$ and $|3\rangle$ have spontaneous emission channels to decay back to the ground level $|1\rangle$, the basic properties of the above analysis still hold. The reason is that the more chance the atom has at lying at the final excited state $|4\rangle$, the less chance it stays at the intermediate levels and makes a decay. For the general cases including the spontaneous emission, the density matrix approach is needed. The overall observation is that the picture of the interference holds.

6.1.2 Time Dependent Rabi Frequencies

Now consider the case where the uv and ir lasers are pulsed and in the STIRAP configuration. The result of a numerical study is shown in Fig. 6.6.

As explained previously, when the polarizations of the two lasers are not parallel to each other, the STIRAP adiabatic state of the usual sense, which establishes a direct connection between the ground state and the final state, ceases to exist. However, each adiabatic state of H_4 in (6.3) is still going to evolve adiabatically in time, provided the laser pulses satisfy the STIRAP condition as we have assumed.

There are some differences. All four adiabatic states will inevitably have populations in the intermediate levels $|2\rangle$ and $|3\rangle$ during the adiabatic evolution. There is no null adiabatic state whose adiabatic light shift is zero all the time, as can be seen from the fact that the determinant of H_4 is not zero if $\Omega_{uv}, \Omega_{ir} \neq 0$. This is different from the three level case that produces CPT and EIT. Therefore, during the course of the adiabatic evolution, those adiabatic states will develop a non-zero phase different from each other. When in the end those two adiabatic states recombine their wave function at $|4\rangle$, the accumulated phases result in interference.

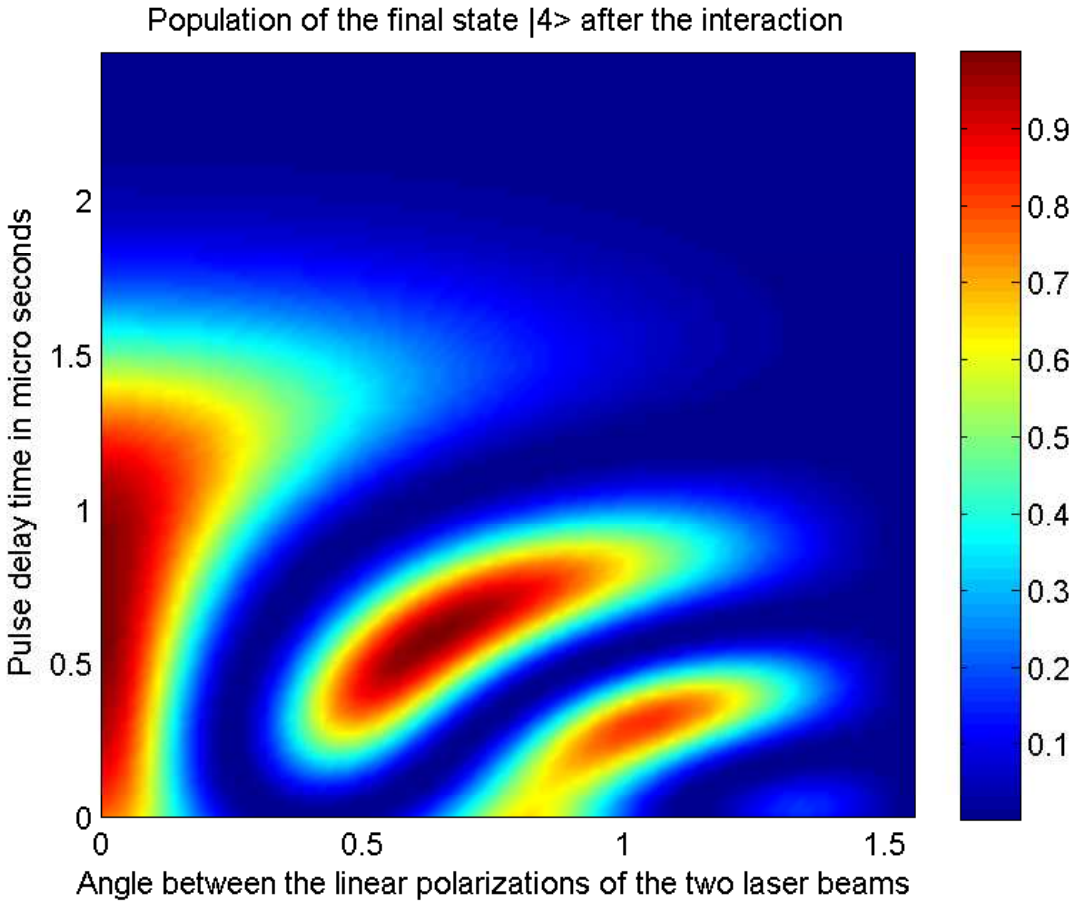

Figure 6.6: The numerical simulation for the diamond system of Fig. 6.2 when the two laser pulses are in the STIRAP configuration. Both the lasers are set to be on resonance, the ir laser pulse is ahead of the uv laser pulse with pulse width 2 μs, and the peak Rabi frequencies are 3.4 MHz. The unit of the angle is in terms of rad. This simulation shows how the population of the final state $|4\rangle$ changes as the relative directions of the polarizations of the lasers and the relative pulse delay time vary. Spontaneous emission is not considered in this simulation.

More specifically, according to the analysis given by (6.4) and (6.6), the four adiabatic states that H_4 allows have adiabatic energies $\pm\lambda_1$ and $\pm\lambda_2$, where $\lambda_1 = \sqrt{\lambda_{MM^\dagger,1}}$ and $\lambda_2 = \sqrt{\lambda_{MM^\dagger,2}}$. And when subject to a pair of pulses in the STIRAP configuration, the time evolution of the adiabatic states can be summarized as in Fig. 6.7.

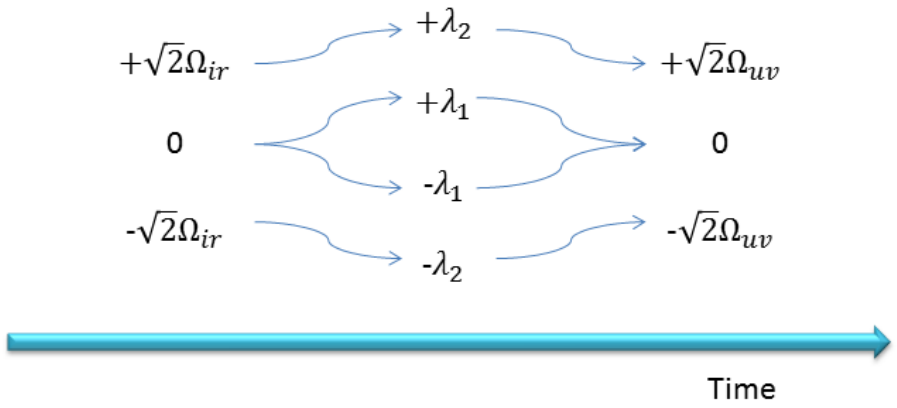

Figure 6.7: A pictorial demonstration of the time evolution of the adiabatic states, labeled by their adiabatic energies, when a diamond system whose linkage pattern is given by Fig. 6.2 is subject to laser pulses Ω_{uv} and Ω_{ir} in STIRAP configuration. Adiabatic states are represented by their adiabatic energies which are changing with time. Here the interference is taking place between the two intermediate adiabatic states.

The adiabatic states carrying population in the final level $|4\rangle$ are the two with adiabatic energies $+\lambda_1(t)$ and $-\lambda_1(t)$ as shown in Fig. 6.7. At the beginning and in the end, they are degenerate at the adiabatic state with adiabatic energy 0. Everything seems to be just as usual, except for the fact that during the time evolution they accumulate different phases. These two adiabatic states all end up as a pure $|4\rangle$ in the end of the time evolution. When the two adiabatic states finally recombine their wave function at $|4\rangle$, this phase difference results in interference, namely, $\exp(+i\int dt\lambda_1) + \exp(-i\int dt\lambda_1) = 2\cos(\int dt\lambda_1)$. The phase difference $\int dt\lambda_1$ is the reason of the strip pattern in Fig. 6.6. Loosely speaking, the change of the pulse delay time is equivalent to the change of effective Rabi frequency, and the change of the polarizations affect how much of the effective Rabi frequency is directed to λ_1. Numerical study is capable of revealing the details so we won't go further in the analytical aspect for now.

6.2 The 11 State System

The transition we drive in our STIRAP experiment is $2^3S_1 \rightarrow 3^3P_2 \rightarrow n^3S_1$, and hence its linkage pattern contains more than a diamond structure. Without spontaneous emission, the linkage pattern can be summarized as in Fig. 6.8.

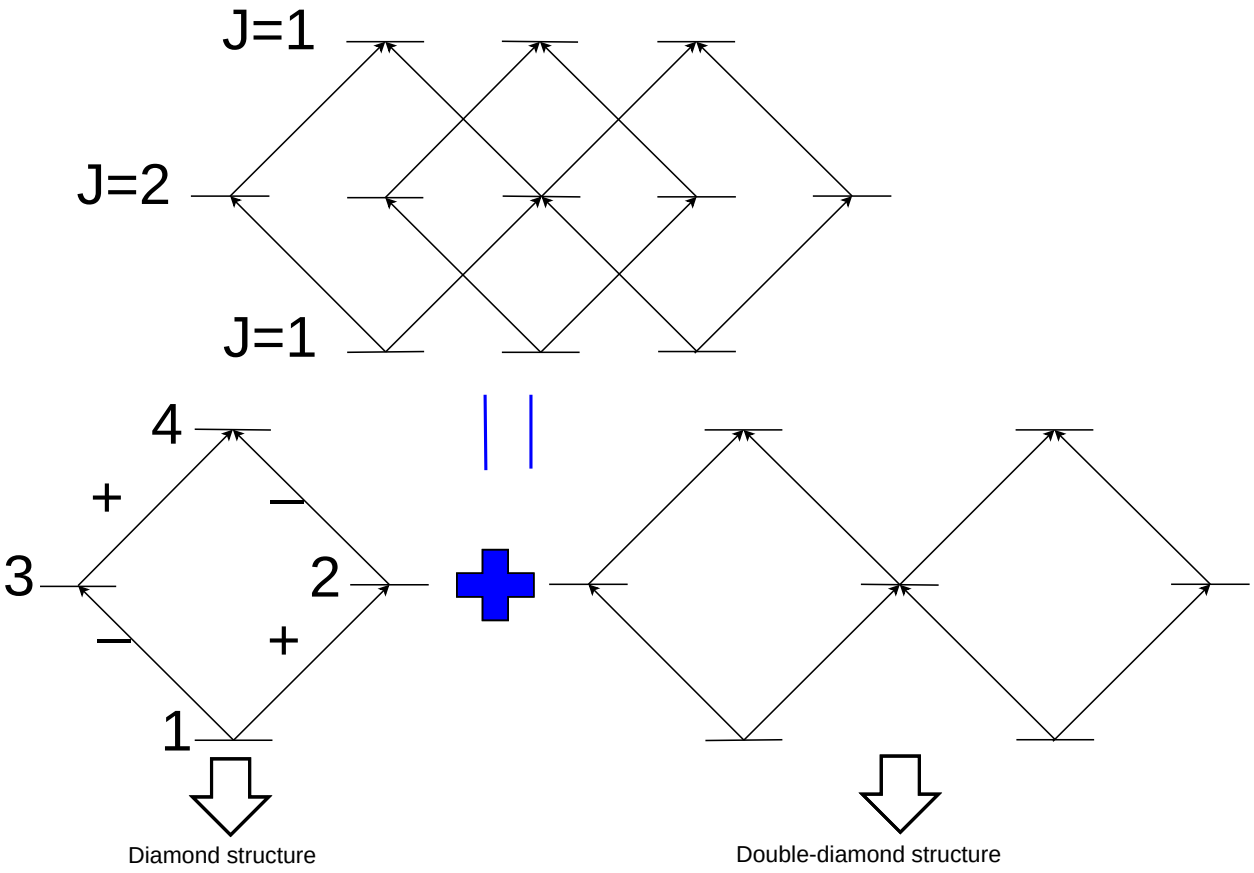

Figure 6.8: The level scheme and detailed linkage pattern of the 11 state system of the STIRAP transition $2^3S_1 \rightarrow 3^3P_2 \rightarrow n^3S_1$. It contains two independent subsystems, one diamond structure and one double-diamond structure.

We have already discussed how the lasers' polarizations affect the diamond structure in the previous section. Similar path interference effects also exist in the double-diamond structure in Fig. 6.8, induced again by the polarizations. Because the number of the intermediate

states is more than that of the ground and the final, there is no Morris-Shore transformation capable of separating the double-diamond structure into independent uncoupled pure three level subsystems.

The result of a numerical study on the transition $2^3S_1 \rightarrow 3^3P_2 \rightarrow n^3S_1$ including all of the magnetic sublevels is shown in Fig. 6.9.

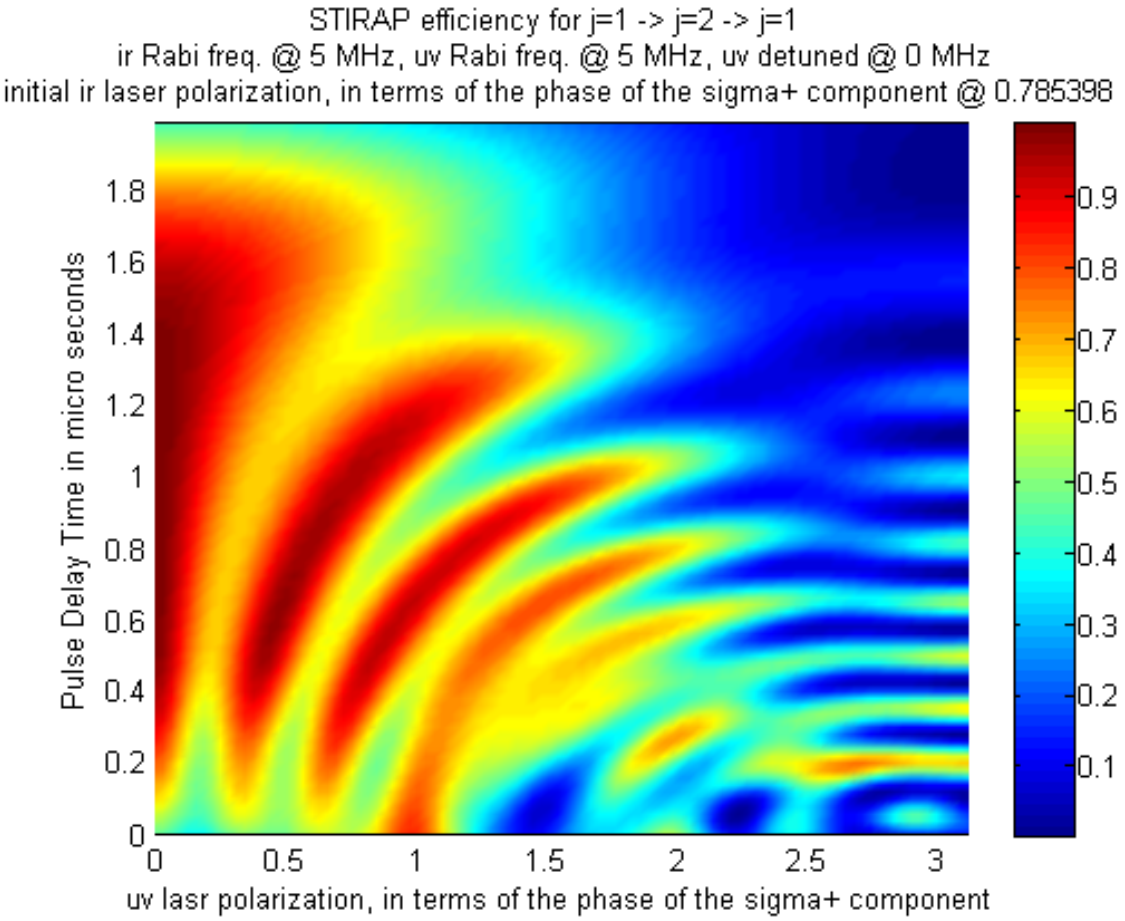

Figure 6.9: The numerical simulation for the transition $2^3S_1 \rightarrow 3^3P_2 \rightarrow n^3S_1$ of Fig. 6.8 when the two laser pulses are in the STIRAP configuration. Both the lasers are set to be on resonance, the ir laser pulse is ahead of the uv laser pulse with pulse width 2μs, and the peak Rabi frequencies are 5 MHz. This simulation shows how the population of the final state $|4\rangle$ changes as the relative directions of the polarizations of the lasers and the relative pulse delay time vary. Spontaneous emission is not considered in this simulation.

The interference pattern in Fig. 6.9 is a direct result of the path interference induced by the different phases accumulated through paths, induced by the polarization differences in the excitation lasers. It is obvious that the different polarizations lead to different excited state population. It might seem a little confusing why the pattern has to do with the pulse delay time. The different pulse delay times lead to different effective Rabi frequencies during the given time period of interaction, which in the end change the total accumulated phases of the paths, as illustrated in Fig. 6.7.

6.2.1 Detuning and Spontaneous Emission

The interference patterns in Fig. 6.6 and Fig. 6.9 require that all the quantum levels in the system remain highly coherent all the time during the interaction. However, in the experiment, these conditions could not be satisfied because of the existence of the spontaneous emission of the intermediate state(s), the one photon detuning, and the two photon detuning, as a result of the transverse velocity spread (which is also discussed in Chapter 5).

Effectively, the consequence of the spontaneous emission is to wash out the details of the interference patterns, because the adiabatic states containing the intermediate state(s) are subject to decay and can no longer faithfully remember the phase of the path. The experimental parameters we have for the Rabi frequencies and the interaction time are not capable of resisting the spontaneous emission of the intermediate state(s).

Therefore, the experimental results we are expecting is sketched in Fig. 6.10, for the case of one–photon detuning (i.e. the energy conservation criteria is still fulfilled). This implies that it is hard to pursue the very interesting interference patterns in Fig. 6.9 by varying the pulse delay. Therefore the experimental effort would only be put towards the direction to manifest the path interference induced by the polarizations, in some sense as a conceptual

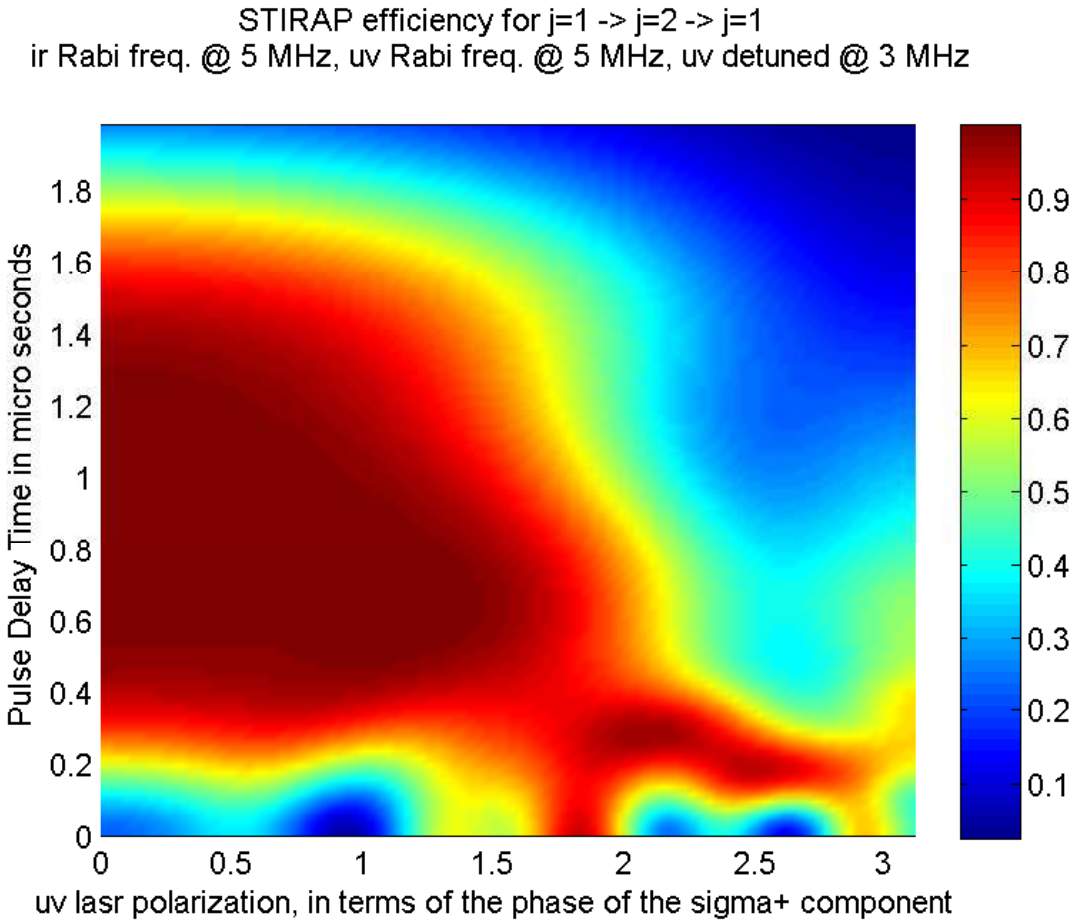

Figure 6.10: The numerical simulation for the transition $2^3S_1 \rightarrow 3^3P_2 \rightarrow n^3S_1$ of Fig.6.8 when the two laser pulses are in the STIRAP configuration, but have one–photon detuning. This simulation shows how the population of the final state $|4\rangle$ changes as the relative directions of the polarizations of the lasers and the relative pulse delay time vary. Spontaneous emission is not considered in this simulation, however the effect of spontaneous emission on the path interference of STIRAP is similar.

test.

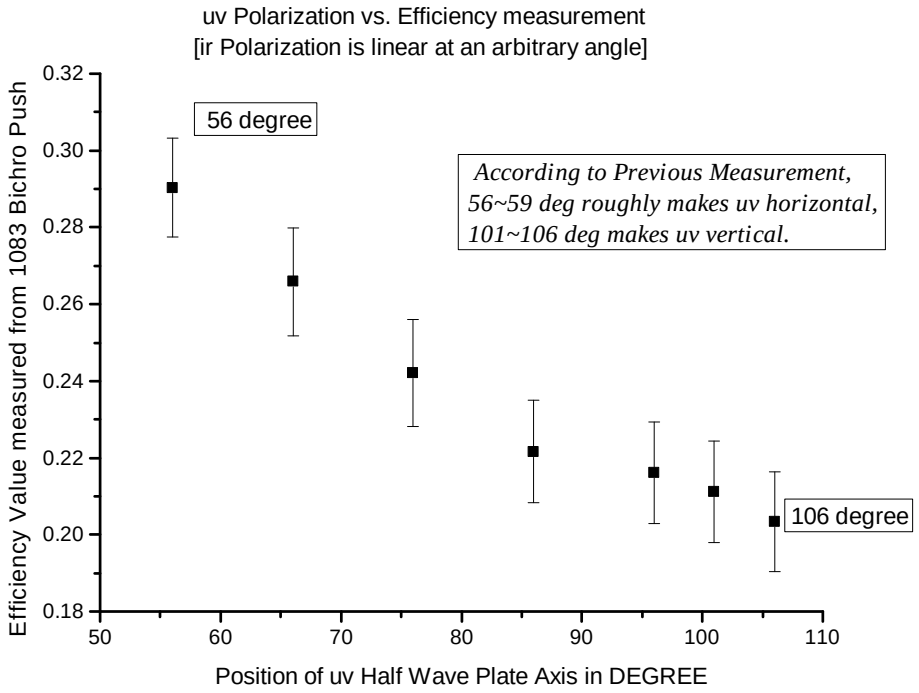

Figure 6.11: Result of the polarization induced path interference corresponding to the scheme shown in Fig. 6.8. The associated transitions are $2^3S_1 \rightarrow 3^3P_2 \rightarrow n^3S_1$. The uv and ir lasers are kept in STIRAP configuration, the uv laser frequency is locked to the $2^3S_1 \rightarrow 3^3P_2$ transition, while the ir laser frequency is scanned. The polarizations of both of the lasers are kept linear. This is the raw efficiency data directly from the absolute measurement, which has not been modified for the decay and other compromising effects, including the transverse velocity spread. The position of the uv half wave plate is expressed in terms of the angle between its fast axis and the vertical direction.

6.3 Preliminary Experimental Results

For an optical interferometer, we usually measure the light intensity as the signal. Here, the consequence of the interference is how much of the atom wave function ends up in the final excited state (the Rydberg level). Therefore we are going to detect the population in the Rydberg state(s) as the signal. We have two methods of doing this, the first one is to detect the ion signal induced by the black body radiation from the Rydberg atoms (see also

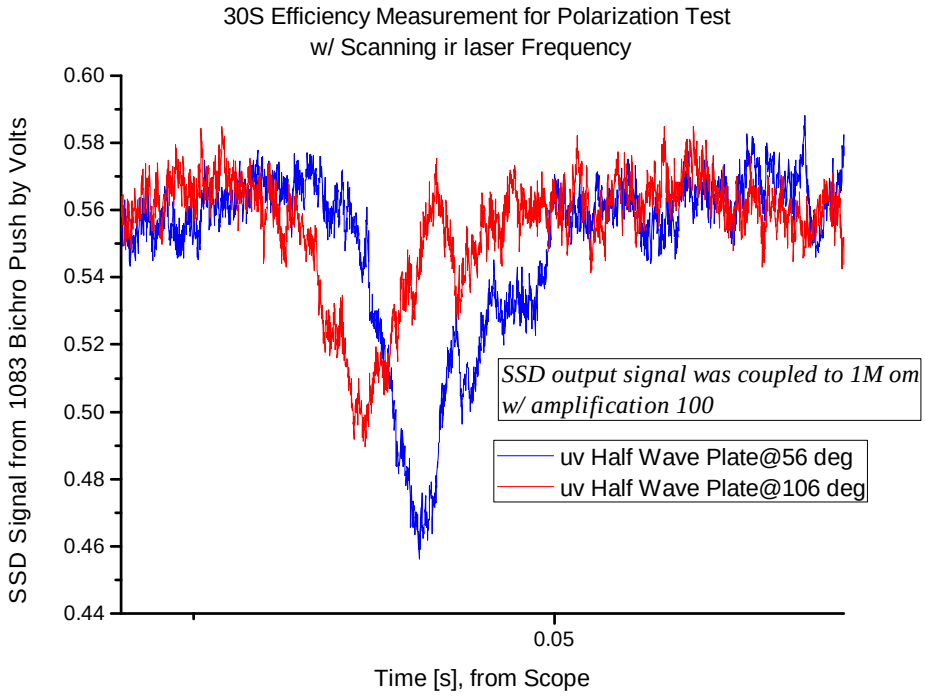

Figure 6.12: The SSD efficiency measurement signals for the most constructive and most destructive cases in Fig. 6.11. The traces are both directly recorded from the oscilloscope when the ir laser frequency is scanned, with a time triggering signal. This signal represents the metastable atoms that get pushed over to the SSD. The fact that less atoms pushed means that more atoms are staying in the Rydberg state. Therefore the deeper the dip is, the more Rydberg atoms are produced.

Chapter 4), and the second one is to physically separate the metastable ground state atoms and the Rydberg atoms by applying the bichromatic force via the 1083 nm laser to establish an absolute measurement for the efficiency (see also Chapter 5).

In the ideal scenario the signals of the two different methods shall be proportional to each other, so we regard the difference between those two methods only as technical. We have experimentally observed repeatedly that within a good error margin the ion signal and the efficiency signal are proportional. However, the proportionality constant is different for different Rydberg states, since it is mostly determined by the ionization rates.

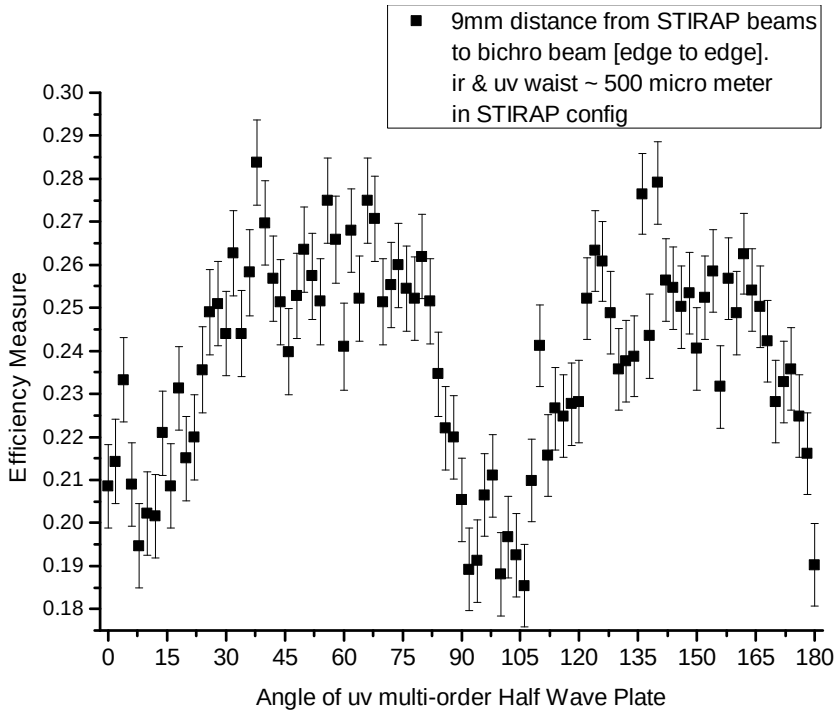

Figure 6.13: Result of the STIRAP efficiency vs. uv laser polarization indicating polarization induced path interference, corresponding to the scheme shown in Fig. 6.8. The associated transitions are $2^3S_1 \rightarrow 3^3P_2 \rightarrow n^3S_1$. The uv and ir lasers are kept in STIRAP configuration, the uv laser frequency is locked to the $2^3S_1 \rightarrow 3^3P_2$ transition, while the ir laser frequency is scanned. The polarizations of both of the lasers are kept linear. This is the raw efficiency data directly from the absolute measurement.

The result of a typical STIRAP experiment with polarization induced path interference is shown in Fig. 6.11, which corresponds to the situation of Fig. 6.8. The polarization of the ir laser is fixed, while the angle of the linear polarization of the uv laser is gradually scanned. It shows that the interference takes place as the population in the final Rydberg state (in this case, $30S$) varies while the angle of the uv polarization changes.

Another interesting interpretation (and a possible application) of Fig. 6.11 is that with the help of this interferometer built inside an atom, we can find the angle of some unknown linear polarization of the ir laser by scanning the uv laser polarization to find the constructive

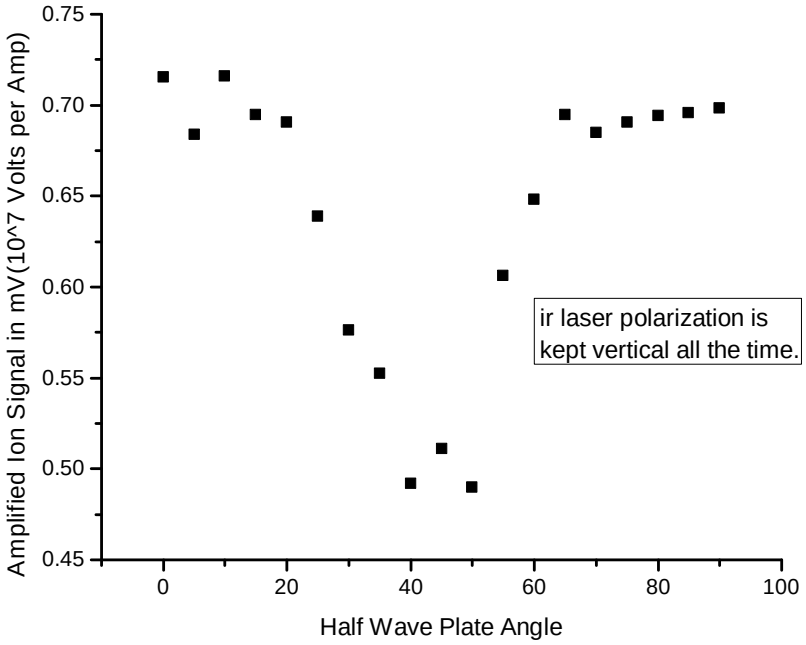

Figure 6.14: Result of the STIRAP's Rydberg ion signal vs. uv laser polarization indicating polarization induced path interference, corresponding to the scheme shown in Fig. 6.8. The associated transitions are $2^3S_1 \rightarrow 3^3P_2 \rightarrow n^3S_1$. The uv and ir lasers are kept in STIRAP configuration, the uv laser frequency is locked to the $2^3S_1 \rightarrow 3^3P_2$ transition, while the ir laser frequency is scanned. The ion signal is collected with no external electric field, by the ion detector right above the interaction region through the holes in the upper field plate. The source of the ionization is the black body radiation at room temperature. The error bar is smaller than the marker hence omitted.

interfering point. In Fig. 6.11 we can claim that the polarization of the ir laser is along the direction of the uv laser with the half wave plate turned at 56 degrees.

To clearly demonstrate the difference between the constructive interference and the destructive interference cases, we put the SSD signals of these two cases from Fig. 6.11 together into Fig. 6.12.

Next we can fix the polarization of the ir laser and perform a finer scan of the uv laser polarization to reveal the details in the interference pattern. The outcome is summarized in

Fig.6.13.

As discussed in the beginning of this section, we can also measure this interference effect with the ion signal. The advantage of the ion signal is that the signal to noise ratio is better than that of the absolute efficiency measurement. The result is shown in Fig. 6.14.

6.3.1 Change the Path Structure by Optical Pumping

In the efforts towards determining the effect of transverse velocity spread on the STIRAP efficiency, we put a one dimensional optical molasses laser beam of 1083 nm driving the $2^3S_1 \rightarrow 2^3P_2$ transition immediately before the STIRAP lasers. This 1083 nm laser beam is parallel to the STIRAP laser beams and has a waist more than 5 mm. If we set the 1083 nm laser to be circularly polarized, then we can optically pump all the population of the atoms to one of the magnetic sublevels. This will change the structure the path interference induced by the polarizations. Details of the linkage pattern are shown in Fig. 6.15.

To explore the polarization induced path interference effects in this setting, we perform the same measurement of STIRAP efficiency as a function of the uv laser polarization when the linear polarization of the ir laser is fixed, similar to what we have done in Fig. 6.13. The result of this measurement is also shown in Fig. 6.15.

According to the linkage pattern shown in Fig. 6.15, ideally the population difference between the constructive and destructive interference cases shall be half of the total. This can be seen from the following simple reasoning. Half of the population of $|1\rangle$ goes to $|2\rangle$ and the other half goes to $|3\rangle$. Among the population in $|2\rangle$, half goes to $|5\rangle$ and the other half goes to $|4\rangle$ and participates in the interference. In the end, a quarter of the population in the path through $|2\rangle$ and another quarter through $|3\rangle$ interfere – namely, half of the total population is subject to interference while the other half stays there forever. The fact that

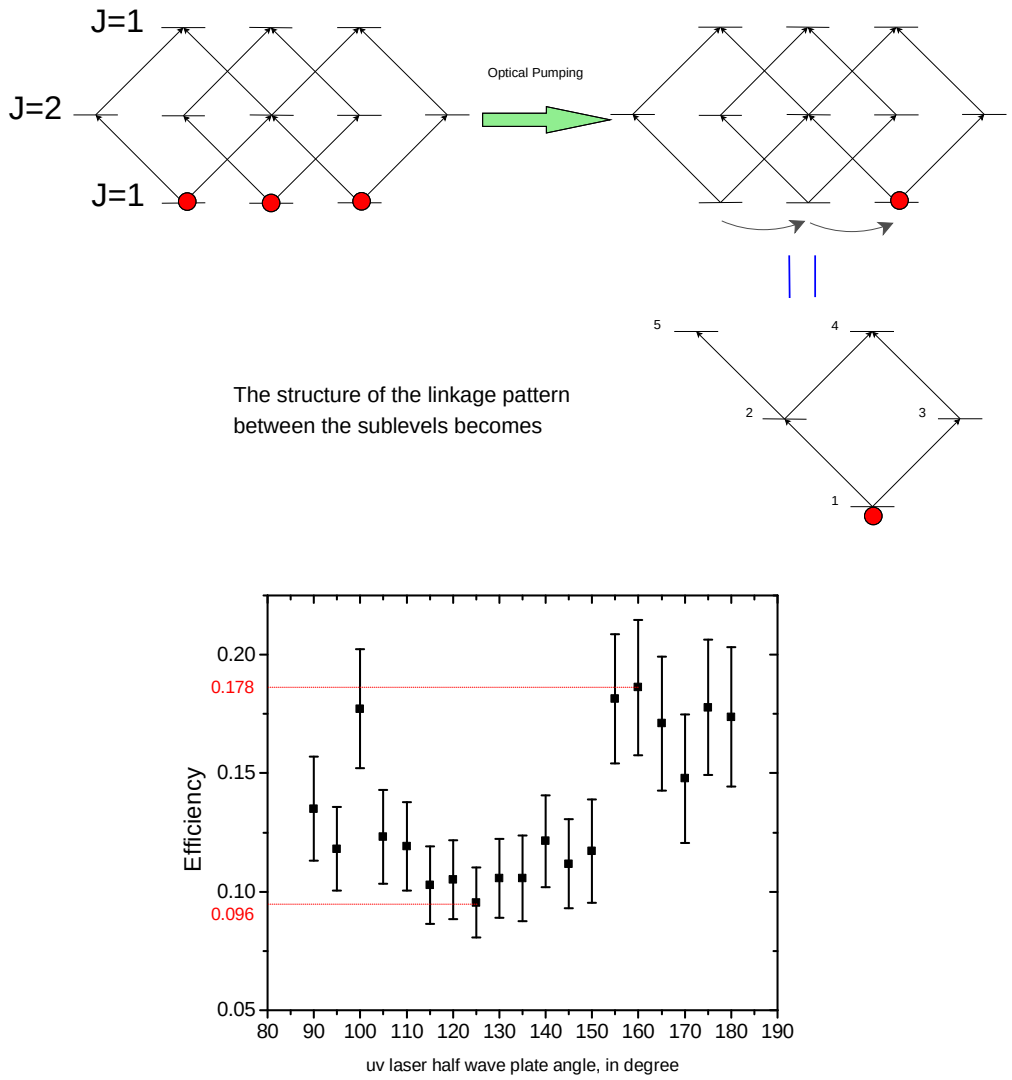

Figure 6.15: Top: the linkage pattern of the magnetic sublevels when the atom is suject to optical pumping of the 1083 nm laser first. Bottom: the measured efficiency vs. uv laser half wave plate angle.

STIRAP is taking place certainly complicates this simple reasoning a bit. Yet, the maximum and minimum efficiency of Fig. 6.15 are 0.178 and 0.096 separately, fairly close to this naive analysis.

6.4 Another Type of EIT?

EIT (Electromagnetically induced transparency) usually occurs in a pure three level system, with the experimental signature that a medium's absorption of light drops to zero over a narrow spectral range within an absorption line (see also the discussions in the end of section 7.1).

Of particular interest in EIT is the dispersion relation in the range of the transparency window, which has important consequences such as slow light. The question we want to ask here is, whether we have an analogue of EIT in the case of the path interferences?

Therefore let us switch gears for now and check what happens to the light after it drives the path interference in the atom. We start with the situation of cw light.

Once the polarizations of the uv and ir lasers are not parallel, the EIT of the traditional sense ceases to exist because there is no longer such a dark state, which is in essence the same situation as the non-existence of the usual STIRAP adiabatic state, as is in the discussion following Fig. 6.5.

When the polarizations of the uv and ir lasers are orthogonal to each other, the atom becomes transparent to the ir laser, although the ir laser's frequency is on resonance of the transition. This certainly reminds us of EIT, however, the transparency window here by the polarization path interference bears no dispersion for the propagation of the ir light, which is very different from EIT.

What happens to the ir light if its polarization is at some angle to the polarization of the uv light, which is not necessarily orthogonal? One such situation is shown in Fig. 6.16.

If the spontaneous decay rates of the intermediate levels $|2\rangle$ and $|3\rangle$, and the final level $|4\rangle$ are high compared to the Rabi frequencies of the lasers driving them, within the time that the atomic wave function is still coherent, we may regard the atomic wave function $|\varphi\rangle$ in $|2\rangle$

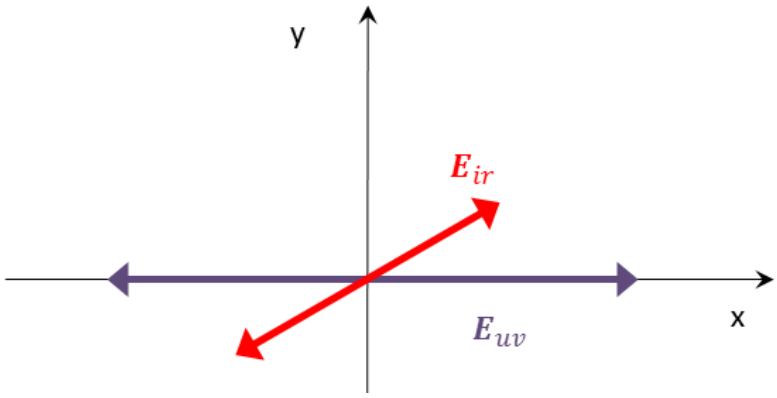

Figure 6.16: An illustration of lasers' polarizations.

and $|3\rangle$ as in (6.8) up to the lowest order. In the situation of (6.8), the component of the ir laser whose polarization is orthogonal to that of the uv laser drives no dipole transition at all hence it won't be absorbed by the atom. On the other hand, the component of the ir laser whose polarization is parallel to that of the uv laser does drive a transition and therefore will get absorbed. This very intuitive discussion does not consider the effect of EIT for the moment.

$$\begin{bmatrix} \langle 2|\varphi\rangle \\ \langle 3|\varphi\rangle \end{bmatrix} = -i \begin{bmatrix} \Omega_{uv}t \\ \alpha^*\Omega_{uv}t \end{bmatrix} \tag{6.8}$$

Therefore, an ensemble of atoms with the diamond energy structure can act as a polarizer for the ir laser. Even more interesting, which polarization component of the ir laser gets transmitted is controlled by the polarization of the uv laser. This is a highly non-linear interaction between the two lasers via the atom medium, and can serve as an optically controlled polarizer and/or all optical transistor.

Let us look a little bit further into the details, and check the induced dipole moment by the orthogonal and parallel component (with respect to the polarization of the uv laser,

the x-axis in Fig. 6.16) of the ir laser separately: $\langle\varphi|\hat{D}_\perp|\varphi\rangle$ and $\langle\varphi|\hat{D}_\parallel|\varphi\rangle$. For the current purpose, it is enough to investigate $\langle\varphi(|2\rangle\langle 2|+|3\rangle\langle 3|)\hat{D}_\perp|4\rangle\langle 4|\varphi\rangle$ for $\langle\varphi|\hat{D}_\perp|\varphi\rangle$ and the similar for $\langle\varphi|\hat{D}_\parallel|\varphi\rangle$.

Without loss of generality, suppose $\alpha = 1$. The four adiabatic states have the adiabatic energies $\pm\lambda_1$ and $\pm\lambda_2$ separately. The adiabatic states are listed in the following (6.9).

$$+\lambda_1 \sim \begin{bmatrix} x_1 \\ z_1 \\ w_1 \\ y_1 \end{bmatrix}, -\lambda_1 \sim \begin{bmatrix} x_1 \\ -z_1 \\ -w_1 \\ y_1 \end{bmatrix}, +\lambda_2 \sim \begin{bmatrix} x_2 \\ z_2 \\ w_2 \\ y_2 \end{bmatrix}, -\lambda_2 \sim \begin{bmatrix} x_2 \\ -z_2 \\ -w_2 \\ y_2 \end{bmatrix} \tag{6.9}$$

And further assume that at the beginning the atomic wave function all lies in $|1\rangle$, and its projection onto the adiabatic states associated with $\pm\lambda_1$ is a_1 while its projection onto the adiabatic states associated with $\pm\lambda_2$ is a_2. The initial conditions also impose a relation specified in (6.10). It is now enough to investigate $\langle 2|\varphi\rangle - \langle 3|\varphi\rangle$, $\langle 2|\varphi\rangle + \langle 3|\varphi\rangle$ and $\langle 4|\varphi\rangle$.

$$a_1 x_1 + a_2 x_2 = \frac{1}{2} \tag{6.10a}$$

$$a_1 y_1 + a_2 y_2 = 0 \tag{6.10b}$$

$\langle 2|\varphi\rangle - \langle 3|\varphi\rangle$ corresponds to the contribution of the orthogonal polarization component of the ir light, while $\langle 2|\varphi\rangle + \langle 3|\varphi\rangle$ corresponds to the contribution of the parallel polarization component of the ir light. Now it is the time to write them down. $\langle 2|\varphi\rangle - \langle 3|\varphi\rangle$ is:

$$a_1(\beta-1)\Omega_{ir}\frac{y_1}{\lambda_1}\cdot 2i\sin\lambda_1 t + a_2(\beta-1)\Omega_{ir}\frac{y_2}{\lambda_2}\cdot 2i\sin\lambda_2 t \tag{6.11}$$

$\langle 2|\varphi\rangle + \langle 3|\varphi\rangle$ is:

$$a_1\{2\Omega_{uv}\frac{x_1}{\lambda_1} + (\beta+1)\Omega_{ir}\frac{y_1}{\lambda_1}\}\cdot 2i\sin\lambda_1 t + a_2\{2\Omega_{uv}\frac{x_2}{\lambda_2} + (\beta+1)\Omega_{ir}\frac{y_2}{\lambda_2}\}\cdot 2i\sin\lambda_2 t \qquad (6.12)$$

And the wave function in the level $|4\rangle$, $\langle 4|\varphi\rangle$ is:

$$a_1 y_1\cdot 2\cos\lambda_1 t + a_2 y_2\cdot 2\cos\lambda_2 t \qquad (6.13)$$

To simply the discussion, we assume that $\Omega_{ir} \ll \Omega_{uv}$. Then $\lambda_2 \approx \sqrt{2}\Omega_{uv}$ while $\lambda_1 \approx \sqrt{2}\Omega_{ir}$. An immediate observation is that $\|\langle 2|\varphi\rangle - \langle 3|\varphi\rangle\| \ll \|\langle 2|\varphi\rangle + \langle 3|\varphi\rangle\|$. Namely, the absorption of the orthogonal polarization component of the ir laser is much smaller than that of the parallel component.

Imagine a scenario where the ir laser is propagating in the medium of such atoms while the strong uv laser is pumping. Then $|a_1 y_1|$ and $|a_2 y_2|$ terms are all approximately $\frac{\Omega_2}{2\Omega_1}(1+\beta^*)$. As the light travels further and further, the parallel polarization component gets absorbed so much more that β is closer to 1, and this in turn makes the absorption in the orthogonal polarization component even smaller. Therefore, this medium is then a good absorber or scatter for the ir laser's polarization component which is parallel to that of the uv laser, but transparent to the ir laser's polarization component which is orthogonal to that of the uv laser.

If the ir laser is pulsed, then its parallel polarization component will be in the transparency window opened up by the EIT hence becomes slow. Its orthogonal polarization component, on the other hand, doe not have to do with EIT therefore remains propagation at the speed of light while keeping its transparency for path interference reasons. Then the medium, pumped by the uv laser, effectively acts as a polarization beam splitter.

Chapter 7

Other Spectroscopic Effects Associated with STIRAP

7.1 Autler Townes Effect

The Autler Townes effect was named the AC Stark effect [84] when it was first observed in 1955, since the experiment was conducted by an rf field, before the laser era. Later when people had the ability to address each single quantum level of atoms precisely, thanks to the laser, the concept of the Autler Townes effect has been brought up again and again. The Autler Townes effect typically appears as a splitting in the spectrum of the probe, hence it is sometimes called Autler Townes splitting as well.

The basic picture consists of 3 quantum levels: $|1\rangle$, $|2\rangle$ and $|3\rangle$ and two laser fields, with the transition $|1\rangle$ to $|2\rangle$ driven by the pump field, and the transition $|2\rangle$ to $|3\rangle$ driven by the Stokes field. Usually the transition strength induced by the Stokes field is weaker than that of the pump field.

Suppose that both of the laser fields are cw in time, and that the pump field is exactly

on resonance, let us write down the equation of motion for this three level system, under the commonly used rotating wave approximation:

$$i\frac{d}{dt}\begin{pmatrix} C_1(t) \\ C_2(t) \\ C_3(t) \end{pmatrix} = \begin{pmatrix} 0 & \frac{1}{2}\Omega_p & 0 \\ \frac{1}{2}\Omega_p & 0 & \frac{1}{2}\Omega_S \\ 0 & \frac{1}{2}\Omega_S & \Delta \end{pmatrix} \cdot \begin{pmatrix} C_1(t) \\ C_2(t) \\ C_3(t) \end{pmatrix} \tag{7.1}$$

where $C_j(t), j = 1, 2, 3$ denotes the probability wavefunction of the three levels, Ω's denote the Rabi frequency of the laser fields, and Δ denotes the detuning of the Stokes laser field. The pump laser is set to be on resonance of the corresponding transition all the time.

Let us treat this problem by perturbation theory. Decompose the Hamiltonian in (7.1) like the following:

$$\begin{pmatrix} 0 & \frac{1}{2}\Omega_p & 0 \\ \frac{1}{2}\Omega_p & 0 & \frac{1}{2}\Omega_S \\ 0 & \frac{1}{2}\Omega_S & \Delta \end{pmatrix} = \underbrace{\begin{pmatrix} 0 & \frac{1}{2}\Omega_p & 0 \\ \frac{1}{2}\Omega_p & 0 & 0 \\ 0 & 0 & \Delta \end{pmatrix}}_{H_0} + \underbrace{\begin{pmatrix} 0 & 0 & 0 \\ 0 & 0 & \frac{1}{2}\Omega_S \\ 0 & \frac{1}{2}\Omega_S & 0 \end{pmatrix}}_{H_1} \tag{7.2}$$

where H_0 is the unperturbed part and H_1 is the perturbation.

For H_0, the three unnormalized eigenstates are:

$$a_1 = \begin{pmatrix} 1 \\ 1 \\ 0 \end{pmatrix}, a_2 = \begin{pmatrix} 1 \\ -1 \\ 0 \end{pmatrix}, a_3 = \begin{pmatrix} 0 \\ 0 \\ 1 \end{pmatrix} \tag{7.3}$$

with eigenvalues $\frac{1}{2}\Omega_p$, $-\frac{1}{2}\Omega_p$ and Δ respectively.

Let us first try time-independent perturbation theory and find the perturbed energy eigenstates. By adding a perturbation term to the eigenstates and the eigenvalues, we can

get the solutions on the order of $O(\frac{\Omega_S}{\Omega_p})$, with eigenstates being:

$$\begin{pmatrix} 1 \\ 1 \\ \frac{\frac{1}{2}\Omega_S}{\frac{1}{2}\Omega_p - \Delta} \end{pmatrix}, \begin{pmatrix} 1 \\ -1 \\ \frac{\frac{1}{2}\Omega_S}{\frac{1}{2}\Omega_p + \Delta} \end{pmatrix}, \text{and} \begin{pmatrix} \frac{\frac{1}{2}\Omega_p \cdot \frac{1}{2}\Omega_S}{\Delta^2 - (\frac{1}{2}\Omega_p)^2} \\ \frac{\Delta \cdot \frac{1}{2}\Omega_S}{\Delta^2 - (\frac{1}{2}\Omega_p)^2} \\ 1 \end{pmatrix} \tag{7.4}$$

and their energy eigenvalues being $\frac{1}{2}\Omega_p$, $-\frac{1}{2}\Omega_p$ and Δ respectively (the energy eigenvalues do not have any $O(\frac{\Omega_S}{\Omega_p})$ order perturbation correction).

Suppose that at the very beginning the atom is sitting at the ground level $|1\rangle$. From the 3 eigenstates of (7.4) we can deduce the behavior of the time evolution of the system defined by (7.1). We simply project this initial wavefunction, $|1\rangle$, onto the three eigenstates and consider what happens as a function time. Even from a glance, we can see that the system behaves very differently when Δ is near $+/-\frac{1}{2}\Omega_p$ while other values of Δ yield trivial outcomes.

When Δ is around 0, i.e. the lasers appear to be 'on resonance', up to order of $O(\frac{\Omega_S}{\Omega_p})$ the three eigenstates are the same as those in (7.3); the initial wavefunction can only project onto the first two adiabatic states hence the system would only allow the Rabi oscillations between $|1\rangle$ and $|2\rangle$ with very little population, if ever, excited into $|3\rangle$. Instead, when Δ is close to $\frac{1}{2}\Omega_p$, $\frac{1}{2}\Omega_S$ is comparable with $|\frac{1}{2}\Omega_p - \Delta|$, the initial wavefunction $|1\rangle$ would project onto all the 3 adiabatic states. The consequence is that, the time evolution of the system includes the level $|3\rangle$ for this case and the atom wavefunction has a finite chance of entering that level $|3\rangle$.

Finally, when Δ precisely equals $\pm\frac{1}{2}\Omega_p$, the perturbation method leading to (7.4) breaks down, so we need to use degenerate perturbation theory instead. Namely, we choose the energy eigenstates of H_0 that diagonalize the perturbation H_1. The three normalized energy eigenstates are:

$$\begin{pmatrix} \frac{1}{2} \\ \frac{1}{2} \\ \frac{1}{\sqrt{2}} \end{pmatrix}, \begin{pmatrix} \frac{1}{2} \\ \frac{1}{2} \\ -\frac{1}{\sqrt{2}} \end{pmatrix}, \text{and} \begin{pmatrix} \frac{1}{\sqrt{2}} \\ -\frac{1}{\sqrt{2}} \\ 0 \end{pmatrix} \tag{7.5}$$

with energy eigenvalues $\frac{1}{2}\Omega_p + \frac{1}{2}\Omega_S$, $\frac{1}{2}\Omega_p - \frac{1}{2}\Omega_S$ and $-\frac{1}{2}\Omega_p$.

Say again we start with $|1\rangle$. Then half of the population goes to $\begin{pmatrix} \frac{1}{\sqrt{2}} \\ -\frac{1}{\sqrt{2}} \\ 0 \end{pmatrix}$ and is trapped there. Another half of the population goes to the mixture of $\begin{pmatrix} \frac{1}{2} \\ \frac{1}{2} \\ \frac{1}{\sqrt{2}} \end{pmatrix}$ and $\begin{pmatrix} \frac{1}{2} \\ \frac{1}{2} \\ -\frac{1}{\sqrt{2}} \end{pmatrix}$, where it actually goes through a Rabi oscillation between $\begin{pmatrix} \frac{1}{\sqrt{2}} \\ \frac{1}{\sqrt{2}} \\ 0 \end{pmatrix}$ and $\begin{pmatrix} 0 \\ 0 \\ 1 \end{pmatrix}$, with an oscillation Rabi frequency $\frac{1}{2}\Omega_S$. This Rabi oscillation is stronger than the case when Δ is close but not equal to $\frac{1}{2}\Omega_p$, if evaluated by how much of the initial population is involved. The case of $\Delta = -\frac{1}{2}\Omega_p$ is the same.

There is yet another more concise way to look at this problem, via time-dependent perturbation method.

Again we decompose as in (7.2), view H_0, H_1 as principle and perturbation respectively, and have the unperturbed eigenstates as in (7.3). We are interested in the transition probabilities between those eigenstates, especially those transition probabilities into a_3: c_{13} from a_1 to a_3, c_{23} from a_2 to a_3. We compute c_{13} as an example.

According to formula 5.6.22 on page 329 from [85], for the first order perturbation we have:

$$|c_{13}^{(1)}|^2 = \frac{\Omega_{probe}^2}{|\Delta - \frac{1}{2}\Omega_{pump}|^2} \sin^2[\frac{(\Delta - \frac{1}{2}\Omega_{pump})t}{2}] \tag{7.6}$$

It is clear from (7.6) that when Δ varies from 0 to $\frac{1}{2}\Omega_p$ the transition described by $|c_{13}^{(1)}|^2$ would be stronger and stronger. When $\Delta = 0$ this transition is weakest and close to 0. Yet when $\Delta = \frac{1}{2}\Omega_p$, this transition is strongest, yielding that for t small enough, $|c_{13}^{(1)}| = \Omega_S t/2$. The situation of c_{23} is analogous.

If we are detecting either the population in $|3\rangle$ or the absorption of the probe beam, what we get would be a splitting of two peaks, occuring at $\pm\frac{1}{2}\Omega_p$ detunings, over the probe beam spectrum. Hence follows the name Autler Townes splitting.

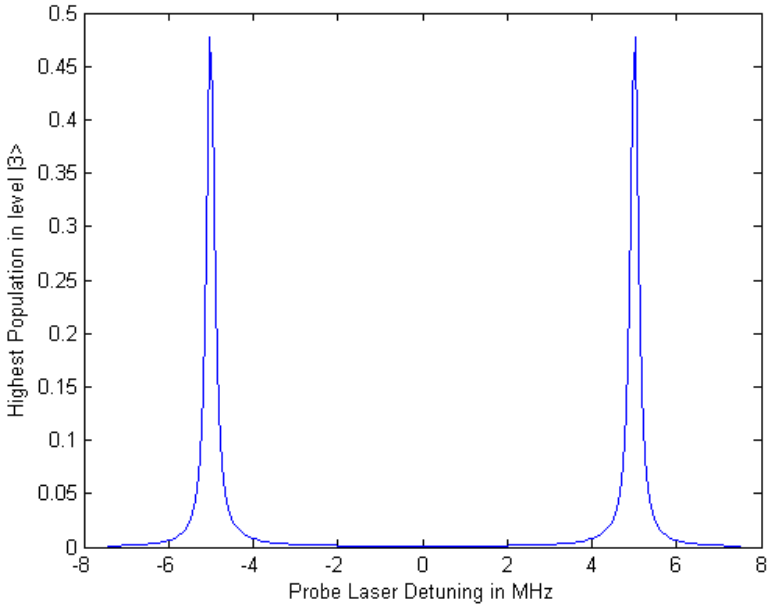

Figure 7.1: Numerical results of Autler-Townes splitting.

To demonstrate this, we put $\Omega_p = 10$ MHz, $\Omega_S = 1$ MHz and then numerically solve (7.1). Then the population in level 3, which is the square of the absolute value of $C_3(t)$, oscillates with time. If we plot the highest value which the population in level 3 ever reaches

versus different values of Δ, which is the probe laser detuning, we get Fig. 7.1.

The width of a single peak in Fig. 7.1 is another point of interest. Roughly speaking, the width or shape reflects the range of Δ which populates level $|3\rangle$ in a non-negligible way. According to the discussion following (7.4), and (7.6), we know that for a non-trivial population in level $|3\rangle$, $|\Delta - \frac{1}{2}\Omega_p|$ needs to be comparable with Ω_S. This is the same as saying the single peak width is approximately $2\Omega_S$. More precisely, depending on your definition of 'width', the width of a single peak here is proportional to Ω_S. This also can be easily shown by numerical methods.

The Autler Townes effect can cause a spectral splitting when the laser pulses are in STIRAP configuration under special conditions, the details, both computational and experimental, would be discussed in the following section.

Spontaneous emission is not necessary for the Autler Townes effect, neither does it have a lot to do with the physics of Autler Townes effect. However, to make the story complete, we will introduce the spontaneous emission into the three level system. In the absorption spectrum the Autler Townes effect can still be observed, as revealed by the numerical simulations in Fig. 7.2, according to the level scheme of Fig. 7.3.

When spontaneous emission is present, other interesting coherent effect can occur, namely, EIT: *Electromagnetically Induced Transparency*. A careful discussion on this topic can be found in Petr's recent article [86]. EIT is quite different from the Autler Townes effect. It mostly focus on the absorption of the probe light with or without the coupling light. And typically the roles of the probe and the pump in EIT are exchanged from that of the Autler Townes effect. For EIT to be observed experimentally, spontaneous emission is necessary in the sense that during the interaction the laser has to be scattered to cause an absorption.

Yet, to include the effect of spontaneous emission, the setup of a wavefunction approach such as (7.1) is incomplete. We are forced to adopt the density matrix approach.

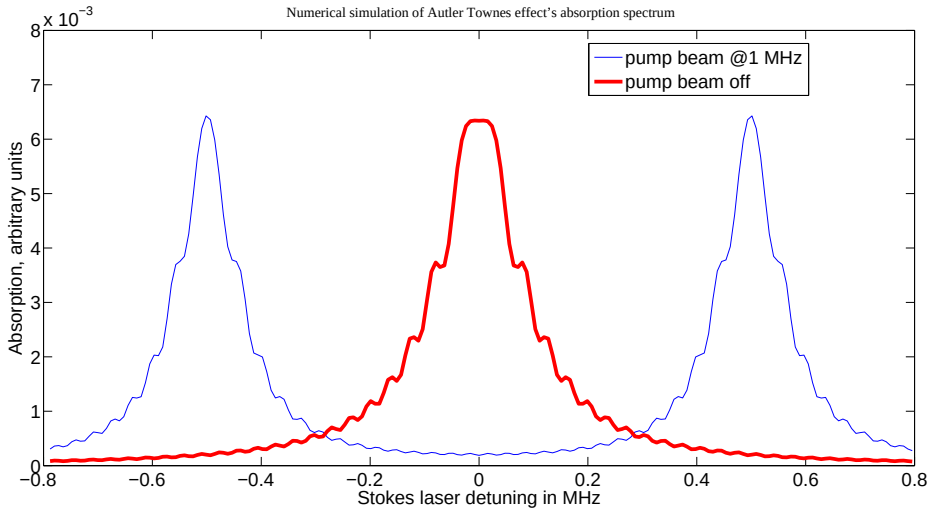

Figure 7.2: Numerical simulation of the absorption of laser in the Autler Townes effect. It shows the absorption of the Stokes beam under the conditions with and without the pump beam. In the condition where the pump beam is off, the atom is assumed to have a initial state with all population concentrated in the level 3. The corresponding level scheme of this simulation is presented in (7.8). However, to simplify the situation, instead of the density matrix, the time-dependent Schrödinger equation (TDSE) is used, with the spontaneous decay built in. The absorption is calculated by the method discussed in section 1.2.

We will write down the equation of motion for the density matrix of such a system step by step. First, let us write down the version without spontaneous emission.

$$\frac{d}{dt}\rho_{11} = \frac{i}{2}(\Omega^*_{probe}\rho_{21} - \Omega_{probe}\rho_{12}) \tag{7.7a}$$

$$\frac{d}{dt}\rho_{22} = \frac{i}{2}(\Omega_{probe}\rho_{12} - \Omega^*_{probe}\rho_{21}) + \frac{i}{2}(\Omega_{pump}\rho_{32} - \Omega^*_{pump}\rho_{23}) \tag{7.7b}$$

$$\frac{d}{dt}\rho_{33} = \frac{i}{2}(\Omega^*_{pump}\rho_{23} - \Omega_{pump}\rho_{32}) \tag{7.7c}$$

$$\frac{d}{dt}\rho_{12} = -i\delta\rho_{12} + \frac{i}{2}\Omega_{probe}(\rho_{22} - \rho_{11}) \tag{7.7d}$$

$$\frac{d}{dt}\rho_{32} = -i\delta\rho_{32} + \frac{i}{2}\Omega_{pump}(\rho_{22} - \rho_{33}) \tag{7.7e}$$

Phenomenologically spontaneous emission would reduce the population of the excited

states, in the familiar form $\frac{d}{dt}N = -\gamma N$. The spontaneous emission can reduce not only the population in the excited states, but also the coherence terms with them. The reason could be seen from the expression of the coherence term for a pure state wavefunction ϕ: $\rho_{ab} = \langle a|\phi\rangle\langle\phi|b\rangle$. Say b is an excited state with decay, then $\langle\phi|b\rangle$ has to decay too since population is the square of the absolute value of $\langle\phi|b\rangle$. Therefore now we can safely put the spontaneous emission into the equations, though this is not the strict approach.

$$\frac{d}{dt}\rho_{11} = \frac{i}{2}(\Omega^*_{probe}\rho_{21} - \Omega_{probe}\rho_{12}) + \gamma_{21}\rho_{22} + \gamma_{31}\rho_{33} \tag{7.8a}$$

$$\frac{d}{dt}\rho_{22} = \frac{i}{2}(\Omega_{probe}\rho_{12} - \Omega^*_{probe}\rho_{21}) + \frac{i}{2}(\Omega_{pump}\rho_{32} - \Omega^*_{pump}\rho_{23}) - \gamma_{21}\rho_{22} \tag{7.8b}$$

$$\frac{d}{dt}\rho_{33} = \frac{i}{2}(\Omega^*_{pump}\rho_{23} - \Omega_{pump}\rho_{32}) - \gamma_{31}\rho_{33} \tag{7.8c}$$

$$\frac{d}{dt}\rho_{12} = -i\delta\rho_{12} + \frac{i}{2}\Omega_{probe}(\rho_{22} - \rho_{11}) - \frac{1}{2}\gamma_{21}\rho_{12} \tag{7.8d}$$

$$\frac{d}{dt}\rho_{32} = -i\delta\rho_{32} + \frac{i}{2}\Omega_{pump}(\rho_{22} - \rho_{33}) - \frac{1}{2}\gamma_{31}\rho_{32} - \frac{1}{2}\gamma_{21}\rho_{32} \tag{7.8e}$$

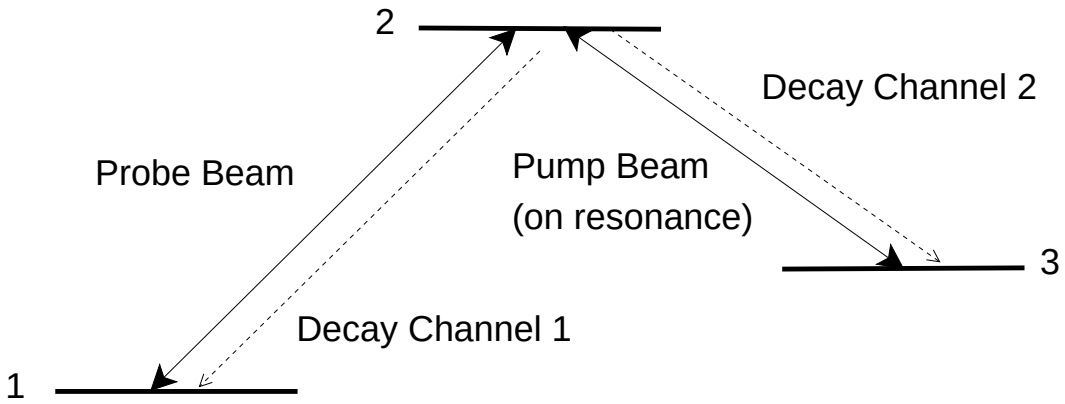

Figure 7.3: Level scheme of a lambda system with decay. The spontaneous emission is included in such a way that in this configuration EIT is allowed.

For EIT, we need a different configuration of levels, as given in the following Fig. 7.3. In EIT, the status of the pump and probe beams are in some sense 'reversed' compared to

that of the Autler Townes effect. And the EIT probe beam absorption lineshape will be very different from that of the Autler Townes effect.

7.2 Autler Townes Effect and STIRAP

Generally when the Rabi frequencies of the Stokes beam and the pump beam are comparable, there is no such observable effect as Autler Townes effect if the interaction is in STIRAP configuration. The reason is that STIRAP is tolerant to one–photon detuning and will always coherently transfer the population which is in the dark state $|0\rangle$ no matter what, as also can been obviously seen from the discussions in the first two sections of Chapter 3.

However, in some extreme cases, Autler Townes effects can take place during a seemingly STIRAP experiment. For example, when the two lasers are in counter–intuitive order while the Stokes beam's Rabi frequency is much weaker than that of the pump beam at the overlapping region, the STIRAP process is very much damaged and effectively the situation belongs to the Autler Townes effect. The extreme conditions of this type do not concern us for our purpose therefore we are not going to the details here.

7.2.1 Autler Townes Effect and Laser Parameters

We have been describing the atom's interaction with the laser mainly by the Rabi frequency. Yet in the lab we only directly measure the intensity profiles of the lasers. Rabi frequency can be viewed as the laser's strength when driving a highly coherent process, where intensity can be viewed as the laser's strength (to be precise, square of the 'strength') in a non–coherent process.

We overlap the uv and ir laser beams, with the ir laser beam much weaker than the uv. In this configuration the Autler–Townes effect is expected, and is experimentally observed

as in Fig. 7.4. The splitting is caused by the transition $2^3S_1 \rightarrow 3^3P_2$ driven by the uv laser. Non–strictly speaking, the splitting is approximately the Rabi frequency of the uv laser, according to the discussions in section 7.1.

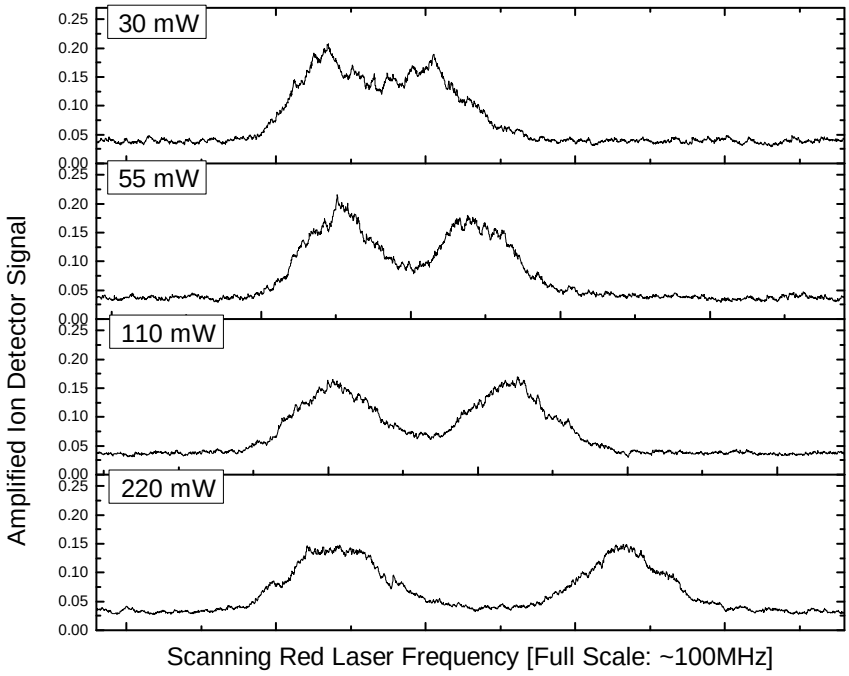

Figure 7.4: The experimentally measured Autler–Townes effect, showing the splitting caused by the uv laser Rabi frequency.

In Fig. 7.4, ir laser is driving the transition $3^3P_2 \rightarrow 24^3S_1$ at zero electric field, and the ion signal from 24^3S_1 is measured. As the power of the uv laser is increased, the splitting becomes wider. The relation between the uv laser power and the splitting is further explored in Fig. 7.5.

Fig. 7.5 is essentially verifying the linear relations between the Rabi frequency and the square root of the intensity provided in Table 1.3, since for fixed beam profile, the total power is proportional to the intensity at given points. According to the measured uv laser beam

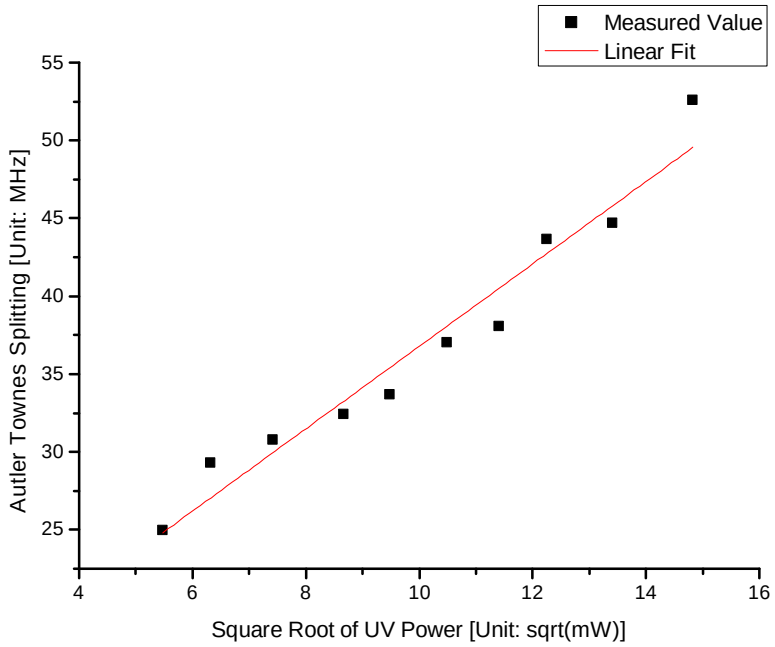

Figure 7.5: The measured Autler–Townes splitting and the square root of the power of the uv laser.

profile, the Rabi frequency is $\Omega_p \approx 2.89\sqrt{P_{\rm uv}}$ where Ω_p is in MHz and $P_{\rm uv}$ is in mW. The reason for this to be approximate relation is that transitions with different m_j have slightly conversion relations as shown in Table 1.3, and for comparison purpose we are taking an average here. In Fig. 7.5, we know from the slope of the fitted line that $\Omega_p = 2.79(.22)\sqrt{P_{\rm uv}}$. Those number agree well and serve as the test of the laser parameters for the experiment.

Fig. 7.4 contains rich information more than the Rabi frequency of the uv laser. The individual peaks have a FWHM of ~ 12 MHz, which may arise from the power broadening from the ir probe laser (Rabi frequency ~ 4 MHz), residual uv laser intensity variation in the ir probe region (~ 4 MHz), and possibly the transverse velocity spread.

7.3 A Two Level Atom Driven by a Noisy Laser

The time evolution of a two level atom in a monochromatic radiation field is a standard part of the atomic textbooks. However, 'monochromatic radiation' is merely an idealization of what is actually used in experiments. Lasers have line width and fluctuations which can not just be ignored.

The study of the interaction between a two level atom and a laser with fluctuations began very early, almost immediately after the invention of laser. The stochastic nature of practical lasers (especially for the multi-mode lasers) has been carefully examined and the effect on the atoms has been carefully calculated by reasonable stochastic and statistical methods. The literature on this subject is rich, some good references can be found at [87] and [88]. C. W. Gardiner and P. Zoller even published a very good book on this topic [89].

Recently there are quite some interest in this problem of the noise effect on an effective two level system, for example [90].

In this section I will try to explore this issue with simple methods compared to those thorough calculations mentioned above. I would like to show the consequences of inherent randomness associated with actual lasers on the time evolution of a two level atom. Hence, pictorially, the content to be discussed is 'driving a two level atom with a fluctuating laser'.

7.3.1 Intensity Fluctuations

The first instability to be discussed is the fluctuations in the laser intensity. Suppose within a time interval t_0, the Rabi frequency Ω of the laser is a random variable X. For all the time within this interval of t_0, X would stay a constant, but the value of this constant is probabilistic, and the detailed distribution of X can be anything prescribed. And suppose that the laser is on resonance all the time.

Now we shine such a laser on a two level atom without spontaneous emission. The time evolution can be described by the following equation:

$$i\frac{d}{dt}\begin{pmatrix} c_1 \\ c_2 \end{pmatrix} = \frac{1}{2}\begin{pmatrix} 0 & \Omega \\ \Omega & 0 \end{pmatrix}\begin{pmatrix} c_1 \\ c_2 \end{pmatrix} \tag{7.9}$$

If instead, we consider this problem under the dressed atom picture, i.e., we take the base kets to be $\frac{1}{\sqrt{2}}(1,1)^T$ and $\frac{1}{\sqrt{2}}(1,-1)^T$, then the time evolution of the coefficients a_+ and a_- can be written as:

$$i\frac{d}{dt}\begin{pmatrix} a_+ \\ a_- \end{pmatrix} = \frac{1}{2}\begin{pmatrix} \Omega & 0 \\ 0 & -\Omega \end{pmatrix}\begin{pmatrix} a_+ \\ a_- \end{pmatrix} \tag{7.10}$$

$$\text{with } a_+ = \begin{pmatrix} c_1 & c_2 \end{pmatrix}\cdot\frac{1}{\sqrt{2}}\begin{pmatrix} 1 \\ 1 \end{pmatrix} \text{ and } a_- = \begin{pmatrix} c_1 & c_2 \end{pmatrix}\cdot\frac{1}{\sqrt{2}}\begin{pmatrix} 1 \\ -1 \end{pmatrix} \tag{7.11}$$

Let's say, at the first time interval t_0, the Rabi frequency is a random variable Ω_1, at the second time interval t_0, the Rabi frequency is a random variable Ω_2, and so on. An extra important assumption is independence. Namely, $\Omega_1, \Omega_2, \cdots, \Omega_n$ are assumed all to be independent of each other. Then the solution, after n time intervals, of (7.10) can be worked out explicitly.

$$a_+ = a_+(0)\exp(-\frac{i}{2}\sum_1^n \Omega_j \cdot t_0) \tag{7.12}$$

$$a_- = a_-(0)\exp(\frac{i}{2}\sum_1^n \Omega_j \cdot t_0) \tag{7.13}$$

For the condition when n is large, we can resort to the central limit theorem to evaluate $\sum_1^n \Omega_j$. Given the expectation value of Ω_j is Ω_{avg} and the variance is Ω_{var}, we know that $\sum_1^n \Omega_j \approx n\Omega_{avg} + \sqrt{n}N(0, \Omega_{var})$. Here $N(0, \Omega_{var})$ stands for a normal distribution with average 0 and variance Ω_{var}. Then, when n is large the above solutions could be reduced to:

$$a_+ = a_+(0)\exp(-\frac{i}{2}\Omega_{avg}nt_0 - \frac{i}{2}\sqrt{n}N(0, \Omega_{var})t_0) \tag{7.14}$$

$$a_- = a_-(0)\exp(\frac{i}{2}\Omega_{avg}nt_0 + \frac{i}{2}\sqrt{n}N(0, \Omega_{var})t_0) \tag{7.15}$$

While, without the intensity fluctuations, the dressed states evolve deterministically with time:

$$a_+ = a_+(0)\exp(-\frac{i}{2}\Omega_{avg}nt_0) \tag{7.16}$$

$$a_- = a_-(0)\exp(\frac{i}{2}\Omega_{avg}nt_0) \tag{7.17}$$

The consequence of the intensity fluctuation is contained in the phase term $\frac{i}{2}\sqrt{n}N(0, \Omega_{var})t_0$ of the dressed states. Compared to the no-noise perfect scenario, the phase of the dressed states now are no longer deterministic. Rather, they become random. The worse the fluctuation is (i.e. a larger Ω_{var}), the more random the final phase will be (i.e. $\sqrt{n}N(0, \Omega_{var})t_0$ becomes more spread out).

P. Zoller uses density matrix a lot in his discussions for this and other related problems. The density matrix is good and proper in the sense that it predicts observables. The essence of the density matrix approach is to 'take the average value'. While, in comparison, the probability method I am using here is to reveal the the detailed probabilistic nature of the

problem. If the average value or expectation is taken, the result here would reduce to that of the density matrix approach.

This problem can also be treated by the Fokker-Planck equation. However, it is beyond the scope here.

7.3.2 Frequency Fluctuations

Another source of laser instability is the fluctuations in frequency. We can continue this discussion by borrowing the same picture we previously used for the intensity instability. To begin with, I want to simply assume that for each time interval t_0 the frequency of the laser is a random variable. The random variables of different time intervals are independent with each other.

Now, within the jth interval t_0, the time evolution is described by the following (familiar) equation. Here I am going to follow the dressed states picture, similar to the previous section.

$$i\frac{d}{dt}\begin{pmatrix} c_1 \\ c_2 \end{pmatrix} = \frac{1}{2}\begin{pmatrix} 0 & \Omega \\ \Omega & \Delta_j \end{pmatrix}\begin{pmatrix} c_1 \\ c_2 \end{pmatrix} \tag{7.18}$$

An exact treatment to get the final result by tracing all the time intervals might be hard. However, a preliminary result is possible, under one suitable approximation that the dressed states are adiabatically followed all the time. Namely, there is no transition or cross between the two dressed states. Then analogous to (7.10) we can establish the time evolution for the dressed states. Of particular interest is the phase as a function of time.

$$i\frac{d}{dt}\begin{pmatrix} a_+ \\ a_- \end{pmatrix} = \frac{1}{2}\begin{pmatrix} \frac{\Delta+\sqrt{\Delta^2+\Omega^2}}{2} & 0 \\ 0 & \frac{\Delta-\sqrt{\Delta^2+\Omega^2}}{2} \end{pmatrix}\begin{pmatrix} a_+ \\ a_- \end{pmatrix} \tag{7.19}$$

$$\text{with } a_+ = \begin{pmatrix} c_1 & c_2 \end{pmatrix}\cdot\frac{1}{\sqrt{2}}\begin{pmatrix} 1 \\ 1 \end{pmatrix} \text{ and } a_- = \begin{pmatrix} c_1 & c_2 \end{pmatrix}\cdot\frac{1}{\sqrt{2}}\begin{pmatrix} 1 \\ -1 \end{pmatrix} \tag{7.20}$$

Let us model the details of the frequency fluctuation in the following simple way, again similar to the intensity fluctuation case. Assume Δ_j's of the jth interval t_0 are all independent with each other, and have expectation 0 and variance Δ_{var}. Henceforth the results of (7.19) are:

$$a_+ = a_+(0)\exp(\frac{i}{2}\sum_1^n(\Delta_j + \sqrt{\Delta_j^2+\Omega^2})\cdot t_0) \tag{7.21}$$

$$a_- = a_-(0)\exp(\frac{i}{2}\sum_1^n(\Delta_j - \sqrt{\Delta_j^2+\Omega^2})\cdot t_0) \tag{7.22}$$

Let's say the laser is not fluctuating so much that Δ_{var} is small compared to Ω. Then $\sqrt{\Delta_j^2+\Omega^2}$ is approximately Ω. With the help of the central limit theorem we know that $\sum_1^n \Delta_j \approx \sqrt{n}N(0,\Delta_{var})$. With all that information, the time evolution of the dressed states is summarized in the following, when n is large.

$$a_+ = a_+(0)\exp(-\frac{i}{2}\Omega n t_0 + \frac{i}{2}\sqrt{n}N(0,\Delta_{var})t_0) \tag{7.23}$$

$$a_- = a_-(0)\exp(\frac{i}{2}\Omega n t_0 + \frac{i}{2}\sqrt{n}N(0,\Delta_{var})t_0) \tag{7.24}$$

The randomness in the frequency induces randomness in the phases of the the dressed states, whose effect is summarized in the term $\frac{i}{2}\sqrt{n}N(0,\Delta_{var})t_0$.

All these terminologies such as 'frequency noise', 'frequency instability', 'phase noise'... are actually describing the same thing if the discussion is limited to the context of (7.19). After all, we know that phase is merely frequency integrated over time. The simple and direct discussion within this section is enough to model the consequences.

7.3.3 SDE and Feynman's Path Integral Approach

The discussion in the previous two sections is straightforward and mostly shows the nature of the problem. However, the assumptions and methods are still a bit artificial. A more natural way is to use stochastic differential equation (SDE) to study the details of the time evolution.

Generally speaking, this problem falls in the category of a two or three level atomic system interacting with lasers having classical noise. This topic has been extensively explored in the 70's and 80's, both experimentally and theoretically. Many people pioneered in this area, including S. J. Smith and P. Zoller. Numerous work has been published. Two good experimental references can be found at [91] and [92]. Different theoretical methods can be found at [93] [94] [95] [96] [97] [98] [99] [100]. This phase noise in the SDE is multiplicative in nature and therefore is naturally hard to tackle. Yet, as mentioned in those references above, a combination of density matrix approach [101] (which usually includes the effect of the spontaneous emission) and SDE could yield satisfying results and lineshapes corresponding to experimental data.

Here I want to use the Schrödinger equation combined with SDE to deal with this problem. The reason for this choice of the Schrödinger equation over the density matrix approach

is that, in the two possible applications of this calculation, spontaneous emission does not have an important role and can be regarded as never happening in the ideal case, which are STIRAP and light force on atom at a time scale shorter than one lifetime.

Another difference from the referenced works is that I am going to use a method similar to that of the Feynman's path integral approach to reveal the nature of the stochastic process in terms of time evolution, though approximations would be used to get a result.

Suppose the laser has both frequency fluctuations and intensity fluctuations. We can regard them as white noise, and therefore use Brownian motion to model them. Namely, instead of the usual $\Omega\cos(\omega_0 t)$ as the transition term induced by the laser, we now have $(\Omega + \frac{dW_\Omega}{dt})\cos(\omega_0 t + W_\delta)$. W_Ω and W_δ are scaled Brownian motions, and are independent of each other, with the implication that the noise in the intensity has nothing to do with the noise in the frequency. Sometimes this fluctuation in frequency is also called 'phase diffusion' [92]. The involved stochastic calculus here is in the sense of Itô calculus.

The starting point is the Schrödinger equation for a two level atom after the rotating wave approximation, in the rotating wave frame of the atomic resonance frequency. For ease of notation, let $\Omega' = \Omega + \frac{dW_\Omega}{dt}$.

$$i\frac{d}{dt}\begin{pmatrix} c_1 \\ c_2 \end{pmatrix} = \frac{1}{2}\begin{pmatrix} 0 & \Omega' e^{iW_\delta} \\ \Omega' e^{-iW_\delta} & 0 \end{pmatrix}\begin{pmatrix} c_1 \\ c_2 \end{pmatrix} \text{ where } H = \frac{1}{2}\begin{pmatrix} 0 & \Omega' e^{iW_\delta} \\ \Omega' e^{-iW_\delta} & 0 \end{pmatrix} \tag{7.25}$$

The instantaneous energy eigenvalue, or dressed states, are:

$$|+\rangle = \frac{1}{\sqrt{2}}\begin{pmatrix} 1 \\ e^{-iW_\delta} \end{pmatrix} \text{ with energy } \frac{1}{2}\Omega' \; ; \; |-\rangle = \frac{1}{\sqrt{2}}\begin{pmatrix} 1 \\ -e^{-iW_\delta} \end{pmatrix} \text{ with energy } -\frac{1}{2}\Omega' \tag{7.26}$$

Now we go on to construct the propagator that connects the future $t_n = T$ to the past t_0 with time intervals $\Delta t = \frac{T-t_0}{n}$:

$$\Theta = (1 - iH(t_{n-1})\Delta t) \cdots (1 - iH(t_0)\Delta t) \tag{7.27}$$

And then:

$$\text{Propagator} = \lim_{\Delta t \to 0} \Theta = \lim_{\Delta t \to 0} (1 - iH(t_{n-1})\Delta t) \cdots (1 - iH(t_0)\Delta t) \tag{7.28}$$

To evaluate (7.27), we need to look into:

$$g^{t_j} = (|+, t_{j+1}\rangle\langle +, t_{j+1}| + |-, t_{j+1}\rangle\langle -, t_{j+1}|)(1 - iH(t_j)\Delta t)(|+, t_j\rangle\langle +, t_j| + |-, t_j\rangle\langle -, t_j|) \tag{7.29}$$

A little calculation shows, up to first order:

$$\langle +, t_{j+1}|+, t_j\rangle = \frac{1}{2} \begin{pmatrix} 1 & e^{iW_\delta(t_{j+1})} \end{pmatrix} \begin{pmatrix} 1 \\ e^{-iW_\delta(t_j)} \end{pmatrix} \approx 1 + \frac{1}{2} i \Delta W_\delta \tag{7.30}$$

The sense of 'first order' in (7.30) needs a careful justification. As mentioned above, $W_\delta = s_\delta W_0$ is a scaled Brownian motion with scaling factor s_δ. Here we regard s_δ as small and perform a perturbative calculation up to the first order of s_δ. Then we apply Itô's lemma to $e^{-iW_\delta(\Delta t)} - 1$, keep up to the first order, and then arrive at (7.30). By the same virtue, we have all 3 other terms in (7.31). And therefore g^{t_j} in matrix format is given in (7.32).

$$\langle +, t_{j+1}|-, t_j\rangle = -\frac{1}{2}i\Delta W_\delta \tag{7.31a}$$

$$\langle -, t_{j+1}|+, t_j\rangle = -\frac{1}{2}i\Delta W_\delta \tag{7.31b}$$

$$\langle -, t_{j+1}|-, t_j\rangle = 1 + \frac{1}{2}i\Delta W_\delta \tag{7.31c}$$

$$g^{t_j} = \begin{pmatrix} 1 + \frac{1}{2}i\Delta W_\delta - \frac{1}{2}i\Omega'\Delta t & -\frac{1}{2}i\Delta W_\delta \\ -\frac{1}{2}i\Delta W_\delta & 1 + \frac{1}{2}i\Delta W_\delta + \frac{1}{2}i\Omega'\Delta t \end{pmatrix} \tag{7.32}$$

In order to evaluate $g = g^{t_{n-1}} \cdots g^0$, we take the logarithm $\ln g = \ln(g^{t_{n-1}} \cdots g^0)$. For Δt sufficiently small $\ln g$ is as in (7.33) up to the first order.

$$\ln g^{t_j} = \begin{pmatrix} \frac{1}{2}i\Delta W_\delta - \frac{1}{2}i\Omega'\Delta t & -\frac{1}{2}i\Delta W_\delta \\ -\frac{1}{2}i\Delta W_\delta & \frac{1}{2}i\Delta W_\delta + \frac{1}{2}i\Omega'\Delta t \end{pmatrix} \tag{7.33}$$

If $\ln(g^{t_{j-1}} \cdots g^0) = \ln g^{t_{j-1}} + \cdots + \ln g^0$ holds, then in the process of letting $\Delta t \to 0$, it is essentially taking the integral of the building blocks of (7.33). And in the end, suppose the time starts at $t_0 = 0$, we arrive at (7.34), in matrix format:

$$g = \exp \begin{pmatrix} \frac{1}{2}iW_\delta - \frac{1}{2}i\Omega T - \frac{1}{2}iW_\Omega & -\frac{1}{2}iW_\delta \\ -\frac{1}{2}iW_\delta & \frac{1}{2}iW_\delta + \frac{1}{2}i\Omega T + \frac{1}{2}iW_\Omega \end{pmatrix} \tag{7.34}$$

Before delving into the physical meaning of (7.34), let us figure out the validity of the condition $\ln(g^{t_{j-1}} \cdots g^0) = \ln g^{t_{j-1}} + \cdots + \ln g^0$. At a glance of (7.33), it seems that $\ln g^{t_j}$ for different j's all look the same and hence shall be commutative with each other. Yet, thanks to the Markovian property of the Brownian motion, the truth is that ΔW_δ's at different

times are independent, hence the above commutativity argument fails.

By the virtue of Baker–Campbell–Hausdorff formula, the expansion of $\ln(g^{t_{j-1}} \cdots g^0)$ contains infinite numbers of higher order terms besides $\ln g^{t_{j-1}} + \cdots + \ln g^0$. Here I want to make an argument that up to first order $\ln g^{t_{j-1}} + \cdots + \ln g^0$ is what we have. The sense of this 'first order' can be understood from two aspects. The first point is that, only terms in the first order of the scaling factor is kept, which is consistent with what we begin with: a perturbative computation up to 1st order in the scaling factor, for both W_δ and W_Ω. The second point is a bit subtle. If we take the expectation values of $\ln g^{t_j}$, we see that the $E(\ln g^{t_j})$ all commute with each other; moreover, because of the independence, we have $E(g^{t_{j-1}} \cdots g^0) = E(g^{t_{j-1}}) \cdots E(g^0)$. Put into words, the expectation value always evolve adiabatically as expected.

Now it is time to see what (7.34) tells us. It qualitatively verifies the discussions of 7.3.1 and 7.3.2, and provides further details, which could be regarded as the non–adiabaticity part, i.e. the probability that a transition between the dressed states occur.

7.4 Measuring the Laser Linewidth

I guess most often we wish to quantitatively measure the linewidth of a laser before shinning it onto the atoms. In this section, I wish to establish the connection between the laser linewidth and the laser noise. Especially, I want to show how the experimental measure of laser linewidth shall be interpreted, even if the measure is performed without an rf spectrum analyzer.

Laser linewidth is a repeatedly discussed topic in literature. Ever since the very early days, insightful discussions have been around. Good theoretical references can be found at [102] and [103]. For the early experimental effort to measure the linewidth and a thorough

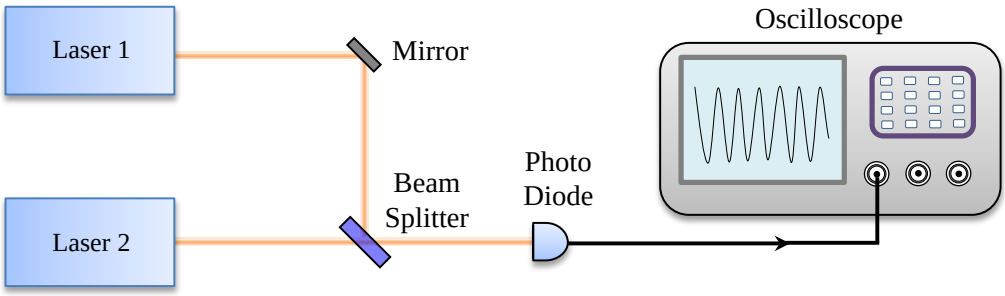

Figure 7.6: The schematics of the experimental setup to measure the linewidth of the two Ti:Sapphire lasers by recording their beat signal

understanding of the nature of this kind of measurements, [104] is a good starting point.

Here I want to avoid diving into the physics nature and origin of the laser noise. Rather, I plan to use probability methods as a tool to show how simple and direct model of laser noise can lead to experimentally observed laser linewidth. From the point of view of the narrow interest on interpreting the data, laser noise is 'God given' such that what's left is to give an efficient description and study phenomenology.

In order to have an idea of the linewidth of the lasers for the STIRAP, we set up an experiment to beat the two Ti:Sapphire lasers, as shown in Fig 7.6. In the actual experiment we have used a fiber coupled beam combiner to overlap the light. We tune the two lasers to about a couple of hundred MHz apart, and then record the trace from the oscilloscope.

The the question is: how to interpret the recorded data? Moreover, what is the link between the measurement and its effect on the atoms?

Let us first see how the phase noise could result in laser linewidth. We regard the phase noise phenomenologically as a Brownian motion, and write the electric field of the two lasers separately as: $\cos(\omega_1 t + W_1(t))$ and $\cos(\omega_2 t + W_2(t))$, where $W_1(t)$ and $W_2(t)$ are independent

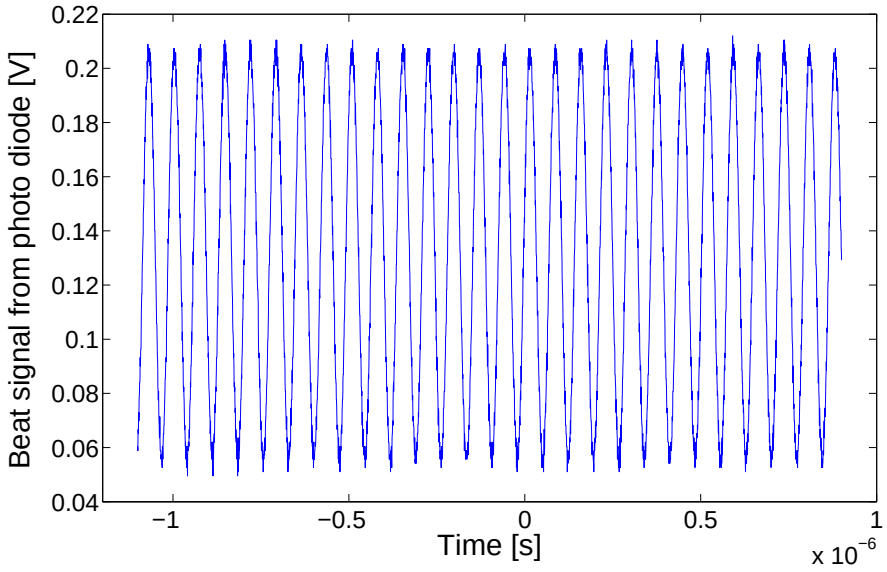

Figure 7.7: The beat signal of the two Ti:Sapphire lasers. Here for illustration purpose only showing a part of the time interval of the total recorded data.

scaled 1 dimensional Brownian motions.

$$\begin{aligned}
&(\cos(\omega_1 t + W_1(t)) + \cos(\omega_2 t + W_2(t)))^2 \\
=&2 + 2\cos(\omega_1 t + W_1(t))\cos(\omega_2 t + W_2(t)) + 2\omega_1.\&2\omega_2.\text{terms} \\
=&2 + \cos((\omega_1 - \omega_2)t + (W_1 - W_2)) + \cos((\omega_1 + \omega_2)t + (W_1 + W_2)) + 2\omega_1.\&2\omega_2.\text{terms}
\end{aligned} \tag{7.35}$$

The intensity of the electric field at the photo detector is shown at (7.35). Due to the frequency response of the photo diode, except for a dc term, the photo detector 'sees': $\cos((\omega_1 - \omega_2)t + (W_1 - W_2))$. Say the beat frequency $\delta = \omega_1 - \omega_2$, therefore the actual detected signal is of the form $\cos(\delta t + W)$, where W is a scaled Brownian motion. We set the scaling factor to be s and have that $W = sW_0$, where W_0 is a standard Brownian motion or the so-called Wiener process.

Since $\cos(\delta t+W)$ is a random process, it is not the same as the signal we see on the scope. Suppose we have recorded the signal from time 0 to time T, with a typical trace shown in Fig 7.7. And then we are to take the Fourier transform of it, following the standard procedure.

The question is how to understand the recorded signal. We can always say the experimental data is some sort of average, yet, we have two ways to establish this 'average': $E(\cos(\delta t + W))$ and $E(\int_0^T \exp(i\omega t)\cos(\delta t + W)dt)$.

The Fourier transform of the trace shall be very close or the same as $E(\int_0^T \exp(i\omega t)\cos(\delta t+W)dt)$. A simple but not strict argument could be, by abusing the central limit theorem a bit, after long enough time, the measured value is the expectation with very little fluctuation, no matter what the underlying distribution is. Yet the details will become clear once $E(\int_0^T \exp(i\omega t)\cos(\delta t + W)dt)$ is computed.

Let $f(W_0(t), t) = \exp(i\omega t)\exp(isW_0(t))$, and apply Itô's lemma to f:

$$e^{i\omega T}e^{isW_0(T)} = 1 + \int_0^T ise^{i\omega t}e^{isW_0(t)}W_0(dt) + \int_0^T \{-\frac{1}{2}s^2e^{i\omega t}e^{isW_0(t)} + i\omega e^{i\omega t}e^{isW_0(t)}\}dt \quad (7.36)$$

Take the expectation on both sides of (7.36), and note that the expectation of an Itô integral is zero:

$$E(e^{i\omega T}e^{isW_0(T)}) = 1 + 0 + (i\omega - \frac{1}{2}s^2)E(\int_0^T e^{i\omega t}e^{isW_0(t)}dt) \quad (7.37)$$

$W_0(T)$ is a Gaussian random variable with variance T, hence $E(e^{isW_0(T)}) = e^{-\frac{s^2T}{2}}$. Then:

$$E(\int_0^T e^{i\omega t}e^{isW_0(t)}dt) = \frac{e^{i\omega T}e^{-\frac{s^2T}{2}} - 1}{i\omega - \frac{1}{2}s^2} \quad (7.38)$$

And henceforth the long expected result could be calculated:

$$E(\int_0^T \exp(i\omega t)\cos(\delta t + sW_0)dt) = \frac{1}{2}\{\frac{e^{i(\omega+\delta)T}e^{-\frac{s^2T}{2}}-1}{i(\omega+\delta)-\frac{1}{2}s^2} + \frac{e^{i(\omega-\delta)T}e^{-\frac{s^2T}{2}}-1}{i(\omega-\delta)-\frac{1}{2}s^2}\} \tag{7.39}$$

From (7.39) it is clearly a double-peak structure with some line shape. But what is this line shape? Let us take one branch from (7.39) and clean the form a bit.

$$\frac{e^{i(\omega+\delta)T}e^{-\frac{s^2T}{2}}-1}{i(\omega+\delta)-\frac{1}{2}s^2} = \frac{(e^{i(\omega+\delta)T}e^{-\frac{s^2T}{2}}-1)(\frac{1}{2}s^2+i(\omega+\delta))}{(\omega+\delta)^2+(\frac{1}{2}s^2)^2} \tag{7.40}$$

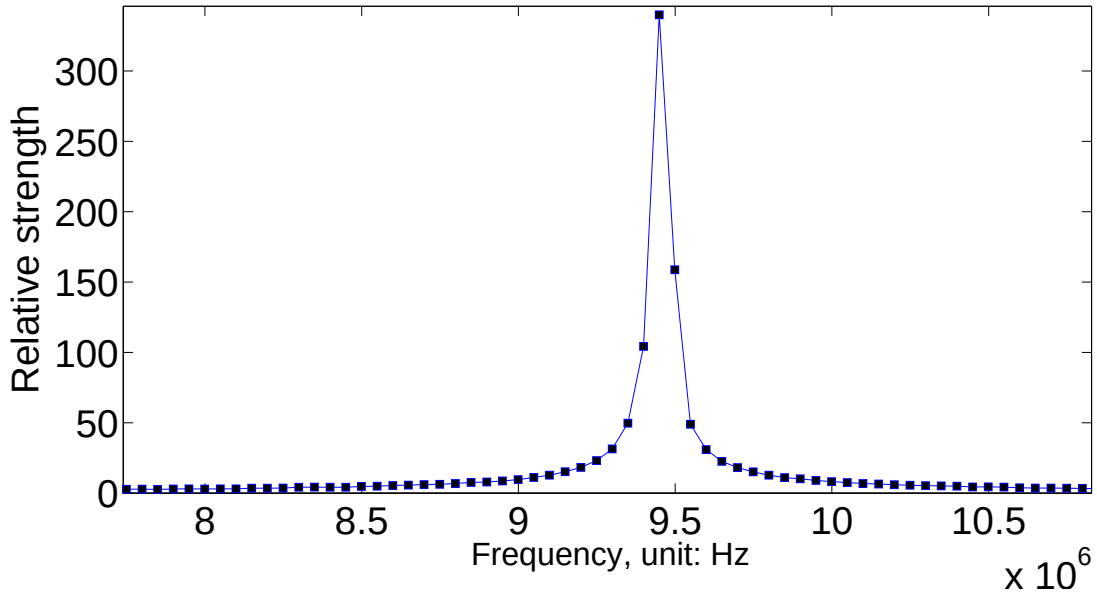

Figure 7.8: The Fourier spectrum of the beat signal of the two Ti:Sapphire lasers, as the result of the linewidth measurement.

A technical point about the Fourier transform is that, since the computer is actually performing FFT, for all the discrete ω values in the outcome, ωT is always multiples of 2π. Therefore, $e^{i\omega T}$ is always 1. Take the absolute value:

$$|\frac{e^{i(\omega+\delta)T}e^{-\frac{s^2T}{2}}-1}{i(\omega+\delta)-\frac{1}{2}s^2}| = |e^{i\delta T}e^{-\frac{s^2T}{2}}-1|\frac{1}{\sqrt{(\omega+\delta)^2+(\frac{1}{2}s^2)^2}} \tag{7.41}$$

It would be entertaining to rephrase (7.41) in terms of plain English: the intensity of the Fourier transform spectrum of the beat signal is of the line shape of Lorentzian. The linewidth is then $\frac{1}{2}s^2$, and this would establish the relation between measured data and the parameter of laser noise behavior.

The Fourier spectrum of the recorded beat signal is shown in Fig 7.8. To be more precise, it is the absolute value of the Fourier spectrum. Since it is from FFT hence black markers are used to indicate the real FFT output points. We are experimentally beating two Ti:Sapphire lasers, therefore the linewidth from Fig 7.8 shall be regarded as the sum of the linewidth of the two lasers, as explained previously in this section.

Bibliography

[1] E. Urban, T. A. Johnson, T. Henage, L. Isenhower, D. D. Yavuz, T. G. Walker, and M. Saffman. Observation of Rydberg blockade between two atoms. *Nat Phys*, 5: 110–114, Feb 2009. doi: 10.1038/nphys1178. URL `http://www.nature.com/nphys/journal/v5/n2/suppinfo/nphys1178_S1.html`.

[2] M. D. Lukin, M. Fleischhauer, R. Cote, L. M. Duan, D. Jaksch, J. I. Cirac, and P. Zoller. Dipole blockade and quantum information processing in mesoscopic atomic ensembles. *Phys. Rev. Lett.*, 87:037901, Jun 2001. doi: 10.1103/PhysRevLett.87.037901. URL `http://link.aps.org/doi/10.1103/PhysRevLett.87.037901`.

[3] D. Tong, S. M. Farooqi, J. Stanojevic, S. Krishnan, Y. P. Zhang, R. Côté, E. E. Eyler, and P. L. Gould. Local Blockade of Rydberg Excitation in an Ultracold Gas. *Phys. Rev. Lett.*, 93:063001, Aug 2004. doi: 10.1103/PhysRevLett.93.063001. URL `http://link.aps.org/doi/10.1103/PhysRevLett.93.063001`.

[4] Y. O. Dudin and A. Kuzmich. Strongly Interacting Rydberg Excitations of a Cold Atomic Gas. *Science*, 336(6083):887–889, 2012. doi: 10.1126/science.1217901. URL `http://www.sciencemag.org/content/336/6083/887.abstract`.

[5] Otto Stern. Bending a molecular ray by crystal lattice face. *Naturwissenschaften*, 17: 391–391, 1929. ISSN 0028-1042. 10.1007/BF01506798.

[6] B. Friedrich and D. Herschbach. Stern and Gerlach: How a bad cigar helped reorient atomic physics. *Physics Today*, 56:53–59, 2003.

[7] I. Estermann. History of molecular beam research: Personal reminiscences of the important evolutionary period 1919-1933. *Am. J. Phys*, 43:661–671, 1975.

[8] T. W. Hänsch and A. L. Schawlow. Cooling of gases by laser radiation. *Optics Communications*, 13(1):68–69, Jan. 1975.

[9] H. J. Metcalf and P. van der Straten. *Laser Cooling and Trapping*. Springer, Berlin, 2002.

[10] D. S. Hall. Resource Letter: BEC-1: Bose-Einstein condensates in trapped dilute gases. *Am. J. Phys.*, 71(7):649–660, 2003.

[11] Richard J. Cook and Richard K. Hill. An electromagnetic mirror for neutral atoms. *Optics Communications*, 43(4):258–260, Oct. 1982.

[12] Philip E. Moskowitz, Phillip L. Gould, Susan R. Atlas, and David E. Pritchard. Diffraction of an atomic beam by standing-wave radiation. *Phys. Rev. Lett.*, 51(5):370–373, Aug 1983.

[13] Peter J. Martin, Bruce G. Oldaker, Andrew H. Miklich, and David E. Pritchard. Bragg scattering of atoms from a standing light wave. *Phys. Rev. Lett.*, 60(6):515–518, Feb 1988.

[14] J. J. Berkhout, O. J. Luiten, I. D. Setija, T. W. Hijmans, T. Mizusaki, and J. T. M. Walraven. Quantum reflection: Focusing of hydrogen atoms with a concave mirror. *Phys. Rev. Lett.*, 63(16):1689–1692, Oct 1989.

[15] Gregg M. Gallatin and Phillip L. Gould. Laser focusing of atomic beams. *J. Opt. Soc. Am. B*, 8(3):502–508, March 1991.

[16] J. L. Cohen, B. Dubetsky, and P. R. Berman. Atom focusing by far-detuned and resonant standing wave fields: Thin-lens regime. *Phys. Rev. A*, 60(6):4886–4901, Dec 1999.

[17] R. B. Doak, R. E. Grisenti, S. Rehbein, G. Schmahl, J. P. Toennies, and Ch. Wöll. Towards realization of an atomic de Broglie microscope: helium atom focusing using Fresnel zoneplates. *Phys. Rev. Lett.*, 83(21):4229–4232, Nov 1999.

[18] Heung-Ryoul Noh, Kazuko Shimizu, and Fujio Shimizu. Imaging of an atomic beam with electrostatic lenses. *Phys. Rev. A*, 61(4):041601, Feb 2000.

[19] Juris G. Kalnins, Jason M. Amini, and Harvey Gould. Focusing a fountain of neutral cesium atoms with an electrostatic lens triplet. *Phys. Rev. A*, 72(4):043406, Oct 2005.

[20] B. Brezger, Th. Schulze, U. Drodofsky, J. Stuhler, S. Nowak, T. Pfau, and J. Mlynek. Nanolithography with neutral chromium and helium atoms. *J. Vac. Sci. Technol. B*, 15(6):2905–2911, 1997.

[21] S. Nowak, T. Pfau, and J. Mlynek. Nanolithography with metastable helium. *Appl. Phys. B.*, 63:203–205, 1996.

[22] S. H. Lee. *Coherent Manipulation of Rydberg Helium Atoms in Inhomogenous Electric Fields*. PhD thesis, SUNY Stony Brook, Stony Brook, NY, August 2006.

[23] Marlan O. Scully and M. Suhail Zubairy. *Quantum Optics*. Cambridge University Press, New York, 1997.

[24] R. Grimm, J. Söding, and Yu. B. Ovchinnikov. Coherent beam splitter for atoms based on a bichromatic standing light wave. *Optics Letters*, 19(9):658, May 1994.

[25] M. R. Williams, F. Chi, M. T. Cashen, and H. Metcalf. Bichromatic force measurements using atomic beam deflections. *Phys. Rev. A*, 61(2):023408, Jan 2000.

[26] M. Partlow, X. Miao, J. Bochmann, M. Cashen, and H. Metcalf. Bichromatic slowing and collimation to make an intense helium beam. *Phys. Rev. Lett.*, 93(21):213004, Nov 2004.

[27] Jason Reeves. *Neutral Atom Lithography Using the 389 nm Transition in Metastable Helium*. PhD thesis, SUNY Stony Brook, Stony Brook, NY, August 2010.

[28] Thomas F. Gallagher. *Rydberg Atoms*. Cambridge University Press, New York, 1994.

[29] Myron L. Zimmerman, Michael G. Littman, Michael M. Kash, and Daniel Kleppner. Stark structure of the Rydberg states of alkali-metal atoms. *Phys. Rev. A*, 20(6): 2251–2275, Dec 1979.

[30] M. D. Lukin, M. Fleischhauer, R. Côté, L. M. Duan, D. Jaksch, J. I. Cirac, and P. Zoller. Dipole blockade and quantum information processing in mesoscopic atomic ensembles. *Phys. Rev. Lett.*, 87(3):037901, Jun 2001.

[31] T. Förster. *Modern Quantum Chemistry*. Academic Press, New York, 1996.

[32] I. Mourachko, D. Comparat, F. de Tomasi, A. Fioretti, P. Nosbaum, V. M. Akulin, and P. Pillet. Many-Body effects in a frozen Rydberg gas. *Phys. Rev. Lett.*, 80(2): 253–256, Jan 1998.

[33] M. P. Robinson, B. Laburthe Tolra, Michael W. Noel, T. F. Gallagher, and P. Pillet. Spontaneous evolution of Rydberg atoms into an ultracold plasma. *Phys. Rev. Lett.*, 85(21):4466–4469, Nov 2000.

[34] Denis B. Tretyakov Igor I. Ryabtsev and Ilya I. Beterov. Spontaneous evolution of Rydberg atoms into an ultracold plasma. *J. Phys. B: At. Mol. Opt. Phys.*, 38(2): S421–S436, Jan 2005.

[35] M. J. Seaton. Quantum defect theory. *Reports on Progress in Physics*, 46(2):167, Feb. 1983.

[36] C. J. Lorenzen and K. Niemax. Quantum defects of the $n^2P_{1/2,3/2}$ levels in ^{39}KI and ^{85}RbI. *Physica Scripta*, 27(4):300–305, July 1983.

[37] (private communications) Thomas Bergeman. *Department of Physics and Astronomy, Stony Brook University.*

[38] G. W. F. Drake. Theory of relativistic magnetic dipole transitions: Lifetime of the metastable 2^3s state of the helium-like ions. *Phys. Rev. A*, 3(3):908–915, Mar 1971.

[39] A. Derevianko and W. R. Johnson. Two-photon decay of 2^1S_0 and 2^3S_1 states of heliumlike ions. *Phys. Rev. A*, 56:1288–1294, Aug 1997. doi: 10.1103/PhysRevA.56.1288. URL `http://link.aps.org/doi/10.1103/PhysRevA.56.1288`.

[40] H. Hotop. *Experimental Methods in the Physical Sciences*, volume 29B. Academic Press, New York.

[41] K. Shimizu F. Shimizu J. Kawanaka, M. Hagiuda and H. Takuma. Generation of an intense low-velocity metastable-Neon atomic beam. *Appl. Phys. B: Lasers Opt.*, 56: 21–24, 1993.

[42] H. C. Mastwijk, J. W. Thomsen, P. Van der Straten, and A. Niehaus. Optical collisions of cold, metastable helium atoms. *Phys. Rev. Lett.*, 80(25):5516–5519, Jun 1998. ISSN 0031-9007.

[43] Xiaoxu Lu. *Excitation of Helium to Rydberg States Using STIRAP.* PhD thesis, SUNY Stony Brook, Stony Brook, NY, May 2011.

[44] Wikipedia: Microchannel plate detector. URL `http://en.wikipedia.org/wiki/Microchannel_plate_detector`.

[45] J. L. Wiza. Microchannel plate detectors. *Nuclear Instruments and Methods*, 162: 587–601, 1979.

[46] F. B. Dunning, R. D. Rundel, and R. F. Stebbings. Determination of secondary electron ejection coefficients for rare gas metastable atoms. *Rev. Sci. Instrum.*, 46(6):697–701, 1975.

[47] T.W. Hänsch and B. Couillaud. Laser frequency stabilization spectroscopy of a reflecting reference cavity. *Optics Communications*, 35(3):441, 1980.

[48] R. V. Pound. Electronic frequency stabilization of microwave oscillators. *Rev. Sci. Inst.*, 17:490, 1946.

[49] R. W. Drever and J. L. Hall. Laser phase and frequency stabilization using an optical resonator. *Appl. Phys. B*, 31:97, 1983.

[50] C. J. Foot. *Atomic Physics*, volume 7 of *Oxford Master Series in Physics.* Oxford University Press, Oxford, UK, 2005.

[51] T. W. Hänsch, I. S. Shahin, and A. L. Schawlow. High-resolution saturation spectroscopy of the sodium D lines with a pulsed tunable Dye Laser. *Phys. Rev. Lett.*, 27 (11):707–710, September 1971.

[52] *Instruction manual, CW single-frequency ring Ti:Sapphire laser model TIS-SF-07, Tekhnoscan Company.*

[53] M. C. Keller. Optical manipulation of helium atoms with application to neutral atom lithography. Master's thesis, SUNY Stony Brook, Stony Brook, NY, August 2006.

[54] Claire Allred. *Neutral Atom Lithography with Metastable Helium.* PhD thesis, SUNY Stony Brook, Stony Brook, NY, May 2009.

[55] M. Cashen, O. Rivoire, L. Yatsenko, and H. Metcalf. Coherent exchange of momentum between atoms and light. *Journal of optics B–quantum and semiclassical optics*, 4(1): 75–79, Feb. 2002.

[56] F. T. Hioe and J. H. Eberly. N-level coherence vector and higher conservation laws in quantum optics and quantum mechanics. *Phys. Rev. Lett.*, 47:838, 1981.

[57] J. Oreg, F. T. Hioe, and J. H. Eberly. Adiabatic following in multilevel systems. *Phys. Rev. A*, 29(2):690–697, Feb 1984.

[58] U. Gaubatz, P. Rudecki, M. Becker, S. Schiemann, M. Kulz, and K. Bergmann. Resonant light pressure forces in a strong standing laser wave. *Chem. Phys. Lett.*, 149:463, 1988.

[59] U. Gaubatz, P. Rudecki, S. Schiemann, and K. Bergmann. Population transfer between molecular vibration levels. *J. Chem. Phys.*, 92:5363, 1990.

[60] K. Bergmann, H. Theuer, and B. W. Shore. Coherent population transfer among quantum states of atoms and molecules. *Rev. Mod. Phys.*, 70(3):1003, 1998.

[61] J. Martin, B. W. Shore, and K. Bergmann. Coherent population transfer in multilevel systems with magnetic sublevels. iii. experimental results. *Phys. Rev. A*, 54(2):1556–1569, Aug 1996.

[62] N. V. Vitanov, M. Fleischhauer, B. W. Shore, and K. Bergmann. Coherent manipulation of atoms and molecules by sequential laser pulses. *Adv. Atom. Mol. Opt.*, 46:55, 2001.

[63] N. V. Vitanov, T. Halfmann, B. W. Shore, and K. Bergmann. Laser-induced population transfer by adiabatic passage techniques. *Annu. Rev. Chem.*, 52:763–809, 2001.

[64] J. R. Kuklinski, U. Gaubatz, F. T. Hioe, and K. Bergmann. Adibatic population transfer in a three-level system driven by delayed laser pulses. *Phys. Rev. A*, 40(3): 6741, 1989.

[65] A. Marsman, M. Horbatsch, and E. A. Hessels. Shifts due to distant neighboring resonances for laser measurements of $2\,^3S_1$-to-$2\,^3P_J$ transitions of helium. *Phys. Rev. A*, 86:040501, Oct 2012. doi: 10.1103/PhysRevA.86.040501. URL `http://link.aps.org/doi/10.1103/PhysRevA.86.040501`.

[66] T. F. Gallagher and W. E. Cooke. Interactions of blackbody radiation with atoms. *Phys. Rev. Lett.*, 42:835–839, Mar 1979. doi: 10.1103/PhysRevLett.42.835. URL `http://link.aps.org/doi/10.1103/PhysRevLett.42.835`.

[67] W. E. Cooke and T. F. Gallagher. Effects of blackbody radiation on highly excited atoms. *Phys. Rev. A*, 21:588–593, Feb 1980. doi: 10.1103/PhysRevA.21.588. URL `http://link.aps.org/doi/10.1103/PhysRevA.21.588`.

[68] P.R. Koch, H. Hieronymus, A.F.J. VanRaan, and W. Raith. Direct observation of the interaction between Rydberg atoms and blackbody radiation. *Physics Letters A*, 75: 273–275, Jan 1980.

[69] William P. Spencer, A. Ganesh Vaidyanathan, Daniel Kleppner, and Theodore W. Ducas. Measurements of lifetimes of sodium Rydberg states in a cooled environment. *Phys. Rev. A*, 24:2513–2517, Nov 1981. doi: 10.1103/PhysRevA.24.2513. URL `http://link.aps.org/doi/10.1103/PhysRevA.24.2513`.

[70] John W. Farley and William H. Wing. Accurate calculation of dynamic Stark shifts and depopulation rates of Rydberg energy levels induced by blackbody radiation. Hydrogen, helium, and alkali-metal atoms. *Phys. Rev. A*, 23:2397–2424, May 1981. doi: 10.1103/PhysRevA.23.2397. URL `http://link.aps.org/doi/10.1103/PhysRevA.23.2397`.

[71] I. L. Glukhov and V. D. Ovsiannikov. Thermal photoionization of Rydberg states in helium and alkali metal atoms. *J. Phys. B: At. Mol. Opt. Phys.*, 42(7):075001, January 2009.

[72] I. L. Glukhov, E. A. Nekipelov, and V. D. Ovsiannikov. Blackbody-induced decay, excitation and ionization rates for Rydberg states in hydrogen and helium atoms. *J. Phys. B: At. Mol. Opt. Phys.*, 43(12):125002, June 2010.

[73] T. F. Gallagher, L. M. Humphrey, W. E. Cooke, R. M. Hill, and S. A. Edelstein. Field ionization of highly excited states of sodium. *Phys. Rev. A*, 16:1098–1108, Sep 1977. doi: 10.1103/PhysRevA.16.1098. URL `http://link.aps.org/doi/10.1103/PhysRevA.16.1098`.

[74] Xiaoxu Lu, Yuan Sun, and Harold Metcalf. Rydberg atom spectroscopy enabled by blackbody radiation ionization. *Phys. Rev. A*, 84:033402, Sep 2011. doi: 10.1103/PhysRevA.84.033402. URL http://link.aps.org/doi/10.1103/PhysRevA.84.033402.

[75] U. Fano. Effects of configuration interaction on intensities and phase shifts. *Phys. Rev.*, 124:1866–1878, Dec 1961. doi: 10.1103/PhysRev.124.1866. URL http://link.aps.org/doi/10.1103/PhysRev.124.1866.

[76] A. Nussenzweig, E. E. Eyler, T. Bergeman, and E. Pollack. Line shapes of ionizing stark resonances in helium. *Phys. Rev. A*, 41:4944–4957, May 1990. doi: 10.1103/PhysRevA.41.4944. URL http://link.aps.org/doi/10.1103/PhysRevA.41.4944.

[77] B. W. Shore, J. Martin, M. P. Fewell, and K. Bergmann. Coherent population transfer in multilevel systems with magnetic sublevels. i. numerical studies. *Phys. Rev. A*, 52:566–582, Jul 1995. doi: 10.1103/PhysRevA.52.566. URL http://link.aps.org/doi/10.1103/PhysRevA.52.566.

[78] J. Martin, B. W. Shore, and K. Bergmann. Coherent population transfer in multilevel systems with magnetic sublevels. ii. algebraic analysis. *Phys. Rev. A*, 52:583–593, Jul 1995. doi: 10.1103/PhysRevA.52.583. URL http://link.aps.org/doi/10.1103/PhysRevA.52.583.

[79] J. Martin, B. W. Shore, and K. Bergmann. Coherent population transfer in multilevel systems with magnetic sublevels. iii. experimental results. *Phys. Rev. A*, 54:1556–1569, Aug 1996. doi: 10.1103/PhysRevA.54.1556. URL http://link.aps.org/doi/10.1103/PhysRevA.54.1556.

[80] Hong Yuan Ling, Yong-Qing Li, and Min Xiao. Coherent population trapping and electromagnetically induced transparency in multi-zeeman-sublevel atoms. *Phys. Rev. A*, 53:1014–1026, Feb 1996. doi: 10.1103/PhysRevA.53.1014. URL http://link.aps.org/doi/10.1103/PhysRevA.53.1014.

[81] Z. Kis, A. Karpati, B. W. Shore, and N. V. Vitanov. Stimulated Raman adiabatic passage among degenerate-level manifolds. *Phys. Rev. A*, 70:053405, Nov 2004. doi: 10.1103/PhysRevA.70.053405. URL http://link.aps.org/doi/10.1103/PhysRevA.70.053405.

[82] A. A. Rangelov, N. V. Vitanov, and B. W. Shore. Extension of the Morris-Shore transformation to multilevel ladders. *Phys. Rev. A*, 74:053402, Nov 2006. doi: 10.1103/PhysRevA.74.053402. URL http://link.aps.org/doi/10.1103/PhysRevA.74.053402.

[83] James R. Morris and Bruce W. Shore. Reduction of degenerate two-level excitation to independent two-state systems. *Phys. Rev. A*, 27:906–912, Feb 1983. doi: 10.1103/PhysRevA.27.906. URL http://link.aps.org/doi/10.1103/PhysRevA.27.906.

[84] S. H. Autler and C. H. Townes. Stark effect in rapidly varying fields. *Phys. Rev.*, 100 (2):703–722, Oct 1955.

[85] J. J. Sakurai. *Modern Quantum Mechanics*. Pearson Education Asia, Singapore, 2002.

[86] Petr M. Anisimov, Jonathan P. Dowling, and Barry C. Sanders. Objectively Discerning Autler-Townes Splitting from Electromagnetically Induced Transparency. *Phys. Rev. Lett.*, 107:163604, Oct 2011. doi: 10.1103/PhysRevLett.107.163604. URL http://link.aps.org/doi/10.1103/PhysRevLett.107.163604.

[87] R. Walser, H. Ritsch, P. Zoller, and J. Cooper. Laser-noise-induced population fluctuations in two-level systems: Complex and real Gaussian driving fields. *Phys. Rev. A*, 45:468–476, Jan 1992. doi: 10.1103/PhysRevA.45.468. URL http://link.aps.org/doi/10.1103/PhysRevA.45.468.

[88] H. Ritsch and P. Zoller. Atomic transitions in finite-bandwidth squeezed light. *Phys. Rev. Lett.*, 61:1097–1100, Aug 1988. doi: 10.1103/PhysRevLett.61.1097. URL http://link.aps.org/doi/10.1103/PhysRevLett.61.1097.

[89] C. W. Gardiner and P. Zoller. *Quantum Noise*. Springer, New York, 2000.

[90] S. Berger, M. Pechal, A. A. Abdumalikov, C. Eichler, L. Steffen, A. Fedorov, A. Wallraff, and S. Filipp. Exploring the effect of noise on the Berry phase. *Phys. Rev. A*, 87: 060303, Jun 2013. doi: 10.1103/PhysRevA.87.060303. URL http://link.aps.org/doi/10.1103/PhysRevA.87.060303.

[91] D. S. Elliott, M. W. Hamilton, K. Arnett, and S. J. Smith. Two-photon absorption from a phase-diffusing laser field. *Phys. Rev. Lett.*, 53:439–441, Jul 1984. doi: 10.1103/PhysRevLett.53.439. URL http://link.aps.org/doi/10.1103/PhysRevLett.53.439.

[92] M. W. Hamilton, K. Arnett, S. J. Smith, D. S. Elliott, M. Dziemballa, and P. Zoller. Saturation of an optical transition by a phase-diffusing laser field. *Phys. Rev. A*, 36: 178–188, Jul 1987. doi: 10.1103/PhysRevA.36.178. URL http://link.aps.org/doi/10.1103/PhysRevA.36.178.

[93] H. Ritsch and P. Zoller. Systems driven by colored squeezed noise: The atomic absorption spectrum. *Phys. Rev. A*, 38:4657–4668, Nov 1988. doi: 10.1103/PhysRevA.38.4657. URL http://link.aps.org/doi/10.1103/PhysRevA.38.4657.

[94] S. N. Dixit, P. Zoller, and P. Lambropoulos. Non-Lorentzian laser line shapes and the reversed peak asymmetry in double optical resonance. *Phys. Rev. A*, 21:1289–1296, Apr 1980. doi: 10.1103/PhysRevA.21.1289. URL http://link.aps.org/doi/10.1103/PhysRevA.21.1289.

[95] G. S. Agarwal. Quantum statistical theory of optical-resonance phenomena in fluctuating laser fields. *Phys. Rev. A*, 18:1490–1506, Oct 1978. doi: 10.1103/PhysRevA.18.1490. URL http://link.aps.org/doi/10.1103/PhysRevA.18.1490.

[96] J. H. Eberly. Atomic relaxation in the presence of intense partially coherent radiation fields. *Phys. Rev. Lett.*, 37:1387–1390, Nov 1976. doi: 10.1103/PhysRevLett.37.1387. URL http://link.aps.org/doi/10.1103/PhysRevLett.37.1387.

[97] P. Avan and C. Cohen-Tannoudji. Two-level atom saturated by a fluctuating resonant laser beam. calculation of the fluorescence spectrum. *Journal of Physics B: Atomic and Molecular Physics*, 10(2):155, 1977. URL http://stacks.iop.org/0022-3700/10/i=2/a=006.

[98] P. Zoller. Resonant multiphoton ionization by finite-bandwidth chaotic fields. *Phys. Rev. A*, 19:1151–1160, Mar 1979. doi: 10.1103/PhysRevA.19.1151. URL http://link.aps.org/doi/10.1103/PhysRevA.19.1151.

[99] P. L. Knight, W. A. Molander, and C. R. Stroud. Asymmetric resonance fluorescence spectra in partially coherent fields. *Phys. Rev. A*, 17:1547–1549, Apr 1978. doi: 10.1103/PhysRevA.17.1547. URL http://link.aps.org/doi/10.1103/PhysRevA.17.1547.

[100] A. T. Georges, P. Lambropoulos, and P. Zoller. Saturation and Stark Splitting of Resonant Transitions in Strong Chaotic Fields of Arbitrary Bandwidth. *Phys. Rev. Lett.*, 42:1609–1613, Jun 1979. doi: 10.1103/PhysRevLett.42.1609. URL http://link.aps.org/doi/10.1103/PhysRevLett.42.1609.

[101] P. Zoller. Saturation of two-level atoms in chaotic fields. *Phys. Rev. A*, 20:2420–2423, Dec 1979. doi: 10.1103/PhysRevA.20.2420. URL http://link.aps.org/doi/10.1103/PhysRevA.20.2420.

[102] A. L. Schawlow and C. H. Townes. Infrared and optical masers. *Phys. Rev.*, 112:1940–1949, Dec 1958. doi: 10.1103/PhysRev.112.1940. URL http://link.aps.org/doi/10.1103/PhysRev.112.1940.

[103] Robert D. Hempstead and Melvin Lax. Classical noise. vi. noise in self-sustained oscillators near threshold. *Phys. Rev.*, 161:350–366, Sep 1967. doi: 10.1103/PhysRev.161.350. URL http://link.aps.org/doi/10.1103/PhysRev.161.350.

[104] E. D. Hinkley and Charles Freed. Direct Observation of the Lorentzian Line Shape as Limited by Quantum Phase Noise in a Laser above Threshold. *Phys. Rev. Lett.*, 23: 277–280, Aug 1969. doi: 10.1103/PhysRevLett.23.277. URL `http://link.aps.org/doi/10.1103/PhysRevLett.23.277`.